HEAT RELEASE EFFECTS IN A TURBULENT, REACTING SHEAR LAYER

Thesis by
James Carl Hermanson

In Partial Fulfillment
of the Requirements for the Degree of
Doctor of Philosophy

California Institute of Technology
Pasadena, California

1985
(Submitted April 29, 1985)

ACKNOWLEDGEMENTS

It is a pleasure to thank my advisor, Professor P. E. Dimotakis, for years of guidance, encouragement, and patience. His enthusiasm during the course of this research was most appreciated. The expert advice and generous assistance of Dr. M. G. Mungal were invaluable in running the experiment and greatly appreciated. I would also like to thank Dr. G. L. Brown for introducing me to the problem, Professor H. W. Liepmann for his advice during my time at GALCIT, and Dr. J. E. Broadwell for many helpful comments. I am also very grateful for the help of C. E. Frieler and Dr. R. C. Miake-Lye in the successful running of the facility. Many months of technical assiatance were furnished by Mr. Earl E. Dahl and are gratefully acknowledged. I would also like to thank Professor L. Hesselink for his helpful advice in designing the schlieren system. I have benefited greatly from the many helpful discussions, ideas and especially the friendship of Drs. M. M. Koochesfahani, T. Rösgen and F. A. Roberts.

In addition, I am grateful to the entire GALCIT community. I am indebted to Dr. D. B. Lang for his electronics and computer genius, which were often vital to the success of this work, and also for the electrical assistance of Mr. Clarence B. Hemphill. Most of the figures were made by use of the plotting program written by Dr. J. M. Cimbala. I would especially like to thank Mrs. Linda Malaby and Mrs. Jackie Beard for many helpful moments and for their encouragement. The illustration help of Mrs. Betty Wood and the fine photographic work of Mr. Harry Hamaguchi are most appreciated. I am thankful for the support of Mr. George Lundgren and the Aero Machine Shop Staff.

The financial support by the California Institute of Technology is gratefully acknowledged. This research was sponsored by AFOSR Contract No. F49620- 79-

C-0159 and Grant No. AFOSR-83-0213.

Finally, I would like to especially thank my wife, Andrea, and my sister, Karen, for their love and patience, especially during many difficult times. Without their support completing this work would not have been possible. I would like to dedicate this thesis to my parents, Carl and Betty Hermanson, and also to the loving memory of my maternal grandfather, Walter L. McCambridge.

ABSTRACT

The effects of heat release were studied in a planar, gaseous reacting mixing layer formed between free streams containing hydrogen and fluorine in inert diluents. Sufficiently high concentrations of reactants were employed to produce adiabatic flame temperature rises of up to 940 K (1240 K absolute). The Reynolds number at the measuring station, based on velocity difference, 1% temperature thickness and cold kinematic viscosity was approximately 6×10^4. The temperature field was measured with cold wire resistance thermometers and thermocouples. Flow visualization was accomplished by schlieren spark and motion picture photography. Mean velocity information was extracted from mean pitot probe dynamic pressure measurements.

Though the displacement thickness of the layer, for zero streamwise pressure gradient, increased with increasing heat release, the actual growth rate of the layer did not increase, but instead decreased slightly. The overall entrainment into the layer was seen to be substantially reduced as a consequence of heat release. Calculations showed that the decrease in layer growth rate can be accounted for by a corresponding reduction in turbulent shear stress.

The mean temperature rise profiles, normalized by the adiabatic flame temperture rise, were not greatly changed in shape by heat release. A small decrease in normalized mean temperature rise with heat release was observed. Large scale coherent structures were observed to persist at all levels of heat release in this investigation. The mean structure spacing decreased with increasing temperature. This decrease exceeded the rate of layer growth rate reduction, and suggests that the mechanisms of vortex amalgamation were, to some extent, inhibited by heat release.

Imposition of a favorable pressure gradient resulted in additional thinning of the layer, and caused a slight increase in the mixing and amount of chemical product formation. The change in layer growth rate can be shown to be related to a change in free stream velocity ratio induced by pressure gradient.

TABLE OF CONTENTS

LIST OF FIGURES

LIST OF SYMBOLS

Symbol	Description
A_0	contraction exit area
A_1^*, A_1^*	high speed, low speed sonic metering throat area
$\hat{a}$	shear stress weighting parameter, § 4.1
$\tilde{a}$	vortex growth rate parameter, equation (5.13)
$b_1 - b_6$	mean velocity profile curve fit constants, equation (2.4)
$\hat{b}$	velocity profile shape parameter, equation (3.8)
$\hat{C}_p$	molar heat capacity
c	concentration, § 3.5
$c_1 - c_5$	mean temperature rise curve fit constants, equation (2.2)
c_{01}, c_{02}	high speed, low speed free stream reactant concentration
$\bar{c}_p$	mean concentration , equation (3.12)
$\hat{c}$	structure temperature weighting parameter, equation (4.12)
E_v	volumetric entrainment ratio, equation (3.18)
f	velocity-density function, § 4.1
g	gravitational acceleration
H	mixture enthalpy
h_1, h_2	high speed, low speed channel height, § 5.2
l	vortex spacing, § 3.6
$\hat{l}$	mixing length, equation (4.9)
P_c	concentration probability density function, § 3.5
P_m	mixed fluid probability, equation (3.12)
P_λ	vortex spacing probability, equation (3.3)
p	static pressure
p_0	external surge tank pressure

p_s	sidewall static pressure
p_t	measured pitot pressure
Δp	layer pressure decrement, equation (4.13)
ΔQ	molar heat of reaction
$\tilde{q}$	heat release parameter, § 3.5
R	mixture gas constant
Re_x	Reynolds number, $U_1 x / \nu$
Re_{δ_1}	Reynolds number, $\Delta U \delta_1 / \nu$
Ri	Richardson number, $\frac{\Delta\rho}{\rho_0} \frac{g \delta_1}{(\Delta U)^2}$
r	free stream velocity ratio, U_2 / U_1
s	free stream density ratio, ρ_2 / ρ_1
$\hat{s}$	density function, § 4.1
ΔT	temperature rise
ΔT_F	adiabatic flame temperature rise
ΔT_{MAX}	maximum temperature rise per data record, § 3.5
$\overline{\Delta T}$	mean temperature rise, equation (2.2)
$\overline{\Delta T}_{MAX}$	maximum mean temperature rise, § 3.2
$< \overline{\Delta T} >$	mean temperature in layer, 3.5
t	time
U	mean streamwise velocity
U_1, U_2	high speed, low speed free stream velocity, Figure 3.1
U_{01}, U_{02}	high speed, low speed reference velocity, equation (5.4)
ΔU	velocity difference, $U_1 - U_2$
u	streamwise velocity, § 3.1
V	mean transverse velocity
V_1, V_2	high speed, low speed transverse velocity, Figure 3.1
$\dot{V}$	total volumetric entrainment rate per unit span, § 3.3

$\tilde{V}$	mass weighted transverse velocity, equation (3.1)
Ve	local entrainment velocity, equation (5.11)
Ve_1	high speed entrainment velocity, equation (3.16)
Ve_2	low speed entrainment velocity, equation (3.17)
v	transverse velocity, § 3.1
$\hat{v}$	transverse fluctuating velocity function, $\frac{\overline{v'^2}}{\Delta U^2}$, § 4.2
x	streamwise coordinate, Figure 3.1
x_0	virtual origin, Figure 3.1
y	transverse coordinate, Figure 3.1
β	low speed sidewall deflection angle, Figure 3.1
γ	mixture specific heat ratio
$\hat{\gamma}$	shear layer intermittency, § 3.3
δ	layer characteristic width, § 3.1
$\delta_{P_{1,2}}$	product fraction thickness, equation (3.20)
δ_{viz}	shear layer visual thickness, § 3.2
δ_ω	vorticity or maximum slope thickness, equation (3.7)
δ_1	shear layer 1% thickness, Chapter 3
δ_{10}	shear layer 10% thickness, § 3.3
δ^*	displacement thickness, equation (3.3)
$\delta^*_{P_{1,2}}$	total product thickness, equation (3.28)
ε	layer growth rate parameter, equation (3.6)
η	similarity variable, $y/\delta(x)$
η_h	arbitrary point outside layer, equation (3.4)
η_0	dividing streamline, equation (3.5)
η_1, η_2	layer high speed, low speed edge, Figure 3.1
θ_1	high speed splitter plate boundary layer momentum thickness

Λ	layer growth parameter, equation (5.2)
λ	normalized vortex spacing, l / δ_1
μ	viscosity, § 4.4
μ_t	eddy viscosity, equation (4.9)
ν	kinematic viscosity
Π	pressure gradient parameter, $\frac{dp / dx}{\rho_0 U_{02}^2}$, equation (5.6)
ρ	density
$\bar{\rho}$	mean density in layer
ρ_0	average free stream density, $(\rho_1 + \rho_2) / 2$
ρ_1, ρ_2	high speed, low speed free stream density
ρ^*	large structure density, § 4.1
$\Delta\rho$	maximum density difference, § 2.4
σ^2	variance of vortex spacing histogram, § 3.6
$\hat{\sigma}$	Bernal shape parameter, § 3.6
τ	turbulent shear stress, § 4.1
τ_{MAX}	peak value of shear stress, § 4.1
τ_0	cold flow turbulent shear stress, equation (4.11)
φ	equivalence ratio, c_{02} / c_{01}, equation (2.5)
ψ	stream function, equation (4.5)
ω	vorticity, § 4.3
$\hat{\omega}$	viscosity exponent, § 4.4

Appendix A and Appendix B Symbols

c_w	probe wire specific heat
D	probe wire diameter
G_{ik}	mixture function, equation (B.13)

h	probe heat transfer coefficient
I	cold wire current
k_g	gas thermal conductivity
k_i	gas mixture component thermal conductivity
k_{mix}	gas mixture thermal conductivity, equation (B.12)
k_w	probe wire thermal conductivity
L	probe wire length
L_t	exposed support prong length, equation (A.11)
L^*	support prong heat diffusion length, equation (A.11)
$\hat{M}$	species molar mass
Nu	Nusselt Number
R	probe wire resistance
R_p	support prong resistance, equation (A.11)
T	gas temperature
T_p	support prong temperature
T_w	probe wire temperature
T_1, T_2	model high and low temperatures, Figure B.1
α	first coefficient of resistivity
α_p	prong material resistivity
β	second coefficient of resistivity
β_1	heat transfer parameter, equation (A.3)
$\hat{V}$	$\frac{\Delta V}{\Delta T}$ in linear range, § A.3
ΔV	Voltage Rise
ε_w	probe wire emissivity
η, η_1	heat transfer parameters, equation (A.1)
λ_0	Kolmagorov scale
μ_i, μ_k	species viscosity
ρ_w	probe wire density

σ	Stefan-Boltzmann constant
τ_1, τ_2	probe characteristic time, § B.1
χ	mixture component number fraction

Appendix C Symbols

C_p	mass specific heat capacity
c_0^*	concentration for normalization, equation (C.20)
D_i	mass diffusivity of species i
f^*	mass stoichiometric ratio
Le_i	Lewis Number, $\frac{\rho C_p D_i}{k_i}$
$\dot{m}_i$	reactant mass consumption rate of reactant i
n_0	ambient number density
$\dot{n}_i$	number consumption rate of reactant i
q	heat of reaction per unit mass
U	velocity parallel to flame zone
V	velocity normal to flame zone
x	coordinate parallel to flame zone
y	coordinate normal to flame zone
ε, ε_0	strain rate
ζ_1, ζ_2	flame zone variable, equation (C.10)
Θ	ratio of ambient mass diffusivities
κ_i	mass fraction of reactant i
ρ	total mass density
ρ_i	mass density, species i
τ,t	time
φ^*	concentration ratio parameter, $\frac{\kappa_{01}}{\kappa_{02}} \frac{1}{f^*}$

φ^*_i inferred concentration ratio parameter

$\hat{\xi}, \xi^*$ Howarth transformation variables, equations (C.2), (C.7)

ξ_φ concentration parameter, $\varphi^*/(1+\varphi^*)$

Appendix D Symbols

A Arraneus Factor, Table D.1

a temperature exponent, Table D.1

Da_x Damköhler number, $\frac{\tau_x}{\tau_{chem}}$

$Da_{\delta 1}$ Damköhler number, $\frac{\tau_{\delta_1}}{\tau_{chem}}$

k reaction rate constant

k_0 reference reaction rate, Table D.1

U_c convection velocity, $(U_1 + U_2)/2$

τ_{chem} characteristic chemical time

τ_x time of flight

τ_{δ_1} large scale characteristic time

Modifiers

$\overline{(\,)}$ time averaged quantity

$(\,)'$ fluctuating quantity

$(\,)_{0,01,02}$ ambient or free stream quantity

$\vec{(\,)}$ vector quantity

$\Delta(\,)$ change in quantity

$(\,)^*$ F_2 carrying free stream, Appendix B;
quantity at flame zone, Appendix C

Chapter 1

INTRODUCTION

1.1. Background

Combustion processes in turbulent flows are of great interest and have significance in many practical applications. As chemical reactions can occur only when fluids are molecularly mixed, understanding the flow processes leading to mixing is vital to the understanding of turbulent combustion. In many cases, the amount of chemical product formed and heat released as a result of mixing is limited by the entrainment of species into the layer, which is itself related to the dynamics of the turbulent flow structure.

A major advance in understanding turbulent shear flow was the discovery that the flow processes in a shear layer are dominated by large scale coherent structures. This was reported by Brown & Roshko [1974] in a high Reynolds number gas phase shear layer and also by Winant & Browand [1974] and Dimotakis & Brown [1976] in liquid shear layers. The discovery of large scale coherence has motivated new measurements of composition. Konrad [1976] measured the probability density function of the concentration of individual species in a nonreacting gas shear layer. Those results allowed estimation of the amount of product that would be obtained in a chemically reacting shear layer. Another significant finding reported in that work was an asymmetry in the shear layer entrainment, with more high speed than low speed fluid entrained. Detailed concentration measurements were performed in a liquid shear layer by Koochesfahani [1984]. Those measurements indicated that the transport in the layer is dominated by large scale structures. It was also shown that, at high Reynolds numbers, the composition of the mixed fluid appears to be quite uniform within

the individual structures.

The amount of mixing and product formation in a gaseous shear flow with chemical reaction was studied by Mungal & Dimotakis [1984], utilizing the hydrogen-fluorine reaction. That investigation was conducted under the conditions of low heat release, with no apparent coupling between heat release and the fluid mechanics. Exploratory reacting shear layer studies in liquid were performed by Dimotakis & Brown [1976] and more systematically by Breidenthal [1978], who determined the integral amount of product in the layer, and by Koochesfahani [1984], who was able to provide detailed measurements of product concentration and its average profile across the layer.

Much of the recent research in flows with combustion has been directed towards understanding the effects of the flow field on the combustion process. The effect of the flow field on small flame elements has led to the development of analytical models, for example, the strained-flame models of Marble & Broadwell [1977] and Broadwell & Breidenthal [1982], which have made substantial contributions to the understanding of reacting shear flows. Little research effort has been directed, however, at the reverse problem: understanding how the combustion processes affect the flow field, that is, the layer growth, entrainment, and large scale structure dynamics. The study of these effects was the focus of the present investigation.

An investigation into the effects of heat release was conducted by Wallace [1981] who used the nitric oxide-ozone reaction to study the mixing and combustion in a reacting shear layer. The maximum adiabatic flame temperature rise attained during that investigation was about 400 K. Studies in reacting shear layers at high temperatures ($\approx$ 1400 K flame temperature rise) were performed by Ganji & Sawyer [1979], Keller & Daily [1983] and Pitz & Daily [1983]. In all of these investigations large scale structures were observed to

persist in the flow at high temperatures.

The present work is a sequel to the low heat release experiments of Mungal & Dimotakis [1984], and can be considered to fill the gap between the low heat release studies of Mungal & Dimotakis [1984], and Wallace [1981], and the high heat release investigations of Ganji & Sawyer [1980], Keller & Daily [1983] and Pitz & Dailey [1983]. The reactants employed in the present experiments, hydrogen and fluorine, allowed the systematic study of heat release effects over a wide range of temperatures. In this work the flame temperature rise ranged from 186 K to 940 K.

1.2. Research Program Objectives

The objective of this work was to determine the effects of heat release due to combustion in a reacting shear layer. Specifically, this work studied the effects of heat release on the layer growth and entrainment, the amount of mixing and chemical product formation, and the large scale structure dynamics.

It is not obvious a priori whether the release of heat by a reacting flow would serve to increase or decrease the growth rate of a shear layer. The earlier results of Wallace [1981] suggested a slight decrease in layer growth rate with increasing heat release. Wallace [1981] also found some decrease in layer entrainment with heat release. The total amount of entrainment is of course directly related to the growth rate of the layer. An interesting question is how the entrainment ratio might be altered by heat release. Growth and entrainment information in the present study was obtained from mean temperature and velocity profiles, as well as by schlieren flow visualization.

Different methods exist for measuring or inferring the amount of mixing that occurs in a shear layer. Two methods which have been employed are the so-called passive scalar technique and the chemical reaction technique. In the

passive scalar technique (see e.g. Konrad [1976]), the concentration of a nonreacting entity in the fluid (e.g. dye or a selected species) is measured and then used to determine the amount of mixing (Konrad [1976], Rebollo [1973] in gases; Koochesfahani [1983] in liquids). The chemical reaction method relies on the molecular mixing to allow the formation of some sort of product, which once measured is used to infer the amount of molecular mixing that occurred (in gas, Wallace [1981], Mungal & Dimotakis [1984], Briedenthal [1978]; in liquid Koochesfahani [1984]). The present work used the chemical reaction technique, with the measured temperatures used to determine the amount of product formed.

The existence of large scale structures as a characteristic of turbulent shear flows has become increasingly well accepted. Statistical investigations of the large scale motion have been undertaken in the cases of turbulent shear layers without heat release (Brown & Roshko [1974], Bernal [1981]) which have documented the convection trajectories and the spacings of the structures. How heat release affects these features was investigated in the present work by use of schlieren motion picture flow visualization.

The effects of pressure gradient in conjunction with high heat release was also investigated. The effects of pressure gradient in reacting flow are of interest because many practical devices have fixed geometry and do not have a means of manipulating the pressure gradient. Some investigators, for example Bray & Libby [1981] and Spalding [1984] have suggested that a pressure gradient might serve to enhance the mixing and combustion in a reacting flow. The effects of pressure gradient on the layer growth and flow structure were investigated by Rebollo [1973] in a nonreacting shear flow. In some cases reported in the present work, a favorable pressure gradient was imposed on the flow. The

layer growth, entrainment, large structure dynamics and product formation under these conditions were investigated.

Chapter 2

EXPERIMENTAL FACILITY AND INSTRUMENTATION

2.1. Flow Apparatus

The experiments described here were conducted in the blow-down facility documented by Mungal & Dimotakis [1984]. A planar shear flow was established between free streams resulting from the discharge of separate volumes of fluorine in an inert diluent and hydrogen in an inert diluent. The hydrogen-fluorine reaction has the advantages of simple and fast chemistry, high exothermicity, and the ability to be sustained over a wide range of reactant concentrations. A small concentration of nitric oxide was included in the hydrogen-carrying stream to help sustain proper ignition. The species under these conditions can be regarded as reacting spontaneously upon becoming molecularly mixed, thus eliminating the need for ignitors and flame holders. Details of the hydrogen-fluorine reaction are presented in Appendix D.

A schematic overview of the facility is shown in Figure 2.1. The charges of chemicals for each run were loaded into two separate gastight Teflon FEP bladder bags, each of which is contained in a Teflon coated steel reactant tank of 0.57 m^3 volume. The desired concentrations of each species were obtained by a partial pressure technique. The loading procedure was estimated to be accurate in absolute concentration to $3-5\%$ by Mungal & Dimotakis [1984]. The reactant tanks are pressurized by an external surge tank of 12.7 m^3 volume.

In this investigation, most runs were conducted with nominally matched free stream densities. To offset the density difference that would have resulted from varying amounts of hydrogen in one stream, the densities of the free streams

were matched for most cases by using as a diluent a mixture of nitrogen and a small amount of helium, on the fluorine side, and a mixture of nitrogen and a small amount of argon on the hydrogen side. The intent of this procedure was also to match the heat capacities of the two free streams, allowing the measured temperature rise to be simply related to the heat release in the flow. Details of matching gas mixture properties are provided in Appendix B.

The gas mixtures were discharged through sonic orifices into the contraction section. The sonic orifices ensured choked flow and served to decouple the mixture supplies from the downstream sections of the facility. The mass flux therefore depended only upon the conditions in the large external surge tank. During a typical run, the pressure decrease in the external tank caused the mass fluxes to decrease by about 5%, corresponding to a change in mass flux during the data acquisition interval of about 1%. See also Mungal & Dimotakis [1984].

In order to keep the free stream conditions constant from run to run, the throat areas of the sonic metering orifices were adjusted to minimize variations in free stream velocity which could have resulted from the differences in gas properties of the various mixtures employed. The sonic metering valve open area, A_i^*, was estimated by the following formula:

$$A_i^* = \frac{(R\,T_0)^{\frac{1}{2}}}{P_0\,\Gamma(\gamma)}\,\rho_i\,U_i\,A_i \quad , \quad \Gamma(\gamma) \equiv \gamma^{\frac{1}{2}}\left[\frac{2}{\gamma+1}\right]^{\frac{1}{2}\left[\frac{\gamma+1}{(\gamma-1)}\right]} , \tag{2.1}$$

where:

R = mixture gas constant

T_0 = ambient temperature

p_0 = external surge tank pressure

γ = mixture specific heat ratio

ρ_i = free stream density

U_i = free stream velocity

A_i = contraction exit area

Each stream entered a Teflon TFE lined settling and contraction section for turbulence suppression. The high speed stream emerged from a 6:1 contraction with an exit area of 5×20 *cm*; and the low speed stream, from a 4:1 contraction in a 7.5×20 *cm* exit area. The two streams met at the tip of a horizontal stainless steel splitter plate, with a trailing edge included angle of 3.78°. The high speed free stream turbulence level was cited by Mungal, Dimotakis & Broadwell [1984] to be about 2/3%.

The high speed upper sidewall was fixed for all runs at 0° (horizontal) and the divergence angle of the low speed lower sidewall was adjusted before each run for the desired streamwise pressure gradient. The wedge-like geometry of the planar shear layer displacement allow this simple means of accommodating or imposing any desired pressure gradient. Externally controlled actuators were installed to allow adjustment of the wall divergence without the need to open the test section. The contraction and test section dimensions are indicated in Figure 2.2. A new contraction on the low speed side was constructed to ensure that enough test section wall divergence was available at the highest expected levels of heat release for this investigation.

The test section vertical sidewalls, through which the flow was viewed, consisted of a 1 *inch* (25 *mm*) thick outer Pyrex plate (Corning borosilicate 7740) combined with an inner sacrificial 1/8 *inch* (3.2 *mm*) thick polished Pyrex

sheet. The inner sheets became etched by the flow and were periodically replaced. Pyrex was selected for its thermal toughness, high strength, and relatively low cost. Unfortunately, Pyrex is not an especially good material for optical visualization. This was not a serious problem for the present work due to the large optical signal strength at high heat release. Further, the thick outer plate was optically polished to help improve the flow visualization results.

The test section is connected to the exhaust gas catch bags by a 51 *cm* diameter stainless steel duct with a high pressure atomizing spray system, which cooled and partially neutralized the hot exhaust flow with an aqueous sodium hydroxide solution. A photograph of the facility, showing the contraction, test section and exhaust duct, is shown in Figure 2.3. Additional photographs of the facility can be found in Mungal [1983].

The exhaust collection system consists of a double set of catch bags. The inner bags are of Teflon FEP film, 0.005 *inch* (0.13 *mm*) thick, with a total capacity of approximately 13 m^3. For additional safety in handling high concentrations of hydrogen and fluorine, each inner bag is completely enclosed in an outer bag made of Dupont Tedlar film, 0.004 *inch* (0.10 *mm*) thick. Tedlar was selected for its high strength, low cost, and excellent weatherability, and it also has good resistance to fluorine and hydrogen fluoride. All bags in the facility were fabricated in house with an Accuseal Series 60 heat sealing machine. The interspaces between the two sets of bags were purged with nitrogen to help sweep away any exhaust gases which might escape the inner bag. The interspaces were positively vented by an air ejector connected to a sodium hydroxide scrubber bath to remove any reaction products before venting to the atmosphere. The exhaust gases in the catch bags were scrubbed after each run to remove any remaining toxic components after which inerts and any unreacted hydrogen were vented to the atmosphere.

2.2. Diagnostics

Five diagnostic techniques were employed during the course of this investigation: schlieren/shadowgraph flow visualization, cold-wire resistance thermometer and thermocouple temperature measurement, pitot probe mean dynamic pressure transverse profile measurement, and two-point streamwise pressure gradient measurement.

2.2.1. *Flow Visualization.* An optical system was constructed for the facility to allow schlieren/shadowgraph flow visualization. The schlieren method is more sensitive than the shadowgraph technique and is better suited to low heat release runs. At higher heat release, enough optical thickness variation was present in the flow to permit shadowgraphy, but it was found for the conditions of this investigation that the schlieren technique resulted in better large scale structure resolution. The schlieren/shadowgraph system is shown in Figure 2.4.

The system is a variation of the schlieren system employed by Liepmann [1947]. The folded configuration utilized was selected for two reasons: first, to allow the entire optical system to be housed in a single box assembly; and second, to permit easy positioning of the optics. This allowed selection of the portion of the flow to be photographed and also provided access to the test section without dismantling and realigning the optical setup.

The schlieren heads are 10 *inch* (254 *mm*) diameter f6.5 spherical mirrors (Scott Optical), and the lower mirrors are 14.5 *inch* (368 *mm*) diameter circular flat mirrors (Drews Optical). All mirrors in the system were figured to one tenth of a wavelength of visible light. The entire setup is housed in a wooden box, reenforced for strength and rigidity. A 5 *mW* He-Ne laser (Spectra Physics Model 155A) was employed periodically to aid in optical alignment. It was found, however, that the wooden structure was sufficiently stable so that realignment was seldom required.

High time resolution spark photographs were taken with a spark source ($\approx$ 3 μsec *duration*), synchronized with a motor-driven 35 mm camera, at a rate of approximately three frames per second. Motion picture data were taken with a high-speed pin register camera (Teledyne Model DBS 55) at a rate of 450 frames per second. Illumination was provided by a 200 *Watt* continuous mercury vapor lamp (Ealing Stabilarc 250 Lamphouse, with a 250 *Watt* Universal Power Supply).

A circular source mask and a circular hole spatial filter were used in place of the conventional source slit and knife edge in an effort to give equal weights to gradients in index of refraction in all directions and thus better resolve the large scale structure of the flow. The hole sizes were increased with increasing flow temperature to optimize (reduce) sensitivity as needed. Some of the design criteria for the schlieren system were suggested by the discussion in Merzkirch [1974]; the final design benefitted from discussions with L. Hesselink, presently at Stanford University.

2.2.2. *Temperature Measurement.* Temperature data were recorded with a rake of eight 2.5 μm diameter platinum-10% rhodium cold wires, with a typical wire span of 1.5 mm, welded to Inconel prongs of 0.014 *inches* (0.36 mm) diameter. This was the same type of probe employed by Mungal & Dimotakis [1984]. The welding was accomplished with a Unitek 60 microwelder power supply. The wires were run with a constant current of 0.4 mA, which produced, under conditions of natural convection, an estimated 0.2 K overheat. This was negligible compared with the combustion temperatures measured and, as a consequence, the probe sensitivity was independent of velocity to a very good approximation.

It was found that the 2.5 μm resistance wires in the hottest regions did not survive runs in which the adiabatic flame temperature rise exceeded approximately 600 K (900 K absolute). For this reason, a rake of 25 μm Chromel-

Alumel thermocouples was employed for the hottest runs. The leads of the 25 μm thermocouple junctions (Omega Engineering CHAL-001) were welded to prongs consisting of Chromel and Alumel wires of 0.010 *inches* (250 μm) diameter. Figure 2.5 shows construction details for both the cold wire and thermocouple probes.

Both the cold wire and thermocouple rakes were positioned across the transverse extent of the layer. The spacing for both types of probes was nominally 0.97 cm. The total data rate for the resistance wires was 80 kHz, corresponding to 10 kHz per probe. This rate was comparable with the estimated frequency response of the wires and was selected to give the desired amount of data during the data acquisition interval. The length of the data acquisition interval was selected to ensure the passage of a minimum number of large scale flow structures (typically about 140). The thermocouples were sampled at 500 Hz each, for a total data rate of 4 kHz; their considerably lower frequency response than the resistance wires did not warrant a higher rate.

Thermocouples produce a voltage proportional to the junction temperature and normally do not require calibration. The resistance wires were calibrated as described in Mungal, Dimotakis & Broadwell [1984] using a hot and cold jet of known temperature. Both types of probes produce accurate mean temperatures; estimates of the amount of error caused by conduction, radiation, and other effects, are presented in Appendices A and B. The temperatures measured by the thermocouples were typically within 5% of the mean temperatures indicated by the cold wires under the same run conditions.

Following Mungal & Dimotakis [1984], a function of the form

$$\overline{\Delta T} = \exp(c_1 + c_2 y + c_3 y^2 + c_4 y^3 + c_5 y^4) \qquad (2.2)$$

was employed to represent the mean temperature profile. This function generally provided a good fit to the mean temperature rise data. The coefficients for the present investigation were determined by a nonlinear least squares fit and representative values are tabulated in Appendix E.

A typical circuit for temperature signal amplification is shown in Figure 2.6. Note that this circuit allows for selectable impedance matching suitable for either cold wire or thermocouple input. The circuit also contains a third-order low-pass Butterworth filter whose knee (3 dB down point) was set to 8 kHz.

2.2.3. *Velocity Measurement.* The mean velocity was extracted from the mean dynamic pressure profile, which was measured by a pitot probe rake of fifteen probes connected to a miniature manometer bank filled with a fluorine resistant oil (Hooker Chemical Fluorolube FS-5). The bank had an adequate time response to yield a reliable mean dynamic pressure profile during each run. The 17 manometer tubes were sized to be critically damped with an inside diameter of 3 mm. The two outermost tubes were connected to a static port on the low speed sidewall at x = 43.7 cm and were used to provide static references for the other 15 tubes. The bank was photographed by a second motor-driven 35 mm camera. The photographic data were digitized using a Hewlett-Packard HP9874 digitizer and processed to yield dynamic pressure profiles. This technique of measuring the pitot pressure was estimated to be accurate to approximately 5%.

The mean velocity was extracted from the mean dynamic pressure profile by using the relation:

$$U = \left[2R\,(\overline{\Delta T} + T_0)(p_t - p_s)/p_s \right]^{\frac{1}{2}} \tag{2.3}$$

where

R = mixture gas constant

p_s = test section static pressure

p_t = measured mean pitot pressure

$\overline{\Delta T}$ = measured mean temperature rise

Ignoring differential diffusion effects, the gas constant can be determined by the mixture molecular weight, which is exactly known when the free stream densities are equal. In cases where the free stream mixture molecular weights were not exactly equal, the molecular weight of the mixture in the layer was estimated by modeling the mean distribution of each free stream component across the layer with an error function profile. In this calculation the flow could be taken to be nonreacting, since the hydrogen-fluorine reaction does not cause a change in mixture molecular weight.

The calculated velocities for each photographic frame were carefully examined to determine the time of settling of the manometer bank, and only those frames after settling occurred were averaged into the final result. A nonlinear least squares curve fit was applied to the resulting data to represent the mean velocity profile in the form:

$$U(y) = b_5 \tanh\left[b_1 + b_2 y + b_3 y^2 + b_4 y^3 \right] + b_6 \quad . \tag{2.4}$$

Rebollo [1973] estimated that the accuracy of extracting mean velocities from

pitot and test section sidewall static pressures in non-constant density flows is about 4 – 5 %. This error estimate was made by estimating the contributions to the mean measured pitot pressure by the fluctuations correlations $\rho\overline{u'^2}$, $\rho\overline{v'^2}$, and $\overline{\rho' u'}$. The magnitudes of these correlation terms were estimated by Rebollo from his experimental data, which were for a flow with a free stream density ratio of $\rho_2/\rho_1 = 7$. In the present experiment, the density ratio of the cold free streams to the hot layer center is at most three, suggesting that the Rebollo error estimate represents an upper bound under these conditions.

2.2.4. *Sidewall Static Pressure.* The static pressure was measured on low speed lower sidewall at two downstream locations (x = 5.1 cm, x = 30.0 cm) and recorded as a differential by use of a Datametrics type 573 fluorine resistant barocel sensor and a Datametrics type 1013 Modular Signal Conditioner, with the output signal recorded on a strip chart by a Gould Recorder 110. Most of the runs in the present investigation were performed with the sidewalls adjusted to the requisite divergence angle to ensure a zero streamwise pressure gradient. With experience it was possible to anticipate the proper wall setting for the desired pressure gradient. For some runs, the walls were left fixed at the angle required for zero pressure gradient at zero heat release, which allowed the heat release to induce a favorable streamwise pressure gradient (accelerating flow), as a result of the combustion displacement effects. For runs at nominally zero streamwise pressure gradient, the low speed free stream velocity was typically constant to within 3 % throughout the test section.

2.3. Computer Data Acquisition

The temperature data were taken and recorded using the HYDRA-1 system which was designed and integrated by P.E. Dimotakis and D.B. Lang. The system has a Digital Equipment Corporation LSI 11/23 CPU and a Data Translation DT 3362 12 bit, 32 channel A/D converter. The DT3362 has a maximum throughput

rate of 250 kHz. The system also has a Datasouth DS-180 line printer, a Hewlett-Packard HP9872 plotter, and an Andromeda DAC-11 D/A converter. The D/A converter was used by the computer to furnish signal pulses which controlled the run sequence by opening and closing the main opening valves and initiating the data acquisition at preselected times. The motor-driven cameras were also activated in this manner. Post-run data processing was also accomplished on the system, which involved removing pre-run offsets and applying either a calibration constant for the thermocouples or a conversion formula (derived in Appendix A) to the cold output signal.

2.4. Run Conditions

The nominal flow velocities for this investigation were:

$$U_1 = 22\ m/s\ ,\ U_2 = 8.8\ m/s,\ r \equiv U_2/U_1 = 0.40\ ,$$

with equal free stream densities, i.e.,

$$s \equiv \frac{\rho_2}{\rho_1} = 1\ ,$$

at one atmosphere pressure.

One advantage of employing the hydrogen-fluorine reaction is that combustion can be sustained over a wide range of reactant concentrations. Reactant concentrations ranged from 2% fluorine and 2% hydrogen up to 6% fluorine and 24% hydrogen, with adiabatic flame temperature rises in the range

$$186K \leq \Delta T_F \leq 939K\ ,$$

resulting in maximum mean temperature rises in the range

$$124K \leq \overline{\Delta T}_{MAX} \leq 550K \quad .$$

The corresponding peak density changes were

$$0.30 \leq \frac{\Delta\rho}{\rho_0} \leq 0.65 \quad ,$$

where $\Delta\rho$ is the density difference between the cold free streams and the minimum mean density in the layer.

The equivalence ratio, φ, is defined here as the ratio of the low speed free stream molar concentration, c_{02}, to the high speed free stream molar concentration, c_{01}, divided by the low speed to high speed molar stoichiometric ratio:

$$\varphi \equiv \frac{(c_{02}/c_{01})}{(c_{02}/c_{01})_s} \quad , \tag{2.5}$$

or,

$$\varphi = \frac{c_{02}}{c_{01}} \quad , \tag{2.6}$$

since the hydrogen-fluorine stoichiometric ratio is unity. Equations (2.5) and (2.6) can be thought of as representing the volume (or mass) of high speed free stream fluid necessary to completely react with a unit volume (or mass) of low speed free stream fluid. Volume and mass, if differential diffusion effects are ignored, are interchangeable in this discussion because the free stream densities in this experiments were nominally equal. For this investigation, the

equivalence ratio was in the range $\varphi = 1$ to $\varphi = 1/8$, with the lean reactant, fluorine, always on the low speed side of the layer. As the heat release was increased, it was determined that no obvious deviation from the simple trends with heat release (to be discussed later) warranted extending the heat release further. This consideration, in addition to issues of safety, restricted the use of high speed free stream hydrogen concentrations in excess of 24%; hence for the higher levels of heat release the extreme value of equivalence ratio was $\varphi = 1/4$.

The measuring station for the cold wires and pitot probes was 45.7 *cm* downstream of the splitter plate trailing edge for all runs. The thermocouple rake was normally positioned at $x = 44.8\ cm$. The local Reynolds number at the measuring station was typically

$$\mathrm{Re}_{\delta_1} \equiv \Delta U\, \delta_1/\nu \approx 6\times10^4 \quad , \tag{2.7}$$

where $\Delta U = U_1 - U_2$, δ_1 is the width indicated by the 1% level of the mean temperature profile, and ν is the cold free stream kinematic viscosity. This value of the Reynolds number is well above that for the mixing transition as reported by Konrad [1976], Breidenthal [1978] and Bernal et al. [1979]. The corresponding Reynolds number based on the high speed free stream velocity and on the downstream distance was typically $\mathrm{Re}_x \equiv U_1 x/\nu \approx 6\times10^6$. The momentum thickness of the high speed boundary layer on the splitter plate, θ_1, was calculated by Thwaite's method and yielded a Reynolds number based on momentum thickness of $U_1\theta_1/\nu \approx 240$. At the measuring station the normalized distance to the splitter plate was estimated to be

$x/\theta_1 \approx 2800$. This is substantially larger than the value of $x/\theta_1 = 1000$ which Bradshaw [1966] suggests may be required for the layer to become self-similar. This value of x/θ_1 is in the range of other shear layer investigations, for example

$x/\theta_1 \approx 2300$ in Dimotakis & Brown [1976]; $x/\theta_1 \approx 2900$, in Browand & Latigo [1979]; and $x/\theta_1 \approx 4000$ for Brown and Roshko [1974].

A composite spark schlieren photograph of two different runs is shown in Figure 2.7. The flow is from left to right with the high speed free stream in the upper half of the figure. The splitter plate tip and the temperature and pitot probe rakes at the measuring station are visible at the extreme left and right edges of the figure, respectively.

All the flows in the present investigation are momentum dominated with negligible effects of buoyancy. The relative importance of buoyancy is indicated by the Richardson number:

$$Ri \equiv \frac{\Delta\rho}{\rho_0} \frac{g\,\delta_1}{(\Delta U)^2} \quad , \tag{2.8}$$

where g is the gravitational constant. For the present investigation, the maximum value of Richardson number is $Ri \approx 0.004$. Koop & Browand [1979] suggest that a minimum value of $Ri \approx 0.05$ is required for buoyancy to become important.

Chapter 3

RESULTS FOR ZERO STREAMWISE PRESSURE GRADIENT

3.1. Shear Layer Displacement

One consequence of heat release and the corresponding density reduction is that the outer flow will tend to be displaced away from the shear layer. The amount of this displacement can be calculated from the steady continuity equation. The continuity equation for this flow can be developed by expressing the components of velocity and density as the sum of mean and fluctuating parts, i.e., $\tilde{u} = U + u'$, $\tilde{v} = V + v'$ and $\tilde{\rho} = \rho + \rho'$, where the primes indicate the fluctuating parts. The mean quantities are shown with no diacritical marks. The resulting continuity equation is

$$\frac{\partial}{\partial x}(\rho U) + \frac{\partial}{\partial y}(\rho \tilde{V}) \approx 0 \tag{3.1}$$

where $\rho \tilde{V} = \rho V + \overline{\rho' v'}$, the bar being used to denote the time average. It is assumed here that $\overline{\rho' u'} << \rho U$. An estimate for the magnitude of $\overline{\rho' u'}$ compared with ρU is presented in § 3.3.

Integration of equation (3.1) over the entire layer relates the transverse velocities in the free streams:

$$\rho_2 V_2 - \rho_1 V_1 = \int_{-\infty}^{\infty} \frac{\partial}{\partial x}(\rho U)\, dy \quad , \tag{3.2}$$

where $\rho_{1,2}$ and $V_{1,2}$ are the free stream densities and transverse velocities on the high speed and low speed sides, respectively. In the present investigation, the

free stream densities were nominally matched, i.e., $\rho_1 = \rho_2$. The low speed lower sidewall divergence generally resulted in $V_2 \neq 0$. The high speed upper sidewall, neglecting its boundary layer displacement effects, guaranteed that $V_1 = 0$. The layer geometry is shown in Figure 3.1. Introduction of the similarity variable $\eta = y / \delta(x)$, where y is the layer transverse coordinate and $\delta(x)$ is some characteristic layer thickness (e.g., δ_1), and normalizing by the low speed free stream conditions gives:

$$\frac{\delta^*}{x - x_0} \equiv \frac{V_2}{U_2} = - \frac{d\delta}{dx} \int_{-\infty}^{\infty} \eta \, \frac{d}{d\eta} \left(\frac{\rho U}{\rho_2 U_2} \right) d\eta \quad . \tag{3.3}$$

This expression provides a means of defining the layer displacement thickness, δ^*. Physically, δ^* is a measure of how much the low speed free stream is deflected owing to the presence of the shear layer.

The displacement calculation requires knowledge of the layer density and velocity profiles. The density can be calculated from the mean temperature rise profile, assuming that the static pressure is uniform across the layer. As will be seen in § 3.5, the similarity shape of the mean temperature rise profile, normalized by the adiabatic flame temperature, does not greatly change with heat release. A single symmetric model profile provides, in fact, an adequate representation of the measured profiles for unity equivalence ratio over all values of heat release. For the purposes of this displacement estimate, the mean velocity profile similarity shape will also be taken as not having changed with heat release. How the mean velocity profile changes with heat release is discussed in § 3.2. It will also be assumed that the peak of the mean temperature profile coincided with the center of the mean velocity profile.

Conservation of mass for the top half of the layer requires that the model profiles satisfy the following condition:

$$\eta_h = \int_{\eta_0}^{\eta_h} \frac{\rho U}{\rho_1 U_1} d\eta \quad . \tag{3.4}$$

where η_h is an arbitrary point in the high speed free stream outside the layer and η_0 corresponds to the location of the dividing streamline. The dividing streamline, η_0, corresponds to the location at which $\rho \tilde{V} = \eta \rho U$. This is also the point at which the shear stress in the layer is a maximum. These conditions are expressed by the following formula, which can be derived by combining the continuity and x-momentum equations:

$$\int_{-\infty}^{\eta_0} \frac{\rho U}{\rho_0 U_1} \left(\frac{U}{U_1} - r \right) d\eta = \int_{\eta_0}^{\infty} \frac{\rho U}{\rho_0 U_1} \left(1 - \frac{U}{U_1} \right) d\eta \quad . \tag{3.5}$$

Equations (3.4) and (3.5) determine the transverse locations of the model profiles.

The calculated displacement from equation (3.3) is compared with the experimental results, including some unpublished data of Mungal, in Figure 3.2. The experimental results were obtained by taking the low speed horizontal sidewall deflection angle, β, as a direct measure of $\delta^* / (x - x_0)$, the tangent of the angle by which the low speed free streamline was shifted owing to the presence of the shear layer. It was assumed for this calculation that the boundary layer displacement thickness on the low speed lower sidewall was small. The parameter $(\rho_0 - \bar{\rho}) / \rho_0$ represents the mean normalized density reduction in the layer due to heat release, where $\bar{\rho}$ is the mean density in the layer and ρ_0 is the average (cold) density of the free streams. It can be noted from Figure 3.2 that the

displacement thickness is less than zero for a layer with no chemical reaction, and becomes positive, increasing steadily with increasing heat release. No dependence of the layer displacement on equivalence ratio was observed. The solid line in Figure 3.2 represents a linear least squares fit to the data; the dashed line is the result of evaluating equation (3.3), here taking the layer growth rate to be $d\delta_1/dx = 0.156$ = constant. The fair agreement between the calculated curve and the data points suggests that the layer growth rate was not greatly changed by heat release. The effect of heat release on layer growth is discussed in detail in the next section.

The mean density reduction parameter, $(\rho_0 - \bar{\rho})/\rho_0$, is of course a function of the adiabatic flame temperature rise, ΔT_F. This dependence is shown for the present investigation in Figure 3.3. Some results calculated from the data of Mungal [1983] are also included. The mean density changed greatly (with adiabatic flame temperature) at low heat release but was seen to change less rapidly at high temperatures. The data suggest, in fact, that there may be a limiting value of $(\bar{\rho} - \rho_0)/\rho_0$ for very high flame temperatures, and the present data suggest that the limiting value for a reacting shear layer is substantially less than unity (perhaps 0.4 to 0.5 for the conditions of this investigation). A limiting value of the mean density reduction might be expected if large scale structures persist at all levels of heat release, resulting in the flow consisting of alternating regions of hot, low density structure fluid and cold, high density free stream fluid. This would imply that even in the extreme case of infinitely high temperatures, where the cores of the structures would consist of fluid with zero density, the regions of cold, unreacted free stream fluid between structures would result in a finite mean density and a value of $(\rho_0 - \bar{\rho})/\rho_0$ less than unity. How the large scale structures are affected by heat release is discussed in § 3.6.

The corresponding value of mean density reduction for the $U_2 = 0$ shear layer of Ganji & Sawyer [1979] is $(\rho_0 - \bar{\rho})/\rho_0 \approx 0.65$ for $\Delta T_F / T_0 = 4.5$. It should be pointed out that their $U_2 = 0$ layer reattached and thus was characterized by the recirculation and entrainment of hot products into the low speed side. This caveat may explain the difference between their result and the present data. On the other hand, their $U_2/U_1 \approx 0$ shear layer data may not necessarily be directly comparable to the $U_2/U_1 \approx 0.4$ data presented here.

3.2. Shear Layer Growth Rate

The actual shear layer growth rate, in spite of large heat release and large density changes, did not increase and, in fact, showed a slight decrease, even though the displacement thickness increased with heat release. This effect was noted by Wallace [1981] and is observed in the present set of experiments, in which the maximum mean flow temperature increase is about three times greater than that of Wallace.

Several different measures of layer thickness are possible. One measure is the observed 1% thickness of the mean temperature profile, δ_1. This parameter has been shown by Mungal [1983] and Koochesfahani [1984] to correlate well with the visual thickness of the layer, δ_{viz}, as defined by Brown & Roshko [1974]. The parameter $\delta_1/(x - x_0)$, which represents the layer growth rate, is plotted versus the mean density in the layer in Figure 3.4. These results and all results in this chapter are at nominally zero streamwise pressure gradient. Since it was difficult to hold the speed ratio exactly equal to the nominal value of 0.40 from run to run and also because the density ratio of the free streams was slightly different from unity for some runs, each value of $\delta_1/(x - x_0)$ was corrected by normalization with the expected growth rate for a cold layer with the identical speed and density ratio, using an expression derived in Dimotakis [1984]:

$$\frac{\delta}{x - x_0} = \varepsilon \frac{1 - r}{1 + s^{1/2} r} \left[1 + s^{1/2} - \frac{1 - s^{1/2}}{1 + 2.9 \frac{1 + r}{1 - r}} \right] , \tag{3.6}$$

where $r \equiv U_2 / U_1$ and $s \equiv \rho_2 / \rho_1$. This formula was shown to work well in predicting the effect of density ratio and speed ratio on the growth rate of a nonreacting shear layer. The parameter ε can be determined using a growth rate formula presented in Brown & Roshko [1974]. In particular, $\varepsilon = 0.38$ if in equation (3.6) $\delta = \delta_{viz}$. This correction was also applied to the data of Mungal [1983] included in Figure 3.4.

A straight line least squares fit to the data in Figure 3.4 suggests that the thinning, for a mean density reduction of 40%, may have been as large as 15%. The main point here is not that the layer thinning was large with heat release, but rather that in no case was the layer growth rate seen to increase with increasing heat release, in spite of the displacement effect. No obvious dependence of the thinning trend on equivalence ratio was observed.

The slight reduction in layer thickness with increasing heat release was confirmed by the mean velocity data. Sample velocity profiles, at different heat release but identical speed and density ratios, are presented in Figure 3.5. Each profile in the figure was shifted to facilitate comparison by the required amount to force $U = (U_1 + U_2)/2$ at $y/x = 0$. In real space, the profiles were shifted towards the low speed side with increasing heat release, a consequence of the high speed upper sidewall being at a fixed horizontal position. It can be seen that the hotter layer profile was noticeably steeper as measured by the maximum slope; in agreement with Wallace [1981]. Normalization of the maximum profile slope by the free stream velocity difference gives the vorticity thickness, δ_ω, of the layer.

$$\frac{1}{\delta_\omega} = \frac{1}{\Delta U}\left(\frac{dU}{dy}\right)_{max} \qquad (3.7)$$

In addition to an increase in maximum slope with heat release, the mean velocity profile was also observed to change somewhat in shape. Velocity profiles at low and high heat release are again plotted in Figure 3.6, against the normalized transverse coordinate y/δ_ω. The dashed line represents a hyperbolic tangent profile with the same maximum slope. The profile at high temperature appears fuller than the corresponding low temperature profile. A modified symmetric fit of the form

$$\frac{U - U_1}{U_1 - U_2} = \frac{1}{2} + \frac{1}{2}\tanh[2\delta_\omega(\frac{y}{\delta_\omega}) + \hat{b}\,(\frac{y}{\delta_\omega})^3] \qquad (3.8)$$

provides a very good fit to mean velocity profiles over all temperatures in this investigation. The parameter $\hat{b}$ can be thought of as a measure of how the profile differs in fullness from a pure hyperbolic tangent profile, and decreases with increasing temperature as the profile becomes more hyperbolic tangent-like. Including the change in profile fullness does not have a significant effect on the model calculations of shear layer displacement described in the previous section.

A plot of the vorticity thickness variation with heat release, $\delta_\omega/(x - x_0)$, with each value corrected for variations in speed ratio and density ratio using equation (3.6), is shown in Figure 3.7. These results are seen to be qualitatively consistent with the mean temperature profile growth rates shown in Figure 3.4. The solid line represents the change in vorticity thickness, δ_ω, implied by the reduction in 1% thickness, δ_1, assuming that $\delta_\omega/\delta_1 \approx 0.55 = constant$. This value of δ_ω/δ_1 is somewhat higher than the corresponding value of Brown & Roshko

[1974], who report a value of $\delta_\omega / \delta_1 \approx 0.48$. The vorticity thickness data, with each point normalized by the corresponding cold flow vorticity thickness, δ_{ω_0}, are shown again in Figure 3.8 for comparison with Wallace [1981]. The portion of the present results at moderate heat release, including some of the unpublished data of Mungal, are seen to be in good agreement with Wallace [1981]. Since the data of Wallace were originally given in terms of $\overline{\Delta T}_{MAX} / T_0$, the maximum mean temperature rise over the ambient temperature, it was necessary to use for the abscissa parameter of Figure 3.8 the quantity $\overline{\Delta T}_{MAX} / (\overline{\Delta T}_{MAX} + T_0)$. This quantity is slightly different than $(\rho_0 - \bar{\rho}) / \rho_0$ because the density is not a linear function of the temperature rise, but nonetheless renders a comparable thinning effect to Figure 3.7.

An investigation, at higher temperatures, by Pitz & Daily [1983] in a combusting mixing layer formed downstream of a rearward facing step found that the vorticity thickness did not appear to change between their cold runs and high heat release runs. Keller & Daily [1983], however, reported that in a reacting mixing layer between a cold premixed reactant stream and a preheated combustion product stream, the vorticity thickness increased significantly with increasing temperature. Possible explanations for the effects of heat release on layer growth rate will be discussed in Chapter 4.

A complicating consideration in any discussion of growth rate is the location of the virtual origin, x_0, since the relevant similarity downstream coordinate is $y / (x - x_0)$. The trends in layer thinning reported here do allow the possibility that part of the effect could be accounted for by a shift in the virtual origin with heat release. Wallace [1981] in fact suggested that up to 1/3 of the observed reduction in layer growth rate could be due to a shift in virtual origin, towards more positive values (downstream direction). This shift was attributed to the heat release tending to suppress the initial shear layer instability. The changes

in x_0 with heat release were investigated by digitizing the edges of photographs and performing by eye a linear fit to the apparent layer edges. The 1% points of the mean temperature profiles were also used to aid in the fitting process. Typical edge fits at high and low heat release are shown in Figure 3.9. The values of x_0 for all levels of heat release in this investigation are presented in Figure 3.10. The possible error in locating x_0 by this method is estimated to be typically about 5% of the downstream distance to the measuring station at $x = 45.7\ cm$. Though the data allow the possibility of some change in virtual origin, they do not support the proposal of any significant increase (to more positive values), as suggested by Wallace [1981]. A decrease in x_0 (to more negative values) would in fact suggest that the reduction in layer growth rate is greater than that reported here. A representative constant value of $x_0 = -3.2\ cm$ was used for all calculations and normalizations in this investigation. This value was also used in normalizing the data of Mungal for comparison with the results of the present study.

It should also be mentioned that the initial conditions (e.g. boundary layer thicknesses on the splitter plate) can have a significant effect on layer growth. This has been discussed, for example, by Browand & Latigo [1979]. See also Batt [1975], Bradshaw [1966], and the discussion in the review paper by Ho & Huerre [1984]. Tripping the high speed splitter boundary layer was seen to cause a significant change in the growth rate of a reacting shear layer by Mungal et al. [1984]. In the present experiment, the boundary layer initial conditions were essentially fixed.

3.3. Shear Layer Entrainment

The volumetric entrainment of free stream fluid into the layer must have been greatly reduced by heat release. This is implied by the observations that the mean velocity profile shape was not greatly changed with increasing temperature, and that the layer growth rate did not increase, while the displacement increased substantially due to the density reduction in the layer. In this section, two methods for calculating the entrainment will be discussed. These will be referred to as the geometric method and the integral method.

The geometric method for entrainment calculation, proposed by J. Brown [1978] and Dimotakis [1984], uses the geometry of the layer as shown in Figure 3.1 to derive an approximate relation for the overall entrainment. That is,

$$\frac{\dot{V}}{(x - x_0)\, U_1} = \eta_1 - (\eta_2 + \tan\beta) r \, \frac{\delta}{x - x_0} \quad , \tag{3.9}$$

where $r = U_1 / U_2$, η_1 and η_2 are the similarity coordinate edges of the shear layer, and β is the deflection angle of the low speed lower sidewall.

The integral method relates the amount of entrainment into the layer to the mean velocity and density (i.e. temperature) profiles as follows:

$$\frac{\dot{V}}{(x - x_0)\, U_1} = \frac{d\delta}{dx} \int_{\eta_2}^{\eta_1} \frac{\rho U}{\rho_0 U_1} d\eta \quad , \tag{3.10}$$

where $\dot{V}$ is the volume flux into the layer per unit span. This expression assumes that the layer is self-similar at the station at which the integral is performed.

Strictly speaking, the temperature and velocity fields cannot be expected to be exactly self-similar in a flow with heat release. This statement is based on the results from Mungal et al. [1984], which suggest that there is a Reynolds number dependence on product formation. Since the growth rate does appear to be a function of product formation (i.e. heat release) it may also change slightly with Reynolds number (downstream distance).

A common difficulty of both the integral and geometric methods involves selection of proper values for η_1 and η_2. Konrad [1976] was able to circumvent the difficulty of edge point selection by incorporating the intermittency. This allows expressing in integral form the entrainment as

$$\frac{\dot{V}}{(x - x_0)\, U_1} = \frac{d\,\delta}{dx} \int_{-\infty}^{+\infty} \hat{\gamma}(\eta)\, \frac{\rho\, U}{\rho_0 U_1} d\eta \quad , \tag{3.11}$$

where $\hat{\gamma}(\eta)$ is the intermittency, that is, the mean fraction of the time that turbulent fluid is encountered. The expressions (3.9) and (3.10) can be thought of as indicating the amount of fluid that is entrained into the overall boundaries of the layer; the expression (3.11) gives the amount that actually enters the turbulence. Equation (3.11) will be referred to as the integral method with intermittency.

An estimate for the intermittency can be made by relating it to the probability of finding mixed fluid at a given location in the layer. Koochesfahani [1984] showed that the total mixed fluid probability, $P_m(y)$, can be related to the average product concentrations, $\overline{c_p}$, at very high and very low equivalence ratios, as follows:

$$P_m(y) = \frac{\overline{c_p}(y\,;\varphi=\infty)}{c_{01}} + \frac{\overline{c_p}(y\,;\varphi=0)}{c_{02}} \quad . \tag{3.12}$$

The average product concentration can, at low heat release, be related to the mean temperature rise (see § 3.5) by $\overline{c_p}(y\,;\varphi) = \overline{\Delta T}(y\,;\varphi)\ \hat{C}_p / \Delta Q$, where ΔQ is the molar heat release of the chemical reaction and $\hat{C}_p$ is the specific heat. This gives for the mixed fluid probability,

$$P_m(y) = \frac{\hat{C}_p}{\Delta Q}\frac{\overline{\Delta T}(y\,;\varphi=\infty)}{c_{01}} + \frac{\hat{C}_p}{\Delta Q}\frac{\overline{\Delta T}(y\,;\varphi=0)}{c_{02}} \quad . \tag{3.13}$$

It was shown by Mungal and Dimotakis [1984] that the amount of product formed is close to the asymptotic limits for $\varphi = 8$ and $\varphi = 1/8$. These limits mean physically that the lean reactant has been burned out. Taking, as an approximation, the intermittency to be equal to the total mixed fluid probability, gives, in similarity coordinates,

$$\hat{\gamma}(\eta;\hat{q}) \approx \frac{\hat{C}_p}{\Delta Q}\frac{\overline{\Delta T}(y\,;\varphi=8)}{c_{01}} + \frac{\hat{C}_p}{\Delta Q}\frac{\overline{\Delta T}(y\,;\varphi=1/8)}{c_{02}} \quad . \tag{3.14}$$

The parameter $\hat{q}$ is used to indicate a possible functional dependence on heat release; a possible choice is $\hat{q} \equiv (\bar{\rho} - \rho_0)/\rho_0$.

It is not clear exactly how intermittency changes with heat release, as in this investigation the cases $\varphi = 8$ and $\varphi = 1/8$ were not run at high heat release. However, it will be seen in § 3.5 that there was some decrease in the heights of the mean temperature rise profiles, normalized by the adiabatic flame temperature rise, with heat release. This allows the possibility that the intermittency may have been affected by heat release.

The resulting entrainment data, using the geometric, integral and integral with intermittency methods, are presented in Figure 3.11. The data sets labeled δ_1 and δ_{10} were calculated without intermittency using for edge points the 1% and 10% points in the mean temperature profiles, respectively. The solid and dashed lines are least squares fits to the data.

The lowest sets of data in Figure 3.11 were calculated by the integral method with intermittency. The data sets in Figure 3.11 labeled $\hat{\gamma}(y;0)$ and $\hat{\gamma}(y;\hat{q})$ are with the intermittency unchanging and changing with heat release, respectively. For the set with changing intermittency, the heights of the intermittency profile was taken to decrease in direct proportion to the decrease in the normalized mean temperature profiles at $\varphi = 1/4$ with heat release, as shown in § 3.5. The data with changing intermittency do not suggest a significantly different trend than the results calculated incorporating the intermittency estimated from the low heat release results. It should be emphasized that this change in the intermittency with heat release is speculative and that the actual dependence of the intermittency on temperature has not yet been established.

It can be seen that, regardless of the choice of method or of reference points, the inference is that the total entrainment into the layer was strongly reduced as a function of heat release, amounting to about 50%, for a mean density in the layer of 40% below its nominal cold value. That the entrainment reduction was in excess of the mean density reduction suggests that the decrease in entrainment flux more than compensated for the additional displacement due to density change.

The incorporation of intermittency understandably indicates a lower entrainment than the calculation without intermittency. With this in mind it should be pointed out that the entrainment results calculated with intermittency should always be below the calculated values without intermittency using the edge

points corresponding to δ_1.

The entrainment reported by Konrad [1976] for an nonreacting shear layer, estimated using intermittency, is included for comparison in Figure 3.11. This value was scaled , as suggested by equation (3.10), by the estimated growth rate at zero heat release in the present experiment, and is in fair agreement with the present results.

The difference between the integral and geometric methods can be used to infer, in an approximate fashion, the amount by which the quantity $\overline{\rho u}$ differs from the approximation ρU used for the computations in this chapter. The difference is the fluctuation correlation term $\overline{\rho' u'}$. Examination of Figure 3.11 suggests that, in view of the apparently very good agreement between the integral and geometric methods over all values of heat release, that the error introduced by neglecting $\overline{\rho' u'}$ is not greater than about 4% over the width of the layer. If it is assumed that the profile $\overline{\rho' u'}(\eta)$ is Gaussian-like in nature, the maximum error near the centerline of the layer could be as much as about 9%. Since the mean velocity itself is only estimated to be accurate to about 4% (Rebollo [1973]), however, the data allow the possibility that $\overline{\rho' u'}$ could be, in fact, on average much smaller than 4% of ρU.

3.4. Entrainment Ratio

Methods analogous to the integral and geometric methods for total entrainment can be developed to give estimates of the volumetric entrainment ratio, that is, the ratio of high speed entrained fluid to low speed entrained fluid. The geometric result is developed in J. Brown [1978] and Dimotakis [1984] and is:

$$E_v \approx \frac{U_1}{U_2} \frac{\eta_1}{-\eta_2 - \tan\beta} \quad . \tag{3.15}$$

An integral method for estimating the entrainment velocities into the layer can be derived from formulas presented in Konrad [1976], here put into linear similarity coordinates:

$$\frac{Ve_1}{U_1} = \frac{d\delta}{dx} \int_{\eta_0}^{\eta_1} \frac{\rho U}{\rho_0 U_1} d\eta \tag{3.16a}$$

and

$$\frac{Ve_2}{U_1} = \frac{d\delta}{dx} \int_{\eta_2}^{\eta_0} \frac{\rho U}{\rho_0 U_1} d\eta \quad , \tag{3.16b}$$

where $Ve_{1,2}$ are the entrainment velocities into the high speed and low speed sides of the layer, respectively. The corresponding integral formulas incorporating the intermittency are:

$$\frac{Ve_1}{U_1} = \frac{d\delta}{dx} \int_{\eta_0}^{\infty} \hat{\gamma}(\eta) \frac{\rho U}{\rho_0 U_1} d\eta \tag{3.17a}$$

and

$$\frac{Ve_2}{U_1} = \frac{d\delta}{dx} \int_{-\infty}^{\eta_0} \hat{\gamma}(\eta) \frac{\rho U}{\rho_0 U_1} d\eta \quad . \tag{3.17b}$$

The corresponding volumetric entrainment ratio is given by

$$E_v = \frac{Ve_1}{Ve_2} \quad . \tag{3.18}$$

The problem is again, for the calculations without intermittency, how to

properly choose the values of η_1 and η_2. This issue here is much more critical than in the evaluation of the methods for the total entrainment, since small errors in Ve_1 and Ve_2 can result in large errors in the ratio E_v. An additional difficulty in the geometric calculation of (3.15) is that the boundary layer on the low speed lower sidewall adds to the apparent layer displacement and can result in an observed value of β which exceeds the actual $\delta^*/(x - x_0)$ of the layer. This could cause (3.15) to indicate a substantially higher entrainment ratio than actually occurred in the flow.

The calculations from the integral entrainment formulas, equations (3.16a) and (3.16b), are presented in Figure 3.12. The solid line represents the calculation using model temperature and velocity profiles described in § 3.1, and the 1% points of the mean temperature profile to get η_1 and η_2. The layer growth rate is allowed here to decrease with heat release as indicated by Figure 3.4. The corresponding calculation for the 10% points gives the dashed line shown in Figure 3.12. The 1% calculation indicates a small increase in volumetric entrainment ratio, that is, a tendency for more high speed than low speed fluid to be entrained, amounting to about 3% from the lowest to the highest heat release in this investigation. The corresponding 10% calculation indicates a decrease in volumetric entrainment ratio with heat release of about 2%. The corresponding calculations using the geometric formula (equation (3.15)) and the 1% and 10% points of the mean temperature profile do not yield substantially different results.

The calculated result from the integral formulas with intermittency (equations (3.17a) and (3.17b)) is shown in Figure 3.12 by the dotted line. This result suggests a decrease in entrainment ratio of approximately 5% over the range of temperatures studied in this investigation. An additional estimate of the change in entrainment ratio with heat release, using large scale structure statistical

information, is presented in § 3.6, and is consistent with these results.

It is worth noting that the actual values of entrainment ratio calculated by the methods without intermittency appear to exceed substantially the values calculated taking intermittency into account, and also the value given by Konrad of $E_v \approx 1.3$ for the non-reacting layer at comparable speed ratio. This suggests that somewhat more high speed fluid may be within the overall boundaries of the layer, but yet unmixed, than low speed fluid. Viewed another way the suggestion is that the intermittency profile is not exactly symmetric about the center of the shear layer.

3.5. Temperature Rise and Amount of Product Formation

Time resolved temperature measurements were performed using the cold wire probes described in § 2.2.2. Sample time traces are presented in Figure 3.13, corresponding to a run with 2 % F_2 and 2 % H_2, with an adiabatic flame temperature rise of 186 K. Similar traces were presented, for conditions of low heat release, by Mungal & Dimotakis [1984]. Figure 3.13 consists of individual traces representing the temperature rise recorded by each individual probe, with the high speed free stream towards the top of the figure; the low speed free stream towards the bottom. The horizontal axes represent 51.2 *msec* of real time, corresponding to 512 data points per probe; each probe was sampled at a data rate of 10 kHz. A run normally consisted of 24 such records of 8×512 data points. The vertical coordinate of each trace is $\Delta T / T_{MAX}$, where ΔT_{MAX} is the maximum temperature rise recorded for each record. The traces are representations of the temperatures sensed by the probes as the hot and cold fluid elements convect past them; hence the leading edge of any fluid element appears in the figure to the left of the corresponding trailing edge. The physical distance between the outermost probes was nominally about 6.8 *cm*, and at the nominal mean convection velocity of 15.4 *m/s* the time axes correspond to 78.8 *cm* of

flight distance. This means that in the figure the probe spacings are exaggerated roughly five times compared with the time axes. Time traces corresponding to a 4% F_2 and 4% H_2 run (ΔT_F = 368 K) and a 6% F_2 and 6% H_2 run (ΔT_F = 553 K) are shown in Figures 3.14 and 3.15, respectively.

The following features can be observed in each of the Figures 3.13 - 3.15: there are large, hot structures, separated by cold tongues of cool free stream fluid which penetrate deep into the layer. These observations are consistent with the findings of Mungal & Dimotakis [1984] at low heat release and suggest that large scale structures continue to play a dominant role in the shear layer at elevated temperatures. The convection velocity and mean structure spacing suggest that roughly seven large structures passed the measuring station during the time interval represented by each time trace. It should be noted that conduction error (see Appendix A and also Scadron & Warshawsky [1952] and Paranthoen et al. [1982]) prevented the probes near the center of the layer from indicating a zero temperature rise, which would have corresponded to the cool, unmixed tongues of recently entrained fluid.

The average, over the entire run, of all time trace records results in a mean temperature rise profile. The resulting profiles, normalized by the corresponding adiabatic flame temperatures, are presented in Figure 3.16 for three different equivalence ratios (φ = 1, 1/2, 1/4) at the lowest level of heat release in this investigation, with 2% free stream fluorine and with the adiabatic flame temperature rise in the range 186 K < ΔT_F < 302 K. The transverse coordinate, y/δ_1, indicates the distance from the splitter plate tip normalized by the corresponding value of δ_1 for each run, with positive values towards the high speed side of the layer. This coordinate was employed to enable easy comparison between profiles with different layer thicknesses. The corresponding set of mean profiles for 4% free stream fluorine, 368 K < ΔT_F < 496 K, is shown in

Figure 3.17, and in Figure 3.18 are displayed the mean temperature profiles for the highest heat releases of this investigation, 6% free stream fluorine, 553 $K < \Delta T_F < 900\ K$. All temperature rise profiles are fitted using the exponential fit given in equation (2.2), § 2.2.2. The fit generally provided a good description of the data. The observations of Wallace [1981] and Mungal & Dimotakis [1984] that the adiabatic flame temperature is not observed in the mean at any point in the layer is seen to persist in the present experiments at high heat release. This suggests that the mean temperature profiles, as is the case at low temperature, resulted largely from a "duty-cycle" phenomenon where each probe spent a greater or lesser portion of the run time immersed in hot structure fluid, depending on its location in the layer, as proposed by Mungal & Dimotakis [1984]. This is consistent with the data shown in Figures 3.13 - 3.15 where distinct large, hot regions of fluid were seen to persist in the layer at elevated temperature. This gives a higher mean temperature near the center of the layer and a lower value out near the layer edges. Employing an excess of high speed reactant (i.e., $\varphi < 1$) results in a shift in the mean temperature rise profile towards the side containing the lean reactant, consistent with the low heat release results of Wallace [1981] and Mungal & Dimotakis [1984].

Konrad [1976] and Koochesfahani [1984] demonstrated in shear flows with no heat release that the composition of the mixed fluid appears to be fairly uniform across the layer. This was also seen to be the case in the low heat work of Mungal & Dimotakis [1984], and appeared to persist, to some extent, in the present experiments. The extent to which the temperature in the large structures was uniform can be inferred by considering the maximum recorded temperatures at each point across the layer. The mean profiles at two selected values of heat release for $\varphi = 1$, and also the maximum and minimum temperatures recorded during the course of the entire run, are shown in Figure 3.19. A similar comparison for $\varphi = 1/4$ is made in Figure 3.20. In both cases, it can be

seen that at lower temperatures the maximum temperatures in the central portions of the layer were relatively uniform, suggesting a fairly uniform temperature in the large structures. It can be seen, however, that above about $\Delta T_F \approx 500K$, the maxima appear somewhat more peaked near the center of the layer, suggesting that at higher temperatures the core regions of the structures may have become relatively hotter than the structure edges. As was the case in Mungal & Dimotakis [1984], none of these data were compensated for conduction error; the probes were incapable of resolving the highest temperature rises (near the adiabatic flame temperature rise) as well as the lowest temperatures (near zero for the cold free stream fluid).

An interesting result is that the mean temperature profiles, normalized by the adiabatic flame temperatures, were not observed at a given equivalence ratio to change greatly in shape, despite the large values of heat release. Runs at different heat release but with identical equivalence ratios are presented in Figures 3.21, 3.22 and 3.23 for $\varphi = 1$, $\varphi = 1/2$, and $\varphi = 1/4$, respectively. In these three figures, the peaks of profiles representing runs with more than 2% F_2 were shifted to coincide with the peak of the 2% F_2 profiles to aid comparison. As previously, the transverse coordinate for each profile is normalized by the corresponding δ_1. There appears to be no qualitative change in the profiles at $\varphi = 1$ and $\varphi = 1/2$; at $\varphi = 1/4$ a slight reduction in the profile height on the high speed side can be observed.

The trends in amount of heat released and product formed can be quantified by use of the following definitions. An integral measure of the amount of product in the layer was used by Breidenthal [1978] and Konrad [1976], to define a "product thickness ":

$$\delta_{P_i} \equiv \int_{-\infty}^{\infty} \frac{c(y)}{c_{0i}} dy \tag{3.19}$$

where the integrand is the local concentration, $c(y)$, normalized by a selected free stream concentration, c_{01} or c_{02}. For the present investigation, c_{0i} is taken to be the lean reactant (low speed free stream), i.e., c_{02}. In the present work, since the density in the flow is strongly changed by heat release, two extensions of (3.19) are possible, depending on whether the product fraction (moles of product divided by total number of moles in the sampling volume) or product concentration (total number of moles) is to be represented. The molar fraction of product can be related to the increase in the enthalpy in the gas, i.e.

$$\delta_{P_2} \equiv \int_{-\infty}^{\infty} \frac{H(T) - H(T_0)}{c_{02} \Delta Q} dy \tag{3.20}$$

where H(T) is the molar enthalpy, and ΔQ is the molar heat release of the chemical reaction. For constant specific heat, $H(T) - H(T_0) = \hat{C}_p \overline{\Delta T}$. The specific heat at constant pressure, $\hat{C}_p$, is constant to within 1.6% in the range of maximum mean temperatures seen in this investigation ($300\ K < \overline{\Delta T} + T_0 < 900\ K$). This gives

$$\delta_{P_2} \equiv \int_{-\infty}^{\infty} \frac{\hat{C}_p \overline{\Delta T}(y)}{c_{02} \Delta Q} dy \quad . \tag{3.21}$$

This relation was used by Mungal and Dimotakis [1984] to relate the temperature rise to the amount of product, i.e., product fraction, and defines what will be called in this work the product fraction thickness. The value of $\hat{C}_p$ employed in this investigation was $\hat{C}_p = 7.052\ cal\ /\ mole$.

The heat release of the chemical reaction can be related to the flame temperature as follows:

$$\frac{c_{02}\Delta Q}{\hat{C}_p} \approx (1+\varphi)\Delta T_F \quad . \tag{3.22}$$

This expression is approximate, as $\hat{C}_p$ of the mixture cannot be taken to be constant at the higher values of ΔT_F (which exceed the maximum mean temperatures by 50% or more). The $\hat{C}_p$ of nitrogen at, for example, 1200 K is about 8% higher than the value at 600 K. Using (3.22) it is possible to give the following approximate expression for the product fraction thickness:

$$\delta_{P_2} \approx \frac{1}{1+\varphi}\int_{-\infty}^{\infty} \frac{\overline{\Delta T}(y)}{\Delta T_F} dy \quad . \tag{3.23}$$

The mean of the temperature profile is given by:

$$<\overline{\Delta T}> \equiv \frac{1}{\delta}\int_{-\infty}^{\infty} \overline{\Delta T}(y)\, dy \quad , \tag{3.24}$$

where δ is a suitable layer width, e.g. $\delta = \delta_1$. This allows simplification of (3.23) to:

$$\frac{\delta_{P_2}}{\delta_1} \approx \frac{1}{1+\varphi} \frac{<\overline{\Delta T}>}{\Delta T_F} \quad . \tag{3.25}$$

The product fraction thicknesses for this investigation are presented in Figure 3.24. Each value of δ_{P_2} is normalized by the corresponding local width, δ_1, which varies, as the case may be, for each value of heat release (as shown in Figure 3.4). Some of the low heat results calculated for the data of Mungal [1983] are

included for comparison. For the present investigations ($c_{02} \geq 2\%$), some decrease in the product fraction thickness for all equivalence ratios with heat release is indicated, amounting to approximately 17% for a mean density reduction of 40%. By contrast, the data suggest an increase in product fraction thickness with heat release between the low heat release results ($c_{02} = 1$) of Mungal [1983] and the present results at $c_{02} = 2$. Possible explanations for these effects are presented in the following discussion.

The mean temperature rise can be related directly to the probability density function of the reactant concentrations as follows:

$$\overline{\Delta T}(y) = \int_0^1 \Delta T(c)\, P(c)\, dc \tag{3.26}$$

where $P(c)$ is the mixed fluid fraction probability density function. The function $\Delta T(c)$ depends only on the chemistry and the equivalence ratio, and is described by Mungal & Dimotakis [1984]. The product fraction thickness can thus be related to the probability density function:

$$\delta_{P_2} \approx \frac{1}{1+\varphi} \int_{-\infty}^{\infty} \int_0^1 \frac{\Delta T(c)}{\Delta T_F} P(c)\, dc\, dy \quad . \tag{3.27}$$

The suggestion has been made (see for example Peters & Williams [1980]) that the probability density function of the reactant concentrations may be strongly changed by heat release. Since it was observed that there was some change in product fraction thickness with heat release, Equation (3.27) suggests that $P(c)$ did change to some extent with increasing temperature. Wallace [1981] suggested that if the volumetric entrainment ratio does not change with heat release, the mixture fraction of the mixed fluid should also be unaltered. This leaves the "mixedness" within the layer as the changeable parameter in the

probability density function. Wallace has suggested that the change in "mixedness" is due to a reduction in the efficiency of mixing owing to the increase in the size of the fine scales with the increased viscosity caused by heat release.

This argument suggests that there should be a decrease in product fraction thickness with increasing heat release, in agreement with the present results ($c_{02} \geq 2$). However, the entrainment results of § 3.4 do allow the possibility that the volumetric entrainment ratio was changed by heat release. Further, as it is not clear how the intermittency changes with increasing temperature, it is not necessarily true that the mixture fraction of the mixed fluid is unaltered by heat release.

Another possible explanation for the decrease in product fraction thickness with heat release is that the actual adiabatic flame temperature rise may be different from the nominal flame temperature rise calculated from the heat of reaction and the product species enthalpies (see Appendix D, equation (D.2)). This phenomenon depends on the ratio of reactant species mass diffusivities and mixture thermal conductivities, which changes with increasing reactant concentrations, and is discused in detail in Appendix C. There it is suggested that, for the $F_2 - H_2$ reactant pair, that increasing reactant concentrations could cause the actual flame temperature rise to decrease in relation to the nominal flame temperature rise.

On the other hand, at low temperatures, the product fraction thickness apparently increased with increasing heat release. One possible explanation for this increase in product fraction thickness at low temperatures is that the characteristic chemical time of the reaction decreased substantially with increasing reactant concentrations, i.e. the chemical reactions became faster. This is quantified in Appendix D. Note, however, that if chemical kinetics were the explanation, the increase in product fraction thickness at low heat release

as the hydrogen concentration was increased ($\varphi = 1 \rightarrow \varphi = 1/4$), would probably have been higher than the corresponding increase at higher heat release (faster chemistry at $\varphi = 1$). That this does not appear to have been the case argues against an explanation based on kinetics.

A second possibility is that a decrease in entrainment ratio with heat release caused an increase in product fraction thickness. A decrease in entrainment ratio would cause relatively more of the lean, low speed reactant to be entrained and would yield a higher mean temperature. A decrease in entrainment ratio is consistent with the results of § 3.4 and is also suggested by the vortex statistics of § 3.6. In any event, the mechanisms responsible for the observed product fraction increase with heat release at low temperature appeared to be outbalanced by other mechanisms at higher amounts of heat release, where a reduction in product fraction was measured.

An alternative definition for a thickness based on the density of product can be obtained by multiplying the local product fraction in the integrand by the local density, as follows:

$$\delta^*_{P_2} \equiv \int_{-\infty}^{\infty} \frac{\hat{C}_p \overline{\Delta T}(y)}{c_{02} \Delta Q} \frac{\overline{\rho}(y)}{\rho_0} dy \quad . \tag{3.28}$$

The thickness defined by this relation will be termed the density-weighted product thickness in this work. The motivation for this alternative definition is to account for the decrease in the concentration of product, as the density in the layer decreases, owing to heat release. The earlier definition, the product fraction thickness defined in equation (3.21), could perhaps indicate a finite value even in the limit of infinite temperature rise (zero density) in the layer. The density-weighted product thickness is the same as the product fraction

thickness for very low temperature rise (i.e., small density changes). Relating the density ratio to the local temperature gives

$$\frac{\delta^*_{P_2}}{\delta_1} \equiv \frac{1}{\delta_1}\int_{-\infty}^{\infty} \frac{\hat{C}_p \overline{\Delta T}(y)}{c_{02}\Delta Q} \frac{T_0}{T_0+\overline{\Delta T}(y)} dy \quad . \tag{3.29}$$

The results of the total product calculation suggested by equation (3.29) are shown in Figure 3.25. It is seen that the total amount of product (analogous also to the total amount of heat release), when normalized by the low speed free stream lean reactant concentration, is seen to substantially decrease with increasing temperature. This decrease is partially due to the decrease in the product fraction in the layer at higher temperatures discussed previously, but appears to be mostly a consequence of the strong reduction in the entrainment of the reactants into the layer due to heat release.

The data in Figure 3.25 suggest a measure for determining some characteristic value of the heat release parameter, $(\rho_0 - \bar{\rho})/\rho_0$, below which the effects of heat release can be ignored. This characteristic value could be defined as the break point in each (constant-φ) curve. Assuming that these curves tend to a constant value as $(\rho_0 - \bar{\rho})/\rho_0$ tends to zero suggests a means for extrapolating the product fraction thickness data, as presented in Figure 3.24, to lower values of heat release. It should, of course, be recognized that the analysis of the amount of product formation in terms of the density-weighted product thickness suggests that the apparently more complicated behavior of the product fraction thickness may be, to some extent, an artifact of its definition.

It was observed by Mungal & Dimotakis [1984] that some ramp-like temperature rise features in the streamwise direction appeared to exist at low heat release. This was interpreted with the aid of a suggested vortex picture by

Bernal [1981] in which secondary streamwise vortices are superimposed on the primary two dimensional structure. The effect of this is to cause slight ramp-like features in the mixed fluid by biasing the fluid concentration in the large structure towards the nearer free stream value. These ramp-like features can be seen to persist in the present experiment, as shown in Figures 3.26 and 3.27, for $\varphi = 1/4$. The ramp-like features do not appear quite as clearly as they would in a $\varphi = 1/8$ case, and appear as though they may have been slightly suppressed by increasing heat release.

3.6. Large Scale Structure Dynamics

The work reported by Wallace [1981] and by Mungal & Dimotakis [1984] showed that the large scale structures which characterize nonreacting shear flows also are found in reacting shear layers at low heat release. Other investigations (Ganji & Sawyer [1979], Pitz & Daily [1983] and Keller & Daily [1983]) have shown that large scale coherence is also observable in shear flows at high temperatures (adiabatic flame temperature rise $\approx 1400K$). This section addresses the question of what effect high heat release has on the large vortical structures. In the present work, vortex statistical information was obtained from motion picture data which were taken at a rate of 450 frames per second over the full range of heat release. Large scale structures were observed to persist for all values of heat release in this investigation. Sample spark schlieren photographs, corresponding to the lowest and to one of the highest levels of heat release in this investigation, are presented in Figure 3.28. The schlieren sensitivity was reduced for the high heat release case and makes qualitative comparison of the fine details between the two flows difficult; in both sample photographs, however, the large scale structures can be clearly discerned. Ganji & Sawyer [1979] argued that the schlieren visibility of the structures suggests that the large structures retain their predominately two-dimensional nature even as the heat release increases.

Statistical vortex distribution data were obtained by digitizing, frame by frame, the schlieren motion picture data using an HP9874A digitizer. The locations of the apparent centers of each identifiable vortex were digitized. In most frames it was possible to readily identify each individual vortex. The phenomenon of vortex pairing occasionally made identification of individual vortices difficult, and in fact in some frames it was difficult to pick out any large scale structures. Ganji & Sawyer [1979] pointed out that heat release might serve to render the boundary between two merging structures invisible, while they might still be two separate fluid entities in the fluid mechanical sense. Nonetheless, a typical motion picture was digitized to provide, typically, about 1600 points corresponding to individual vortex locations. Normally about 1300 frames were digitized, corresponding to about 2.8 *sec* of run time, during which over 300 large scale structures were convected through the test section and the field of view. This technique is estimated to produce mean statistics accurate to about 5%. In addition, the location of the apparent edge of the layer was also digitized, yielding typically about 400 sample edge points. The edge points were used to estimate the location of the virtual origin, as explained in § 3.2.

As noted by Dimotakis [1984], the positions of the individual vortices, in the mean, can be expected to constitute a geometric sequence:

$$x_{n+1} = \left(1 + \frac{\bar{l}}{x}\right) x_n \quad , \tag{3.30}$$

where here the coordinate x_n is taken as the downstream distance of the n^{th} vortex from the virtual origin, x_0, and $\bar{l}$ is the mean vortex spacing.

Sample histograms of four different runs, with varying amounts of heat release, are presented in Figures 3.29 and 3.30. The histograms show the

relative frequency of each value of vortex spacing normalized by the 1 % temperature thickness of the layer, δ_1. Increasing temperature appears to have caused a decrease in the mean normalized vortex spacing, $\bar{l}/\delta_1$. The corresponding profile widths, as characterized by the standard deviation of the histograms, σ, also appear to have been reduced with heat release. The change in width could be partially due to vortex recognition difficulties at high temperature.

The solid lines in Figures 3.29 and 3.30 represent the lognormal distribution predicted by the statistical theory of vortex circulation formulated by Bernal [1981]. The distribution is

$$P_\lambda(\lambda) = \frac{1}{(2\pi)^{1/2}\,\hat{\sigma}\,\lambda} \exp\left[-\frac{1}{2\hat{\sigma}^2}\left[\ln(\lambda/\bar{\lambda}) + \frac{\hat{\sigma}^2}{2}\right]^2\right] \quad . \tag{3.31}$$

Here $\lambda \equiv l/\delta_1$ and $\hat{\sigma}$ is related to the variance of the experimentally determined distribution, σ, by:

$$\sigma^2 = \left(\frac{\bar{l}}{\delta_1}\right)^2\left(e^{-\hat{\sigma}^2} - 1\right) \quad . \tag{3.32}$$

The values of $\hat{\sigma}$ for the theoretical distributions shown in Figures 3.29 and 3.30 were calculated using the $\bar{l}/\delta_1$ and σ indicated by the experimental data.

The parameter $\hat{\sigma}$ in equation (3.31) was shown by Bernal to be related to the relative frequencies of vortex pairing, tripling and tearing. Bernal found a value of $\hat{\sigma} = 0.28$ in the nonreacting layer and showed that this value implies that pairing is the dominant vortex amalgamation mechanism. Increasing the relative frequency of tripling would result in a larger value of $\hat{\sigma}$; increasing tearing, a smaller value of $\hat{\sigma}$. In the present work, the values of $\hat{\sigma}$ calculated from the

measured results were observed to be nearly constant over the entire range of heat release, with a mean value of $\hat{\sigma} = 0.25$. The near-constancy of $\hat{\sigma}$ suggests that the relative frequencies of pairing, tripling and tearing are not affected by heat release. It should be pointed out, however, that an increase (or decrease) of both tripling and tearing relative to pairing could also yield an unchanging value of $\hat{\sigma}$.

The decreasing trend in mean normalized vortex spacing, $\bar{l} / \delta_1$, with heat release is shown in Figure 3.31. The decrease was substantial and appears to have been as large as 25% for a mean density reduction in the layer of 40%. Vortex pairing is the mechanism which accounts for the increase in mean structure spacing with downstream distance. Since the vortex spacing was observed to decrease at a faster rate than the decrease in layer thickness, it appears that the mechanism of vortex pairing may have been inhibited, to some extent, by heat release. Since comparison with the Bernal theory suggests that the relative frequencies of pairing, tripling and tearing are not changed by heat release, it would appear that all three mechanisms were inhibited to a comparable degree by heat release.

The nonreacting case in this experiment is observed to have a mean vortex spacing of $\bar{l}/(x - x_0) \approx 0.27$, compared with the values of 0.31 (Brown & Roshko [1974]); 0.24 (Bernal [1981]); and 0.27 (Koochesfahani et al. [1979]). Schlieren flow visualization in the nonreacting flow was accomplished by using, as free stream fluids, nitrogen and a density matched mixture of helium and argon. There was, for cases with zero streamwise pressure gradient, little observed variation in mean vortex spacing with downstream distance. The end of the mixing transition region ($Re_{\delta_1} = 2 \times 10^4$) was located at approximately $x = 15$ cm, and generally no significant difference in vortex statistics upstream and downstream of this point was observed. The variation of $\bar{l}/(x - x_0)$ is presented versus layer

mean density in Figure 3.32.

The decrease in mean vortex spacing has implications for the volumetric entrainment ratio into the layer. In Dimotakis [1984], the following expression is proposed for estimating the entrainment ratio:

$$E_v = s^{\frac{1}{2}}\left(1 + \frac{\bar{l}}{x}\right) \quad . \tag{3.33}$$

This implies that the reduction in vortex spacing must be accompanied by a reduction in the volumetric entrainment ratio, i.e., a larger fraction of entrained fluid from the low speed free stream. The observed decrease in mean vortex spacing indicates, using equation (3.33), a decrease in entrainment ratio of roughly 4% over the range of heat release in this investigation. This is consistent with the entrainment ratio calculations of § 3.4.

Chapter 4

DISCUSSION OF HEAT RELEASE EFFECTS ON LAYER GROWTH

One result presented in the last chapter was that though the total displacement of the layer increased substantially with heat release, the actual layer growth rate did not increase, and in fact, appeared to decrease slightly. Possible explanations for this phenomenon are presented in this chapter. The following mechanisms are discussed: the decrease in turbulent shear stress caused by the density change owing to heat release; the change in static pressure distribution across the layer caused by heat release; the redistribution of vorticity owing to the action of baroclinic torque; and the change in kinematic viscosity with increasing temperature. The experimental data suggest a decrease in shear stress which can be attributed to the density reduction in the layer caused by heat release.

4.1. Effect of Heat Release on Turbulent Shear Stress

One mechanism which may be responsible for the observed heat release effects on layer growth and entrainment is a decrease in the turbulent shear stress in the layer. It might be expected that a decrease in shear stress could be related to a decreased layer growth rate. This will be quantified in this section.

The turbulent shear stress can be calculated from the time-averaged equations for conservation of mass and x- momentum, which are

$$\frac{\partial}{\partial x}(\rho U) + \frac{\partial}{\partial y}(\rho \tilde{V}) \approx 0 \quad , \tag{4.1}$$

$$\frac{\partial}{\partial x}(\rho U^2) + \frac{\partial}{\partial y}(\rho U \tilde{V}) \approx -\frac{\partial p}{\partial x} + \frac{\partial \tau}{\partial y} \quad . \tag{4.2}$$

The corresponding y-momentum equation is

$$\frac{\partial}{\partial y}(\overline{\rho v'^2}) \approx -\frac{\partial p}{\partial y} \quad . \tag{4.3}$$

where $\rho \tilde{V} = \rho V + \overline{\rho' v'}$, as in § 3.1. The momentum equations (4.2) and (4.3) were developed in the same fashion as the continuity equation in § 3.1. It is assumed that the Reynolds stresses are much larger than the viscous stresses, and also that all fluctuation correlations in u ($\overline{\rho u'^2}$, $2U\overline{\rho' u'}$, and $\overline{\rho' u'^2}$) are small compared with the product ρU^2. The gradients in the y direction are assumed to be much larger than gradients of similar quantities in the x direction. The quantity τ in the x-momentum equation (4.2) is the turbulent shear stress , where $\tau = -\rho \overline{u'v'}$, the Reynolds stress, plus higher order terms ($\overline{\rho' u' v'}$, $U\overline{\rho' v'}$ and $V\overline{\rho' u'}$). For the purposes of this discussion it is not necessary to state exactly which fluctuation terms constitute τ.

The x-momentum and continuity equations can be combined by introducing the similarity variable and also a stream function. Taking $\eta \equiv y/\delta(x)$, where $\delta(x)$ is a characteristic layer width (e.g. δ_1), allows rewriting of the x-momentum equation (4.2) to give

$$-\eta \rho U \frac{dU}{d\eta}\frac{d\delta}{dx} + \rho \tilde{V} \frac{dU}{d\eta} = \frac{d\tau}{d\eta} - \eta \frac{dp}{d\eta}\frac{d\delta}{dx} \quad . \tag{4.4}$$

The continuity equation (4.1) is identically satisfied if the two-dimensional mean velocity components are derived in terms of a stream function of the form:

$$\Psi = \rho_0 U_1 \delta(x) f(\eta) \quad , \tag{4.5}$$

where the velocity-density products are given by

$$\rho U = \frac{\partial \Psi}{\partial y} \quad \text{and} \quad \rho \tilde{V} = - \frac{\partial \Psi}{\partial x} \quad . \tag{4.6a,b}$$

Putting the relations (4.6a) and (4.6b) into linear similarity coordinates gives the following relations for the velocity components:

$$U = U_1 \hat{s} \frac{df}{d\eta} \tag{4.7a}$$

and

$$\tilde{V} = U_1 \hat{s} \left(\eta \frac{df}{d\eta} - f \right) \frac{d\delta}{dx} \quad , \tag{4.7b}$$

where $\hat{s}(\eta) \equiv \rho_1/\rho$. Combining (4.7a) and (4.7b) with (4.4) gives:

$$- \frac{U_1^2}{\Delta U^2} \frac{d\delta}{dx} f \left[\frac{d\hat{s}}{d\eta} f + \hat{s} \frac{d^2 f}{d\eta^2} \right] = \frac{1}{\rho_0 \Delta U^2} \frac{d\tau}{d\eta} - \frac{\eta}{\rho_0 \Delta U^2} \frac{dp}{d\eta} \frac{d\delta}{dx} \quad . \tag{4.8}$$

Equation (4.8) provides, for given $f(\eta)$ and $\hat{s}(\eta)$ profiles, a means of calculating the shear stress profile. The second term on the right hand side (pressure term) is small.

Equation (4.8) can be integrated with respect toη to determine the layer shear stress profile. Enforcing the deflection condition presented in equation (3.4), § 3.1, ensures that the calculated shear stress profile tends to zero shear

stress in both free streams. Calculated turbulent shear stress profiles are shown in Figure 4.1. The density and velocity profiles obtained from the experimental results in Chapter 4 provided the functions $f(\eta)$ and $\hat{s}(\eta)$. The growth rate, $d\delta/dx$, was taken to be that indicated by Figure 3.4. It can be seen that with increasing heat release, a marked decrease in shear stress is indicated. A broadening of the shear stress profile with heat release is also apparent; this results from the broadening of the mean velocity profile $U(\eta)$ as was seen in Figure 3.5. The calculated shear stress at zero heat release agrees well with the values of $\tau = -\rho\overline{u'v'}$ reported by Spencer & Jones [1971] for nonreacting flow. That comparison is made in Figure 4.2.

The decrease in shear stress with heat release is consistent with the mixing length scaling argument of Prandtl [1925]:

$$\tau \approx \mu_t \frac{\partial U}{\partial y} \quad , \quad \mu_t = \rho \hat{l}^2 \left| \frac{\partial U}{\partial y} \right| \quad , \tag{4.9}$$

where $\hat{l}$ is the mixing length. Putting $\partial U/\partial y$ into similarity coordinates gives :

$$\tau \approx \rho \frac{\hat{l}^2}{\delta^2} \left| \frac{dU}{d\eta} \right| \frac{dU}{d\eta} \quad . \tag{4.10}$$

By taking $\hat{l} \sim \delta$, equation (4.10) suggests that if the similarity mean velocity profile is not strongly changed by heat release, the shear stress will decrease with decreasing density. An alternate argument is that if the correlation $\overline{u'v'}$ is not greatly changed by heat release, then the Reynolds stress, $\tau = -\rho\overline{u'v'}$, will decrease with decreasing density. It should be pointed out that some change in the velocity field does apparently occur with increasing heat release. This was seen in the broadening of the mean velocity profiles in Figure 3.6. In addition,

an argument is presented in § 4.3 suggesting that the vorticity distribution within the large structures is altered by heat release, implying a change both in the mean velocity as well as in fluctuating velocity correlation terms. Nonetheless, it is argued here that these changes in the velocity field are not large compared with the change in density caused by heat release, which can therefore be regarded as the dominant effect.

It is unclear, however, what value of density to choose in estimating the turbulent shear stress reduction caused by heat release. One choice is the mean density at the given transverse station in the layer. Another possibility is suggested by considering the large scale nature of the flow. Rajagopalan & Antonia [1981] found in a nonreacting flow that at least 80% of the total shear stress appeared to be contained within the large scale structures. It was seen in § 3.6 that large scale structures appear to persist at all levels of heat release. This suggests that an appropriate method for estimating the shear stress in a flow with heat release might consist of a combination of the cold shear stress and some representative large scale structure shear stress. The shear stress can then be expressed as:

$$\tau(\eta) = (1 - \hat{\alpha})\,\tau_0(\eta) + \hat{\alpha}\,\tau_0(\eta)\,\frac{\rho^*}{\rho_0} \quad , \tag{4.11}$$

where $\tau_0(\eta)$ is the shear stress profile for the nonreacting flow, ρ^* is the structure density, (here taken to be uniform within the structure), and $\hat{\alpha}$ is the fraction of total stress contributed by the large scale structure.

In order to obtain an estimate for the temperature in the structures from the mean temperature profile, it must be kept in mind that, as pointed out by Mungal & Dimotakis [1984], cold tongues of fluid appear to penetrate well into

the layer. It was seen in § 3.7 that this appears to be also the case at high heat release. These statements suggest a value of a representative homogeneous large scale structure temperature somewhat higher than the maximum mean temperature. The structure density can thus be expressed as:

$$\frac{\rho^*}{\rho_0} = \frac{T_0}{T_0 + \hat{c}\,\overline{\Delta T}_{MAX}} \tag{4.12}$$

where $\overline{\Delta T}_{MAX}$ is the maximum mean temperature rise in the layer and $\hat{c}$ is a weighting factor of value greater than unity.

Estimated shear stress profiles at high heat release, calculated by both the mean density method and the cold shear stress method, are shown Figure 4.3. The cold shear stress profiles used in the computations were broadened to match the width of the hot shear stress profile. It appears that the method of equation (4.11) may provide a more suitable match to the calculated shear stress profile than does the method of weighting with local average density, which underpredicts the peak values of shear stress.

The dependence of the peak shear stress on heat release is shown in Figure 4.4. The solid line represents the peak shear stress calculated from the mean velocity and density profiles. The dashed and dotted lines correspond to the peak shear stress predicted by the method of equation (4.11), assuming values of $\hat{\alpha}$ = 0.8, $\hat{c}$ = 1.0 and $\hat{\alpha}$ = 1.0, $\hat{c}$ = 1.1, respectively. These two curves are seen to be above and below the result calculated from the mean velocity and density profiles. This method does not allow determination of $\hat{\alpha}$ and $\hat{c}$ separately. It does, however, suggest that the scaling of equation (4.11) is reasonable and is consistent with the possibility that at least 80% of the shear stress is contributed by the large scale structures. Also included in Figure 4.4 is the trend in

maximum shear stress that would occur if the layer growth rate were constant and unchanged by heat release. The implication is that even if the layer growth rate were constant, the turbulent shear stress must decrease substantially in order to compensate for the additional displacement due to heat release.

It should be noted that the preceding arguments are included as an a posteriori effort to estimate the magnitudes of the various effects that enter in the accounting of the growth rate of the shear layer. It is questionable whether such arguments could have been used to predict these results prior to their establishment by these experiments; that would have required the prediction of the relative insensitivity of the mean velocity profile to heat release.

4.2. Changes in Static Pressure Profile with Heat Release

Heat release changes the distribution of static pressure in the layer. An estimated static pressure profile can be obtained by integration of the lowest order y-momentum equation (4.3), and gives:

$$\Delta p \equiv p - p_1 = \rho \overline{v'^2} \tag{4.13}$$

where p_1 is the free stream static pressure. If it is assumed that the $\overline{v'^2}$ profile is not altered to any significant degree by heat release, then equation (4.13) gives a crude means of calculating the dependence of the pressure profile across the layer on heat release. Using the $\overline{v'^2}$ profile measured in a nonreacting shear layer by Spencer & Jones [1971] results in the calculated curves presented in Figure 4.5. The width of the $\overline{v'^2}$ profile has been scaled to match the width of the shear stress profile calculated from equation (4.8). These results suggest that heat release decreases the static pressure deficit in the layer.

Equation (4.13) does not, however, indicate a difference in static pressure between the two free streams which is known to exist in these flows (Spencer & Jones [1971]). To get an estimate for this requires that higher order terms be included in the y-momentum equation:

$$\frac{\partial}{\partial x}(\rho U V) + \frac{\partial}{\partial y}(\rho V^2) = -\frac{\partial p}{\partial y} + \frac{\partial \tau}{\partial x} - \frac{\partial}{\partial y}(\rho \overline{v'^2})$$

$$- \frac{\partial}{\partial y}(2 V \overline{\rho' v'}) - \frac{\partial}{\partial x}(U \overline{\rho' u'}) \qquad (4.14)$$

Unlike equation (4.2), equation (4.14) does not lend itself to combination of $\overline{\rho' v'}$ and ρV by use of the continuity equation (4.1). It is thus necessary, in order to make use of (4.14), to take $\overline{\rho' v'} \approx 0$ and $\overline{\rho' u'} \approx 0$. Introduction of similarity coordinates $\eta \equiv y / \delta$ gives

$$-\eta \rho U \frac{d\delta}{dx}\frac{dV}{d\eta} + \rho V \frac{dV}{d\eta} = -\frac{dp}{d\eta} - \Delta U^2 \frac{d}{d\eta}[\rho \hat{v}] - \eta \frac{d\tau}{d\eta}\frac{d\delta}{dx} \qquad (4.15)$$

where $\hat{v}(\eta) \equiv \overline{v'^2}/\Delta U^2$. This leads to

$$\frac{U_1^2}{\Delta U^2} f \left(\eta \frac{d\hat{s}}{d\eta}\frac{df}{d\eta} + \eta \hat{s} \frac{d^2 f}{d\eta^2} - \hat{s}\frac{df}{d\eta}\right) + \frac{1}{\hat{s}}\frac{d\hat{v}}{d\eta} - \frac{\hat{v}}{\hat{s}^2}\frac{d\hat{s}}{d\eta}$$

$$= \frac{1}{\rho_0 \Delta U^2}\frac{dp}{d\eta} + \frac{\eta}{\rho_0 \Delta U^2}\frac{d\tau}{d\eta} \qquad (4.16)$$

Integration of (4.16) to obtain the pressure profile can be accomplished directly if the stress term $-\eta\, d\tau/d\eta$ is neglected. Alternatively, this term can be eliminated by combining equation (4.16) with equation (4.7), which gives

$$\frac{U_1^2}{\Delta U^2} f \left(2\eta \frac{d\hat{s}}{d\eta} \frac{df}{d\eta} + 2\eta\hat{s} \frac{d^2 f}{d\eta^2} - \frac{d\hat{s}}{d\eta} f\right) + \frac{1}{\hat{s}} \frac{d\hat{v}}{d\eta}$$

$$- \frac{\hat{v}}{\hat{s}^2} \frac{d\hat{s}}{d\eta} = \frac{1}{\rho_0 \Delta U^2} \frac{dp}{d\eta} \quad . \tag{4.17}$$

Evaluation of (4.17) for conditions of zero and high heat release results in the calculated higher order curves presented in Figure 4.5. While the development leading to (4.16) and (4.17) is crude, it can be seen in Figure 4.5 to indicate two qualitative features. First, a pressure decrement on the low speed side of the layer is indicated. This is in qualitative agreement with the experimental results of Spencer & Jones [1971]. Secondly, the analysis predicts that the pressure difference between the free streams decreases with increasing heat release. The pressure difference across the layer is plotted in Figure 4.6 for all values of heat release in this investigation. Both equation (4.16) and equation (4.17) suggest a reduction in the pressure decrement of about 50% for a mean density reduction of 40%. It should be noted that the magnitudes of all the pressure decrements are very small compared with the dynamic heads in the flow.

It might be expected that the static pressure will be less in the large scale structure cores than in the free streams. A decrease in the pressure difference between the layer center and the free streams could be expected to partially account for the reduced entrainment. The relative contribution of the static pressure change with heat release to the shear stress decrease can be estimated by including the pressure difference, as given by equation (4.13), in the shear stress calculation of equation (4.8). The effect of the small pressure term on the shear stress calculation is shown in Figure 4.7. It can be seen that including the effect of pressure has a small effect on the shear stress calculation, implying

that the effect of the change in static pressure distribution on layer growth is small. The calculated shear stress no longer goes back to zero on the low speed side of the layer because the expression for the pressure profile is approximate.

4.3. Effect of Baroclinic Torque

That baroclinic torque might play a role in influencing the layer entrainment was suggested by Wallace [1981]. The main point of his argument is that the action of baroclinic torque, which results from nonaligned density gradient and acceleration vectors, redistributes the vorticity in the layer. The more diffuse vorticity was argued to result in a reduction in the induced entrainment velocities into the layer.

The argument begins with an examination of the Euler equation

$$\frac{\partial \vec{u}}{\partial t} + \vec{\omega} \times \vec{u} + \nabla \left(\frac{u^2}{2} \right) - \frac{\nabla p}{\rho} = 0 \quad , \tag{4.18}$$

where the vector identity $(\vec{u} \cdot \nabla)\vec{u} \equiv \vec{\omega} \times \vec{u} + \nabla (u^2/2)$ was employed. Taking the curl of (4.18) gives:

$$\frac{D \vec{\omega}}{Dt} + \vec{\omega} (\nabla \cdot \vec{u}) = \frac{1}{\rho^2} \nabla \rho \times \nabla p + (\vec{\omega} \cdot \nabla) \vec{u} \tag{4.19}$$

where $\frac{D}{Dt} = \frac{\partial}{\partial t} + (\vec{u} \cdot \nabla)$ is the substantial derivative. Equation (4.19) can be further simplified by noting that (see, for example, the discussion in Serrin [1959]),

$$\frac{D(\vec{\omega}/\rho)}{Dt} = \frac{1}{\rho}\frac{D\vec{\omega}}{Dt} - \frac{\vec{\omega}}{\rho^2}\frac{D\rho}{Dt} \tag{4.20}$$

$$= \frac{1}{\rho}\frac{D\vec{\omega}}{Dt} + \frac{\vec{\omega}}{\rho}(\nabla \cdot \vec{u})$$

where the continuity equation was used to substitute for $D\rho/Dt$. This can now be combined with equation (4.19) to give:

$$\frac{D(\vec{\omega}/\rho)}{Dt} = \frac{1}{\rho^2}(\nabla p \times \nabla \rho) + (\vec{\omega}\cdot\nabla)\vec{u} \quad . \tag{4.21}$$

Taking the view that the processes in the layer are controlled by structures which are basically two dimensional, the terms $(\vec{\omega}\cdot\nabla)\vec{u}$ in (4.19) and (4.21) can be taken to be zero. It can be seen from (4.21) that the baroclinic torque changes the vorticity. This was illustrated graphically by Wallace [1981] using a figure reproduced in Figure 4.8. Surmised contours of density and velocity were superimposed on a typical large structure. The contours are depicted in a reference frame which is moving with the structures with their convection velocity. Wallace argued that the baroclinic torque action would be strongest at the points labeled "A", and should augment the vorticity at those points. Since a control volume of fixed size enclosing the entire structure will always indicate the same circulation, Wallace argued that the vorticity concentrated at other points (the braids and structure cores) decreases owing to the action of baroclinic torque at points "A". This redistribution of vorticity was concluded to result in a reduced locally induced entrainment velocity and a lower layer growth rate. Winant & Browand [1974] also concluded, using a vortex interaction theory, that a change in the vorticity distribution within the large structures, in the direction of more diffuse vorticity, would lead to a smaller layer growth rate.

A difficulty with the baroclinic torque argument is that it is not readily quantified, especially since it is seen in equation (4.21) that the quantity affected by the action of baroclinic torque is not simply $\vec{\omega}$ but rather $\vec{\omega}/\rho$. Numerical simulations by McMurtry et al. [1985] do however show that the vorticity does in fact appear to be redistributed in the large scale structure by heat release.

4.4. Viscosity Change with Heat Release

Work by Yule et al. [1980] in a reacting propane-air jet found a much longer potential core compared with a nonreacting jet, implying a decrease in the shear layer growth rate. They reported an increase in potential core length from about three initial jet diameters in the cold case to about 20 initial jet diameters in the reacting flow, which had a maximum mean temperature of up to about 1700 K absolute. The change in core length was attributed by Chigier & Yule [1979] to a delay in the establishment of turbulent flow owing to the increase in kinematic viscosity with heat release.

The change in kinematic viscosity with temperature can be estimated by:

$$\nu \equiv \frac{\mu}{\rho} = \frac{\mu_0}{\rho_0}\left[\frac{T}{T_0}\right]^{1+\hat{\omega}} \tag{4.22}$$

where μ_0 is the viscosity at ambient temperature, T_0. The exponent $\hat{\omega}$ has the approximate value $\hat{\omega} \approx 0.73$ for nitrogen. Equation (4.22) indicates an increase in kinematic viscosity of about 20 for the hottest temperatures of the investigations of Yule et al.[1980]. For the present work, by contrast, the highest mean maximum temperature rise was substantially less, amounting to about 580 K (880 K absolute), and would have caused the kinematic viscosity to increase by a factor of about 6. This change in kinematic viscosity sufficed to reduce the

nominal Reynolds number in the present investigation (here based on the hot kinematic viscosity) of $Re_{\delta_1} \approx 6\times10^4$ to $Re_{\delta_1} \approx 1\times10^4$. Since the flow is still at high Reynolds number under these conditions, it seems unlikely that viscosity plays a large role in the reduction in layer growth. Further, it was seen in § 3.2 that the location of the virtual origin, for the present investigation, did not exhibit any significant change with heat release. This suggests no substantial delay in the development of layer growth owing to heat release.

In conclusion, all four mechanisms described in this chapter probably play some role in accounting for the observed layer thinning and reduced entrainment. However, it is seen that the estimated decrease in turbulent shear stress can by itself easily account for these effects and thus may represent the major contribution to the experimentally observed trends. It should be pointed out that this phenomenon is not necessarily inconsistent with the effect of the baroclinic torque.

Chapter 5

RESULTS FOR NONZERO STREAMWISE PRESSURE GRADIENT

Some runs in this investigation were performed with a nonzero streamwise pressure gradient. The effects of pressure gradient in reacting flows are of interest because many practical combustion devices have fixed geometries and thus do not have a means of relieving the induced pressure gradient. In this chapter the effects of heat release combined with streamwise pressure gradient on shear layer growth, entrainment, amount of product formation, and large scale structure dynamics are discussed.

A pressure gradient in the present investigation was imposed by fixing the sidewalls for the reacting flow in a position corresponding to zero pressure gradient in the unreacting flow. This yielded a naturally induced favorable pressure gradient in the case of flow with heat release. In this investigation, such favorable pressure gradient runs were made at reactant concentrations of up to 6% fluorine and 6% hydrogen, corresponding to a flame temperature rise of up to 553 K. This was sufficient to induce a pressure increase, over the distance from the splitter plate tip to the measuring station, of about 1/2 of $\frac{1}{2}\rho_0 U_2^2$, the low speed free stream dynamic head. This served to increase the high speed velocity from the nominal 22 m/s to 23.1 m/s and the low speed velocity from 8.8 m/s to 11.3 m/s between the splitter tip and the measuring station.

5.1. Shear Layer Growth

The thickness of the layer, at a fixed measuring station, appeared to be less for the cases with favorable pressure gradient than for the corresponding reacting flows with no streamwise pressure gradient. This can be seen in Figure 5.1, where comparative mean temperature profiles with identical levels of heat release, but with and without pressure gradient, are shown. The comparison in layer thickness with the least squares fit to the zero pressure gradient cases of Figure 3.2 is given in Figure 5.2. It must be noted that for flow with pressure gradient the parameter $\delta_1/(x - x_0)$ represents simply a normalization by the downstream distance and does not necessarily represent that layer growth rate, since the layer with streamwise pressure gradient is, as will be seen later in this section, not in general self similar. The additional thinning caused by pressure gradient does not seem surprising in an accelerating flow. The change in layer growth rate appears to have been essentially due to a change with downstream distance in speed ratio induced by pressure gradient. This will be quantified in the following discussion.

For nonreacting shear layers with equal free stream densities, a commonly used expression for relating the growth rate to the speed ratio was given by Brown & Roshko [1974]:

$$\frac{\delta_{viz}}{(x - x_0)} = 0.38\ \frac{1 - r}{1 + r} \tag{5.1}$$

where δ_{viz} is the visual thickness of the layer. For the moderate values of the streamwise pressure gradient in this investigation, it can be assumed that this similarity relation holds locally (suggested by M. M. Koochesfahani in private discussions), i.e.,

$$\frac{d\delta}{dx} = \Lambda(\tilde{q}) \frac{1 - r(x)}{1 + r(x)} \tag{5.2}$$

where the parameter $\Lambda(\tilde{q})$ is a growth rate parameter, which is taken to depend only on the amount of heat release. The speed ratio, $r(x) \equiv U_2(x) / U_1(x)$ is here a function of downstream distance. Equation (5.2) is essentially a statement that the layer is in local equilibrium, that is, that the speed ratio changes slowly compared with the rate at which the layer growth adjusts to it. Integration of equation (5.2) gives the layer growth as a function of downstream distance,

$$\delta(x) = \Lambda(\tilde{q}) \int_{x_0}^{x} \frac{1 - r(x)}{1 + r(x)} dx \quad . \tag{5.3}$$

The free stream velocities can be determined from the corresponding Bernoulli equations, assuming that the streamwise pressure gradient $\frac{dp(x)}{dx} = constant$. The results are:

$$U_1^2(x) = U_{01}^2 - \frac{2}{\rho_1}\left[\frac{dp}{dx}\right] x \tag{5.4a}$$

and

$$U_2^2(x) = U_{02}^2 - \frac{2}{\rho_2}\left[\frac{dp}{dx}\right] x \tag{5.4b}$$

where U_{01} and U_{02} are the high speed and low speed free stream velocities, respectively, at some reference point, e.g., at the start of the test section. The

assumption that the pressure gradient, dp/dx, was constant can be evaluated by comparing the velocity indicated by equation (5.4a) with some of the experimental results from Rebollo [1973]. This comparison is made in figure 5.3. The dashed line is the fit suggested by equation (5.4a) assuming that the pressure gradient is constant, with a chosen value of $dp/dx = +0.017\ torr/cm$. The agreement is good and lends support to the idea that the pressure gradient is constant or nearly constant in these flows.

The speed ratio as a function of downstream distance can be expressed by combining (5.4a) and (5.4b). The result is:

$$r(x) = r_0 \left[\frac{1 - 2\Pi x}{1 - 2\Pi r_0^2 s\, x} \right]^{\frac{1}{2}} , \tag{5.5}$$

where

$$\Pi \equiv \frac{dp/dx}{\rho U_{02}^2} \tag{5.6}$$

is introduced as the pressure gradient parameter, which has units of inverse length, and $r_0 \equiv U_{02}/U_{01}$.

The effect of pressure gradient on speed ratio, as expressed by equation (5.5), is plotted in Figure 5.4. The values of $\Pi < 0$ given are typical for this investigation at different levels of heat release. The effect of a favorable pressure gradient is seen to increase the speed ratio (that is, drive it towards unity); for an adverse pressure gradient, to decrease it (drive it towards zero). It can be seen that the speed ratio is affected less by a favorable pressure gradient than by an adverse one of similar magnitude. The adverse pressure gradient solutions become, in fact, singular far enough downstream.

The trend in layer thinning over the full range of heat release of this investigation is shown in Figure 5.5, where the normalized layer thickness at the measuring station (δ_1/δ_{1_0}) is given against $(\rho_0 - \bar{\rho})/\rho_0$, where δ_{1_0} is the layer thickness without pressure gradient. The experimental results are seen to be consistent with the predicted trend.

In this investigation, the layer was not self-similar in the presence of a streamwise pressure gradient. Rebollo [1973] showed that in order to have similarity, the layer growth must be linear and the free stream dynamic heads must be matched. The changing speed ratio precluded linear layer growth, as seen in equation (5.2). Furthermore, in this work the free stream dynamic heads were not matched. Thus the layer in this investigation was not self-similar in the presence of a streamwise pressure gradient.

5.2. Shear Layer Entrainment

The entrainment into the layer with pressure gradient can be calculated by extending the geometric and integral methods employed in § 3.3. The geometric entrainment formula for the total volumetric entrainment into the layer must take into account the change in free stream velocities in the presence of a pressure gradient. For the pressure gradients in this investigation, the free stream velocities given in equations (5.4a) and (5.4b) can be closely approximated by:

$$U_1 \approx U_{01} - \Pi \frac{U_{02}^2}{U_{01}^2} x \tag{5.7}$$

$$U_2 \approx U_{02} - \Pi x \quad . \tag{5.8}$$

Using these relations and the geometry of Figure 3.1 allows calculation of the overall volumetric entrainment into the layer:

$$\frac{\dot{V}}{U_1 x} = (1 - \Pi \frac{U_{02}^2}{U_{01}^2 x})\eta_1 + \Pi \frac{h_1}{x}$$

$$+ r\,(1 - \Pi x)(-\eta_2 + \tan\beta) + \Pi \frac{h_2}{x} \qquad (5.9)$$

where h_1 and h_2 represent the distances from the splitter tip to the upper and lower sidewalls, respectively. This equation does not represent the entrainment locally, but is rather indicative of the entrainment into the entire layer, from splitter tip to the measuring station. Unlike the corresponding zero pressure gradient formula, equation (3.10), § 3.3, equation (5.9) shows that for nonzero streamwise pressure gradient the entrainment depends, to some extent, on the geometry (specifically the initial heights) of the flow channel. In the present investigation, however, the contributions from the terms containing h_1/x and h_2/x are small and can be neglected.

The corresponding geometric volumetric entrainment ratio of the entire layer is:

$$E_v = \frac{U_1}{U_2} \frac{(1 - \Pi\, U_{02}^2 / U_{01}^2\, x)\eta_1}{(1 - \Pi x)(-\eta_2 + x\, \tan\beta)} \qquad (5.10)$$

It can be seen that equations (5.9) and (5.10) reduce to (3.10) and (3.11),§ 3.3, respectively, for the zero streamwise pressure gradient case ($\Pi = 0$).

The comparison between overall entrainment with and without streamwise pressure gradient is made in Figure 5.6. It can be seen that the overall entrainment appears to be substantially higher for the flow with pressure gradient. It might be expected that the converging sidewalls could cause an increase in total

entrainment if the decrease in layer thickness is not large. Qualitative comparisons based on Figure 5.6 are difficult because the layer with pressure gradient is not self-similar. Also, the zero streamwise pressure gradient layer may not be self-similar for as much as 1/3 of the distance from the splitter plate tip to the measuring station, as mentioned in § 2.4.

The integral entrainment formula, taking into account a nonconstant layer growth rate, is

$$\frac{V_e}{U_1} = \frac{d}{dx}\int_{y_2}^{y_1} \frac{\rho u}{\rho_0 U_1}\, dy \approx \frac{d\delta}{dx}\int_{\eta_2}^{\eta_1} \frac{\rho u}{\rho_0 U_1}\, d\eta \quad . \tag{5.11}$$

where here $d\delta/dx$ is a nonconstant function of x. Here the parameter $\eta = y/\delta$ is used locally to allow estimation of the integral; it is not being implied that the layer is self similar. Using the relation given in (5.2) for the growth rate gives:

$$\frac{V_e}{U_1} = \Lambda(\tilde{q})\,\frac{1-r(x)}{1+r(x)}\int_{\eta_2}^{\eta_1} \frac{\rho u}{\rho_0 U_1}\, d\eta \quad . \tag{5.12}$$

In contrast to the geometric entrainment formula (5.9), equation (5.12) represents the local volumetric entrainment into the layer per unit span per unit length, and does not directly relate to the overall entrainment into the layer. Resulting calculations based on this integral entrainment formula are presented in Figure 5.7. The values of $\Lambda(\tilde{q})$ in equation (5.12) were selected to give the correct growth rates in the corresponding zero pressure gradient flows. The solid lines represent the least squares best fit to the experimental results from § 3.3 with zero pressure gradient. The local entrainment at the measuring station is seen to be less in the case of pressure gradient that in the corresponding zero pressure gradient flow. This appears to be primarily a consequence of

the lower layer growth rate in the case of pressure gradient.

5.3. Temperature Rise and Amount of Product Formation

It could be argued that, in reacting flows with substantial density variations and appreciable pressure gradients, an additional mixing mechanism might be operative, resulting from a possible relative acceleration between light fluid elements and heavy fluid elements. This mechanism is referred to as "pressure gradient diffusion" by Bray and Libby [1981] and by Spalding [1984]. The efficacy of such a mechanism would of course depend on the scales at which the density variations would be observed and their relation to the viscous small scales of the flow. If the hot/cold fluid elements are very closely spaced, viscous effects might not permit large relative motions to be established and little or no augmentation of the mixing would be observed.

The results of this experiment, in fact, indicate little change in either the peak temperature of the total amount of product formation as a result of the favorable pressure gradient. This is seen in Figure 5.8, where three of the resulting mean temperature profiles, at the highest heat release and largest value of pressure gradient attained in this investigation, are shown. Temperature profiles at lower temperatures also show little change resulting from pressure gradient. The product fraction thickness, as defined by equation (3.23), § 3.5, is plotted in Figure 5.9 for runs with and without pressure gradient. The cases with pressure gradient are seen to be on average only 2% higher in product fraction than the corresponding flows without pressure gradient; at the highest temperature, the data indicate a possible augmentation of up to 6%. It should be kept in mind that the estimated reproducibility and accuracy of the experimental results are 3 – 5%.

A small increase in product can be accounted for by the change in Reynolds number of the flow caused by pressure gradient. The local value of Reynolds

number, $Re_{\delta_1} \equiv \Delta U \delta_1 / \nu$, at a given downstream location, decreased with pressure gradient. This is because δ_1 decreased, though this decrease was partly offset by the increase in ΔU owing to free stream acceleration. The result was a modest decrease in Reynolds number. The nominal Reynolds number at the measuring station of $Re_{\delta_1} \approx 6.4 \times 10^4$ decreased to as little as $Re_{\delta_1} \approx 5.2 \times 10^4$, for the runs with the largest heat release and pressure gradient.

How the product fraction thickness depends on the Reynolds number was investigated, under conditions of low heat release, by Mungal et al. [1984]. That work suggested a decrease in product formation amounting to roughly 20% per factor of 10 increase in Reynolds number. How that trend might change with heat release was investigated by running one case, 4% fluorine and 4% hydrogen ($\Delta T_F = 368K$) at elevated free stream speeds, $U_1 = 44\ m/s$, $U_2 = 17.6\ m/s$. The results of these runs are shown in Figure 5.10. It can be seen that the trend of product decrease with Reynolds number persists at higher temperatures, and is of approximately the same slope as the earlier low heat results.

The trend in Figure 5.10 suggests, for the present investigation, that the naturally induced pressure gradient could be expected to result in an increase in product formation of up to approximately 3% at the highest temperature and pressure gradient of this investigation. That this result already accounts for most of the small observed increase in product formation suggests that "pressure gradient diffusion", at least for the values of temperature and pressure gradient reported here, does not play a significant role in enhancing the mixing and combustion in a reacting shear layer.

5.4. Large Scale Structure Dynamics

The mean large scale structure spacing, over the entire central part of the layer, was not greatly changed by streamwise pressure gradient, as shown in Figure 5.11. There was, however, some trend in the mean vortex spacing with downstream distance. This can be explained by taking the mean vortex spacing to be related to the layer growth rate, i.e.,

$$\frac{\bar{l}}{x} = \tilde{\alpha}\,\frac{\delta}{x} \tag{5.13}$$

where $\bar{l}$ is the mean vortex spacing. Sample reported values for the constant $\tilde{\alpha}$, taking δ to be the vorticity thickness, δ_ω, are: $\tilde{\alpha}$ = 3.3, Winant & Browand [1974]; $\tilde{\alpha}$ = 3.0, Bernal [1981]; $\tilde{\alpha}$ = 2.9, Brown & Roshko [1974]; and, for the present investigation, $\tilde{\alpha}$ = 3.4 for the case of zero heat release. It was seen in § 3.6 that the mean vortex spacing decreases with increasing temperature, suggesting that $\tilde{\alpha}$ should be taken to be $\tilde{\alpha}(\tilde{q})$, a function of heat release (in an analogous fashion to $\Lambda(\tilde{q})$ introduced in § 5.1). Again assuming that the large structure dynamics accommodate themselves rapidly to the changing free stream conditions, the layer growth calculated by equation (5.3) can be used to estimate the vortex spacing change with downstream distance. Figure 5.12 shows the calculated variation in mean vortex spacing with downstream distance in the presence of a favorable pressure gradient. Appropriate values of the parameter $\tilde{\alpha}$ were chosen to fit the curves through the first data point at x = 9.6 cm. It can be seen that the data are qualitatively consistent with the calculated curves, and suggest that the mean large scale structure spacing normalized by downstream distance, in a similar fashion to the layer growth rate, decreases with the imposition of a favorable pressure gradient.

It could be expected, in a reacting flow with heat release, that a streamwise pressure gradient would cause a differential acceleration of the hot large structures, relative to the cold free streams, and might tend to increase in mean vortex spacing. This differential acceleration is suggested by the mean velocity relations (5.4), which indicate that the acceleration of a fluid element, in the presence of a streamwise pressure gradient, is inversely proportional to its density. It must be noted, however, that equations (5.4), derived from the Bernoulli equation, are not directly applicable to the vortical fluid in the layer.

A differential acceleration of fluid could result in a change in the mean velocity profile. The profile might be expected to be most changed near the center of the layer, where the greatest percentage of hot, large scale structure fluid is encountered, as explained in § 3.5. Mean velocity profiles, at the same level of heat release but with and without streamwise pressure gradient, are presented in Figure 5.13. The profile does not appear to have been greatly changed by the pressure gradient. As in § 3.2, the profile transverse coordinates were normalized by the corresponding vorticity thicknesses, δ_ω, and the profiles were shifted to match at $y / \delta_\omega = 0$. Comparison between the profiles is complicated by the profile shifts in real space owing to the different wall divergences required for flows with and without pressure gradient, and also by the change in layer thickness. Another difficulty associated with using the mean velocity profile to infer hot structure differential acceleration is that the mean dynamic pressure profile, from which the mean velocity is extracted (see § 2.2.3), results from a combination of hot vortex fluid and cold free stream fluid, which could by averaging render the hot structure differential acceleration less apparent.

Nontheless, as it can be seen that the profile shape appears to not have been greatly changed by pressure gradient, it appears that the differential acceleration of the structures relative to the surrounding fluid was not large. That the

mean vortex spacing in the presence of a pressure gradient appeared in fact to decrease slightly with downstream distance, further suggests that, for the conditions of this investigation, the large scale structure dynamics were governed largely by the changing speed ratio, and the differential acceleration of the hot structures relative to the cold free stream fluid was small.

Chapter 6

CONCLUSIONS

The hydrogen-fluorine chemical reaction was used to study the effects of large heat release in a planar, turbulent shear layer at high Reynolds number. A range of reactant concentrations was employed to produce adiabatic flame temperature rises from 186 K up to 940 K, resulting in a maximum mean density reduction in the layer of up to 60%.

The emphasis in this investigation was upon determining the effects of heat release on the properties of the shear layer, specifically, how the heat release affects the growth rate and volumetric entrainment into the layer, the amount and efficiency of chemical production, and the large scale structure dynamics. The effects of an enforced external favorable pressure gradient on these layer properties were also investigated.

6.1. Summary of Results

1. The growth rate of the shear layer, in spite of large heat release and large density changes, did not increase, instead it appeared to show a slight decrease, even though the displacement thickness of the layer increased substantially with heat release. The thinning, at zero streamwise pressure gradient, was observed to be up to 15% for a mean density reduction in the layer of 40%, corresponding to an adiabatic flame temperature rise of about 900 K. The observed change in growth rate did not appear to be the result of any significant change in the location of the virtual origin.

2. The volumetric entrainment of free stream fluid into the layer was substantially reduced by heat release. This is an implication of the fact that the

layer width did not increase but the layer mean density was strongly reduced by heat release. The observed reduction in layer entrainment appears to more than offset the additional displacement of the layer owing to heat release.

3. Theoretical arguments suggest that a large decrease in turbulent momentum transport, as represented by the turbulent shear stress in the layer, accompanies increasing flow temperatures. This decrease in shear stress can be accounted for by the change in density in the core regions of the large scale structures, and suggests that the reduction in turbulent shear stress due to density reduction may be the dominant mechanism responsible for the reduced layer growth and entrainment.

4. The mean temperature rise profiles, normalized by the adiabatic flame temperature, did not change significantly in shape over the entire range of heat release. A slight decrease in normalized mean temperature was observed, which indicates that the relative efficiency with which the layer generates chemical product decreases slightly with increasing heat release. This suggests that the probability density function of the mixed fluid concentration is altered, to some extent, by heat release.

5. Large scale coherent structures appeared to persist in the shear layer at all levels of heat release. The mean structure spacing, normalized by the layer width, was observed to decrease with increasing heat release. This suggests that the mechanism of vortex pairing may be, to some extent, inhibited by heat release.

6. The imposition of a naturally occurring, favorable pressure gradient resulted in an additional layer thinning at all levels of heat release. This change in growth rate can be related analytically to the change in free

stream speed ratio caused by pressure gradient.

7. The pressure gradient was observed to have little effect on the amount of mixing and chemical product formation in the layer. The slight measured increase in product can be largely accounted for by the change in local large scale Reynolds number resulting from the acceleration of the free streams and the layer thinning.

6.2. Suggestions for Further Work

At least two experimental continuations of this work are suggested. First, the effects of heat release could be studied in a shear flow with different free stream densities, yielding three characteristic densities in the flow (two free streams plus the hot layer). This might provide further insight into the mechanisms of layer growth rate and entrainment. Second, the effects of adverse pressure gradient could possibly be studied in an analogous fashion to the favorable pressure gradient study reported in this investigation.

Analytically, it would be of interest to apply a stability analysis to the initial shear layer instability to examine how the initial instability, roll-up, and layer growth are affected by heat release. A vortex dynamics calculation, in which discrete vortex elements are altered by heat release, might also allow further understanding of how heat release effects the processes of vortex pairing, layer growth, and entrainment.

Appendix A

TEMPERATURE MEASUREMENT WITH COLD WIRE AND THERMOCOUPLE PROBES

Each of the two primary temperature diagnostics in this experiment has its own advantages and disadvantages. The 2.5 μm diameter cold wires have the advantage of relatively fast time response but were observed to survive poorly in the hottest regions in runs with adiabatic flame temperature rises greater than about 600 K (900 K absolute). The 25 μm diameter Chromel-Alumel thermocouples were capable of surviving the hottest runs (flame temperature rises of more than 900 K, 1200 Kabsolute) but have much slower time response. In this appendix sources of possible error in temperature measurement and estimates of their magnitude for both types of probes will be discussed.

The error sources discussed here are:

1) Conduction Error;

2) Radiation Error;

3) Nonlinearity of Probe Resistivity with Temperature;

4) Catalytic Error;

5) Nonuniformity in Gas Thermal Conductivity;

6) Probe Parasitic Resistance.

The effects of nonlinear resistivity and probe parasitic resistance relate only to the cold wire probe. The other error sources influence both the cold wires and thermocouples.

A.1. Conduction Error

Conduction error is caused by the heat transfer between the sensing element (cold wire or thermocouple junction) and the supporting prongs or wires. This heat transfer results in the sensing element tending to assume the temperature of the supports, thus suppressing in measurement, to some extent, the temperature fluctuations in the flow. The problem of conduction error is treated in detail in Scadron & Warshawsky [1952] and Paranthoen, et al. [1982], is well summarized in Mungal [1983] and will not be presented in detail here. The principal result, the steady-state temperature distribution along a probe wire, is presented in Figure A.1. Here L is the wire length and x is the distance from the wire center. The parameter ηL is a function of the probe wire material and dimensions, and is calculated as follows:

$$\eta^2 = \eta_1^2 \left(1 + 4\beta_1 \frac{\varepsilon_w}{T}\right) \tag{A.1}$$

$$\eta_1^2 \equiv \frac{4\, Nu\, k_g}{D^2\, k_w} \tag{A.2}$$

$$\beta_1 \equiv D^2 \rho_w \frac{c_w}{4\, Nu\, k_g} \tag{A.3}$$

where:

D = probe wire diameter

k_g = thermal conductivity of gas

k_w = thermal conductivity of probe wire

Nu = Nusselt number

T_w = temperature in probe wire

T_p = support prong temperature

T = gas temperature

ε_w = emisivity of the probe wire

ρ_w = probe wire density

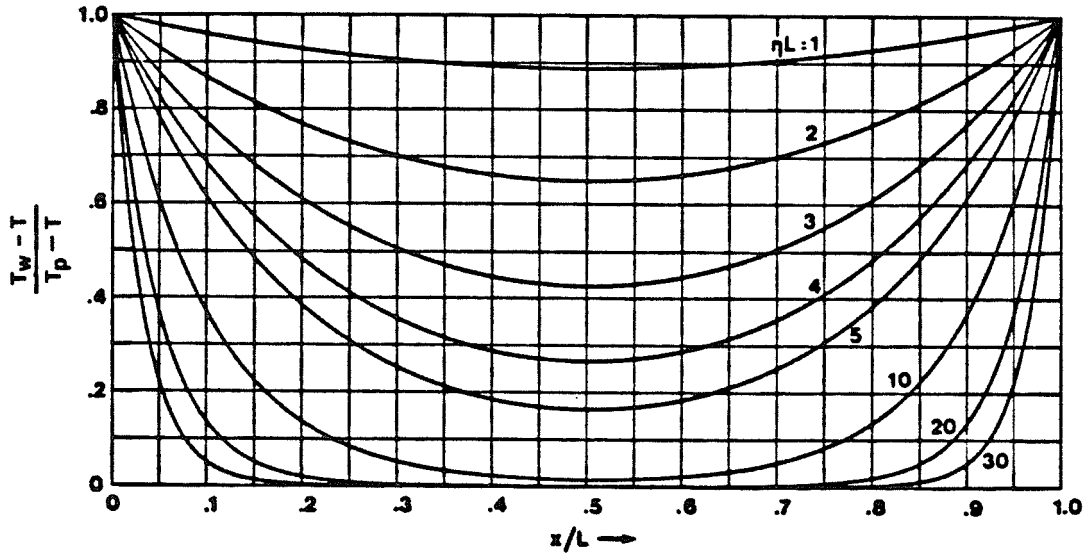

Temperature Distribution Along Simple Wire in Steady State

Figure A.1

The value of ηL for the present experiment was approximately 20 for the cold wires and approximately 2 for the thermocouples, with the corresponding curves included in Figure A.1. It can be seen that the conduction error for the cold wire was relatively small, and that the wire indicated measured temperature fluctuations to within 10−20%. For the thermocouple, by contrast, the

conduction error was substantial, with the corresponding error amounting to 65%. It should be emphasized, however, that conduction error did not prevent either probe from indicating accurate mean temperatures.

A.2. Radiation Error

Radiation error results from the heat exchange by radiation between the probe surface and the surrounding fluid and flow channel walls. A formula for estimating the radiative error is given by Becker & Yamazaki [1978]:

$$(T - T_w) = \varepsilon_w \sigma (T_w^4 - T_0^4) / h \qquad (A.4)$$

$$= \varepsilon_w \sigma (T_w^4 - T_0^4) \frac{k_g D}{Nu}$$

where

T_0 = ambient temperature

h = probe heat transfer coefficient , $h = \dfrac{k_g}{Nu\, L}$

σ = Stefan–Boltzmann constant .

This formula assumes that the flames and hot gases are effectively transparent. The values of Nusselt number for the conditions of this investigation were obtained from Sandborn [1972]. The calculated radiation errors for the cold wire and thermocouple junction are shown in Figure A.2. Also shown is the radiation error for the thermocouple support wires.

It can be seen from Figure A.2 that the radiation errors for both the 25 μm diameter thermocouple and the 2.5 μm diameter cold wire were very small over the temperatures of this investigation. The radiation error for the

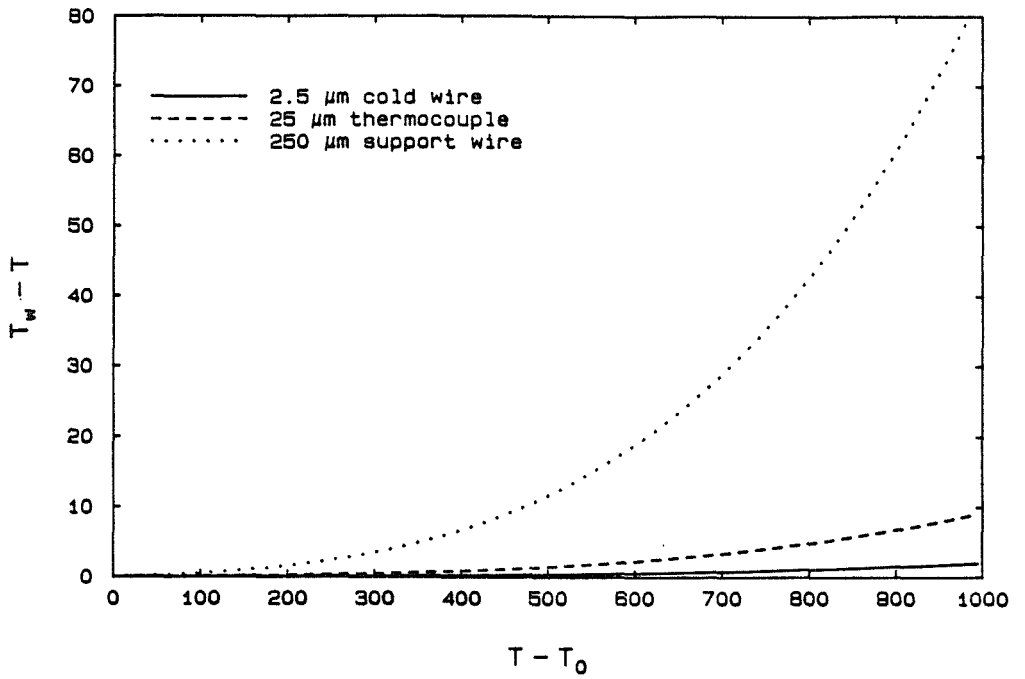

Figure A.2 Radiation Error

thermocouple support wires was substantially higher, owing to their much larger diameter ($250\,\mu m$). It was seen in the last section that the probe temperature is influenced by the support prong temperature through conduction error. Conduction caused an error in thermocouple junction temperature of 65% of the corresponding radiation error in support wire temperature. This amounted to approximately 10 K for the maximum mean measured temperature of 580 K, corresponding to a maximum error of about 1%. The cold wires had negligible radiation error even at the maximum adiabatic flame temperatures. All radiative corrections were thus small and were not applied to any of the temperature data in this investigation.

A.3. Nonlinearity of Resistivity with Temperature

At small temperature rises, it can be assumed that the resistivity of the cold wire element is linear with temperature, thus allowing a simple and direct relation between the temperature rise and the probe voltage change:

$$\frac{\Delta V}{\Delta T} = I \alpha R_0 \tag{A.5}$$

where

ΔV = measured voltage change

ΔT = temperature change

I = wire current

α = first coefficient of resistivity

R_0 = wire cold resistance

Equation (A.5) follows from the linear relation between probe resistance and temperature at low temperatures,

$$R = R_0(1 + \alpha \Delta T) \tag{A.6}$$

where R is the resistance of the wire.

At elevated temperatures, Equation (A.6) is no longer a good representation of the wire resistance. For many materials, including the Platinum-10% Rhodium alloy used for the cold wires in this investigation, a quadratic expression for the resistance at high temperatures is suitable:

$$R = R_0(1 + \alpha T + \beta T^2) \quad , \tag{A.7}$$

where β is the second coefficient of resistivity. Data from Caldwell [1962] suggest the following values for Platinum-10% Rhodium: $\alpha = 1.6 \times 10^{-3}/K$, $\beta = 1.75 \times 10^{-7}/K^2$. The resistivity is plotted in Figure A.3. It can be seen that there is good agreement between the data of Caldwell [1962] and the linear approximation for $\Delta T \leq 300\,K$. At higher temperatures, however, the

agreement is less satisfactory. This disagreement would result, for example at $\Delta T \approx 1000\ K$, in about 10% error in measured temperature if no correction for the nonlinearity were made.

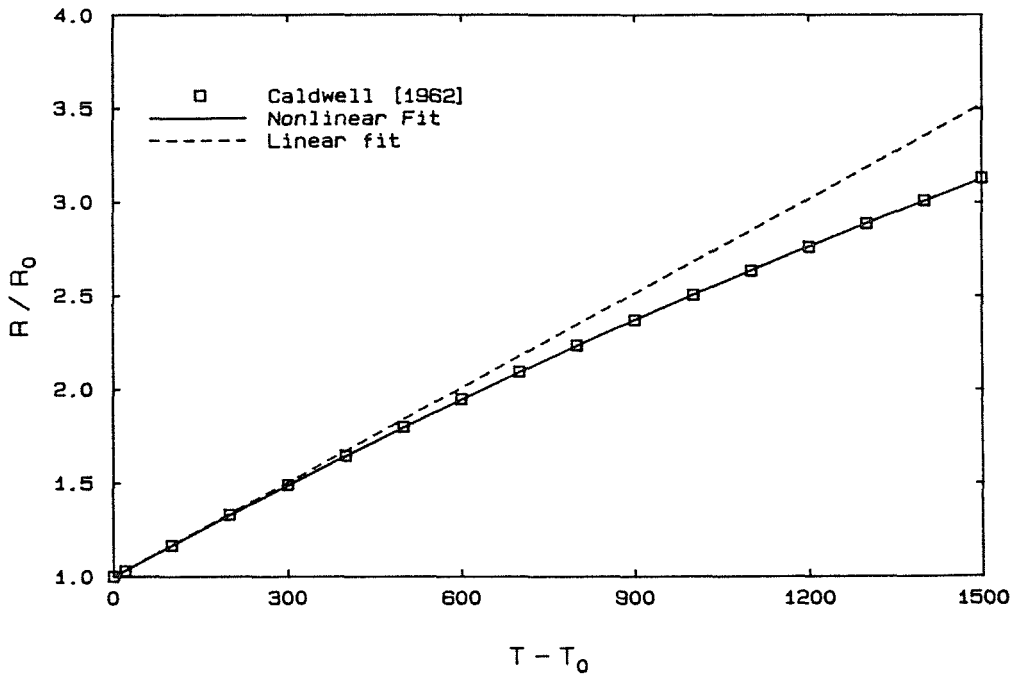

Figure A.3 Actual versus Linear Resistivities

Incorporating the nonlinear sensitivities gives the following relation for the voltage change caused by temperature:

$$\Delta V = I R_0 [\alpha (T - T_0) + \beta (T^2 - T_0^2)]$$

$$= \hat{V} (T - T_0) + \hat{V} \frac{\beta}{\alpha} (T^2 - T_0^2) \qquad \text{(A.8)}$$

where:

$$\hat{V} \equiv \left[\frac{\Delta V}{\Delta T} \right]_{linear} ,$$

as given by equation (A.6) in the linear calibration range, i.e., $\Delta T \leq 300\ K$. The quantity $\hat{V}$ was determined from the probe calibration procedure described in § 2.2.2. The corrected measured temperature rise is

$$T - T_0 = \frac{\alpha}{2\beta}\left\{\left[1 + 4\frac{\beta}{\alpha}\left(\frac{\Delta V}{\hat{V}} + T_0\right)\right]^{\frac{1}{2}} - 1\right\} - T_0 \qquad \text{(A.9)}$$

which is closely approximated by

$$T - T_0 = \frac{\Delta V}{\hat{V}} - \frac{\beta}{\alpha}\left(\frac{\Delta V}{\hat{V}} + T_0\right)^2 \quad . \qquad \text{(A.10)}$$

The second term in equation (A.10) represents the correction for nonlinear resistivity. This correction was applied to all of the cold wire data in this investigation.

A.4. Catalytic Effects

Gaydon & Wolfhard [1960] mention that in some cases, catalysis can occur between reacting gases and the metal surface of a probe. This is an issue in this work since platinum, the primary component in the cold wire probes, is an excellent catalyst. The extent of possible catalytic error was investigated, in some runs, by use of a 25 μm diameter junction Chromel-Alumel thermocouple placed alongside the rake of platinum-rhodium cold wires. Good agreement, typically within 3%, was obtained between the two probes (each of a different material), suggesting that catalytic effects are not a substantial cause of error in this investigation.

A.5. Nonuniformity in Gas Thermal Conductivity

How a probe responds to temperature fluctuations depends on its characteristic time, which depends on the thermal conductivity of the gas in which the probe is immersed. The heat conductivity of hydrogen is much higher than that of nitrogen or fluorine. The implication of this is that any portion of the flow with large amounts of hydrogen allows much faster heat transfer to the probe (resulting in a faster characteristic time) than regions with little hydrogen. This variation in time response can be shown theoretically to result in an error in measured temperature. Since up to 24% hydrogen was employed for some runs, the non-uniformity of heat conductivity is an issue of some concern. This effect is described in detail in Appendix B.

A.6. Probe Parasitic Resistance

It is assumed in equation (A.6) that the resistance change in the wire element is much greater that that in the support prongs. Heat transfer into the exposed and unexposed portions of the prongs did however account for some change in the resistance of the prongs during the course of a run. An approximate expression for the resistance of the prongs is:

$$R_p = R_{p_0}[1 + \alpha_p \Delta T \frac{L^* + L_t}{L}] \qquad (A.11)$$

where:

L^* = heat diffusion length into prongs

L_t = exposed prong tip length

L = total prong material length

α_p = coefficient of resistivity for prong material

R_p = prong resistance

R_{p_0} = prong cold resistance

For the support prongs used in this investigation,

$$\frac{L^* + L_t}{L} \approx 0.11 \quad ,$$

and using the estimated $\alpha_p \approx 0.009$ for the copper-clad Inconel prongs gives, using (A.11),

$$\frac{\Delta R_p}{\Delta T} = 0.001 \ ohms/K \quad .$$

This compares with, for the $2.5\,\mu m$ diameter cold wire probes,

$$\frac{\Delta R}{\Delta T} = 0.084 \ ohms/K \quad ,$$

for an error of about $1/2\,\%$. This error, however, increases with the square of wire diameter, and gives, for example with a $12.5\,\mu m$ diameter wire, an error of more than $7\,\%$. This is one of the reasons thermocouples were introduced for temperature measurement at the higher temperatures of this investigation rather than simply employing thicker and more robust cold wires.

Appendix B

EFFECTS OF GAS THERMAL CONDUCTIVITY ON TEMPERATURE MEASUREMENT

B.1. Error in Temperature Measurement due to Variations in Thermal Conductivity

The extent that a thermocouple or cold wire probe indicates the correct temperature is determined by numerous factors. This appendix will describe the error in temperature measurement caused by variations in thermal conductivity in the gas, and how this error can be minimized.

The extent fluctuating temperatures are smoothed in measurement depends on the thermal inertia of the probe, as indicated by its characteristic time. The characteristic time also determines how well the mean flow temperature is represented by the probe. The characteristic time of the system, here for simplicity neglecting conduction and radiation, is directly dependent on the thermal conductivity of the surrounding gas, i.e.,

$$\tau = \frac{1}{k_g} \frac{D^2 \rho_w c_w}{4\,Nu} \quad , \tag{B.1}$$

where:

D = *probe wire diameter*

Nu = *Nusselt number*

ρ_w = *probe wire density*

c_w = *specific heat of probe wire*

k_g = *gas thermal conductivity*

Equation (B.1) indicates that a probe will respond quickly to temperature changes in gases of high thermal conductivity, and more slowly in gases where the thermal conductivity is low. The variation in characteristic time could have been substantial in the present experiment, where the presence of up to 24% hydrogen significantly increased the thermal conductivity of the gas mixture containing it.

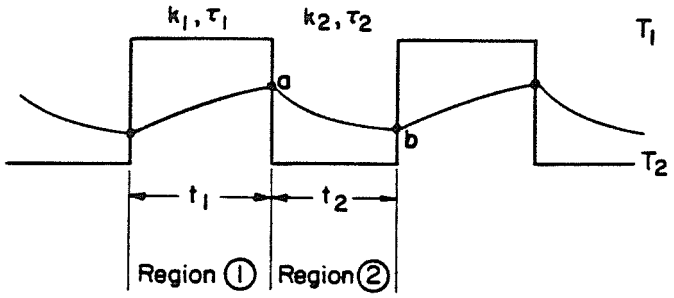

Figure B.1 Model Square Wave Temperature Cycle

An estimate for the amount of error in mean temperature measurement caused by variations in thermal conductivity can be made by calculating the response of a probe to a model temperature field consisting of alternating regions of hot and cold gases, as shown in figure B.1. The thermal conductivity of the gas in the hot regions will be taken to be different than the corresponding thermal conductivity in the cold regions. The curved line represents the response of the probe. A similar analysis with a model sinusoidal variation in gas temperature and thermal conductivity was done by Ballentyne et al. [1976].

Neglecting conduction and radiation error, the probe response is described by the first-order system equation

$$\tau \frac{dT_w}{dt} + T_w = T \quad , \tag{B.2}$$

where T_w is the probe temperature and T is the temperature of the gas. The response of the system to the model temperature cycle of Figure B.1, e.g. between points "a" and "b" (region 2) is

$$T_w = T_2 + (T_a - T_2)\, e^{-t/\tau_2} \quad , \tag{B.3}$$

and in region 1,

$$T_w = T_1 + (T_b - T_1)\, e^{-t/\tau_1} \quad . \tag{B.4}$$

The subscripts 1 and 2 are used to identify regions of different temperature in the model cycle of Figure B.1, and t_1 and t_2 are the corresponding periods. Matching conditions at points "a" and "b" with the adjacent half-cycles, which implies that the probe is in a steady state condition, allows solution for the values of T_a and T_b at the endpoints of each interval. These are:

$$T_a = \frac{T_1 + [T_2(1 - e^{-t_2/\tau_2}) - T_1]\, e^{-t_1/\tau_1}}{1 - e^{-(t_2/\tau_2 + t_1/\tau_1)}} \quad , \tag{B.5}$$

$$T_b = \frac{T_2 + [T_1(1 - e^{-t_1/\tau_1}) - T_2]\, e^{-t_2/\tau_2}}{1 - e^{-(t_2/\tau_2 + t_1/\tau_1)}} \quad . \tag{B.6}$$

Integrating equations (B.3) and (B.4) over a full cycle allows determination of the mean measured temperature :

$$\overline{T_w} = \bar{T} + \frac{(T_1 - T_2)(\tau_2 - \tau_1)(1 - e^{-t_2/\tau_2})(1 - e^{-t_1/\tau_1})}{(t_1 + t_2)[1 - e^{-(t_1/\tau_1 + t_2/\tau_2)}]} \quad , \tag{B.7}$$

where

$$\bar{T} = \frac{T_1 t_1 + T_2 t_2}{t_1 + t_2} \quad .$$

$\bar{T}$ is the true mean temperature of the gas temperature field. The second term in equation (B.7) is the misrepresentation in mean temperature by the probe owing to the change in probe characteristic times caused by the change in thermal conductivity of the gas. The error is zero when $\tau_2 = \tau_1$ and increases with the difference $\tau_1 - \tau_2$. The error in measured temperature increases, for fixed values of τ_1 and τ_2, with decreasing half-periods t_1 and t_2, i.e., with increasing fluctuation frequencies. The limiting error for infinite fluctuation frequencies is, for $t_1 = t_2$,

$$\overline{T_w} - \bar{T} = (T_1 - T_2)\frac{\tau_1 - \tau_2}{\tau_1 + \tau_2} \quad . \tag{B.8}$$

A plot of the error in measured mean temperature is shown in Figure B.2, plotted against the ratio t_1/τ_1. The gas in region 2 is taken to be cold free stream fluid with 24% hydrogen in nitrogen; in region 1, pure nitrogen. All thermal conductivities are the cold values. Under these conditions, $\tau_1/\tau_2 = k_2/k_1 = 1.90$, where k_1 and k_2 are here the thermal conductivities of the corresponding gas mixtures. A parametric set of curves in t_1/t_2 is presented. It can be shown that the maximum error occurs for $t_1/t_2 = (\tau_1/\tau_2)^{\frac{1}{2}} = 1.38$. An error in the mean of as much as 16% is predicted by this analysis. It should be pointed out

that this analysis is conservative because of the extremes of thermal conductivity differences modeled. In the real flow, intermediate values of thermal conductivity between the two extremes of the square-wave model occur, resulting in a smaller error. The estimated error is predicted to decrease with decreasing characteristic times, i.e., a probe with a fast time response will indicate the mean temperature more accurately than a probe with slow time response.

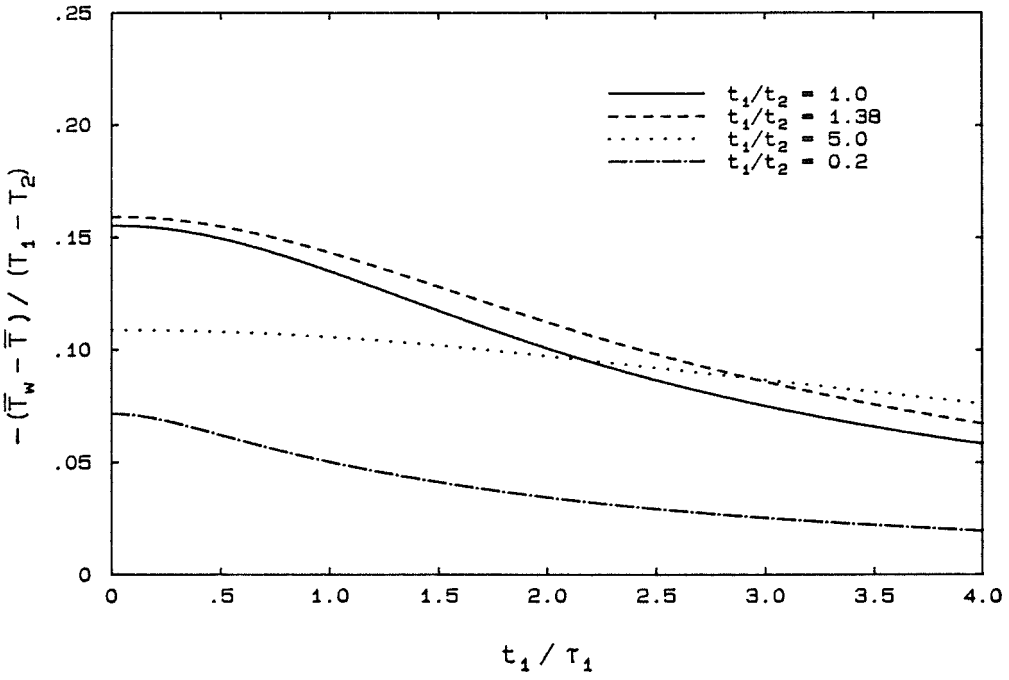

Predicted Error in Mean Temperature Measurement

Figure B.2

In physical terms, using the Kolmogorov scale, λ_0, and the mean velocity, $(U_1 + U_2)/2$, to define the appropriate fluctuation period, gives $t_1 = 2\lambda_0/(U_1 + U_2) \approx 120\,\mu sec$. Using the estimated cold wire response $\tau_1 \approx 330\,\mu sec$ estimated by Mungal & Dimotakis [1984] gives $t_1/\tau_1 \approx 0.40$. For the much slower time response thermocouples, the value of t_1/τ_1 was very close to zero.

B.2. Reduction of Error by Using Gas Mixtures

In this section a technique for reducing the unequal time response error by using gas mixtures will be discussed. Ideally, all gas in the flow would have the same thermal conductivity, resulting in no error in measured temperature due to thermal conductivity nonuniformity. The temperature dependence of thermal conductivity on temperature, unfortunately, makes this impossible in a flow with heat release. It might be expected, however, that the error could be minimized by matching the free stream cold thermal conductivities as closely as possible. As explained in § 2.1, for this investigation it was also intended to match the molar heat capacities and densities of the free streams.

To accomplish these matchings, it was sought to use in each free stream as diluent a combination of inerts (nitrogen plus noble gases helium and argon) to match mixture properties as closely as possible. The condition for the matching of the free stream densities is:

$$\chi_{H_2}\hat{M}_{H_2} + \chi_{N_2}\hat{M}_{N_2} + \chi_{He}\hat{M}_{He} + \chi_{Ar}\hat{M}_{Ar} =$$

$$\chi^*_{F_2}\hat{M}_{F_2} + \chi^*_{N_2}\hat{M}_{N_2} + \chi^*_{He}\hat{M}_{He} + \chi^*_{Ar}\hat{M}_{Ar} \qquad \text{(B.9)}$$

where χ is the number fraction and $\hat{M}$ is the molar mass of each species in the mixtures. The superscript * denotes the fluorine-bearing free stream.

Since the molar heat capacities of nitrogen, fluorine and hydrogen are nearly equal, and since the molar heat capacities of helium and argon are virtually identical, the molar heat capacities of the free streams will be very nearly matched provided that

$$\chi_{H_2} + \chi_{N_2} = \chi^*_{F_2} + \chi^*_{N_2} \quad . \tag{B.10}$$

The number fractions must of course sum to unity,

$$\chi_{H_2} + \chi_{N_2} + \chi_{He} + \chi_{Ar} = \chi^*_{F_2} + \chi^*_{N_2} + \chi^*_{He} + \chi^*_{Ar} = 1 \quad . \tag{B.11}$$

The thermal conductivity for a mixture of gases at high temperature and at low pressure can be evaluated using the approximate formula derived by Mason and Saxena [1958]:

$$k_{mix} = \sum_{i=1}^{n} k_i \left(1 + \sum_{\substack{k=1 \\ k \neq i}}^{n} G_{ik} \frac{\chi_k}{\chi_i}\right)^{-1} \tag{B.12}$$

where

$$G_{ik} = \frac{1.065}{2\sqrt{2}} \left(1 + \frac{\hat{M}_i}{\hat{M}_k}\right)^{-1/2} \left[1 + \left(\frac{\mu_i}{\mu_k}\right)^{1/2} \left(\frac{\hat{M}_k}{\hat{M}_i}\right)^{1/4}\right]^2 \tag{B.13}$$

and k_i, μ_i are the individual species thermal conductivity, and viscosity, respectively, and k_{mix} is the thermal conductivity of the mixture.

Examination of equations (B.9), (B.10) and (B.11) reveals that, with nitrogen and two noble gases as diluents in each free stream, it is possible to simultaneously match the free stream heat capacities and densities. This does not, however, necessarily match the thermal conductivities. The search for an optimum mixture, in which the heat capacities are exactly matched, and the densities and thermal conductivities are as closely matched as possible, results in a parametric plot as shown in Figure B.3. This plot corresponds to a case with 6%

fluorine and 24% hydrogen, the largest concentrations run for the present investigation.

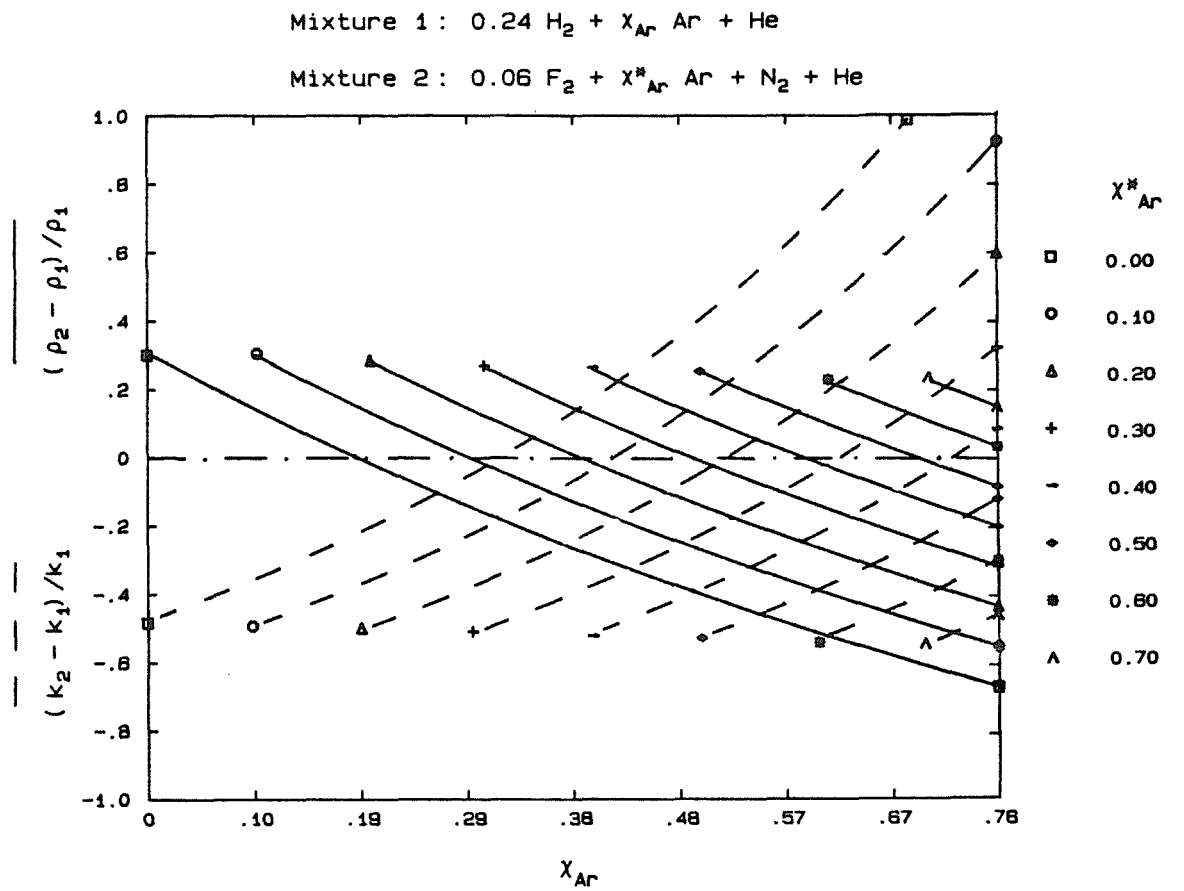

Parametric Plot for Free Stream Density
and Thermal Conductivity Matching

Figure B.3

It can be seen from Figure B.3 that if no noble gases are added to the nitrogen diluents, the thermal conductivity of the free streams for this case would be different by about 45%, and the densities by about 32%. It can be noted that the density matched solution results in reducing the free stream thermal conductivity difference to about 20%. The attainment of the optimum degree of matching appears to be obtainable for these inerts by simply adding some argon to the hydrogen side and some helium to the fluorine side.

Since the estimate of error due to the variation in thermal conductivity in the previous section of this appendix is believed to be conservative, it was necessary to make some comparison runs to evaluate the actual effect of unequal free stream thermal conductivities on the measured mean temperature profiles. Comparisons of mean temperature profiles are presented in Figure B.4. Figure B.4a shows the cold wire measured results with 2% fluorine and 16% hydrogen for a flame temperature rise of about 340 K. The two profiles shown correspond to matched and unmatched cold free stream thermal conductivities. It can be seen that there is no substantial difference in either the height of the profiles or in the area underneath them (normalized by the local profile width), suggesting that for these experiments it was sufficient to match thermal conductivities to within 35%.

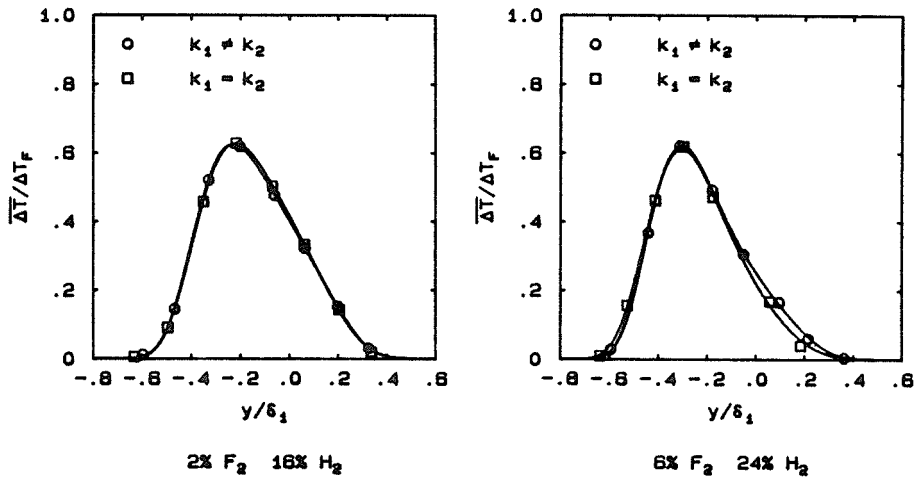

Mean Temperature Profiles, with and without Matched Free Stream Thermal Conductivities

Figure B.4a Figure B.4b

Good agreement was also observed for the thermocouples at concentrations of 6% fluorine and 24% hydrogen (flame temperature rise of about 900 K). This

comparison is presented in Figure B.4b. It was concluded that it was satisfactory, for all high concentration runs, to match the free stream densities and molar heat capacities allowing the free stream thermal conductivities to be slightly unmatched (but within 20%).

Appendix C

STRAINED DIFFUSION FLAMES WITH UNEQUAL REACTANT DIFFUSIVITIES

Any analytical description of a reacting flow must consider some sort of interfacial zones into which the reactants diffuse on a molecular scale. One approach is to model the diffusion zones as strained laminar flame elements (Marble & Broadwell [1977], Broadwell & Breidenthal [1982]). These analyses assume that the thicknesses of the strained laminar flame elements are small compared with the wavelengths of disturbances in the flow, allowing the elements to be considered planar, and that they adjust rapidly to changes in strain rate imposed by the flow field. The derivations presented in Marble & Broadwell [1977] and Carrier et al. [1975] are extended in this appendix by including the effects of unequal reactant diffusivities. This is relevant for the hydrogen-fluorine reaction since the diffusivity of hydrogen into nitrogen is about three times greater than the corresponding diffusivity of fluorine.

C.1. Reactant Concentration Calculation

The diffusion equation for a flame element is

$$\frac{\partial \kappa_i}{\partial t} + V\frac{\partial \kappa_i}{\partial y} = \frac{1}{\rho}\frac{\partial}{\partial y}\left[\rho D_i \frac{\partial \kappa_i}{\partial y}\right] \quad , \tag{C.1}$$

where D_i and κ_i are the mass diffusivity and mass fraction (ρ_i / ρ), respectively, of reactant species i. The quantity ρ is the combined mass density of all species (reactant, product and diluent), and V is the velocity normal to the flame zone. The flame zone is considered to be planar with no variation of concentration or density in the planar direction, with the coordinates x and y taken to be

parallel and normal, respectively, to the plane of the flame zone.

Introducing the transformation by Howarth [1948],

$$\hat{\xi} \equiv \int_0^y \frac{\rho}{\rho_0} dy \quad , \tag{C.2}$$

where ρ_0 is the ambient density (assumed to have the same value on both sides of the flame zone), gives for equation (C.1)

$$\frac{\partial \kappa_i}{\partial \tau} + \left[\int_0^y \frac{\partial}{\partial t} \left(\frac{\rho}{\rho_0} \right) dy \right] \frac{\partial \kappa_i}{\partial \hat{\xi}} + \frac{\rho}{\rho_0} V \frac{\partial \kappa_i}{\partial \hat{\xi}} \tag{C.3}$$

$$= \frac{1}{\rho_0} \frac{\partial}{\partial \hat{\xi}} \left(\rho D_i \frac{\rho}{\rho_0} \frac{\partial \kappa_i}{\partial \hat{\xi}} \right) = D_{0i} \frac{\partial^2 \kappa_i}{\partial \hat{\xi}^2}$$

where $\tau \equiv t$. In the same fashion as Carrier et al. [1975], the density was eliminated from the right hand side of (C.3) by taking $\rho \sim T^{-1}$ (constant pressure), and by taking as an approximate temperature dependence $D_i \sim T^2$. This gives $\rho^2 D_i \equiv {\rho_0}^2 D_{0i} =$ constant, where D_{0i} is the ambient diffusion coefficient of the species i (in general, $D_{01} \neq D_{02}$).

Equation (C.3) can be simplified by use of the equation of continuity, which for this problem is:

$$\frac{\partial \rho}{\partial t} + \rho \varepsilon(t) + \frac{\partial}{\partial y}(\rho V) = 0 \quad , \tag{C.4}$$

where $\varepsilon(t)$ is the strain rate, and the corresponding velocity in the direction parallel to the direction of strain is $U = \varepsilon(t) x$. Integrating (C.4) gives:

$$\frac{\partial}{\partial t}\int_0^y \frac{\rho}{\rho_0}dy + \frac{\rho}{\rho_0}V = -\varepsilon(t)\int_0^y \frac{\rho}{\rho_0}dy = -\varepsilon(t)\,\hat{\xi} \quad . \tag{C.5}$$

Combination of (C.3) and (C.5) then yields a modified diffusion equation:

$$\frac{\partial \kappa_i}{\partial \tau} - \varepsilon(t)\,\hat{\xi} = D_{0i}\frac{\partial^2 \kappa_i}{\partial \xi^2} \quad . \tag{C.6}$$

This can be reduced further by an additional change of variable:

$$\xi^* \equiv \hat{\xi}\, e^{\int_0^t \varepsilon(t')\,dt'} \quad , \tag{C.7}$$

which allows elimination of the $\varepsilon(t)$ term in (C.6) to give:

$$\frac{\partial \kappa_i}{\partial \tau} - D_{0i}\frac{\partial^2 \kappa_i}{\partial \xi^{*2}} = 0 \quad . \tag{C.8}$$

The corresponding solutions are:

$$\kappa_i = A_i\, erf\,(\zeta_i) + B_i \tag{C.9}$$

where A_i and B_i are constants, dictated by the boundary conditions, and

$$\zeta_i = \frac{\xi^*}{2\,(D_{0i}\tau)^{1/2}} \quad . \tag{C.10}$$

The boundary conditions require that each reactant be equal to the corresponding ambient value; i.e., $\kappa_1(\infty) = \kappa_{01}$ and $\kappa_2(-\infty) = \kappa_{02}$. If the chemical kinetics are rapid, then as an approximation each reactant can be taken to vanish at the

flame front, requiring $\kappa_1(\zeta_1^*) = \kappa_2(\zeta_2^*) = 0$. The quantities ζ_1^* and ζ_2^* thus correspond to the location of the flame front. The reactant concentration distributions on each side of the flame front are then:

$$\kappa_1 = \frac{\kappa_{01}}{1 - erf(\zeta_1^*)}[erf(\zeta_1) - erf(\zeta_1^*)] \quad \text{for } \zeta_1 > \zeta_1^* \ , \tag{C.11}$$

$$\kappa_2 = \frac{\kappa_{02}}{1 + erf(\zeta_2^*)}[erf(\zeta_2^*) - erf(\zeta_2)] \quad \text{for } \zeta_2 < \zeta_2^* \ . \tag{C.12}$$

The flame front position can be determined from the requirement that the reactants are consumed stoichiometrically; i.e.,

$$-\frac{D_1}{(D_{01})^{1/2}} \frac{d\kappa_i}{d\zeta_1}\bigg|_{\zeta_1^*} = f^* \frac{D_2}{(D_{02})^{1/2}} \frac{d\kappa_2}{d\zeta_2}\bigg|_{\zeta_2^*} \tag{C.13}$$

where f^* is the mass stoichiometric ratio of the chemical reaction. Noting that $\zeta_2^* = \Theta\zeta_1^*$, where $\Theta \equiv (D_{01}/D_{02})^{1/2}$, yields an implicit expression for ζ_1^*:

$$\Theta\varphi^* \frac{e^{-\zeta_1^{*2}}}{1 - erf(\zeta_1^*)} = \frac{e^{-\Theta^2\zeta_1^{*2}}}{1 + erf(\Theta\zeta_1^*)} \ , \tag{C.14}$$

where $\varphi^* \equiv (\kappa_{01}/\kappa_{02})(1/f^*)$. For the $H_2 + F_2 \rightarrow 2HF$ reaction, $\varphi^* = c_{01}/c_{02}$, the equivalence ratio introduced in section 4.5. The factor $\Theta\varphi^*$ in equation (C.14) suggests that if $\Theta \neq 1$,that is, the diffusivities of the reacting species are not equal, the flame front behavior will be, in some sense, governed by an 'inferred φ^*'. This will be, in general, different than the actual φ^*. This will be quantified in the next section.

The solutions for the concentrations given by equations (C.11) and (C.12) are similar in form to the solutions developed by Carrier et al. [1975] and by Marble & Broadwell [1977]. One consequence of unequal reactant diffusivities is a shift in the position of the flame zone, as indicated by ζ_1^* in equation (C.14). This will be seen in the next section to result in different reactant consumption rates than in the case of equal reactant diffusivities.

C.2. Reactant Consumption Rates

The mass consumption rates of the reactants at the flame front can be calculated as follows:

$$\dot{m}_i = \rho D_i \left.\frac{\partial \kappa_i}{\partial y}\right|_{y^*} = \rho \frac{D_i}{(D_{0i})^{1/2}} \left.\frac{d\kappa i}{d\zeta_i}\right|_{\zeta_i^*} , \tag{C.15}$$

where y^* is the flame front position in physical coordinates. Using the relations for κ_i, equations (C.11) and (C.12) gives:

$$\dot{m}_1 = \rho_0 \kappa_{01} \left(\frac{D_{01}}{\pi \tau}\right)^{\frac{1}{2}} \frac{e^{-\zeta_1^{*2}}}{1 - erf\,(\zeta_1^*)} e^{\int_0^t \varepsilon(t')\,dt'} , \tag{C.16}$$

$$\dot{m}_2 = \rho_0 \kappa_{02} \left(\frac{D_{02}}{\pi \tau}\right)^{\frac{1}{2}} \frac{e^{-\zeta_2^{*2}}}{1 + erf\,(\zeta_2^*)} e^{\int_0^t \varepsilon(t')\,dt'} . \tag{C.17}$$

Taking as simple case $\varepsilon(t) = \varepsilon_0 = constant$, for large values of time, t, allows simplification of the preceding expressions to:

$$\dot{m}_1 = \rho_0 \kappa_{01} \left(\frac{2\,\varepsilon_0 D_{01}}{\pi}\right)^{\frac{1}{2}} \frac{e^{-\zeta_1^{*2}}}{1 - erf\,(\zeta_1^*)} , \tag{C.18}$$

$$\dot{m}_2 = \rho_0 \kappa_{02} \left(\frac{2 \varepsilon_0 D_{02}}{\pi} \right)^{\frac{1}{2}} \frac{e^{-\zeta_2^{*2}}}{1 + erf(\zeta_2^*)} \quad . \tag{C.19}$$

These rates are of the same form as the mass consumption rates derived by Liñan [1980].

The number consumption of each reactant is expressed by $\dot{n}_i = \dot{m}_i / \hat{M}_i$, and gives, for example, for reactant 1,

$$\dot{n}_1 = c_0^* n_0 \sqrt{2} \left(\frac{D_{01} \varepsilon_0}{\pi} \right)^{\frac{1}{2}} \frac{e^{-\zeta_1^{*2}}}{1 - erf(\zeta_1^*)} \quad . \tag{C.20}$$

The quantity n_0 is the ambient total number density, and the quantity c_0^* is selected to represent the consumption rate over a range of φ^* while keeping the lean reactant concentration fixed. This requires $c_0^* = c_{01}$ for $c_{01} > c_{02}$, and $c_0^* = c_{02}$ for $c_{01} < c_{02}$. For the $H_2 + F_2$ reaction, the number production rate of product is equal to twice the number consumption rate of either reactant. It is interesting to note that the mass consumption rates do not depend on the heat release as manifested by the change in density at the flame front.

The reactant number consumption rates given by (C.20) are plotted against $\xi_\varphi \equiv \varphi^*/(1 + \varphi^*)$ in Figure C.1. Each value of $\dot{n}_1$ is normalized by the corresponding value for $\xi_\varphi = 0.5$. This allows determination of the relative dependence of reactant consumption on ξ_φ for each value of Θ. It can be seen that for $\Theta = 1$, the result is symmetric about $\xi_\varphi = 0.5$ ($\varphi^* = 1$). For the case of unequal diffusivity , (e.g., $\Theta = 1.932$, the value for H_2/F_2), however, an asymmetry in $\dot{n}_1$ versus ξ_φ is apparent. This provides a means for quantitative determination of the "inferred φ^*" mentioned in the last section. The "inferred φ^*", φ_i^*, can be defined as the concentration ratio parameter that would be required, in a

matched reactant diffusivity case, to give the same reactant consumption rate as for the actual φ^* in the case of unequal reactant diffusivities. The quantity, φ_i^*, is plotted versus φ^* in Figure C.2. The normalization utilized in Figure C.1 causes $\varphi_i^* = \varphi^*$ at $\varphi^* = 1$. It can be seen that with $\Theta = 1.932$, φ_i^* exceeds φ^* and differs substantially for φ^* far from $\varphi^* = 1$. Sample values for the inferred concentration ratio parameter are 13 and 5.2 for actual concentration ratio values of 8 and 4, respectively.

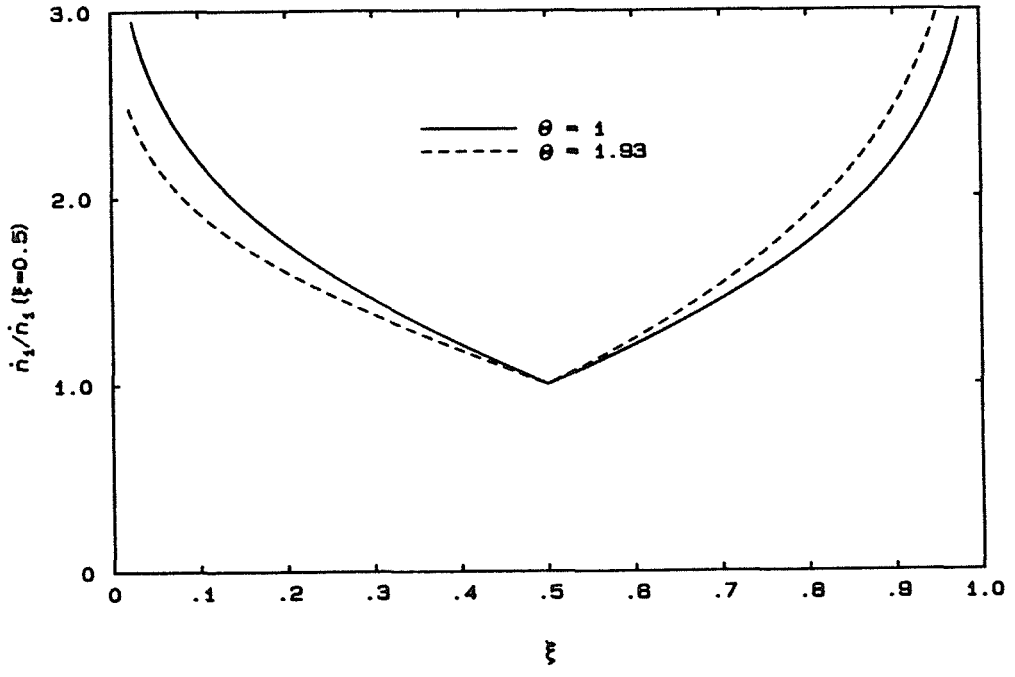

Reactant Consumption Rate

Figure C.1

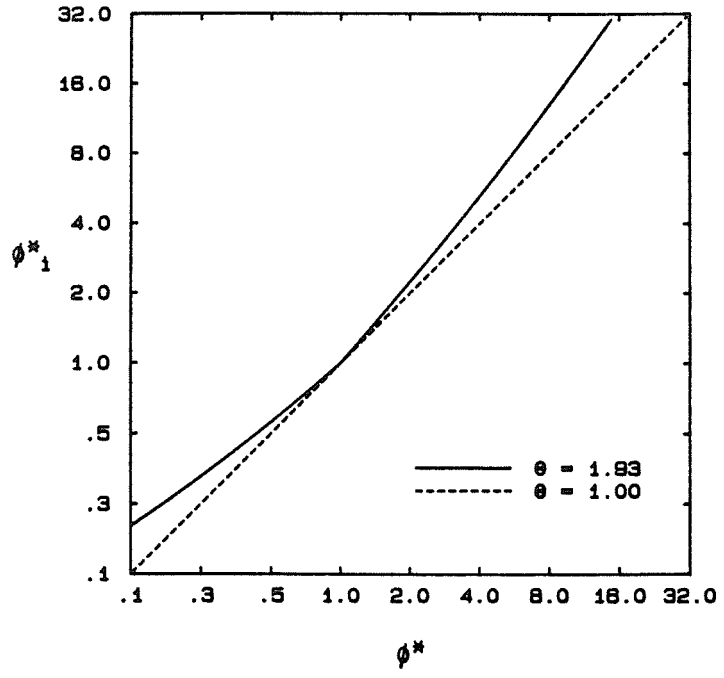

Inferred Concentration Ratio

Figure C.2

C.3. Adiabatic Flame Temperature

The effect of unequal reactant diffusivity on the adiabatic flame temperature is discussed in this section. The derivation begins with the energy equation for the system:

$$\frac{\partial T}{\partial t} + v \frac{\partial T}{\partial y} = \frac{1}{C_p \rho} \frac{\partial}{\partial y} \left[k_i \frac{\partial T}{\partial y} \right] \tag{C.21}$$

where k_i is the thermal conductivity of the mixture on the side containing reactant i, and C_p is the specific heat. This relation (C.21) is in form identical to the diffusion equations (C.1), and using the same continuity equation (C.4) and the same transformations of variables (C.2) and (C.7) yields:

$$\frac{\partial T}{\partial \tau} = \left(\frac{k_{0i}}{C_p \rho_0} \right) \frac{\partial^2 T}{\partial \xi^{*2}} \quad , \tag{C.22}$$

where the approximate temperature dependence $k_i \sim T^2$ was taken to allow $k_{i0}/\rho_0 = k_i/\rho$. The specific heat is assumed to be constant and equal between the two sides of the flame zone.

The factor on the right hand side of (C.22) relates to the Lewis number, which can be defined, for each side of the flame, by

$$Le_i \equiv \frac{\rho_0 C_p D_{0i}}{k_{0i}} \quad . \tag{C.23}$$

Liñan [1980] calculated the effect of Lewis number on the flame temperature of a strained diffusion flame for the case of equal reactant diffusivities. In general, and specifically for the $H_2 - F_2$ reactant pair, $Le_1 \neq Le_2$. The solutions to (C.22) are of similar form to the solutions to (C.9) and are:

$$T = A_i' \, erf\left(\sqrt{Le_i}\, \zeta_i\right) + B_i' \quad , \tag{C.24}$$

where A_i' and B_i' are constants. Enforcing the boundary conditions $T(+\infty) = T(-\infty) = T_0$, the ambient temperature, and $T(\zeta_1^*) = T(\zeta_2^*) = \Delta T_F + T_0$, gives the expression for the temperature distribution on each side of the flame zone:

$$T = \frac{T_F - T_0}{erf\left(\sqrt{Le_1}\, \zeta_1^*\right) - 1} \left[erf\left(\sqrt{Le_1}\, \zeta_1^*\right) - 1 \right] + T_0 \qquad \zeta_1 > \zeta_1^* \quad . \tag{C.25}$$

$$T = \frac{T_F - T_0}{erf\,(\sqrt{Le_2}\,\zeta_2^*) + 1}\,[erf\,(\sqrt{Le_2}\,\zeta_2^* + 1] + T_0 \quad \zeta_2 < \zeta_2^* \quad . \tag{C.26}$$

The value of the flame temperature rise, ΔT_F, can be obtained by enforcing at the flame front the condition that the heat flux away from the reaction zone balances the heat release furnished by the chemical reaction. Mathematically,

$$-k_1 \left.\frac{dT}{d\zeta_1}\right|_{\zeta_1^*} + k_2 \Theta \left.\frac{dT}{d\zeta_2}\right|_{\zeta_2^*} = q\,\rho\,D_1 \left.\frac{d\kappa_1}{d\zeta_1}\right|_{\zeta_1^*} \tag{C.27}$$

where q is the heat release of the chemical reaction per unit mass. Application of (C.27) to the temperature given by (C.25) and (C.26) gives the adiabatic flame temperature rise,

$$\Delta T_F = \frac{q}{C_p}\kappa_0\,Le_1\,\frac{e^{-\zeta_1^{*2}}}{1 - erf\,(\zeta_1^*)}\,(E_2 - E_1)^{-1} \quad , \tag{C.28}$$

where

$$E_1 \equiv \frac{e^{-Le_1\zeta_1^{*2}}}{erf\,(\sqrt{Le_1}\,\zeta_1^*) - 1} \quad , \quad E_2 \equiv \frac{1}{\Theta}\,\frac{Le_1}{Le_2}\,\frac{e^{-Le_2\zeta_2^{*2}}}{erf\,(\sqrt{Le_2}\,\zeta_2^*) + 1} \quad ,$$

and κ_0 is the lean reactant mass fraction. It is interesting to note that the adiabatic flame temperature rise, unlike the reactant consumption rates, does not depend on the strain rate of the flame zone. In the case where $Le_1 = Le_2$, (C.28) reduces to, for all values of Θ,

$$\Delta T_F = \kappa_{01} \frac{q}{C_p} \frac{1}{1+\varphi} \tag{C.29}$$

which is identical in form to the result presented in equation (3.24), § 3.5.

Liñan [1980] also showed that, for equal reactant diffusivities, only in the case of $Le = 1$ does maximum temperature rise in the flame zone equal the flame temperature rise calculated from the stoichiometry, heat of reaction and specific heat, as in equation (C.29). The flame temperature rises represented by (C.28), normalized by $\kappa_0 q / C_p$, are shown in Figure C.3. In all cases shown, $\Theta = 1.932$.

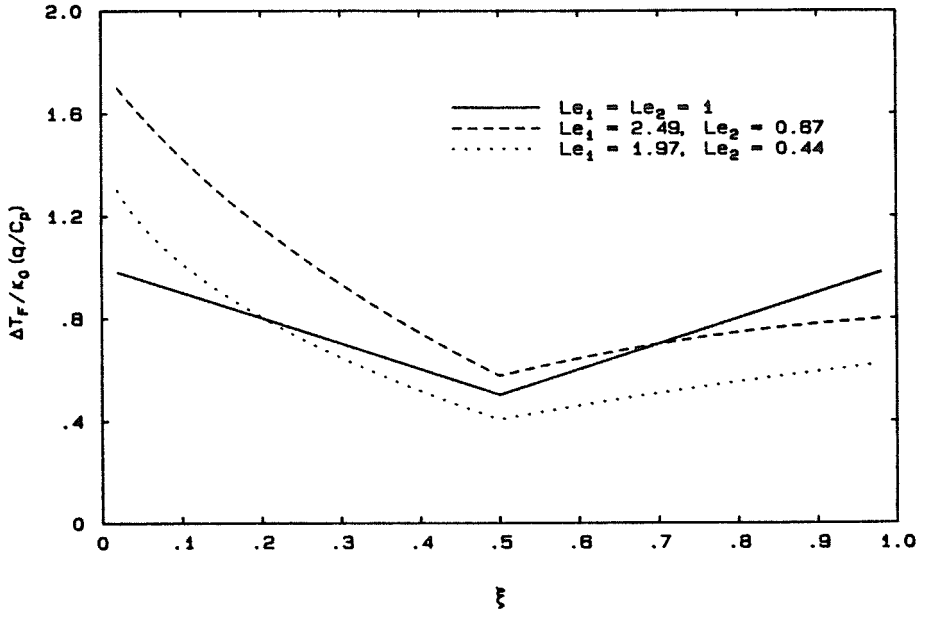

Adiabatic Flame Temperature Rise

Figure C.3

When both Lewis numbers are equal to unity (solid line), the temperature rise is symmetric about $\xi_\varphi = 0.5$, and is linear in ξ_φ. This is not the case, however, for

unequal Lewis numbers. The dashed line represents the flame temperature rise based on the Lewis numbers dictated by the diffusivities of hydrogen and fluorine and the heat conductivity of a pure nitrogen diluent. This corresponds to a case with very low reactant concentrations. The relatively large Lewis number on the hydrogen side results, for most values of ξ_φ, in a significantly higher flame temperature than in the case of unity Lewis numbers. This is in qualitative agreement with the results of Liñan [1980], who showed that the maximum temperature in the flame zone increases with increasing Lewis number. Higher concentrations of reactants, especially of hydrogen, serve to increase significantly the mixture heat conductivity, resulting in lower Lewis numbers. The dotted line shows the adiabatic flame temperature rise calculated for reactant concentrations of 2% fluorine and 16% hydrogen. Increasing the reactant concentrations, therefore, appears to result in lower normalized adiabatic flame temperature rises. This phenomenon may be partially responsible for the observed decrease in normalized temperature rise with increasing reactant concentrations described in § 3.5.

Appendix D

HYDROGEN - FLUORINE CHEMISTRY

The chemical reaction utilized in the present investigation is effectively

$$H_2 + F_2 \rightarrow 2HF \quad , \quad \Delta Q = -130 \ kcal/mole \tag{D.1}$$

This yields a temperature rise of 93 K for 1% fluorine and 1% hydrogen in a nitrogen diluent under constant pressure, adiabatic conditions (this is the so-called adiabatic flame temperature rise). The adiabatic flame temperature may be expressed implicitly by the following formula:

$$2\left(H(T) - H_0\right)_{HF} + \left(H(T) - H_0\right)_{I_1}\left[\frac{1}{\chi_1} - 1\right]$$

$$+ \left(H(T) - H_0\right)_{I_2}\left[\frac{1}{\chi_2} - 1\right] = -\Delta Q \tag{D.2}$$

where $\chi_{1,2}$ represents the mole fraction in the free stream of each reactant, H_0 and $H(T)$ the species enthalpy at ambient and at at elevated temperature, respectively. The subscripts $I_{1,2}$ denote the individual free stream inert mixtures, which consist of nitrogen with small amounts of helium or argon, as described in § 3.4. Equation (D.2) results from combining into a control volume an appropriate ratio of reactant-carrying mixtures to completely consume both reactants.

The chemical reaction of (D.1) actually consists of two second order chain reactions:

$$H_2 + F \overset{k_1}{\rightarrow} HF + H \quad , \quad \Delta Q = -32\ kcal\,/mole \tag{D.3}$$

$$H + F_2 \overset{k_2}{\rightarrow} HF + F \quad , \quad \Delta Q = -98\ kcal\,/mole \quad . \tag{D.4}$$

where $k_{1,2}$ are the rate constants for the reactions. The complete set of reactions includes the following recombination and chain termination reactions:

$$H + H + M \overset{k_3}{\rightarrow} H_2 + M \tag{D.5}$$

$$F + F + M \overset{k_4}{\rightarrow} F_2 + M \tag{D.6}$$

$$F + H + M \overset{k_5}{\rightarrow} HF + M \quad . \tag{D.7}$$

There are also energy transfer reactions of the type

$$HF^* + M \overset{k_6}{\rightarrow} HF + M \quad . \tag{D.8}$$

Considering nitrogen, the major component of the system, as the third body in (D.8) suggests that at room temperature this reaction is 1 to 2 orders of magnitude faster than the pumping reactions (D.3) and (D.4), allowing for efficient deactivation of vibrationally excited HF^* into translational (i.e. thermal) energy. A tabular summary of the rate constants for all reactions is presented in in Table D.1 at the end of this appendix.

Proper chain initiation requires some free F atoms, which were generated in these experiments by premixing a trace amount of nitric oxide into the hydrogen-bearing stream. This allows, upon molecular mixing of the free stream reactant fluids, the reaction

$$F_2 + NO \overset{k_7}{\rightarrow} NOF + F \quad , \tag{D.9}$$

which provides the required small F atom concentration in the layer to sustain proper ignition. There is also a reverse reaction

$$NO + F + M \overset{k_7}{\rightarrow} NOF + M \quad , \tag{D.10}$$

which can compete with (D.9) and can serve to eliminate free F atoms if the concentration of NO is too high. For all runs in this investigation, the NO concentration was maintained at 3% of the free stream fluorine concentration.

For all flows reported here, the resulting chemical time scales were fast compared with the fluid mechanical time scales. The chemical time scales for the reaction, over the entire range of concentrations, were determined using the CHEMKIN chemical kinetics program (Kee et al. [1980]). The chemical rate data for the reactions involved were taken from Cohen & Bott [1982], Cohen [1972] and Baulch [1981], and are listed in Table D.1. In the calculations a value of zero was used as input in place of all rate data not available (indicated by "--" in Table D.1). The results of the simulations are shown in Figure D.1.

The chemical times were determined by taking the steepest slope of the curves shown in figure D.1. It was found that the chemical times vary from $\tau_{chem} \approx 222\,\mu sec$ for the lowest heat release case ($2\%H_2 : 2\%F_2$, $\Delta T_F = 186K$) to $\tau_{chem} \approx 44\,\mu sec$ for the case ($6\%H_2 : 6\%F_2$), $\Delta T_F = 553K$. Omission of the

recombination reactions given by (D.3), (D.4) and (D.5) does not significantly change the calculated chemical rise times.

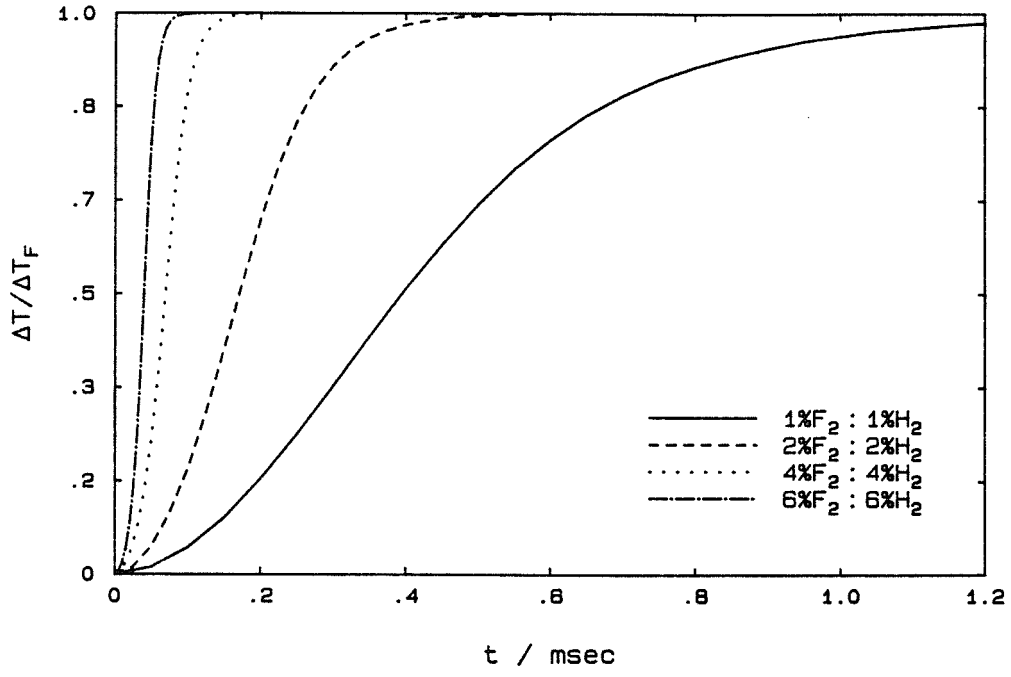

Figure D.1 Chemical Time Response

The fluid mechanical times, for comparison, are given by:

$$\tau_{\delta_1} \equiv \frac{\delta_1}{\Delta U} \approx 5.5\ msec \tag{D.11}$$

$$\tau_x \equiv \frac{x}{U_c} \approx 29.7\ msec \tag{D.12}$$

for typical values of layer thickness and free stream conditions, where τ_{δ_1} is the local, large scale characteristic time, and τ_x is the characteristic time based on the time of flight from the splitter tip to the measuring station. Using (D.10) and (D.11) to define the two Damköhler numbers

$$Da_{\delta_1} \equiv \frac{\tau_{\delta 1}}{\tau_{chem}} \tag{D.13}$$

and

$$Da_x \equiv \frac{\tau_x}{\tau_{chem}} \tag{D.14}$$

results in values of $25 < Da_{\delta_1} < 125$ with increasing reactant concentrations. The corresponding time of flight numbers are $160 < Da_x < 800$. for comparison, the Damköhler numbers for the low heat release data of Mungal and Dimotakis [1984] were $Da_{\delta_1} = 10$ and $Da_x = 60$. In those investigations, the chemistry was shown to be already fast. Chemical kinetics are, consequently, probably not an issue in the present investigation, where the chemistry is much faster as a result of the higher reactant concentration and combustion temperatures.

Table D.1. Chemical Reaction Rate Data

$$k = k_0 T^a \exp\left(-\frac{A}{RT}\right)$$

Reaction	k_0	a	A	Reference
$H_2 + F \rightarrow 2HF + H$	2.6×10^{12}	0.5	610.	Cohen-Bott
$H + F_2 \rightarrow 2HF + F$	3.0×10^{9}	1.5	1680.	Cohen-Bott
$H + H + M \rightarrow H_2 + M$	3.0×10^{15}	--	--	Baulch
$F + F + M \rightarrow F_2 + M$	3.2×10^{14}	--	--	Baulch
$F + H + M \rightarrow HF + M$	2.5×10^{16}	--	--	Baulch
$F_2 + NO \rightarrow NOF + F$	4.2×10^{11}	--	2285.0	Baulch
$NO + F + M \rightarrow NOF + M$	3.0×10^{16}	--	--	Baulch
$HF^* + H_2 \rightarrow HF + H_2$	1.1×10^{10}	--	--	Cohen
$HF^* + F_2 \rightarrow HF + F_2$	2.9×10^{10}	--	--	Cohen
$HF^* + N_2 \rightarrow HF + N_2$	2.4×10^{9}	--	--	Cohen
$HF^* + HF \rightarrow HF + HF$	2.0×10^{12}	--	--	Cohen

-- data not available; value of zero used in computations

Appendix E

TABULAR SUMMARY OF RESULTS

This appendix contains tabular listings of results for representative runs in this investigation, including fit coefficients for the mean temperature and mean velocity profiles. Selected results from unpublished data of Mungal are also included (run numbers 26 - 38).

The run conditions, i.e., the run numbers, free stream velocities, velocity ratios and the density ratios, are enumerated in Table E.1. The layer growth rate, $\delta_1 / (x - x_0)$, was calculated as explained in § 3.2.

Characteristic results are tabulated in Table E.2. The run numbers, equivalence ratios, defined by equation (2.5), § 2.4), and the free stream reactant concentrations are listed. The next three columns contain, respectively, the adiabatic flame temperature rises, the layer mean density reductions, and the normalized mean temperatures in the layer. δ_{P_2} / δ_1 and $\delta^*_{P_2} / \delta_1$ are the two measures of product formation defined in § 3.5 by equations (3.21) and (3.28), respectively. Most of the data are for zero streamwise pressure gradient; the last four runs listed had an imposed favorable streamwise pressure gradient, as described in § 5.1.

Tables E.3 and E.4 contain fit coefficients for the mean temperature and mean velocity profiles, respectively. The measuring station, for both the temperature and velocity information, was at $x = 45.7\ cm$, except where noted.

Table E.1. Run Conditions

Run	$U_1 / \frac{m}{s}$	$U_2 / \frac{m}{s}$	$\frac{U_2}{U_1}$	$\frac{\rho_2}{\rho_1}$	$\frac{\delta_1}{x - x_0}$	$\frac{dp}{dx} / \frac{torr}{cm}$
27*	-	-	-	0.922	0.148	≈ 0
32*	21.85	8.55	0.391	1.000	-	≈ 0
34*	22.66	8.78	0.387	1.013	0.158	≈ 0
35*	22.67	8.88	0.392	1.023	0.155	≈ 0
37*	23.25	8.79	0.378	1.084	0.155	≈ 0
38*	22.89	8.98	0.393	1.042	0.154	≈ 0
88	24.04	8.80	0.366	1.183	0.155	≈ 0
90	22.01	8.21	0.373	1.046	0.152	≈ 0
91	20.91	8.20	0.392	1.040	0.149	≈ 0
92	-	-	-	1.053	0.151	≈ 0
119	21.15	8.32	0.393	1.067	0.148	≈ 0
123	21.17	7.90	0.373	1.000	0.150	≈ 0
125	21.04	8.00	0.380	1.026	0.147	≈ 0
130	21.23	8.12	0.382	1.000	0.147	≈ 0
150	21.54	8.15	0.378	1.000	0.149	≈ 0
152	21.65	8.30	0.384	1.000	0.150	≈ 0
157	21.94	7.99	0.364	1.000	0.149	≈ 0
167	-	-	-	1.000	-	≈ 0
96	23.04	10.25	0.445	1.053	0.133	-0.0202
97	22.78	10.91	0.479	1.026	0.135	-0.0323
148	-	-	-	1.000	0.126	-0.0424
156	22.31	10.30	0.461	1.000	0.133	-0.0414

* results from Mungal [1983]

Table E.2. Run Results

Run	φ	$\%H_2$	$\%F_2$	$\Delta T_F / K$	$\frac{\rho_0 - \bar{\rho}}{\rho_0}$	$\frac{<\overline{\Delta T}>}{\Delta T_F}$	$\frac{\delta_{P2}}{\delta_1}$	$\frac{\delta^*_{P2}}{\delta_1}$
27*	8	8	1	165.0	0.137	0.310	0.035	0.028
32*	-	0	0	0.0	0.000	-	-	-
34*	1	1	1	93.0	0.085	0.313	0.161	0.141
35*	1/2	2	1	124.0	0.104	0.299	0.205	0.173
37*	1/8	8	1	165.0	0.120	0.265	0.242	0.199
38*	1/4	4	1	149.0	0.112	0.270	0.223	0.186
88	1/8	16	2	328.4	0.225	0.303	0.276	0.187
90	1/2	4	2	247.6	0.190	0.320	0.219	0.158
91	1	3	3	278.1	0.206	0.319	0.164	0.114
92	1	4	4	368.2	0.260	0.341	0.174	0.108
119	1	5	5	456.8	0.286	0.323	0.163	0.095
123	1/4	16	4	600.3	0.311	0.281	0.224	0.124
125	1	2	2	186.3	0.162	0.341	0.176	0.135
130	1	6	6	553.8	0.313	0.308	0.155	0.085
150	1/2	8	4	496.3	0.292	0.304	0.204	0.119
152	1/4	8	2	301.9	0.214	0.305	0.250	0.174
157	1/2	12	6	737.4	0.361	0.301	0.198	0.097
167	1/4	24	6	900.8	0.370	0.265	0.207	0.097
96	1	4	4	368.2	0.257	0.333	0.170	0.107
97	1	2	2	186.3	0.170	0.360	0.186	0.142
148	1	6	6	553.8	0.332	0.335	0.168	0.090
156	1	6	6	553.8	0.312	0.307	0.154	0.085

* results from Mungal [1983]

Table E.3. Mean Temperature Rise Coefficients

$$\overline{\Delta T}(y) = \exp(c_1 + c_2 y + c_3 y^2 + c_4 y^3 + c_5 y^4)$$

$\overline{\Delta T}$ in K

y in cm

Run	c_1	c_2	c_3	c_4	c_5
27*	4.6320	-0.09650	-0.02784	-0.09129	-0.01756
34*	4.0830	-0.08369	-0.17642	-0.01036	-0.00915
35*	4.2454	-0.20972	-0.15054	-0.00471	-0.01143
37*	4.2987	-0.31760	-0.10691	0.00184	-0.01347
38*	4.2841	-0.25268	-0.13156	-0.00295	-0.01251
88	4.8838	-0.42921	-0.09452	-0.02969	-0.01951
90	4.8781	-0.37771	-0.16136	-0.01419	-0.01186
91	5.1343	-0.27875	-0.23160	-0.02603	-0.01057
92	5.4155	-0.35560	-0.21779	-0.02422	-0.01027
119	5.4392	-0.57625	-0.28192	-0.03235	-0.00890
123	5.1878	-0.59883	-0.12434	-0.03341	-0.01551
125	4.7250	-0.30081	-0.21844	-0.04285	-0.01440
130	5.5162	-0.58708	-0.25920	-0.03652	-0.01093
150	5.2594	-0.55516	-0.15687	-0.02806	-0.01432
152	4.7322	-0.46578	-0.10612	-0.04425	-0.02246
157**	5.3406	-0.72175	-0.19004	-0.04952	-0.01557
167+	5.4214	-0.63361	-0.09294	-0.01365	-0.00864
96	5.5130	-0.11800	-0.24127	-0.01317	-0.01881
97	4.8253	-0.03921	-0.13929	-0.02189	-0.02706
148	5.7857	-0.33769	-0.25834	-0.05405	-0.02727
156*	5.7714	-0.36848	-0.30815	-0.03238	-0.01712

* results from Mungal [1983]

** measuring station at x = 48.3 cm

+ measuring station at x = 44.8 cm

Table E.4. Mean Velocity Coefficients

$$U(y) = b_5 \tanh(b_1 + b_2 y + b_3 y^2 + b_4 y^{3)} + b_6$$

U in m/s

y in cm

Run	b_1	b_2	b_3	b_4	b_5	b_6
32*	0.1193	0.4445	0.0451	0.0490	6.6503	15.2019
34*	0.3006	0.5695	0.0892	0.0384	6.9409	15.7197
35*	0.3326	0.5549	0.0946	0.0471	6.8967	15.7717
37*	0.3239	0.5366	0.0946	0.0476	7.2264	16.0194
38*	0.3308	0.5393	0.0738	0.0433	6.9589	15.9340
88	0.5567	0.5880	0.1148	0.0449	7.6208	16.4229
90	0.4735	0.5787	0.1635	0.0737	6.8990	15.1087
91	0.5269	0.7739	0.2057	0.0629	6.3535	14.5551
119	0.6934	0.7072	0.1160	0.0326	6.4169	14.7380
123	0.5666	0.5827	0.0969	0.0247	6.6345	14.5378
125	0.4711	0.5729	0.1437	0.0543	6.5232	14.5207
130	0.9271	0.8950	0.2345	0.0566	6.5562	14.6763
150	0.6282	0.6453	0.1481	0.0439	6.6992	14.8454
152	0.4722	0.4802	0.1013	0.0422	6.6734	14.9763
157	0.7267	0.6339	0.0988	0.0190	6.9761	14.9635
96	0.4032	0.9953	0.4220	0.1607	6.3917	16.6455
97	0.2362	0.6538	0.2058	0.1025	5.9360	16.8482
156	0.5407	0.8250	0.2162	0.0716	6.0080	16.3046

* results from Mungal [1983]

References

BATT, R. G. 1975 Some Measurements on the Effect of Tripping the Two-dimensional Shear Layer. *AIAA J.* **13**, 245-247.

BALLANTYNE, A., BOON, D. J. & MOSS, J. B. 1976 Measurements of fluctuating temperature in open diffusion flames employing fine wire thermocouples. *U. of Southampton AASU Memo* **763**

BAULCH, D. L., DUXBURY, J., GRANT, S. J., & MONTAGUE, D. C. 1981 Evaluated Kinetic Data for High Temperature Reactions, Volume 4. *J. Phys. Chem. Ref. Data*, **Vol. 10, Suppl. 1**

BECKER, H. A. and YAMAZAKI, S. 1978 Entrainment, Momentum Flux and Temperature in Vertical Free Diffusion Flames *Comb. Flame* **33**, 123-149.

BERNAL, L. P. 1981 The Coherent Structure of Turbulent Mixing Layers: I. Similarity of the Primary Vortex Structure. II. Secondary Streamwise Vortex Structure. Ph.D. Thesis, Caltech.

BERNAL, L. P., BREIDENTHAL, R. E., BROWN, G. L., KONRAD, J. H. & ROSHKO, A. 1979 On the Development of Three-Dimensional Small Scales in Turbulent Mixing Layers. In **Turbulent Shear Flows 2**, *Second International Symp. on Turbulent Shear Flows*, July 1979, Springer Verlag, 305-313.

BRADSHAW, P. 1966 The effect of initial conditions of the development of a free shear layer. *J. Fluid Mech.* **26(2)**, 225-236.

BRAY, K. N. C. & LIBBY, P. A. 1981 Countergradient Diffusion in Pre-mixed Turbulent Flames, *AIAA J.* **19**, 205-213.

BREIDENTHAL, R. E. 1978 A Chemically Reacting, Turbulent Shear Layer. Ph.D. Thesis, California Institute of Technology; and 1981 Structure in turbulent mixing layers and wakes using a chemical reaction. *J. Fluid Mech.* **109**, 1-24.

BROADWELL, J. E. & BREIDENTHAL, R. E. 1982 A simple model of mixing and chemical reaction in a turbulent shear layer. *J. Fluid Mech.* **125**, 397-410.

BROWAND, F. K. & LATIGO, B. O. 1979 Growth of the Two-Dimensional Mixing Layer from a Turbulent and Non-Turbulent Boundary Layer, *Phys. Fluids* **22(6)**, 1011-1019.

BROWN, G. L., & ROSHKO, A. 1974 On density effects and large structure in turbulent mixing layers. *J. Fluid Mech.* **64(4)**, 775-816.

BROWN, J. L. 1978 Heterogeneous Turbulent Mixing Layer Investigations Utilizing a 2-D 2-Color Laser Doppler Anemometer and Using a Concentration Probe. Ph. D. Thesis, U. Missouri - Columbia.

CALDWELL, F. R. 1962 Thermocouple Materials. *National Bureau of Standards Monograph* 40, United States Department of Commerce, National Bureau of Standards, 7-8.

CARRIER, G. F., FENDELL, F. E. & MARBLE, F. E. 1975 The Effect of Strain Rate on Diffsion Flames. *SIAM J. Appl. Math* .**28(2)**, 463-500.

CHIGIER, N. A. & YULE, A. J. 1979 The Physical Structure of Turbulent Jet Flames. *AIAA Paper* 79-0217, 17*th Aerospace Sciences Meeting, January* 1979.

COHEN, N. 1982 A Review of Rate Coefficient for Reactions in the $H_2 - F_2$ Laser System. *The Aerospace Corporation, Report* **TR-0073(3430)-9**.

COHEN, N. & BOTT, J. F. 1982 Review of Rate Data for Reactions of Interest in HF and DF Lasers. *The Aerospace Corporation, Report* **SD-TR-82-86**.

DIMOTAKIS, P. E. 1984 Entrainment and Growth of a Fully Developed, Two-Dimensional Shear Layer. *AIAA Paper* 84-0368, 22*nd Aerospace Sciences Meeting, January* 1984.

DIMOTAKIS, P. E. & BROWN, G. L. 1976 The mixing mayer at high Reynolds number: large-structure dynamics and entrainment, *J. Fluid Mech.* **78**, 535-560.

GANJI, A. T. & SAWYER, R. F. 1979 An Experimental Study of the Flow Field and Pollutant Formation in a Two Dimensional, Premixed Turbulent Flame. *AIAA Paper* 79-0017, 17*th Aerospace Sciences Meeting, January* 1979.

GAYDON, A. G. & WOLFHARD, H. G. 1960 *Flames, Their Structure, Radiation and Temperature*, 2nd Ed., Chapman & Hall, London, 277-281.

HERMANSON, J. C., MUNGAL, M. G. and DIMOTAKIS, P. E. 1985 Heat Release Effects on Shear Layer Growth and Entrainment. *AIAA paper* 85-0142, 23*rd Aerospace Sciences Meeting, January* 1985.

HO, C. M. and HUERRE, P. 1984 Perturbed Free Shear Layers. *Ann. Review Fluid Mech.* **16**, 365-424.

HOWARTH, L. 1948 Concerning the Effect of Compressibility on Laminar Boundary Layers and Their Separation, *Proceedings of the Royal Society of London A*, **194**, 16-42.

KEE, R. J, MILLER, J. A. , & JEFFERSON, T. H. 1980 CHEMKIN: A General Purpose, Problem Independent, Transportable, Fortan Chemical Kinetics Code Package. *SANDIA Report* **SAND80-8003**.

KELLER, J. O. & DAILY, J. W. 1983 The Effect of Large Heat Release on a Two - Dimensional Mixing Layer. *AIAA Paper* 83-0472, 21*st Aerospace Sciences Meeting, January* 1983.

KONRAD, J. H. 1976 An Experimental Investigation of Mixing in Two Dimensional Shear Flows with Application to Diffusion Limited Chemical Reactions. Ph.D. Thesis, California Institute of Technology.

KOOCHESFAHANI, M. M. 1984 Experiments on Turbulent Mixing and Chemical Reactions in a Liquid Mixing Layer. Ph.D. Thesis, California Institute of Technology.

KOOCHESFAHANI, M. M., CATHERASOO, C. J., DIMOTAKIS, P.E., GHARIB, M. & LANG, D. B. 1979 Two-Point LDV Measurements in a Plane Mixing Layer, *AIAA J.* **17**, 1347-1351.

KOOP, C. G. & BROWAND, F. K. 1979 Instability and turbulence in a stratified fluid with shear. *J. Fluid Mech.* **93(1)**, 135-159.

LIEPMANN, H. W. 1947 The Interaction Between Boundary Layer and Shock Waves in Transonic Flow. *J. Aero. Sci.* **13**, 623-635.

LIÑAN, A. 1980 Lewis Number Effects on the Structure and Extinction of Diffusion Flames due to Strain. In *The Role of Coherent Structures in Modelling Turbulence and Mixing, Proc. Int. Conf.*, J. Jimenez, Ed., Springer Velag, Berlin, 333-339.

MERZKIRCH, 1974 *Flow Visualization* , Academic Press, New York, 86-100.

MARBLE, F. E. & BROADWELL, J. E. 1977 The coherent flame model for turbulent chemical reactions. *Project SQUID Tech. Rep.* **TRW-9-PU**.

MASON, E. A. & SAXENA, S. C. 1958 An Approximate Formula for the Thermal Conductivity of Gas Mixtures. *Phys. Fluids* **1(5)**, 361-369.

McMURTRY, P. A., JOU, W.-H., RILEY, J. J., & METCALFE, R. W. 1985 Direct Numerical Simulations of a Reacting Mixing Layer with Chemical Heat Release. *AIAA Paper* 85-0143, *23rd Aerospace Sciences Meeting, January* 1985.

MUNGAL, M. G. 1983 Experiments on Mixing and Combustion with Low Heat Release in a Turbulent Shear Flow. Ph.D. Thesis, California Institute of Technology.

MUNGAL, M. G. and DIMOTAKIS, P. E. 1984 Mixing and combustion with low heat release in a turbulent shear layer. *J. Fluid Mech.* **148**, 349-382.

MUNGAL, M. G., DIMOTAKIS, P. E. & BROADWELL, J. E. 1983 Turbulent Mixing and Combustion in a Reacting Shear Layer. *AIAA J.* **22(6)**, 797-800.

MUNGAL, M. G., DIMOTAKIS, P. E., & HERMANSON, J. C. 1984 Reynolds Number Effects on Mixing and Combustion in a Reacting Shear Layer. *AIAA Paper* 84-0371, *22nd Aerospace Sciences Meeting, January* 1984.

PARANTHOEN, P., LECORDIER, J. D. & PETIT, C. 1982 Influence of Dust Contamination on Frequency Response of Wire Resistance Thermometers. *DISA Information* **27**, 36-37.

PETERS , N. & WILLIAMS, F. A. 1980 Coherent Structures in Turbulent Combustion. In *The Role of Coherent Structures in Modelling Turbulence and Mixing, Proc. Int. Conf.*, J. Jimenez, Ed., Springer-Verlag, Berlin 1981,364-393.

PITZ, R. W. & DAILY, J. W. 1983 Combustion in a Turbulent Mixing Layer Formed at a Rearward- Facing Step. *AIAA J.* **21(11)**, 1565-1570.

PRANDTL , L. 1925 Bericht über Untersuchungen zur ausgebildeten Turbulenz, *Ztschr. angew. Math. Mech.* **5(2)**, 136-139.

RAJAGOPALAN, S. & ANTONIA, R. A. 1980 Properties of the large structure in a slightly heated turbulent mixing layer of a plane jet. *J. Fluid. Mech.* **105**, 261-281.

REBOLLO , M. R. 1973 Analytical and Experimental Investigation of a Turbulent Mixing Layer of Different Gases in a Pressure Gradient. Ph.D. Thesis, California Institute of Technology.

SANDBORN, V. A. 1972 *Resistance Temperature Transducers*, Metrology Press, 428-431.

SCADRON, M. D. & WARSHAWSKY, I. 1952 Experimental Determination of Time Constants and Nusselt Numbers for Bare-Wire Thermocouples in High-Velocity Air Streams and Analytic Approximation of Conduction and Radiation Errors. *NACA Tech Note* **2599**.

SERRIN, J. 1959 Mathematical Principles of Classical Fluid Mechanics. In *Handbuch der Physik* **8(1)**, Springer-Verlag, Berlin, 1959, 183-190.

SPALDING, D. B. 1984 The Two-Fluid Model of Turbulence Applied to Combustion Phenomena. *AIAA Paper* 84-0476, *22nd Aerospace Sciences Meeting, January* 1984.

SPENCER, B. W., & JONES, B. G. Statistical Investigation of Pressure and Velocity Fields in the Turbulent Two Stream Mixing Layer. *AIAA Paper* 71-613, *11th Aerospace Sciences Meeting, January* 1971.

WALLACE, A.K. 1981 Experimental Investigation of the Effects of Chemical Heat Release in the Reacting Turbulent Plane Shear Layer. Ph.D Thesis, The University of Adelaide; distributed as *AFOSR Report* **AFOSR-TR-84-0650**.

WINANT, C. D. & BROWAND, F. K. 1974 Vortex pairing: the mechanism of turbulent mixing-layer growth at moderate Reynolds number. *J. Fluid Mech.* **63**, 237-255.

YULE, A. J., CHIGIER, N. A., RALPH, S., BOULDERSTONE, R. & VENTURA, J. 1980 Combustion-Transition Interaction in a Jet Flame *AIAA Paper* 80-0077, *18th Aerospace Sciences Meeting, January* 1980.

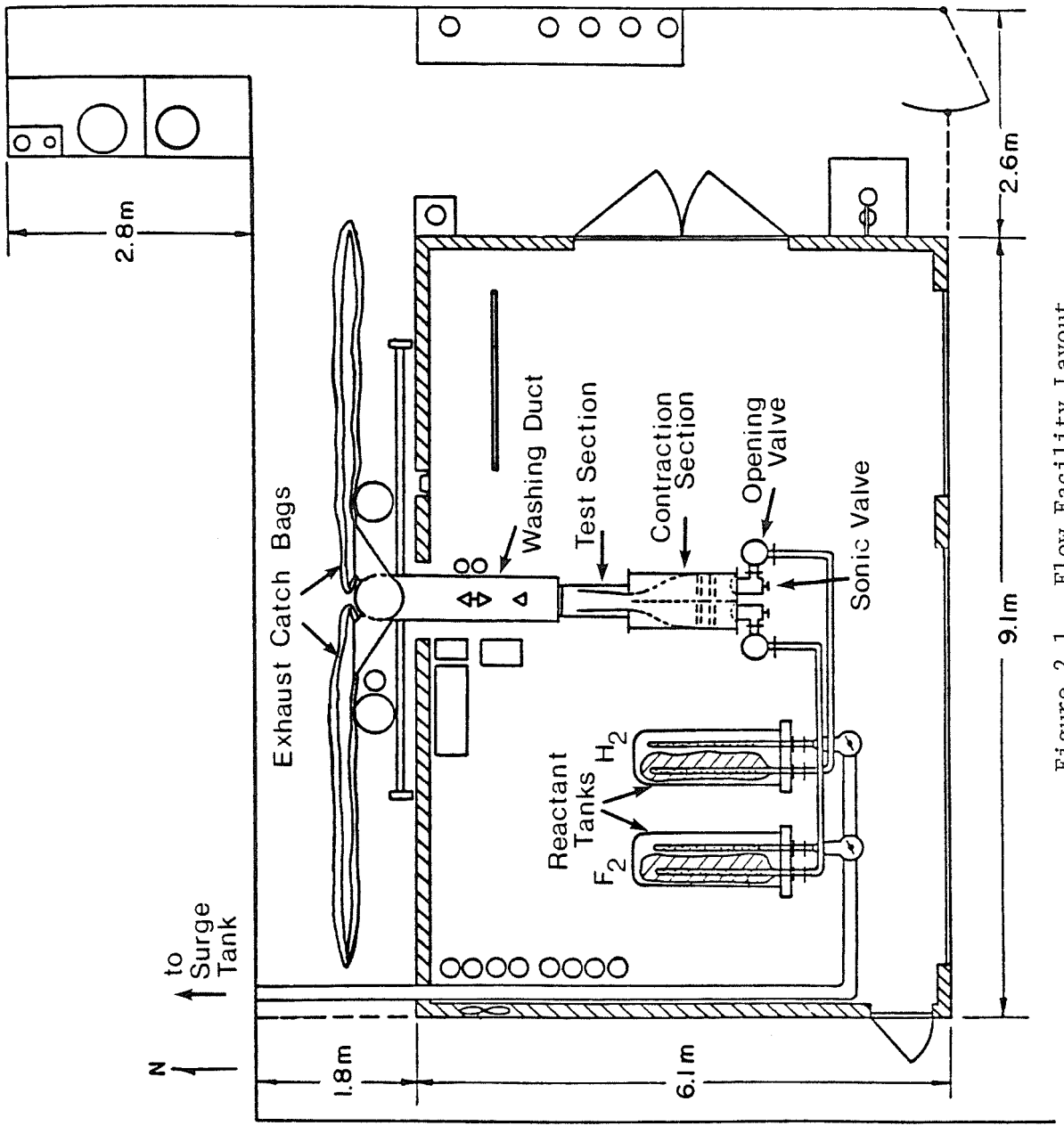

Figure 2.1 Flow Facility Layout

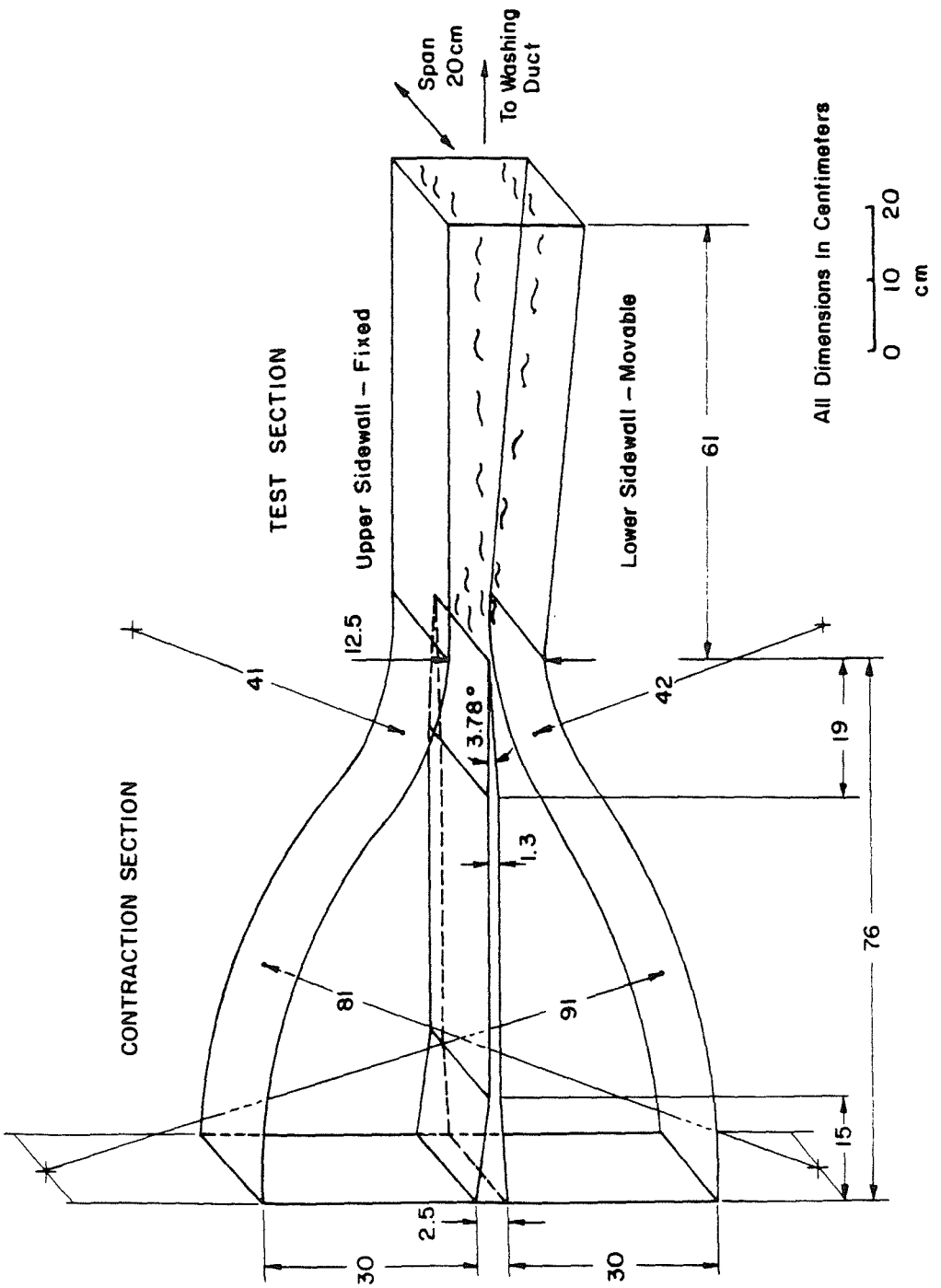

Figure 2.2 Contraction and Test Section Dimensions

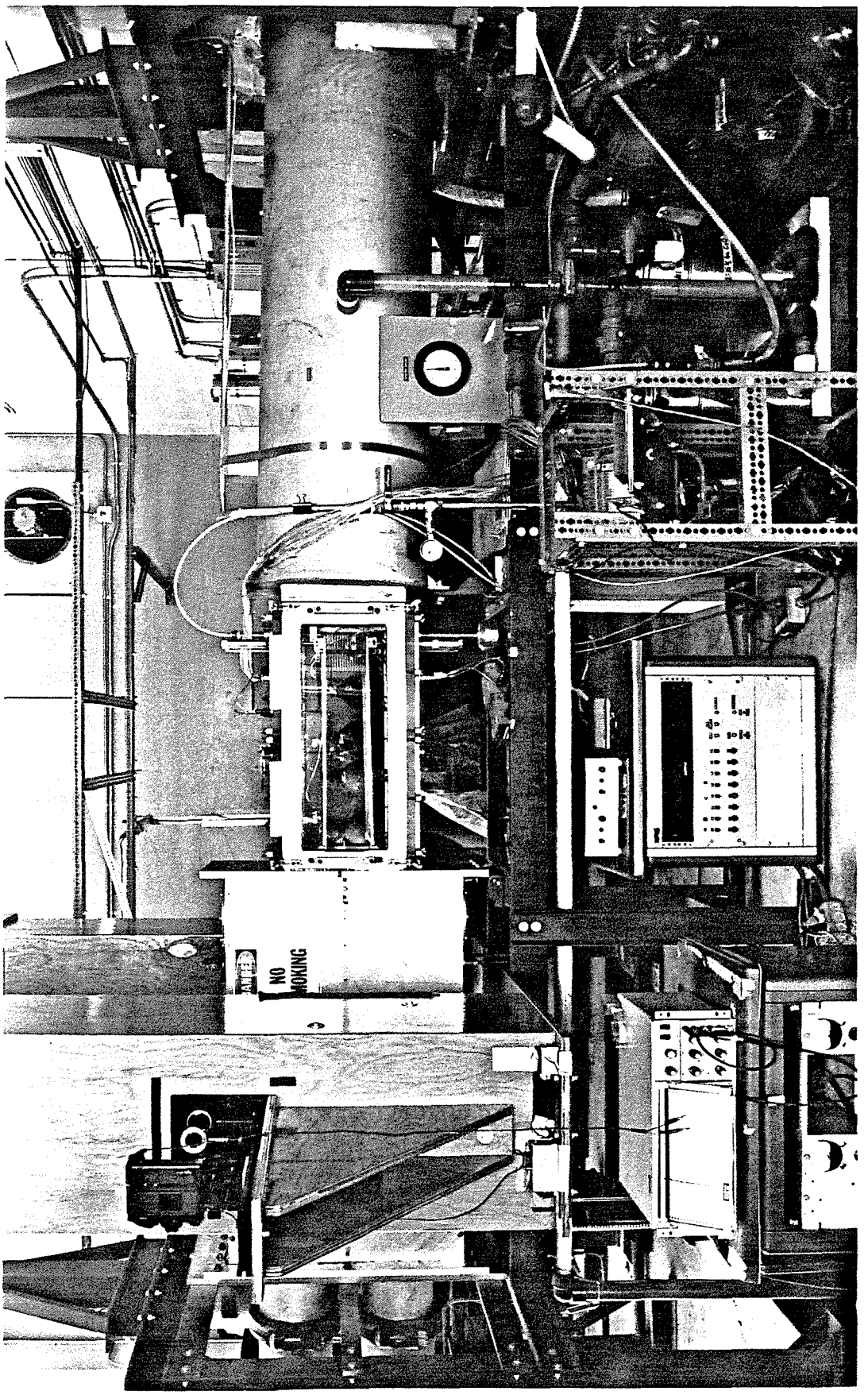

Figure 2.3 Photograph of Facility

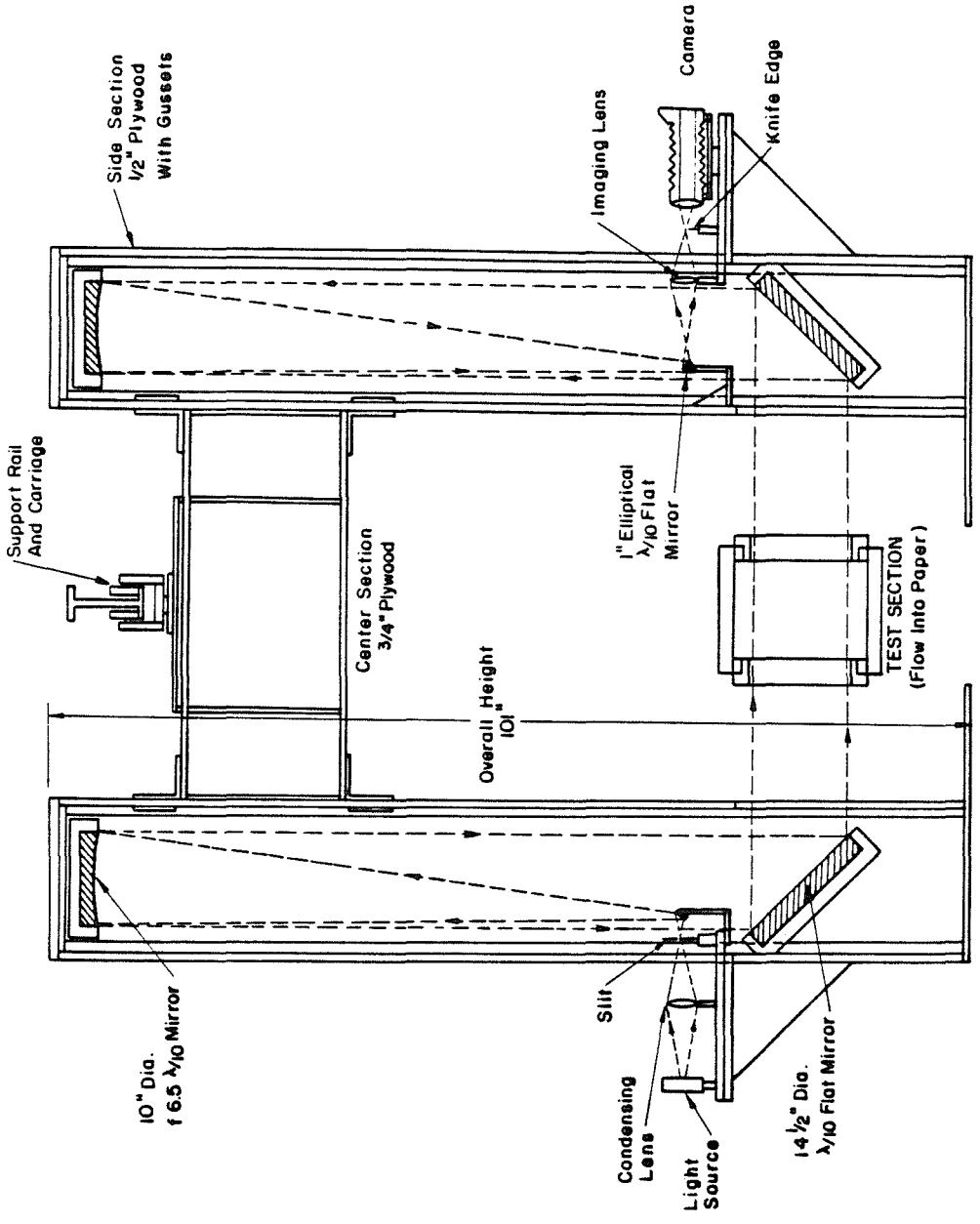

Figure 2.4 Schlieren System Schematic

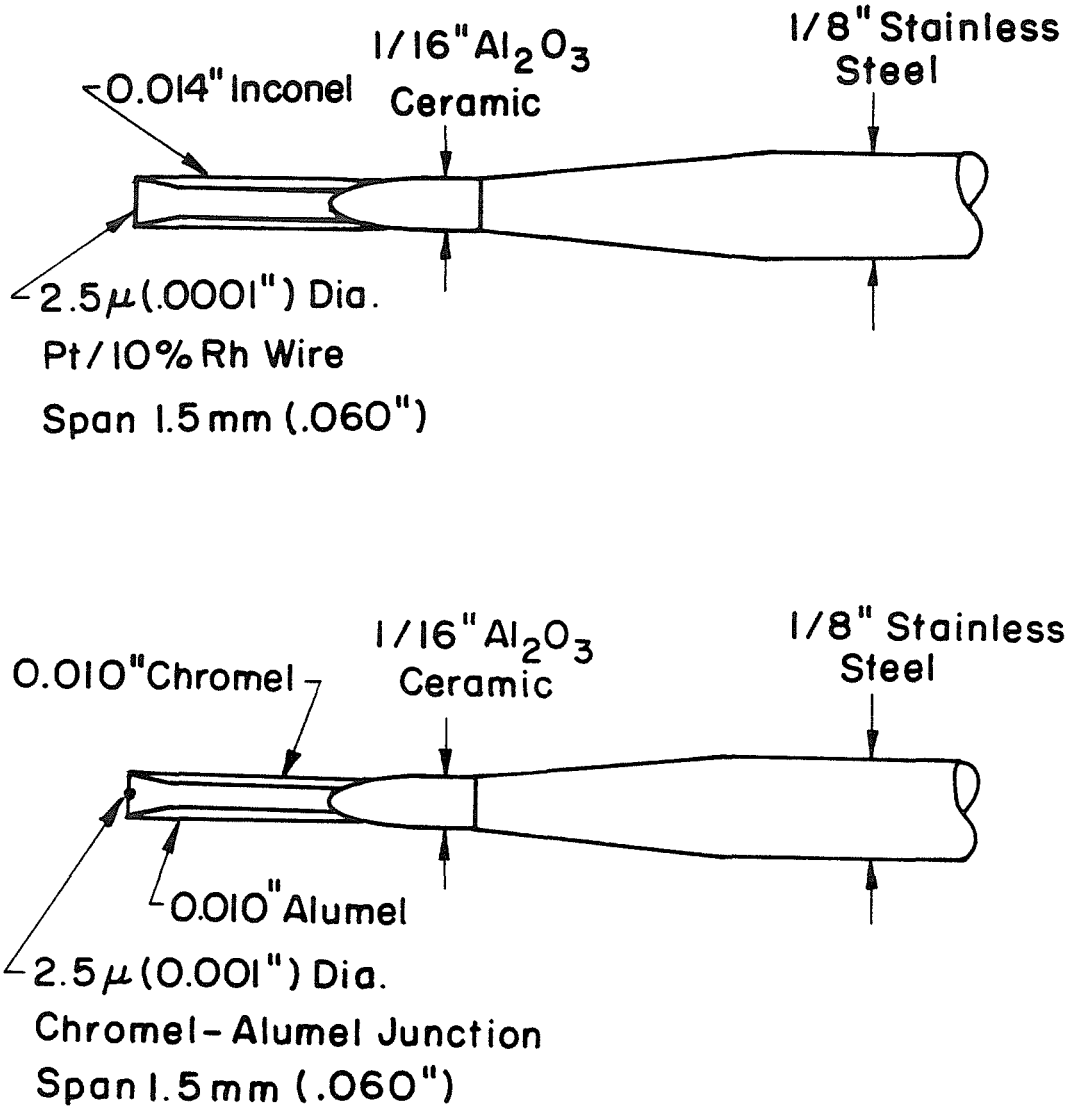

Figure 2.5 Cold Wire and Thermocouple Probe Details

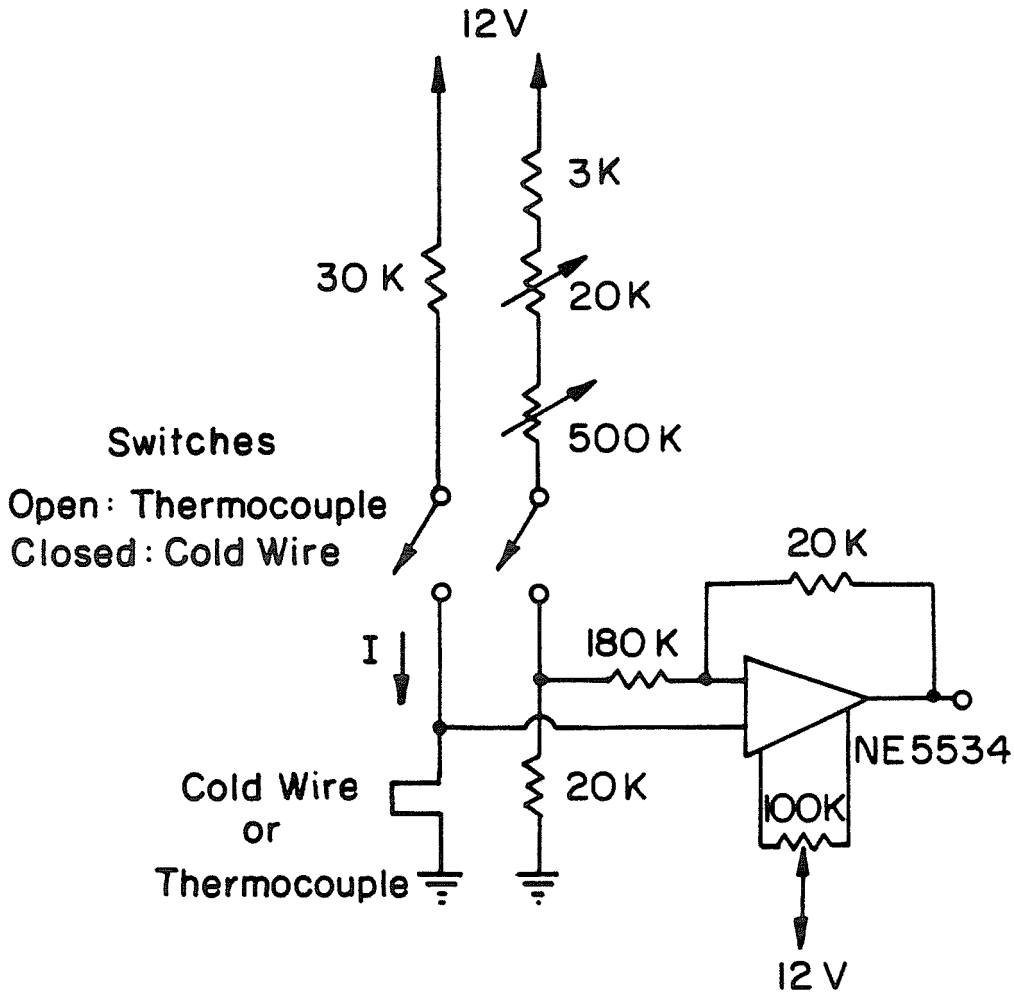

Figure 2.6 Cold Wire/Thermocouple Amplifier Circuit

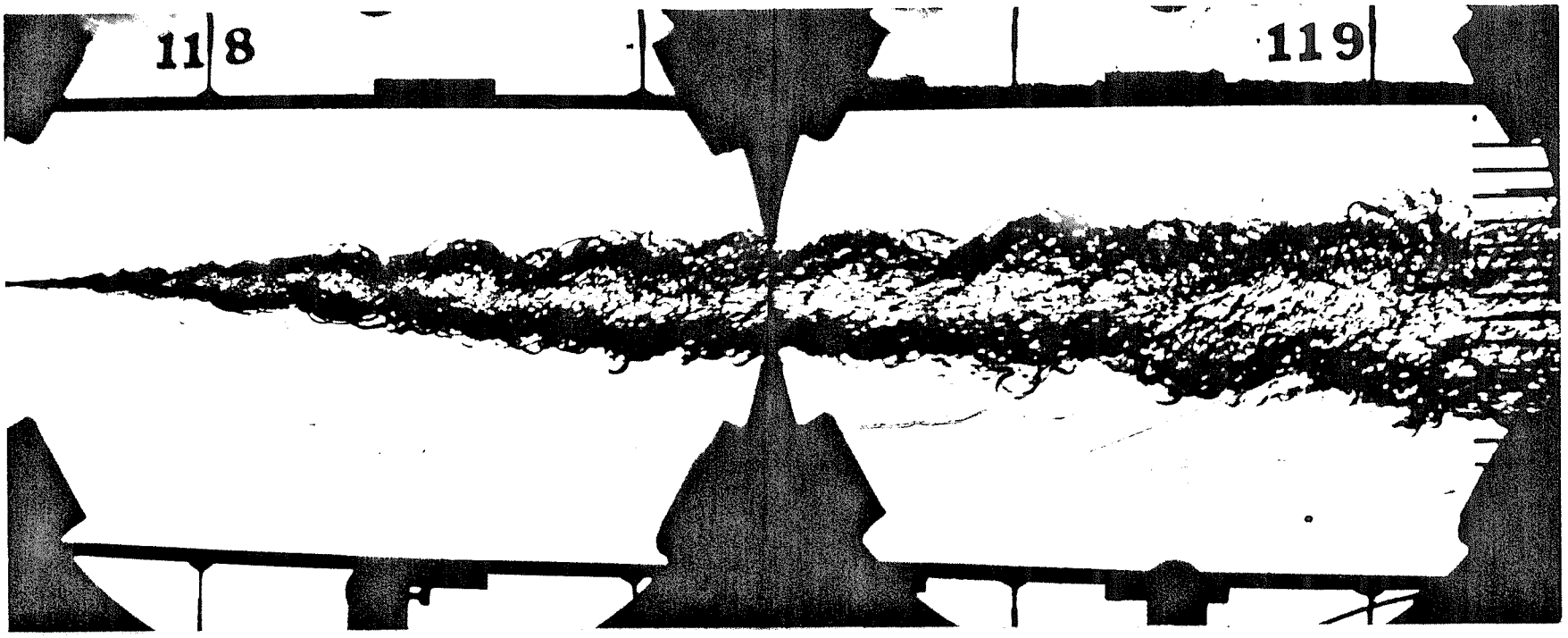

High Speed Stream 5% H_2 ΔT_F = 457 K U_2/U_1 = 0.39

Low Speed Stream 5% F_2 $\overline{\Delta T}/\Delta T_F$ = 0.70 $Re_{\delta 1}$ = 6.2 10^4

Figure 2.7 Composite Spark Schlieren Photograph

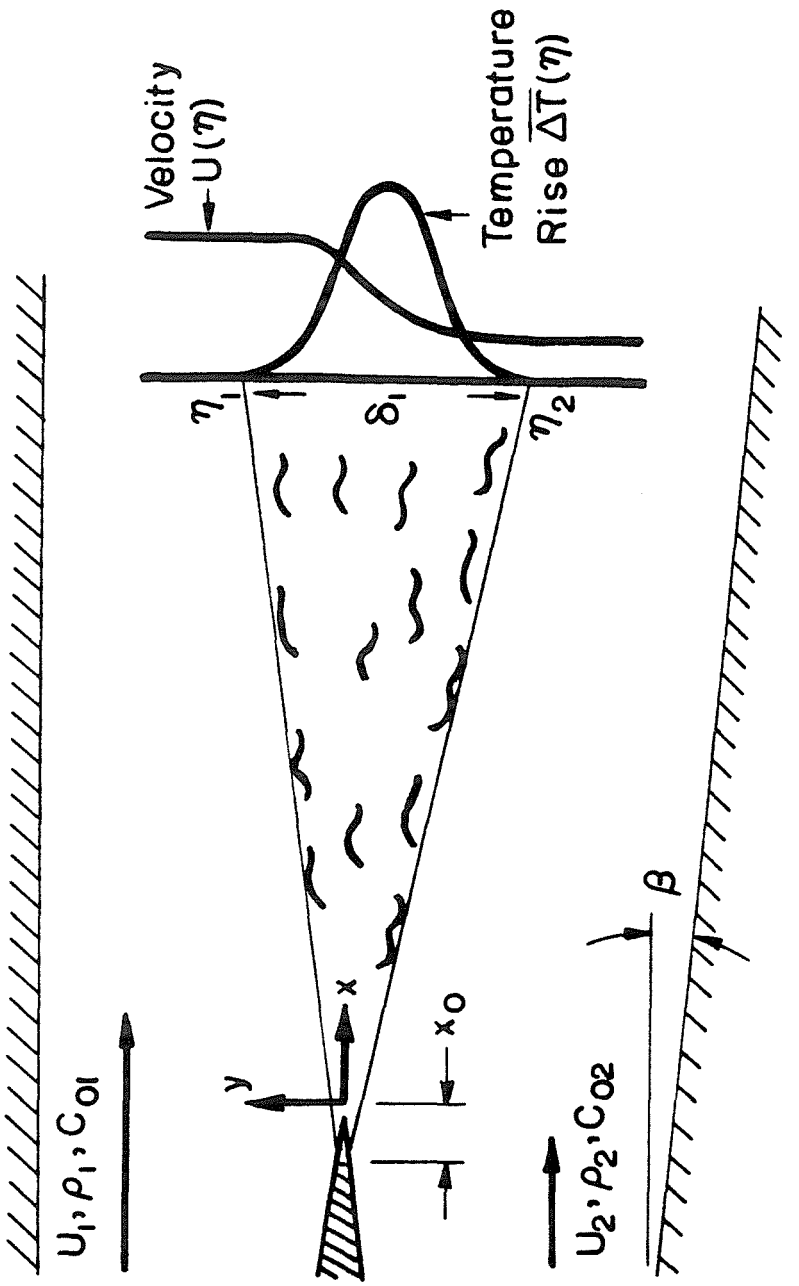

Figure 3.1 Turbulent Shear Layer Geometry

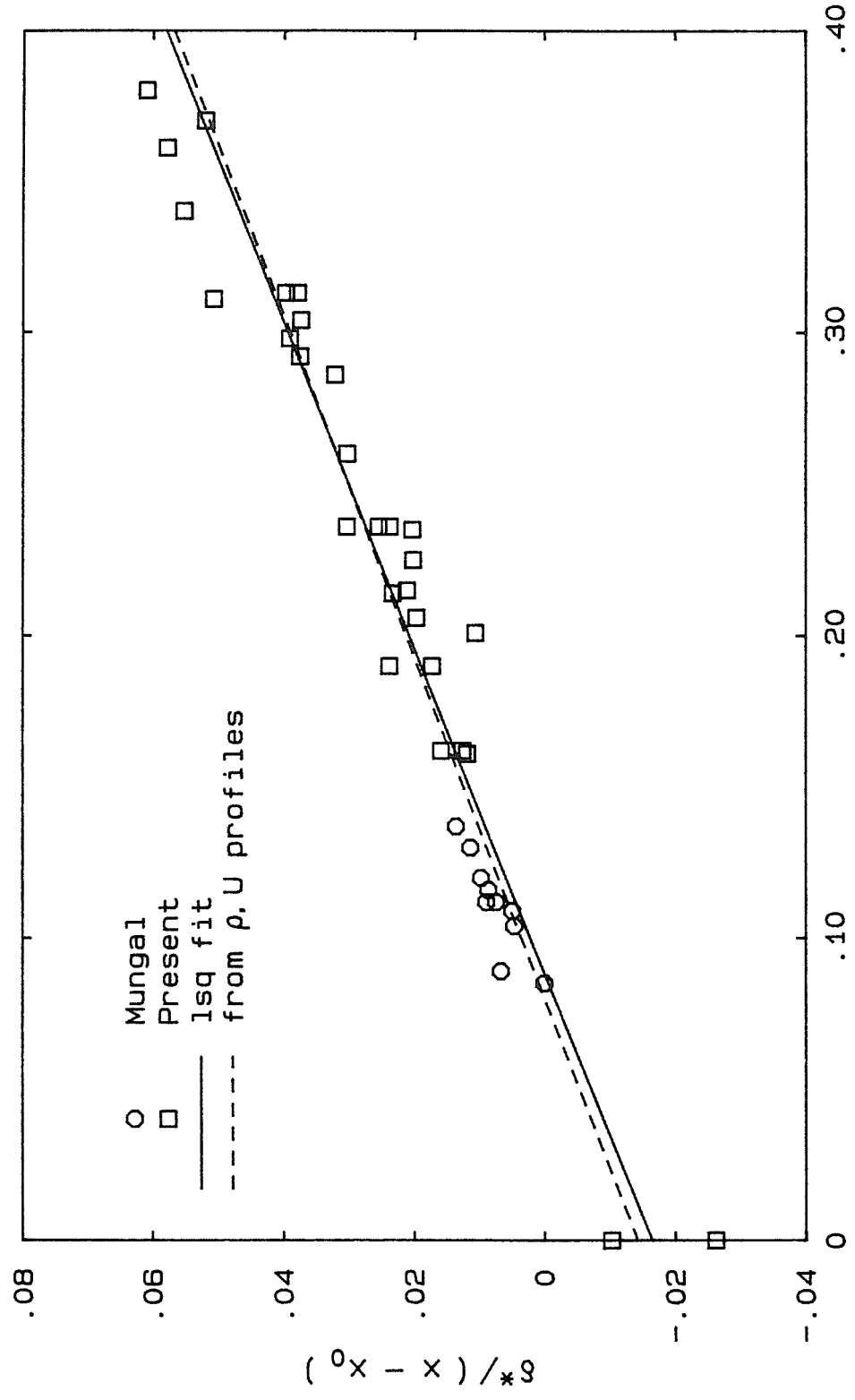

Figure 3.2 Layer Displacement versus Heat Release

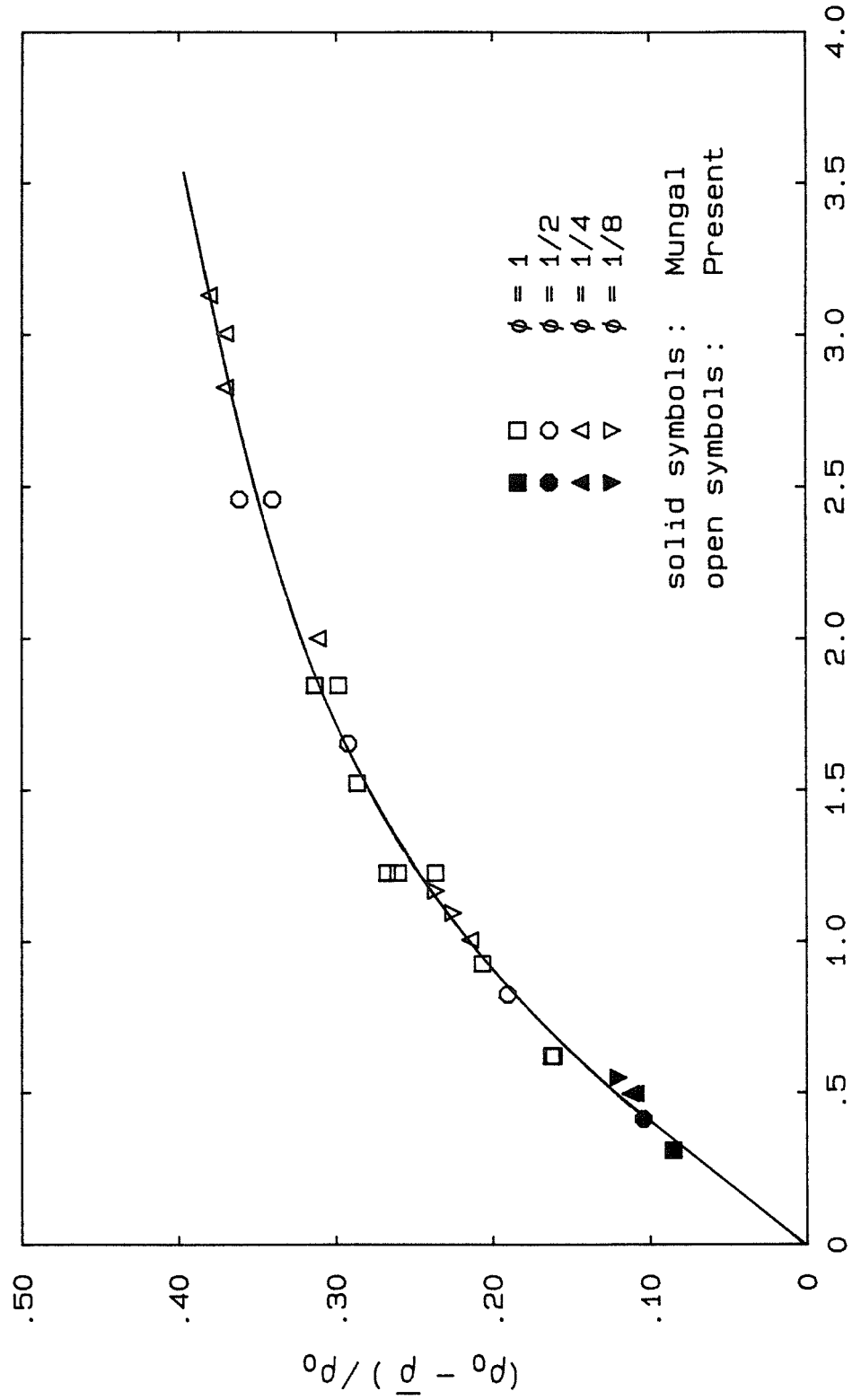

Figure 3.3 Mean Density Reduction versus Adiabatic Flame Temperature

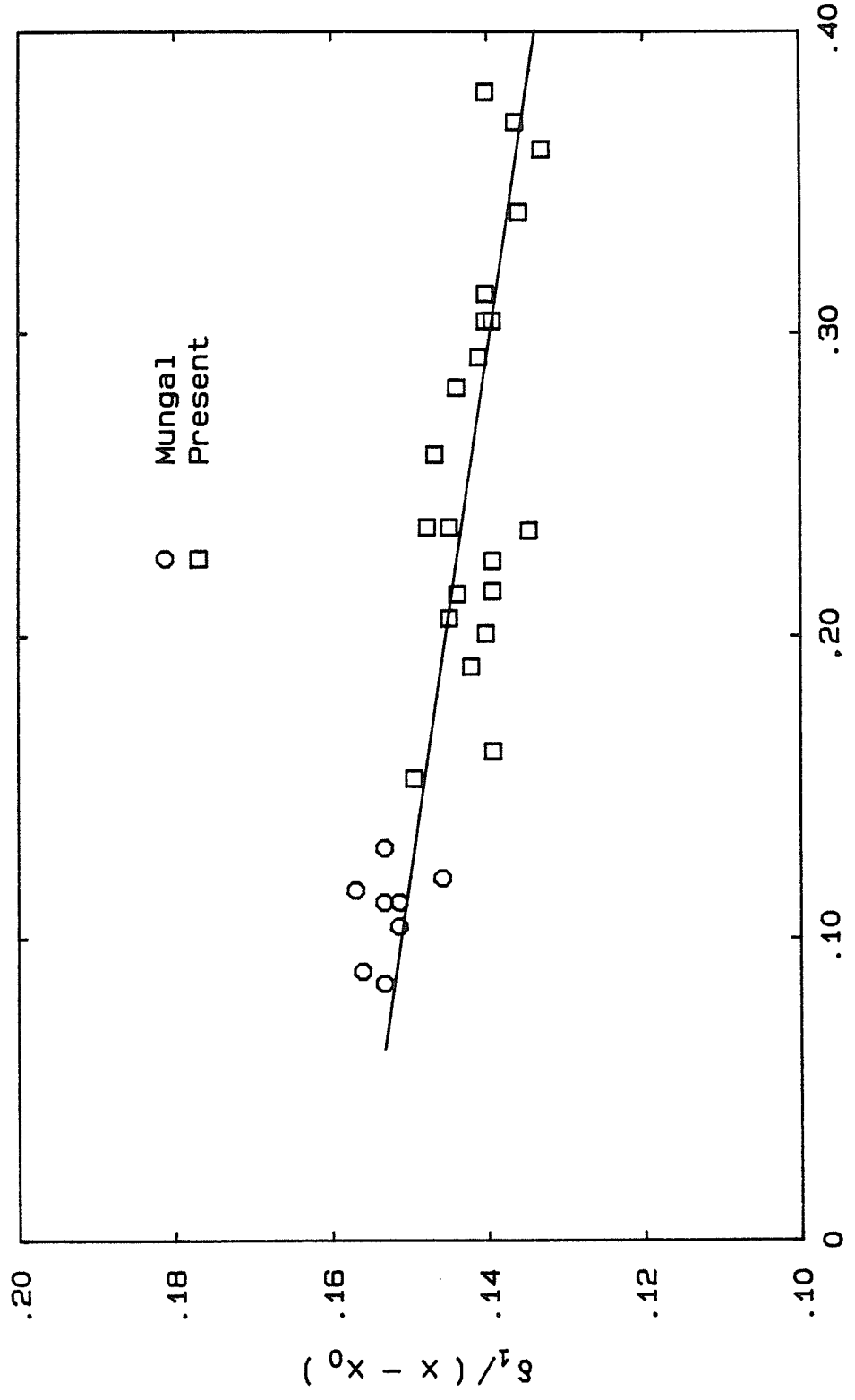

Figure 3.4 Temperature Profile Thickness Growth Rate versus Heat Release

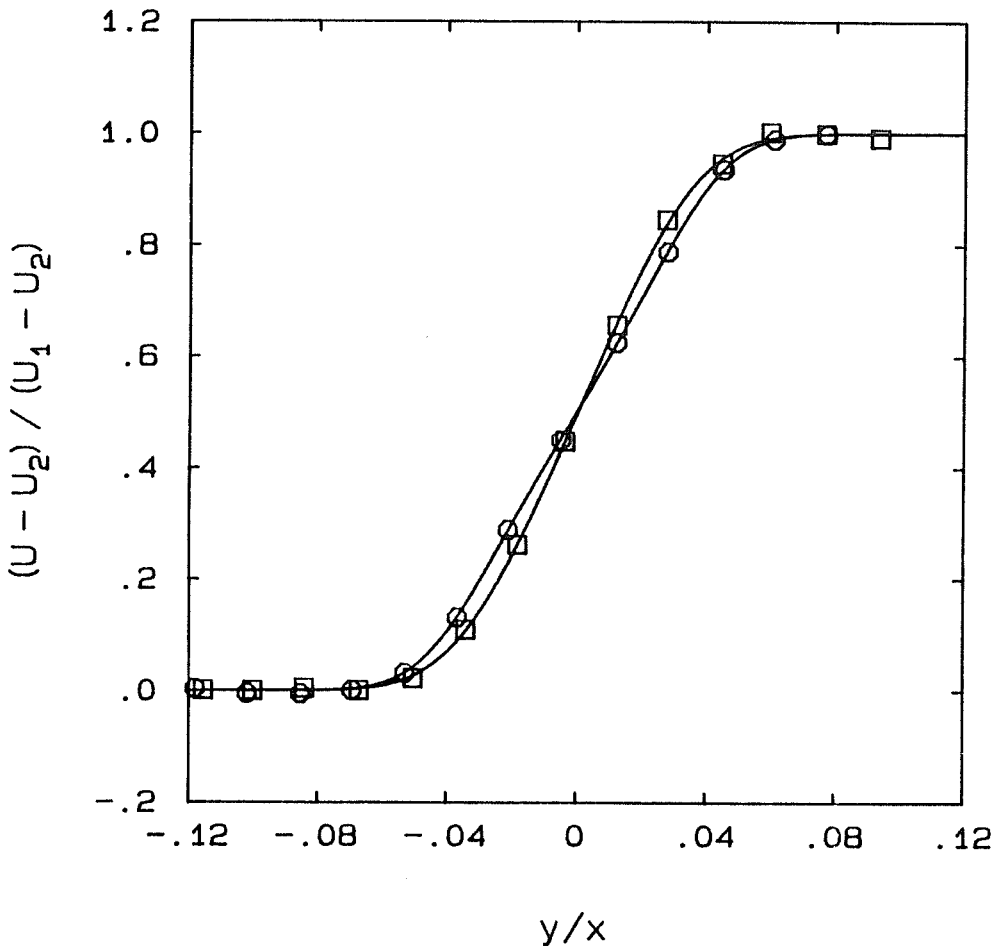

Symbol	○	□
ΔT_F ~ K	0	457
$(\rho_0 - \bar{\rho})/\rho_0$	0.00	0.286

U_1 = 22 m/s

U_2 = 8.8 m/s

Figure 3.5 Mean Velocity Profile Comparison, Nonreacting and at High Heat Release

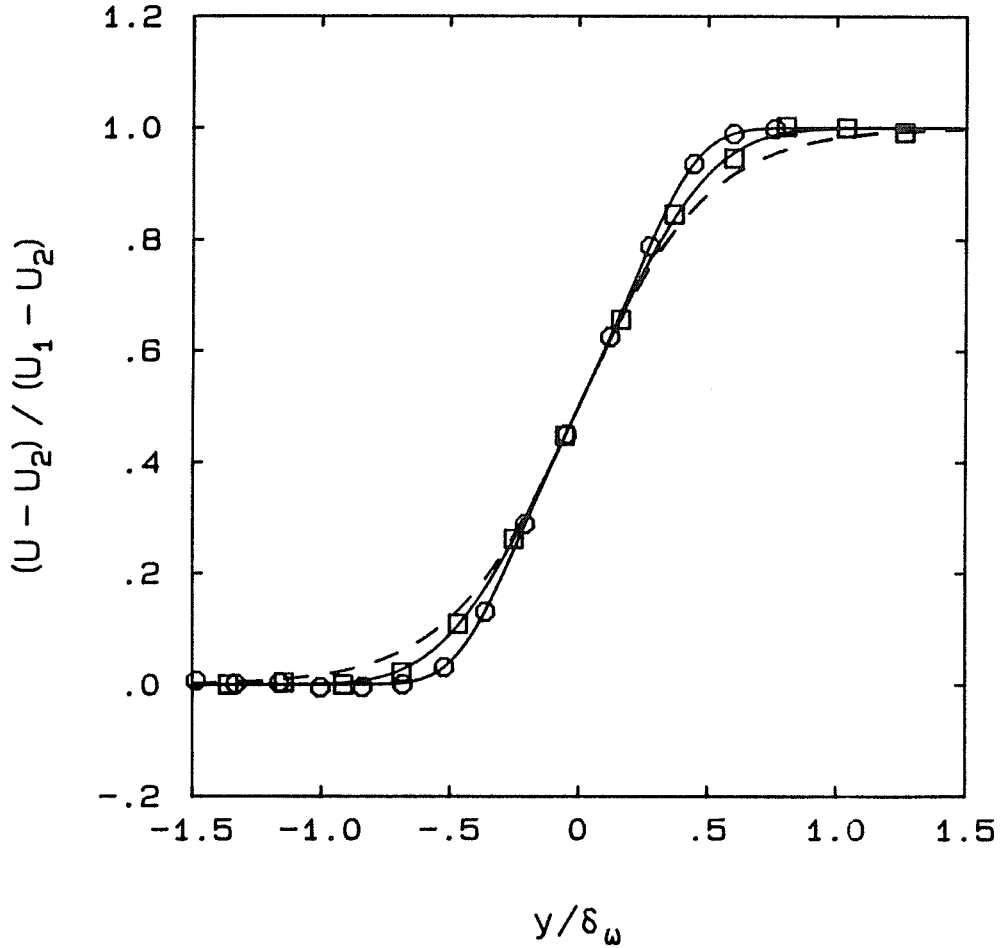

Symbol	o	□
ΔT_F ~ K	0	457
$(\rho_0 - \bar{\rho}) / \rho_0$	0.00	0.286
$\delta_\omega / (x - x_0)$	0.090	0.079

– – – – tanh fit

Figure 3.6 Velocity Profile Shape Change with Heat Release

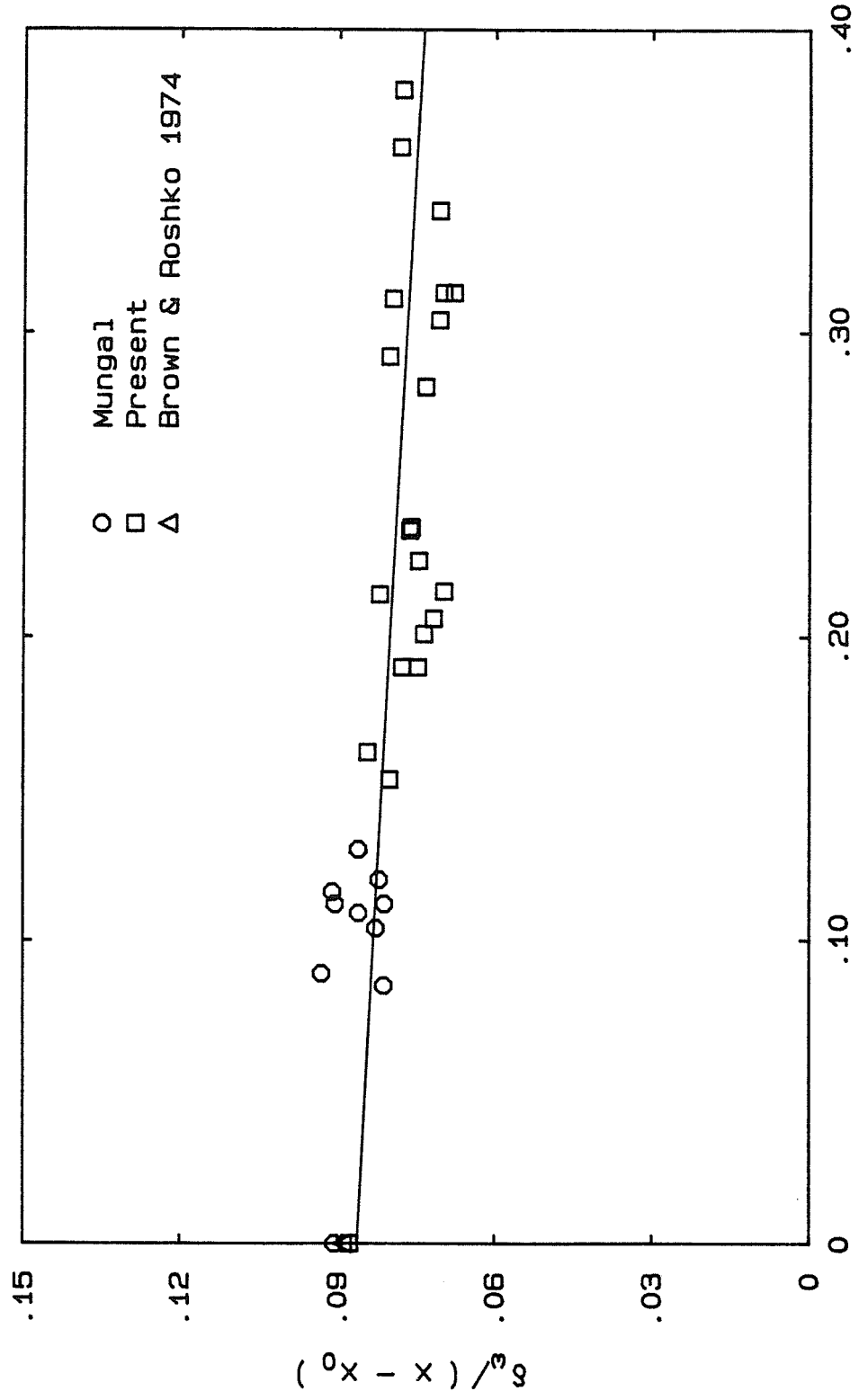

Figure 3.7 Vorticity Thickness Growth Rate versus Heat Release

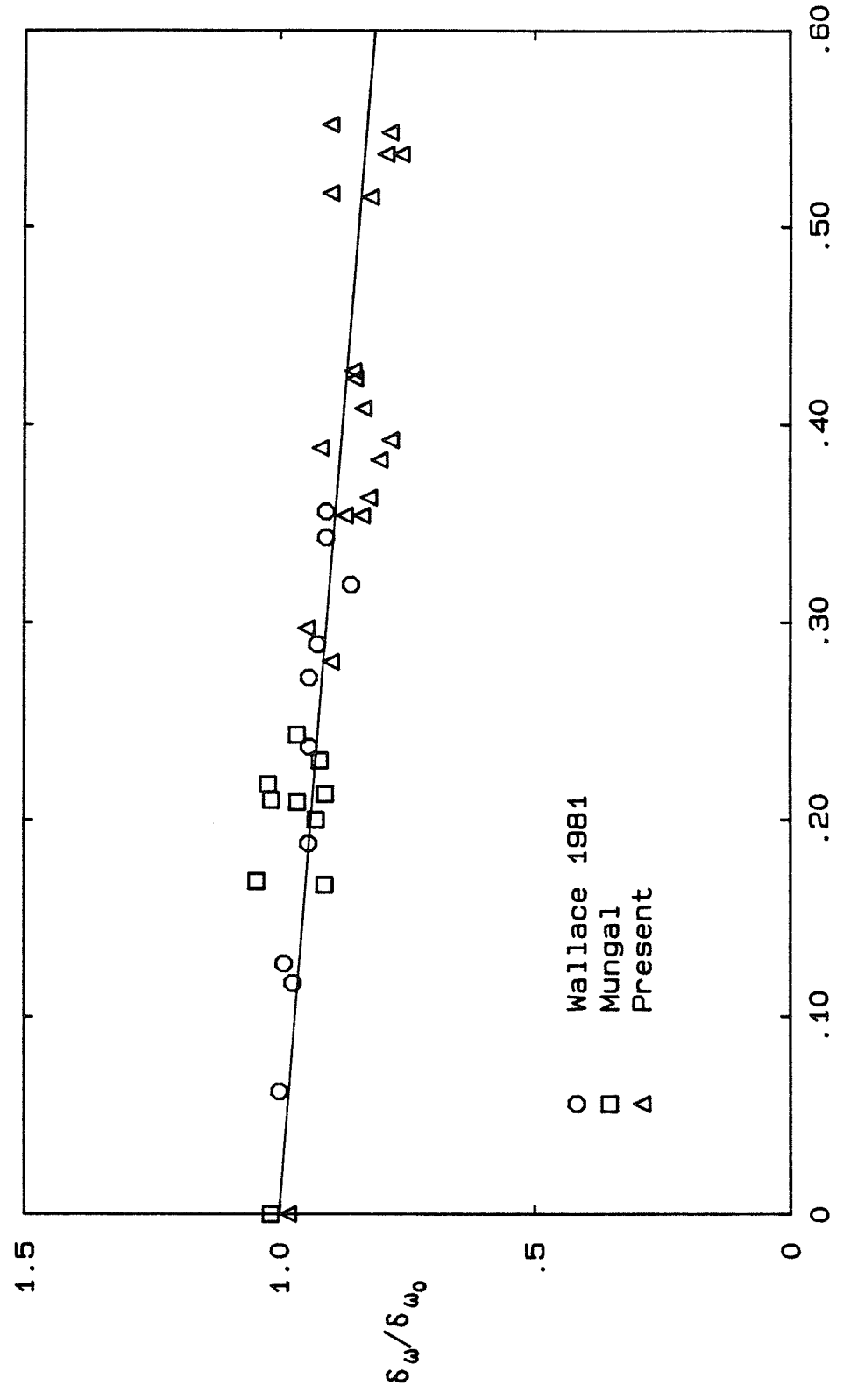

Figure 3.8 Normalized Vorticity Thickness Comparison with Wallace

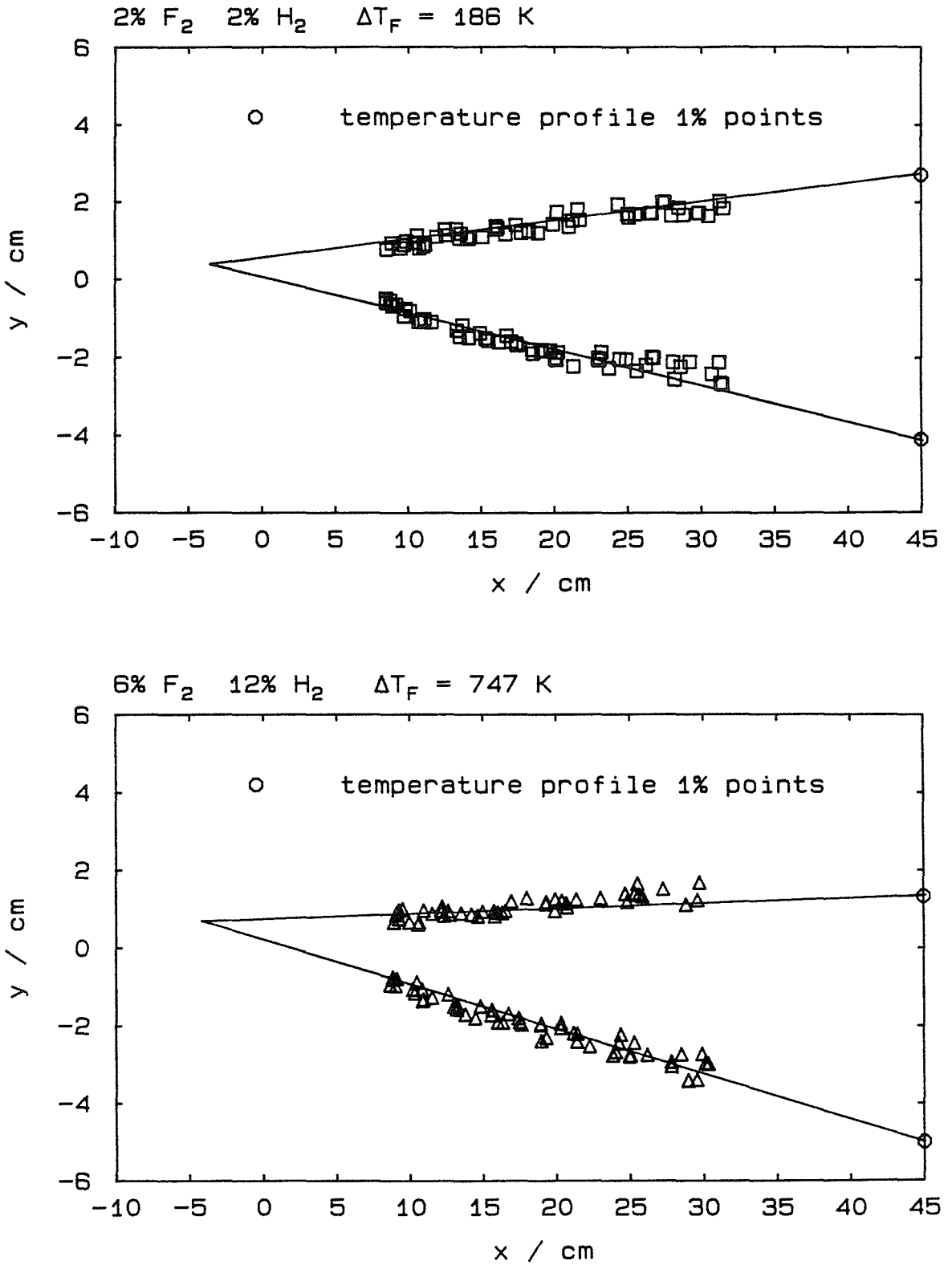

Figure 3.9 Method of Locating Virtual Origin

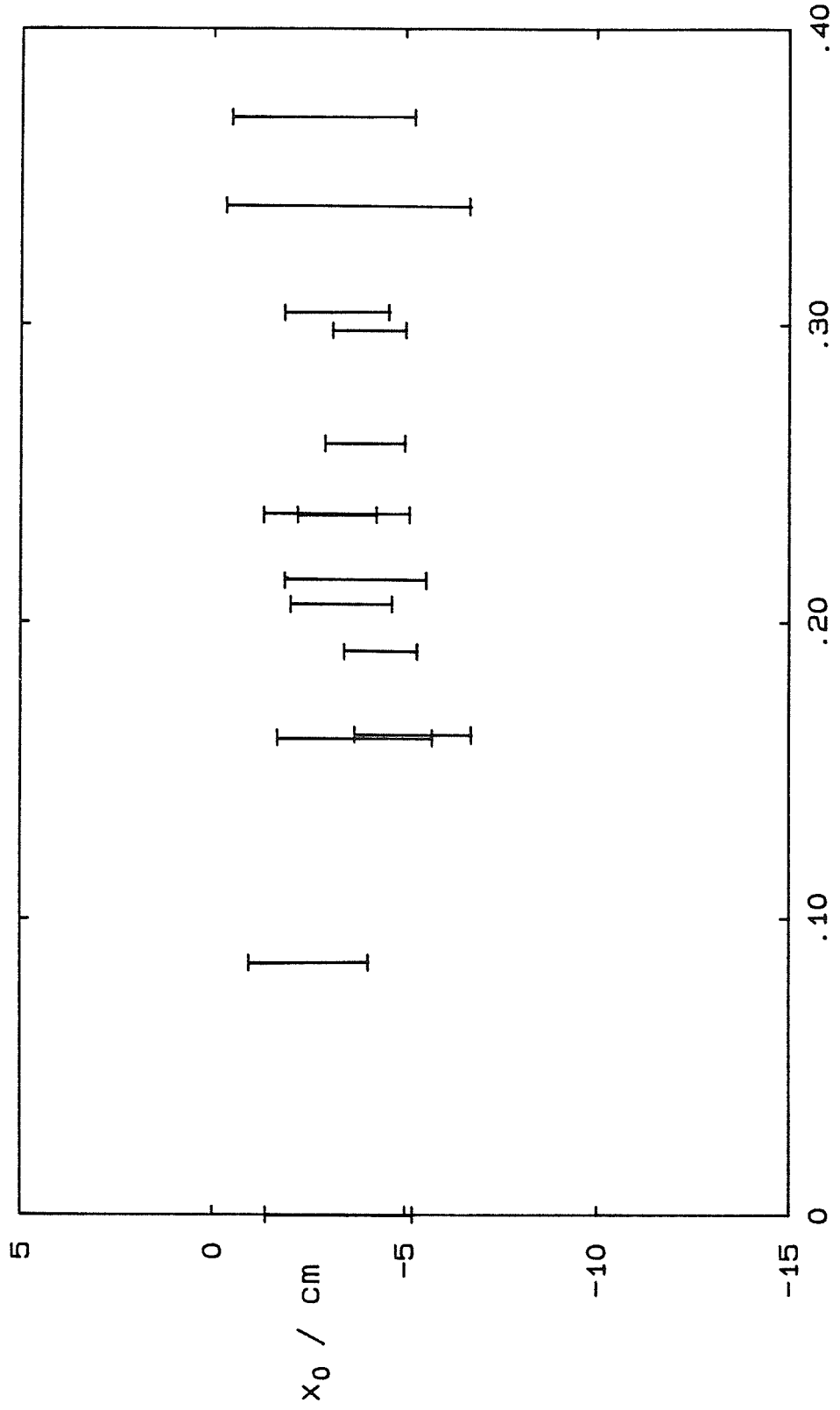

Figure 3.10 Change in Virtual Origin with Heat Release

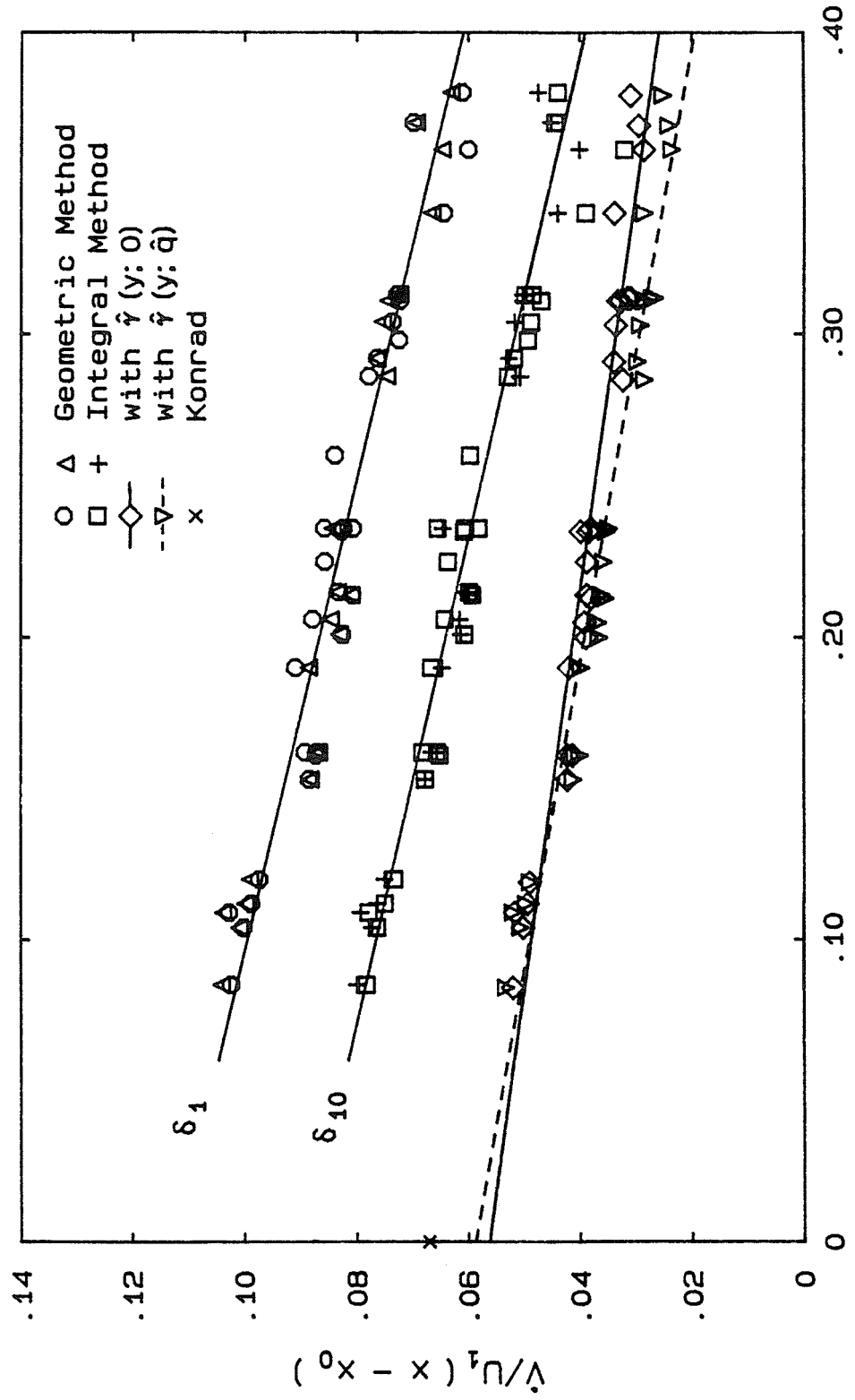

Figure 3.11 Dependence of Volumetric Entrainment on Heat Release

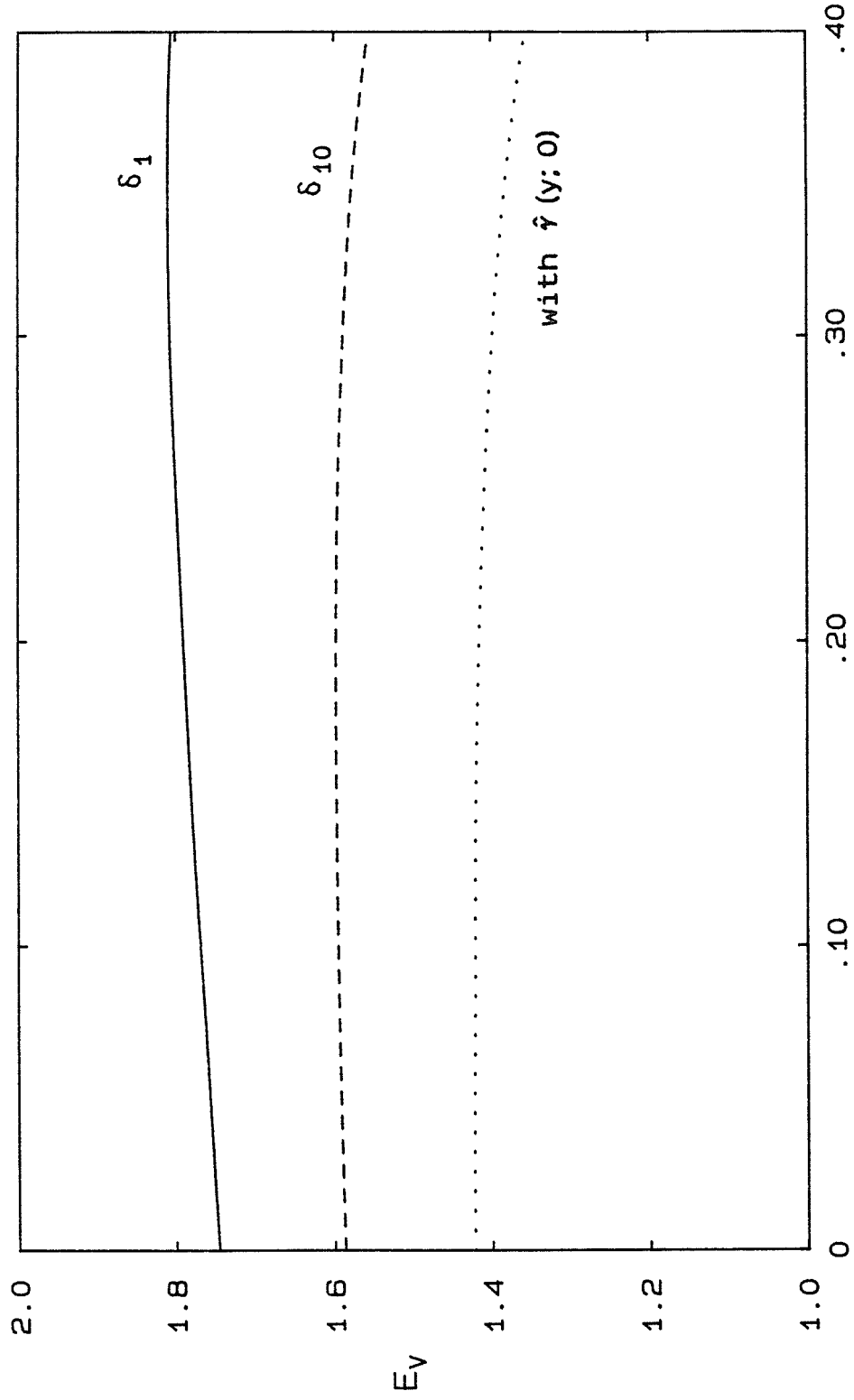

Figure 3.12 Change in Entrainment Ratio with Heat Release

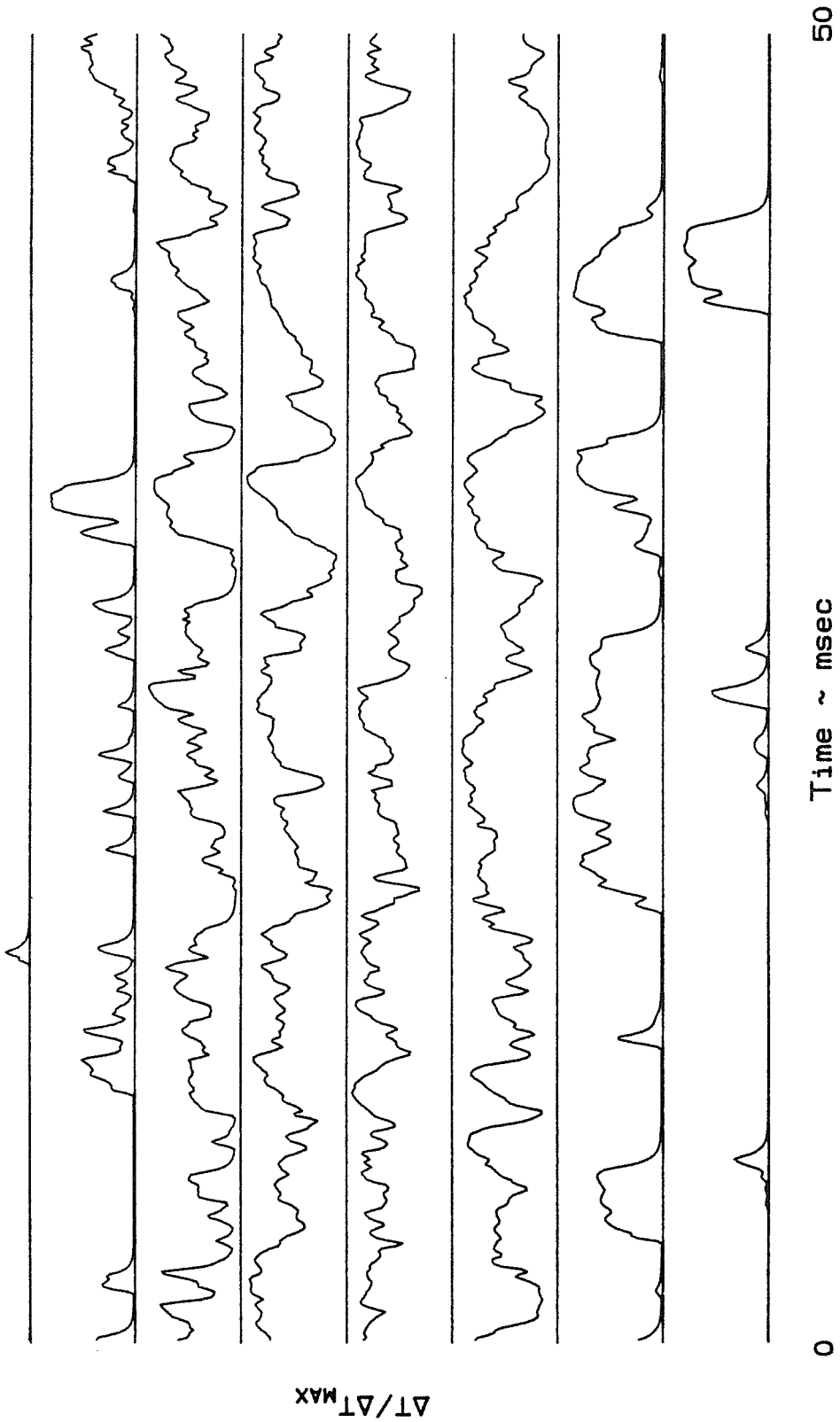

Figure 3.13 Temperature versus Time Traces, 2% F_2:2% H_2

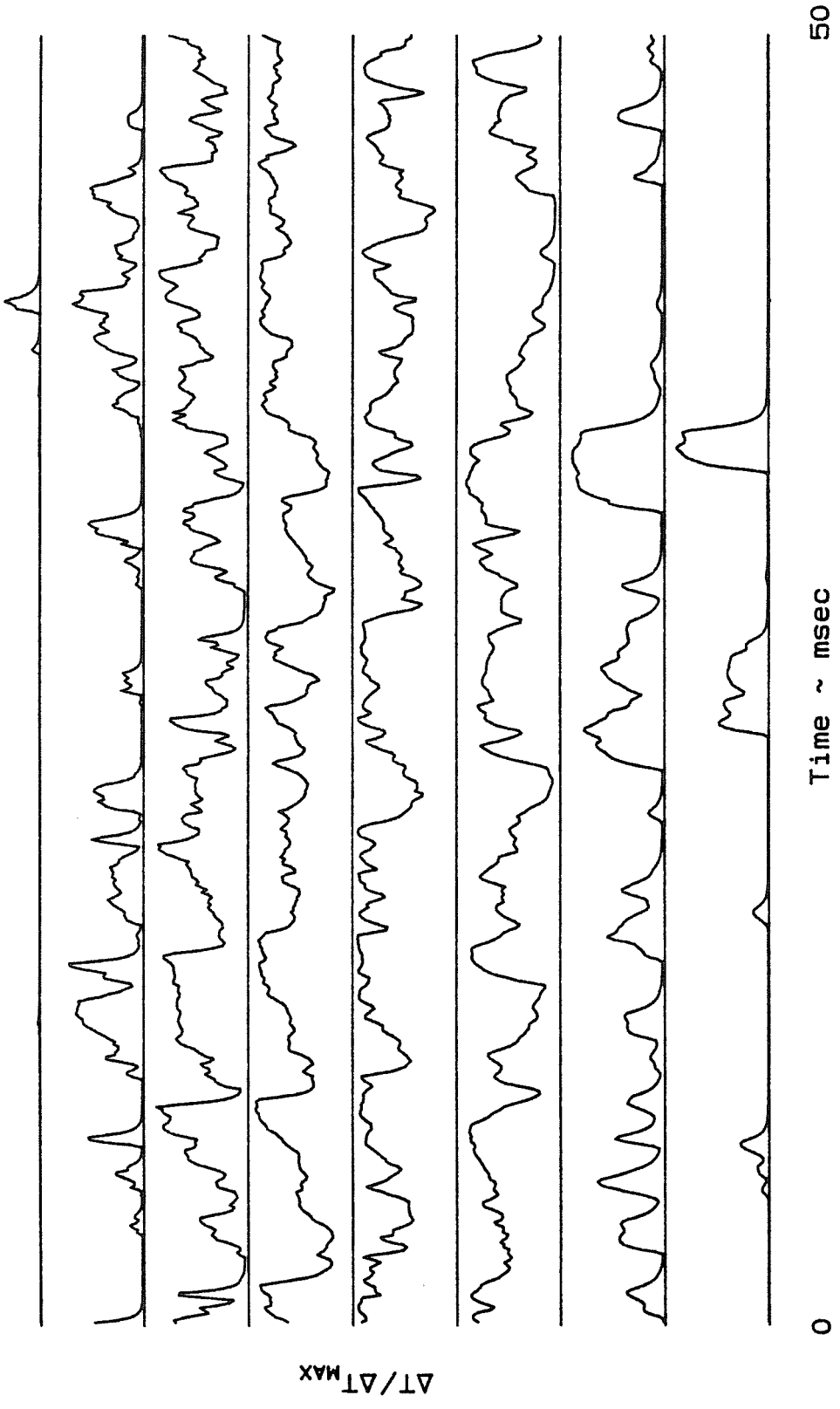

Figure 3.14 Temperature versus Time Traces, 4% F_2:4% H_2

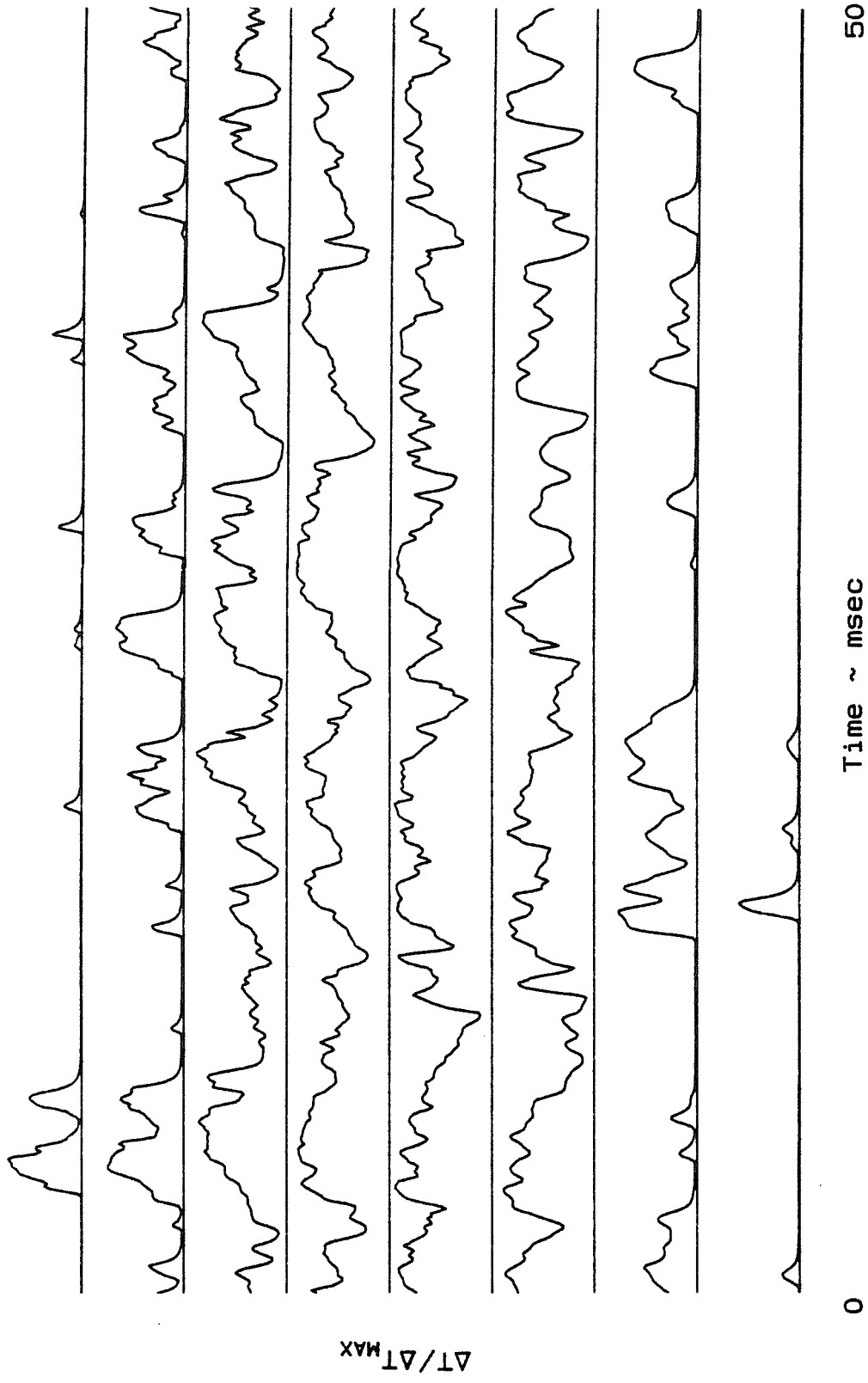

Figure 3.15 Temperature versus Time Traces, 6% F_2:6% H_2

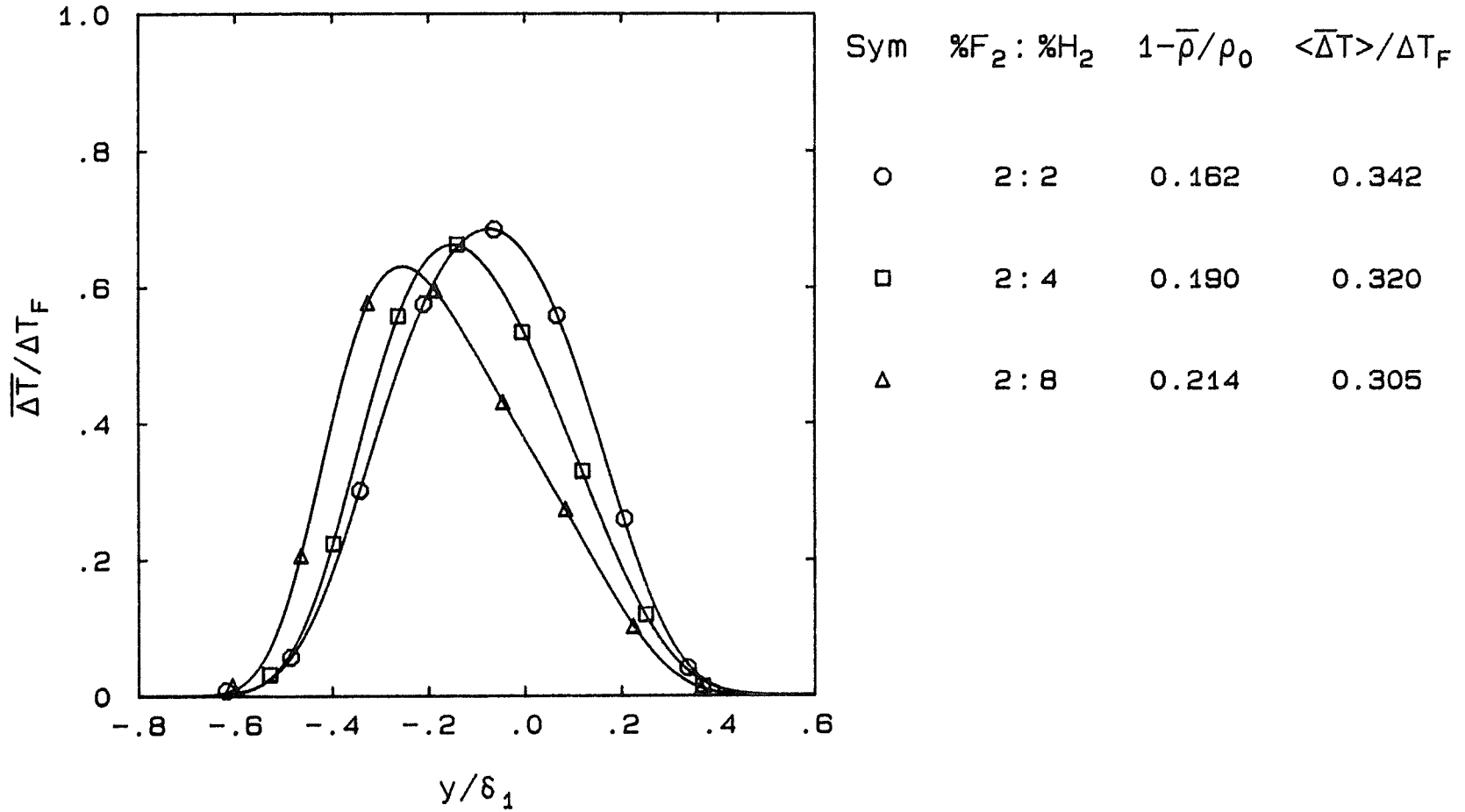

Figure 3.16 Mean Temperature Rise Profiles, 2% F_2, ϕ = 1, 1/2, 1/4

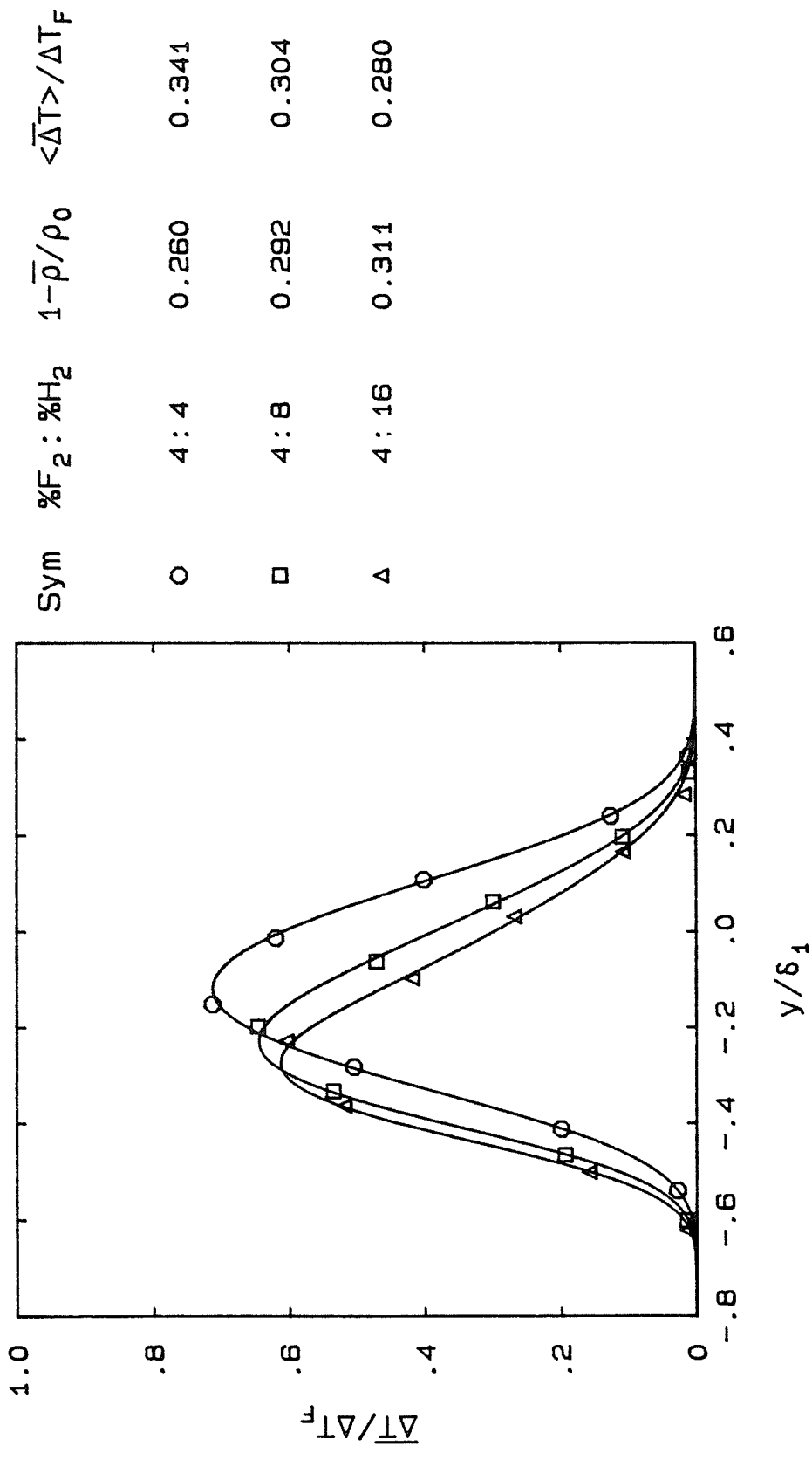

Figure 3.17 Mean Temperature Rise Profiles, 4% F_2, ϕ = 1, 1/2, 1/4

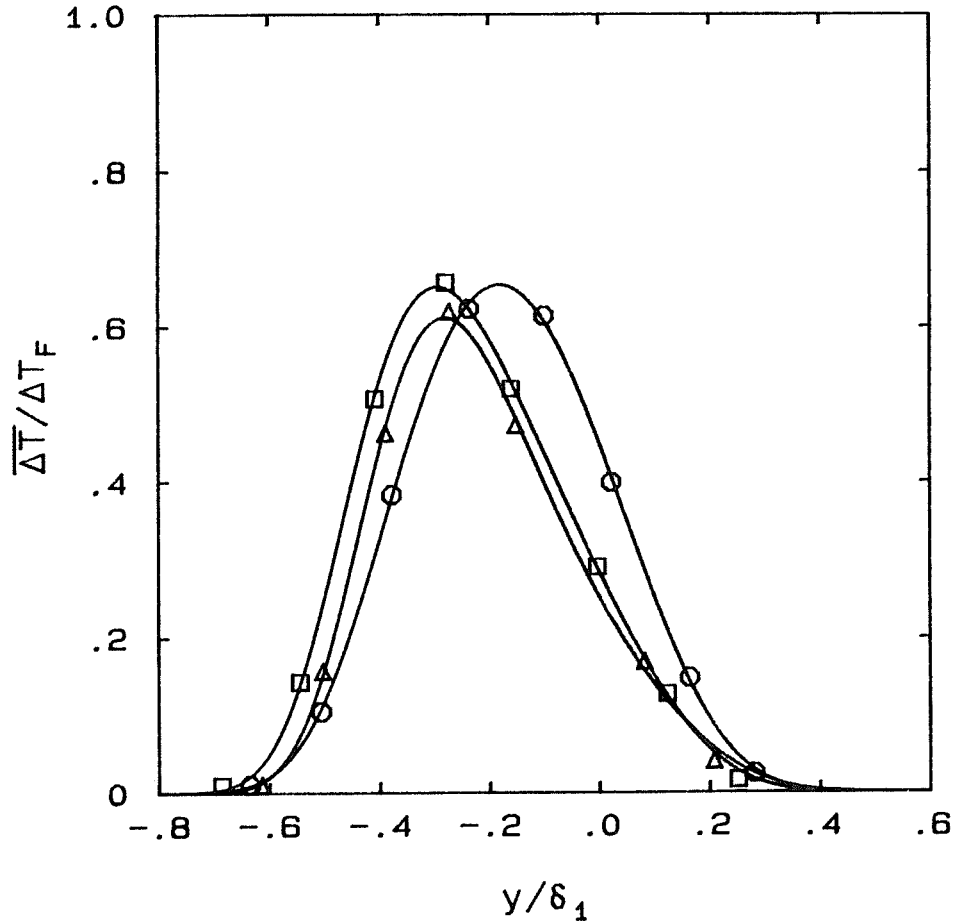

Sym	$\%F_2 : \%H_2$	$1-\overline{\rho}/\rho_0$	$\langle\overline{\Delta T}\rangle/\Delta T_F$
○	6 : 6	0.313	0.301
□	6 : 12	0.361	0.301
△	6 : 24	0.370	0.265

Figure 3.18 Mean Temperature Rise Profiles, 6% F_2, ϕ = 1, 1/2, 1/4

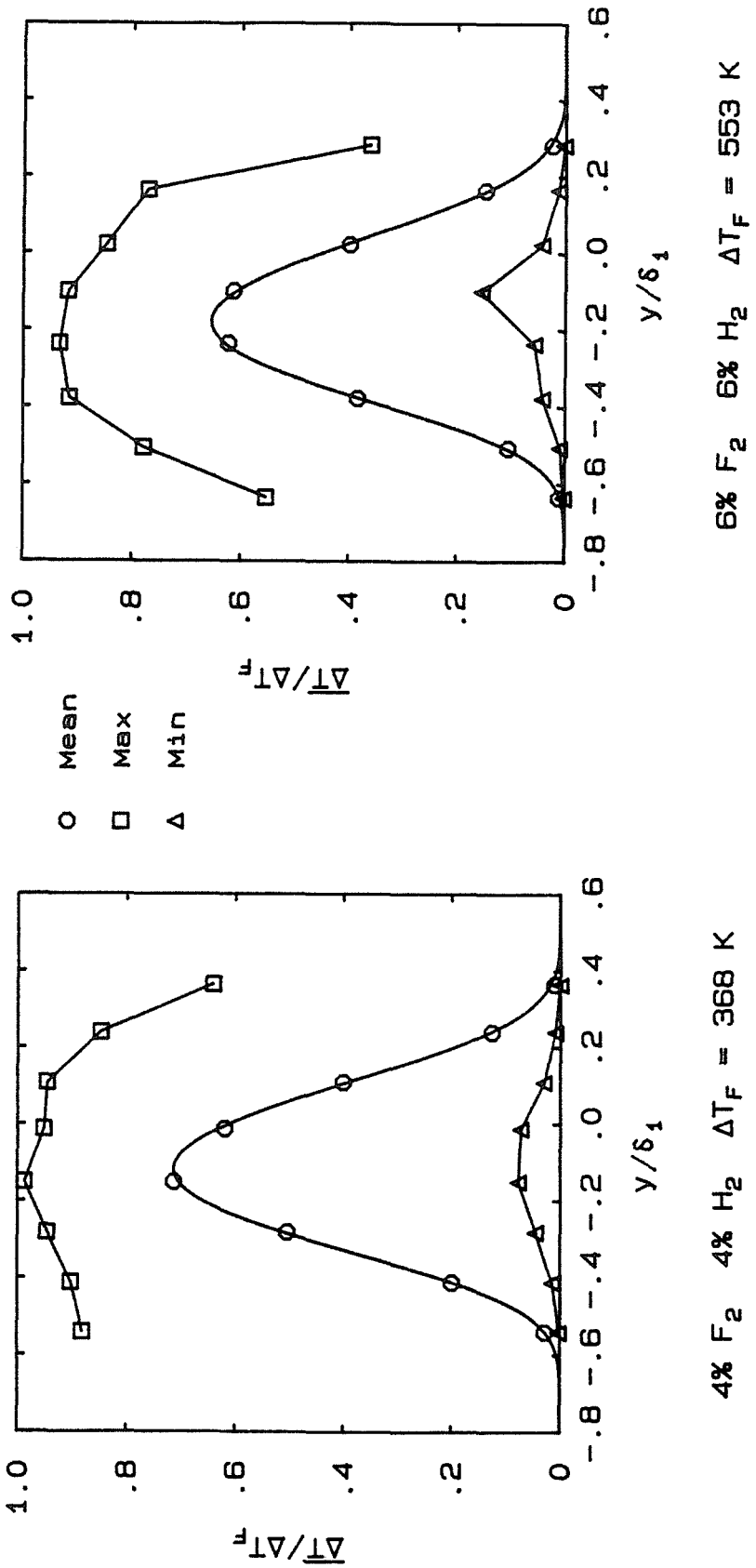

Figure 3.19 Mean Temperature Rise Profiles with Maxima and Minima, $\phi = 1$

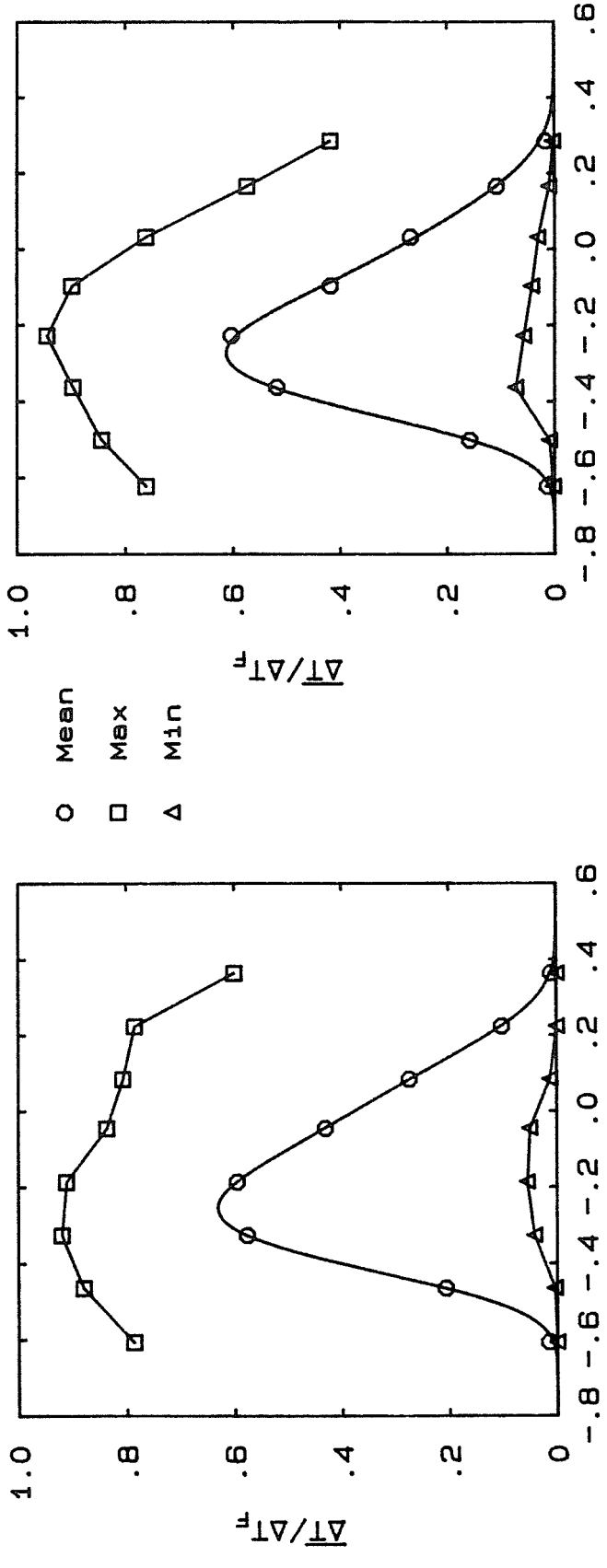

Figure 3.20 Mean Temperature Rise Profiles with Maxima and Minima, ϕ = 1/4

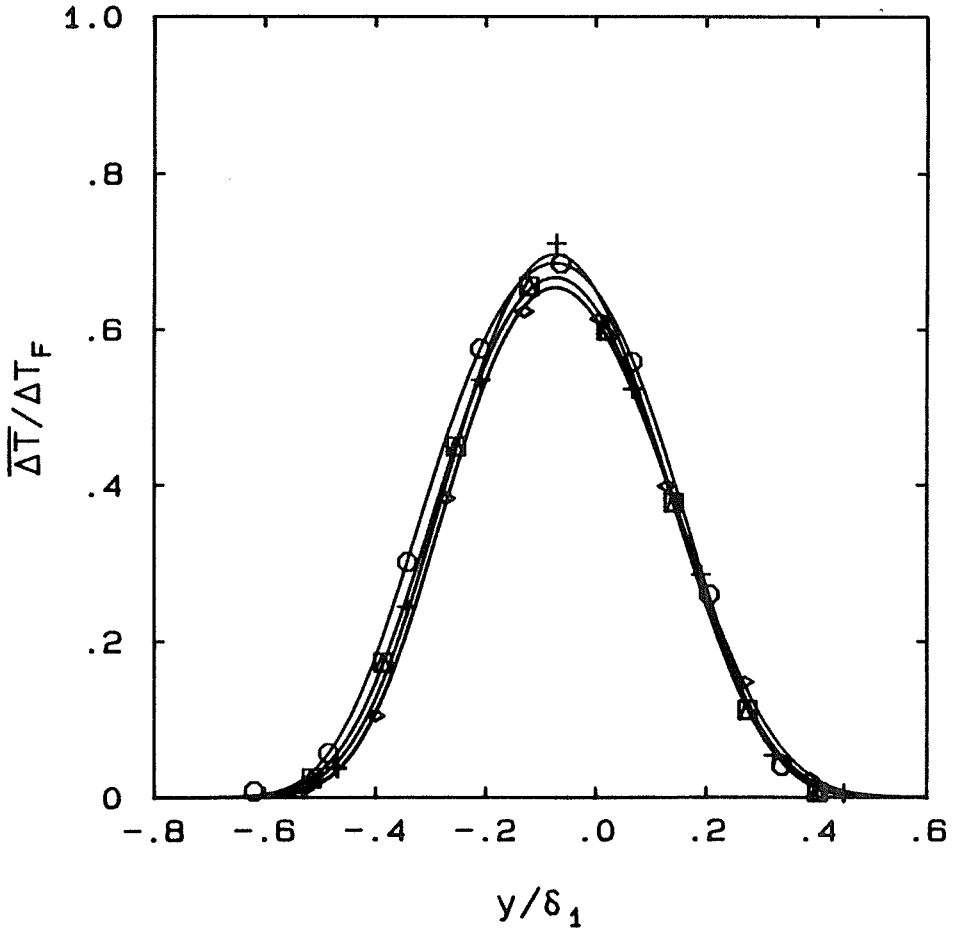

Sym	$\%F_2 : \%H_2$	$1-\overline{\rho}/\rho_0$	$\langle\overline{\Delta T}\rangle/\Delta T_F$
○	2 : 2	0.162	0.342
□	3 : 3	0.206	0.319
△	4 : 4	0.260	0.341
+	5 : 5	0.286	0.323
◇	6 : 6	0.313	0.301

Figure 3.21 Mean Temperature Rise Profiles, $\phi = 1$

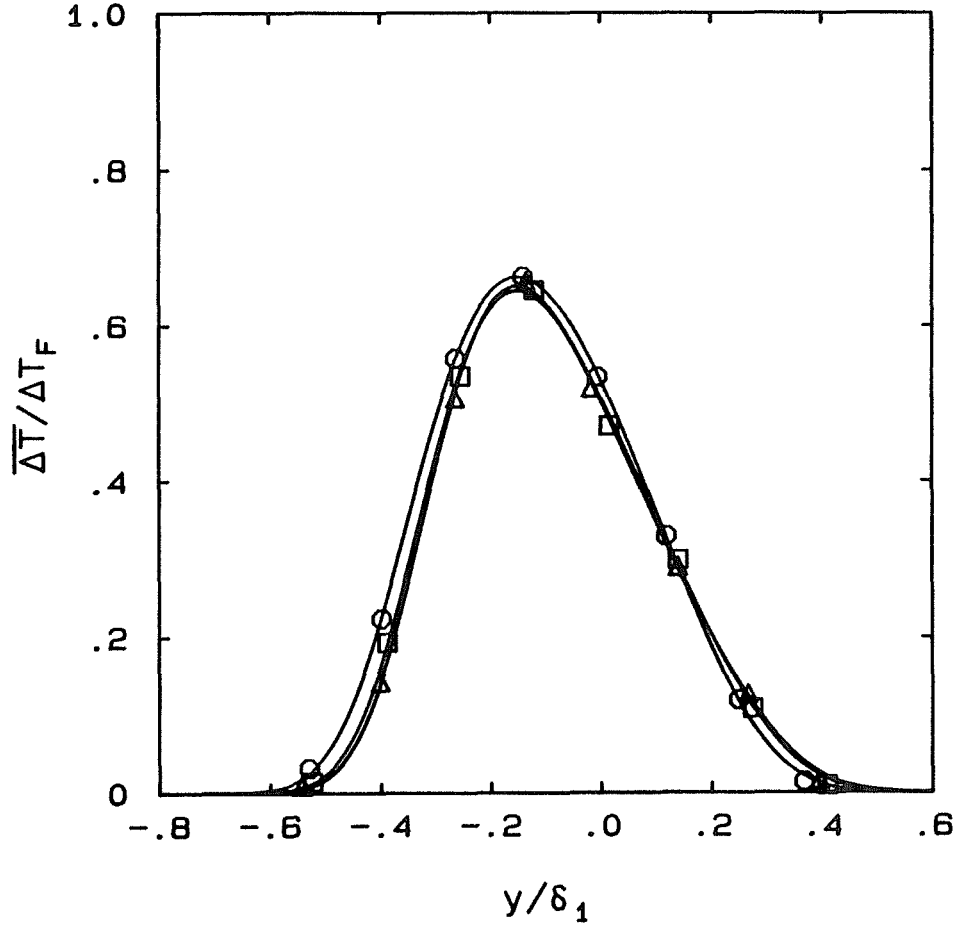

Sym	$\%F_2 : \%H_2$	$1-\overline{\rho}/\rho_0$	$\langle\overline{\Delta T}\rangle/\Delta T_F$
○	2 : 4	0.190	0.320
□	4 : 8	0.292	0.304
△	6 : 12	0.361	0.301

Figure 3.22 Mean Temperature Rise Profiles, ϕ = 1/2

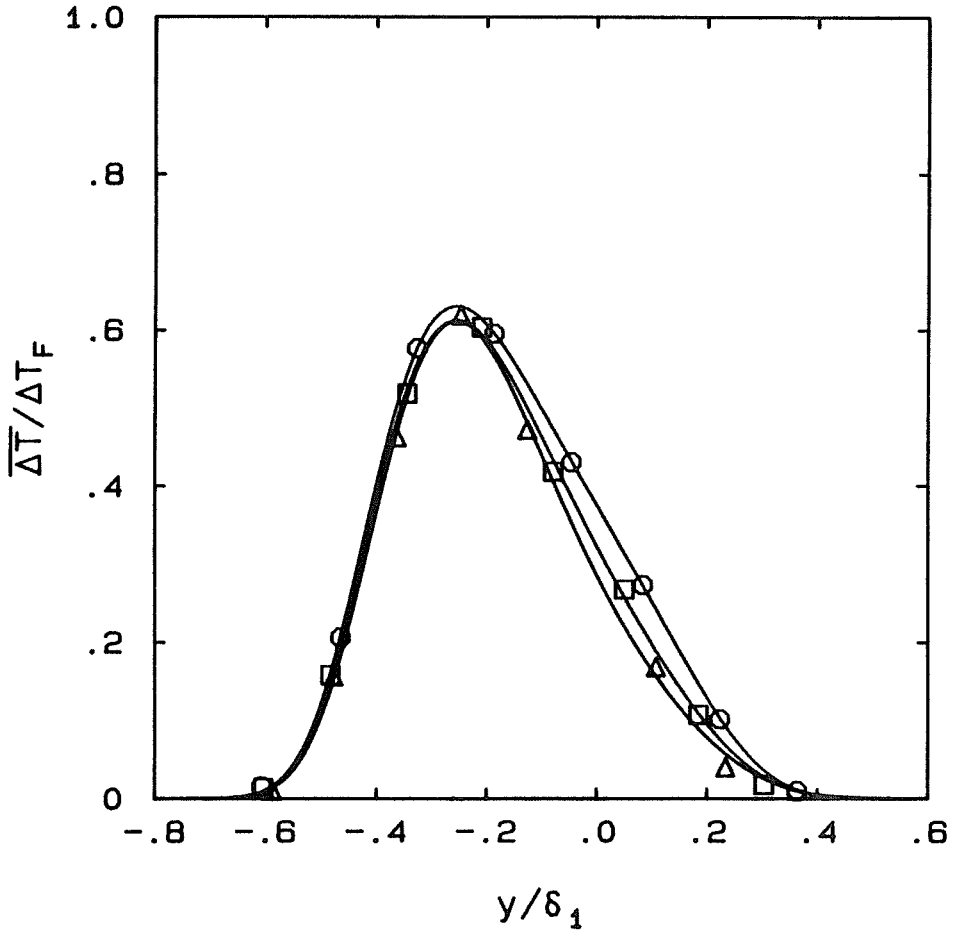

Sym	$\%F_2 : \%H_2$	$1-\overline{\rho}/\rho_0$	$\langle\overline{\Delta T}\rangle/\Delta T_F$
○	2 : 8	0.214	0.305
□	4 : 16	0.311	0.280
△	6 : 24	0.370	0.265

Figure 3.23 Mean Temperature Rise Profiles, ϕ = 1/4

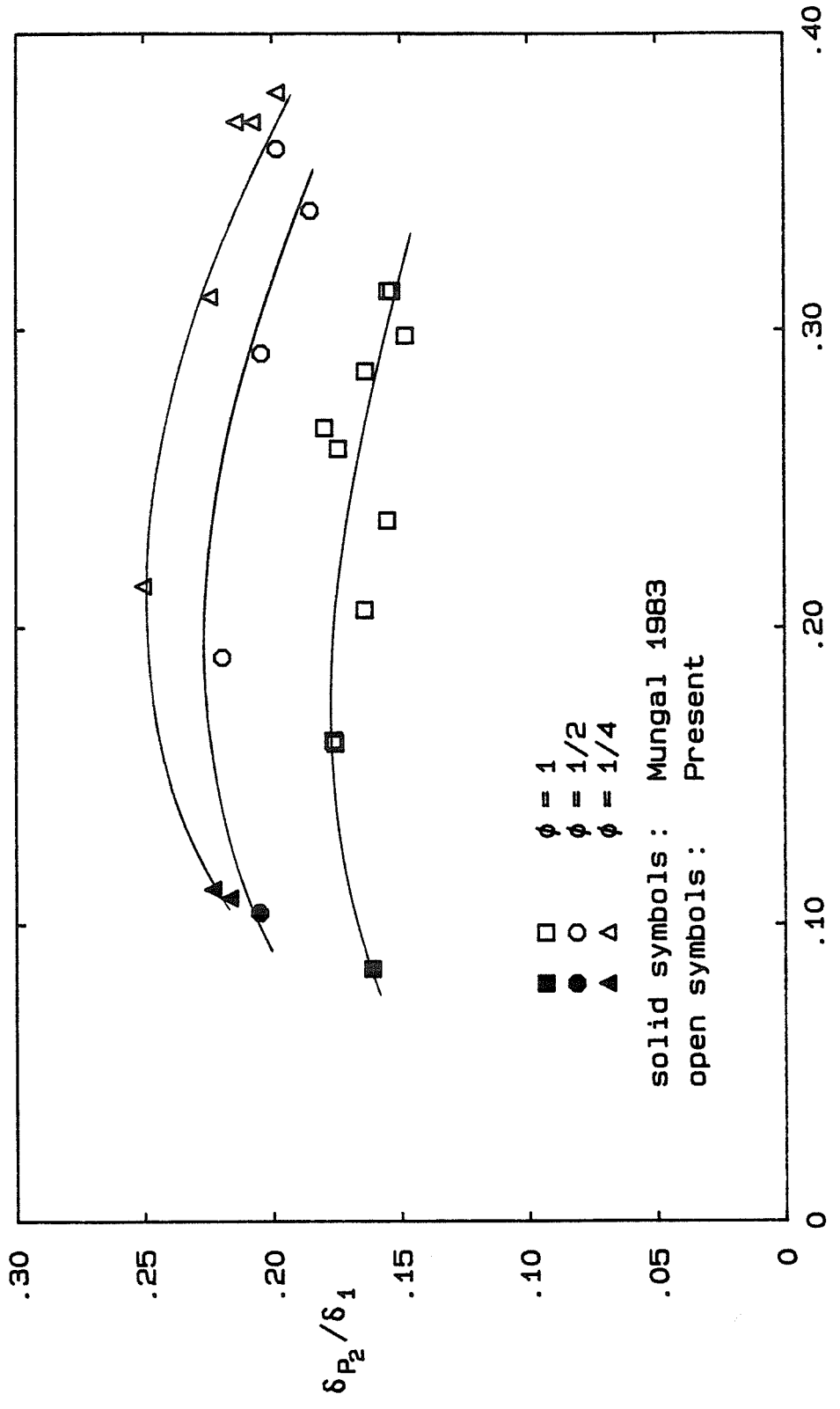

Figure 3.24 Product Fraction Thickness versus Heat Release

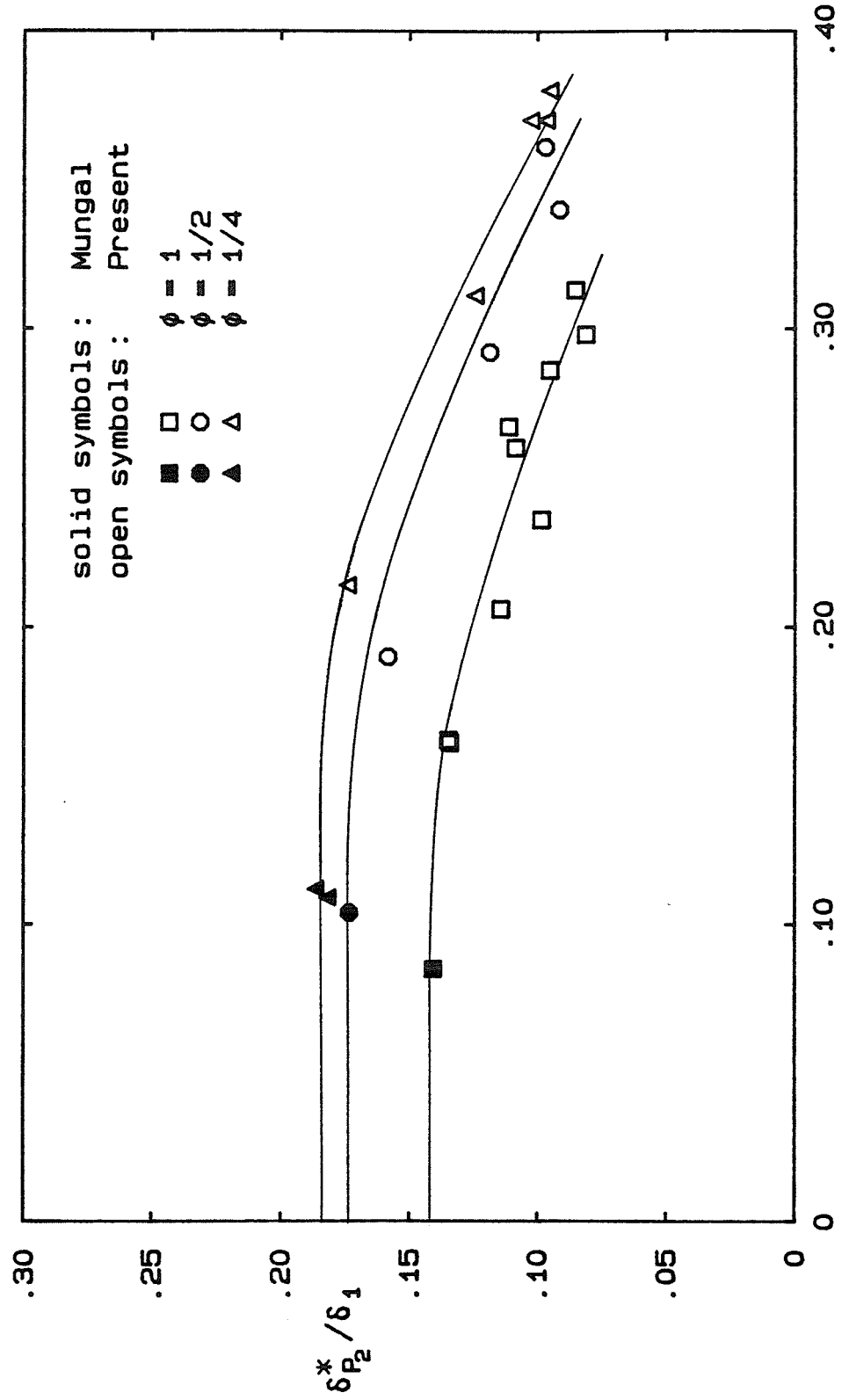

Figure 3.25 Density-Weighted Product Thickness versus Heat Release

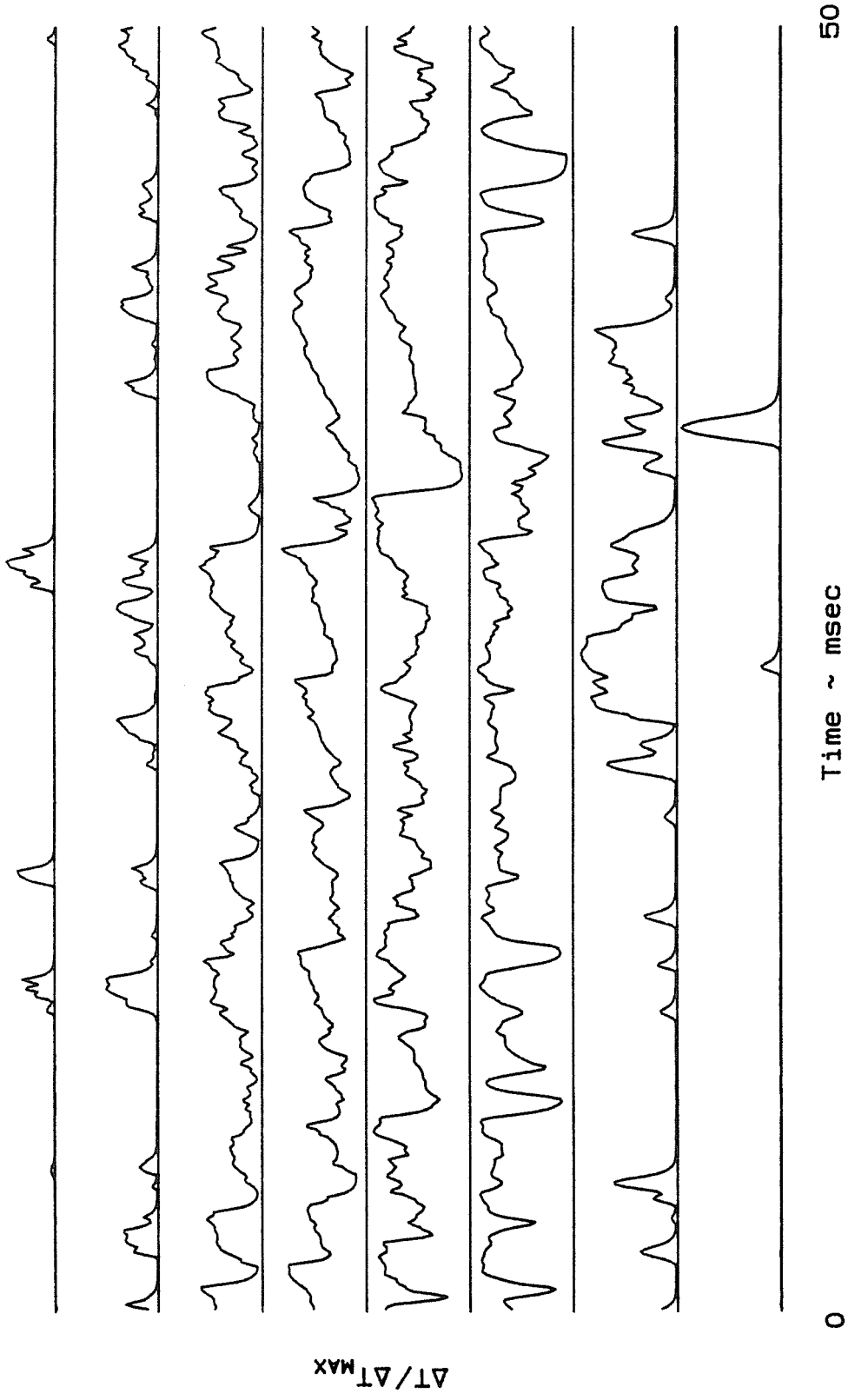

Figure 3.26 Temperature versus Time Traces, ϕ = 1/4, 2% F_2

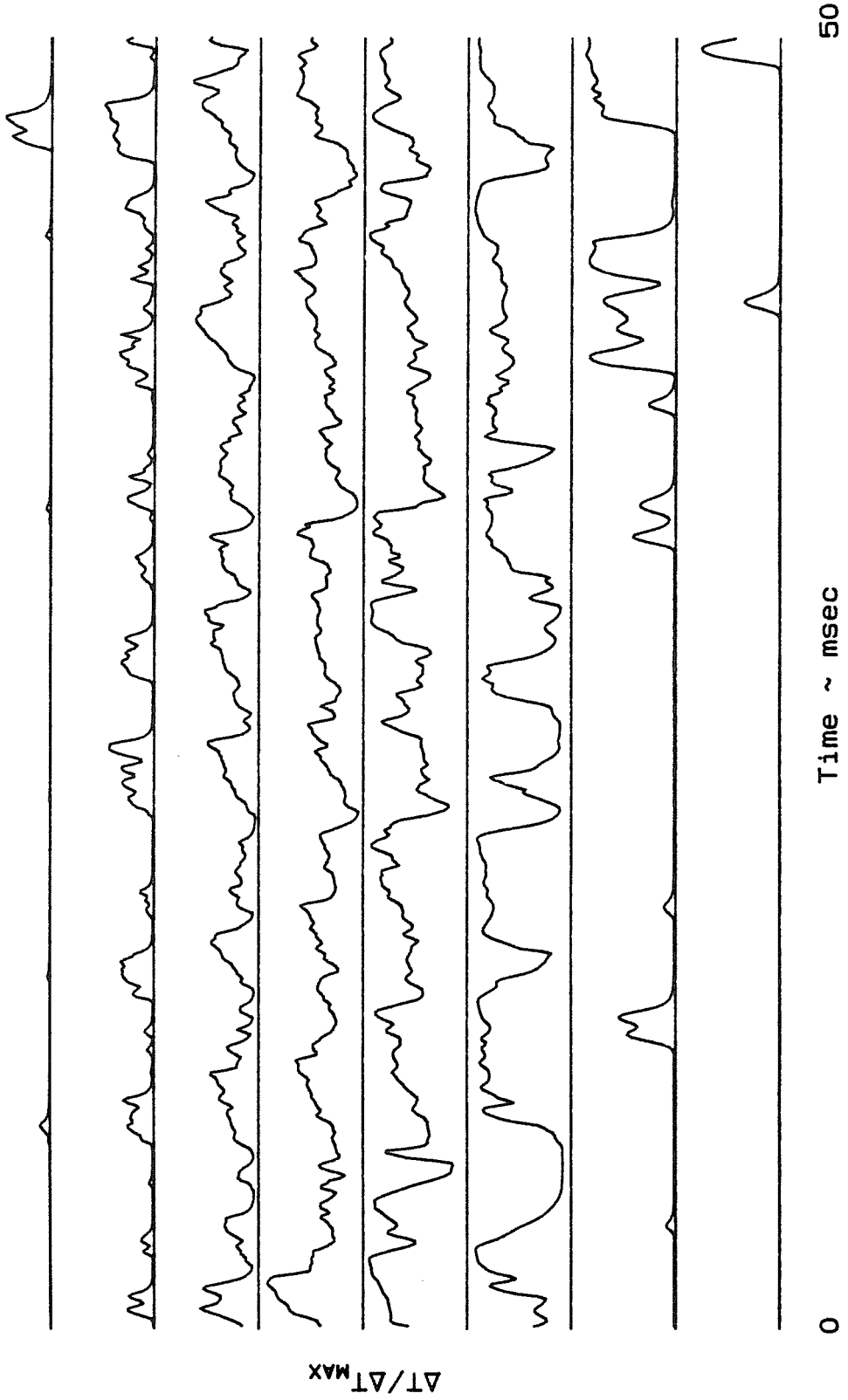

Figure 3.27 Temperature versus Time Traces, $\phi = 1/4$, 4% F_2

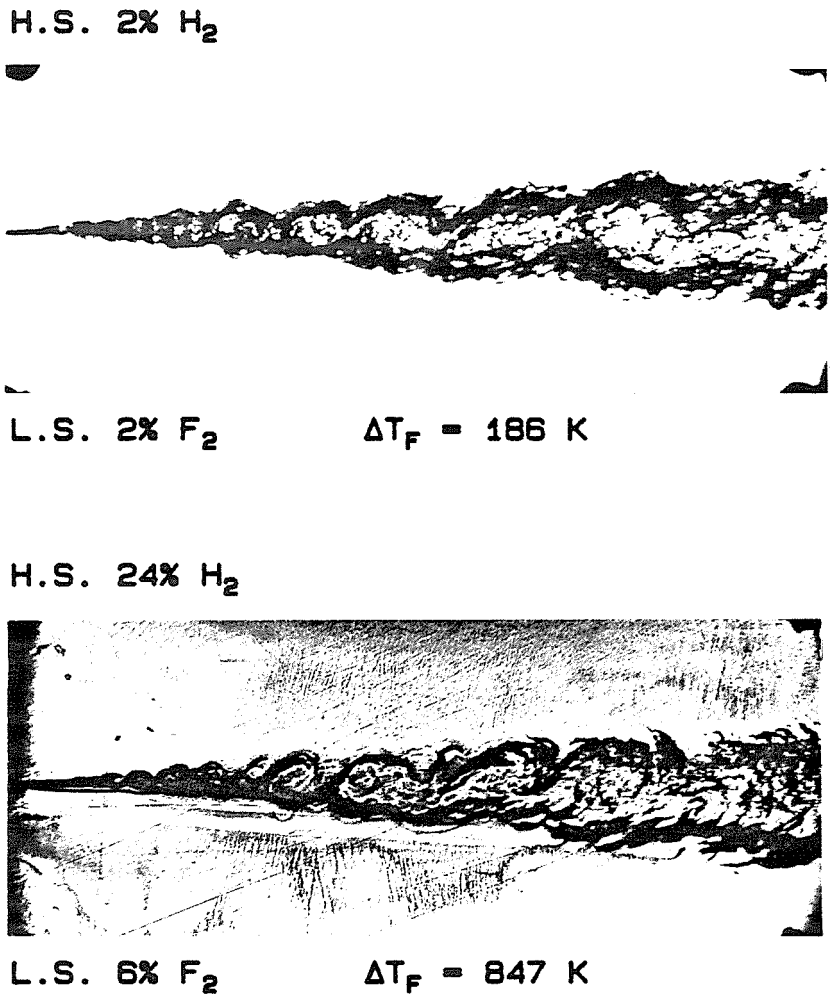

Figure 3.28 Spark Schlieren Photographs at Low and High Heat Release

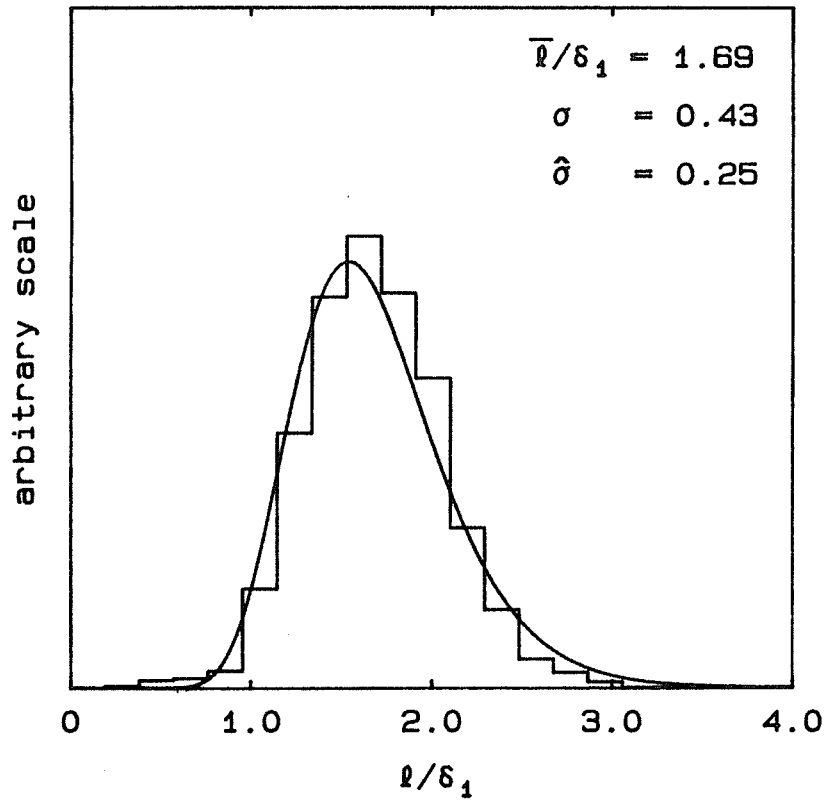

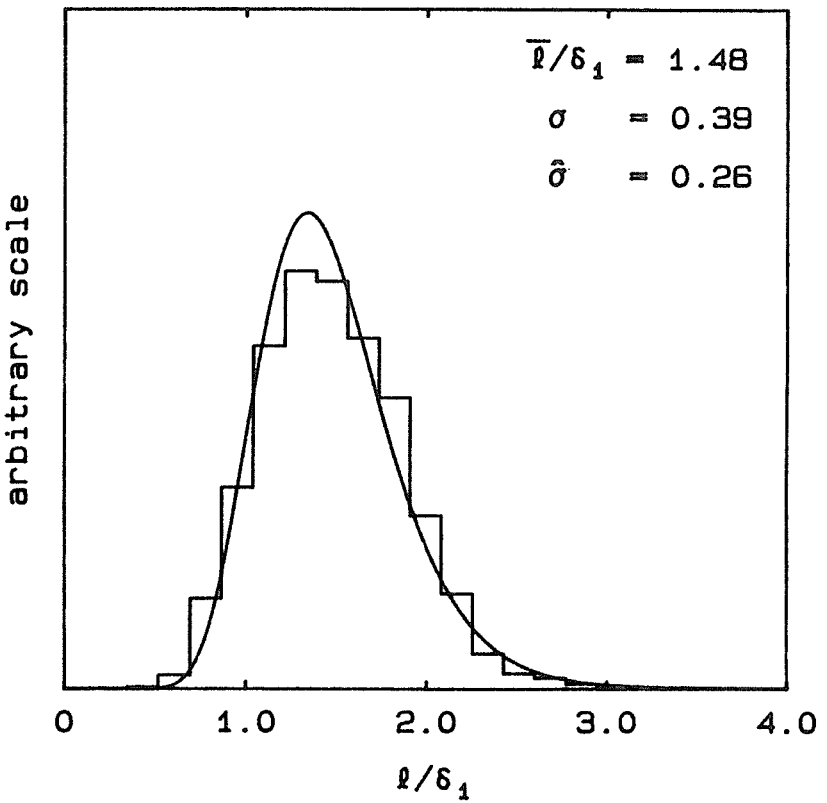

Figure 3.29 Vortex Spacing Histrograms, 2% F_2:2% H_2, 4% F_2:4% H_2

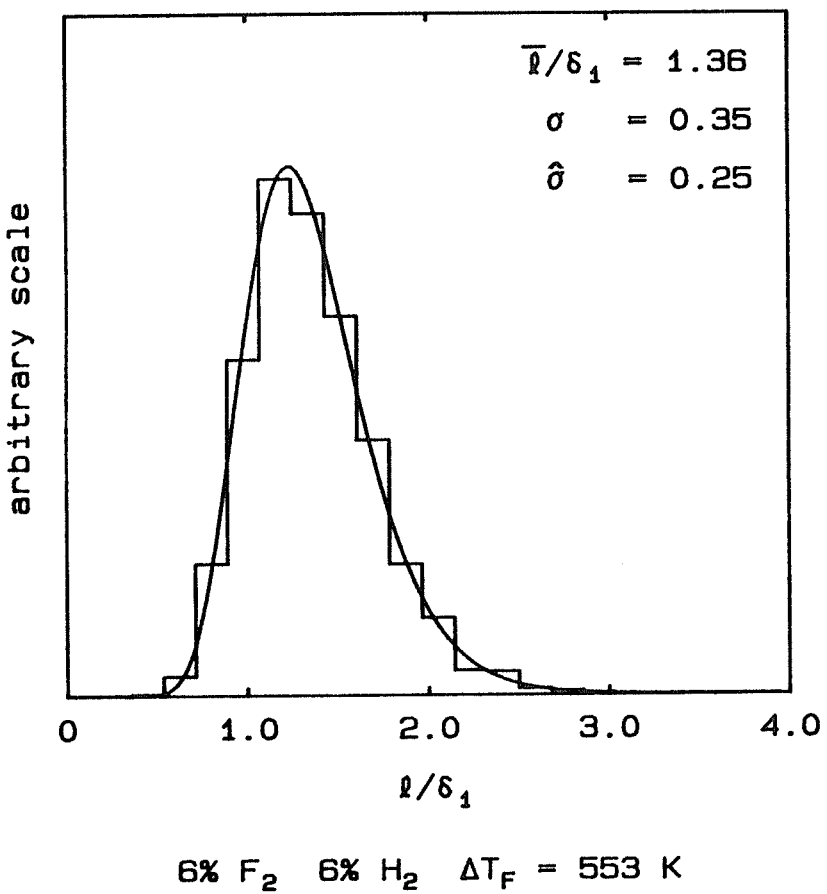

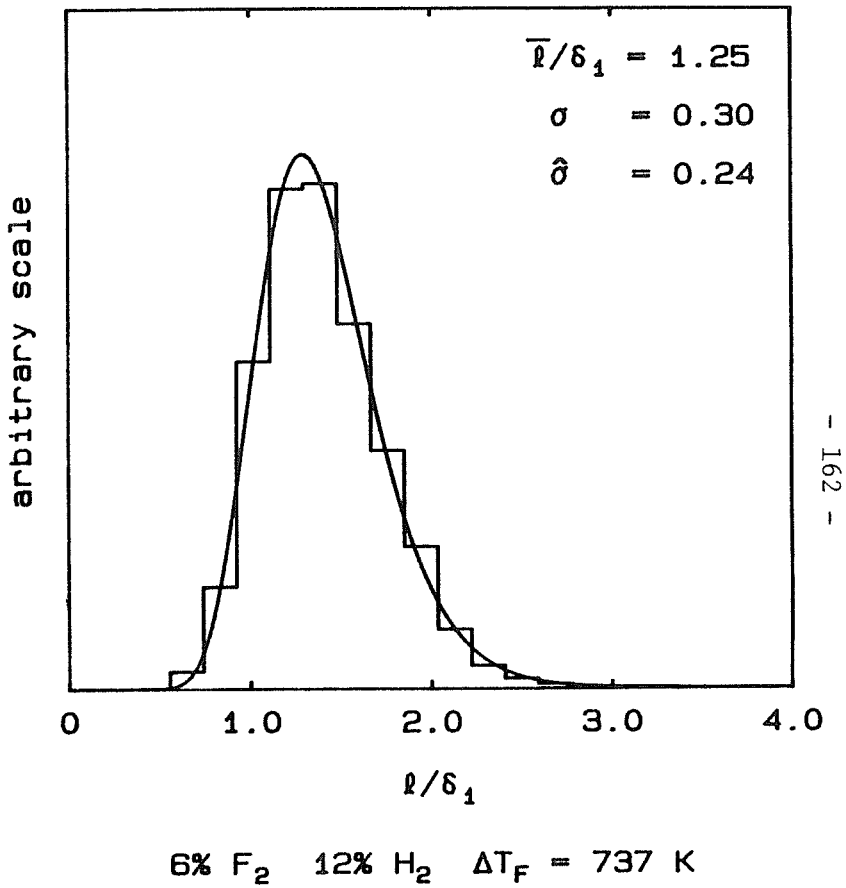

Figure 3.30 Vortex Spacing Histograms, 6% F_2:6% H_2, 6% F_2:12% H_2

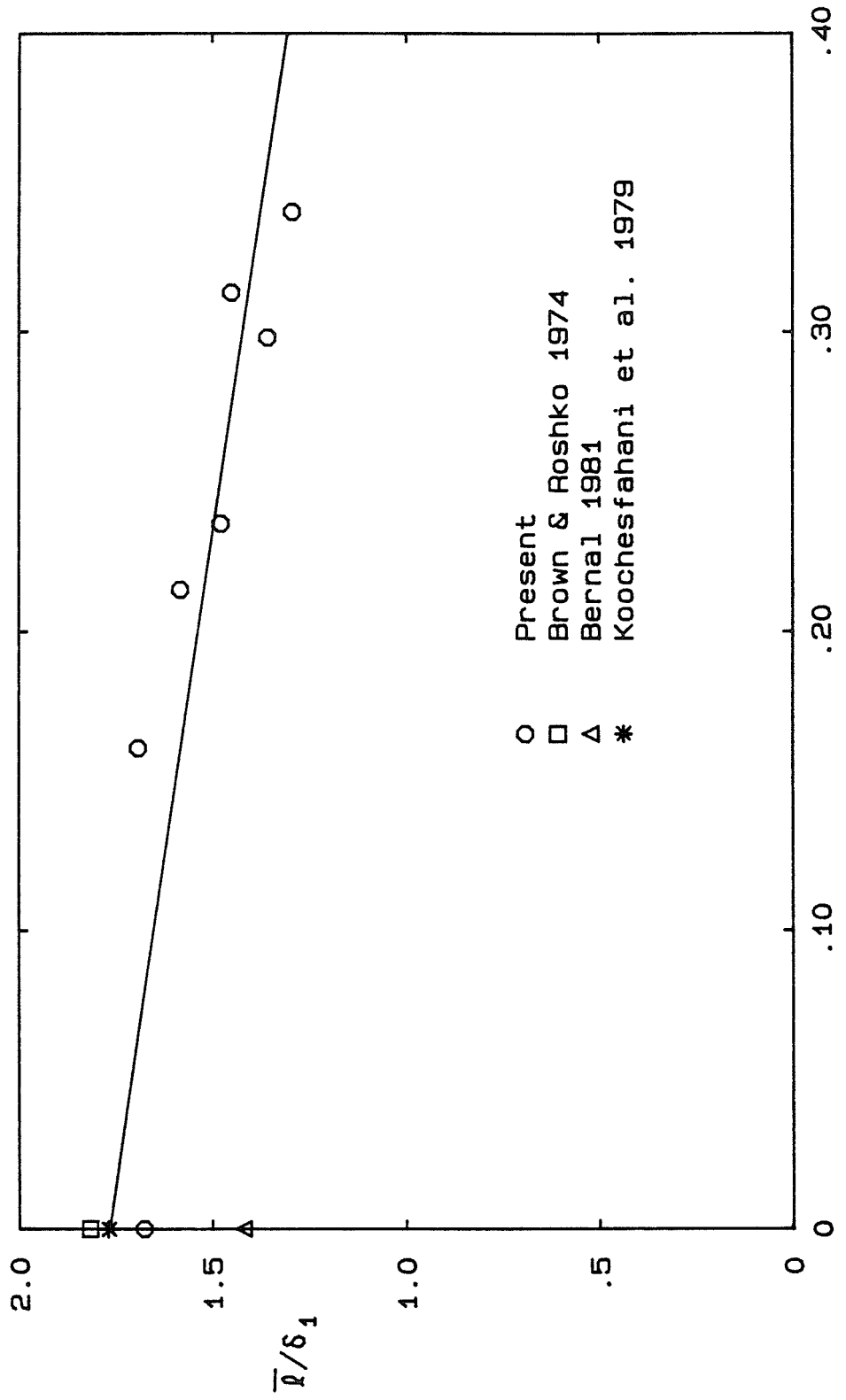

Figure 3.31 Mean Vortex Spacing, $\overline{\ell}/\delta_1$, versus Heat Release

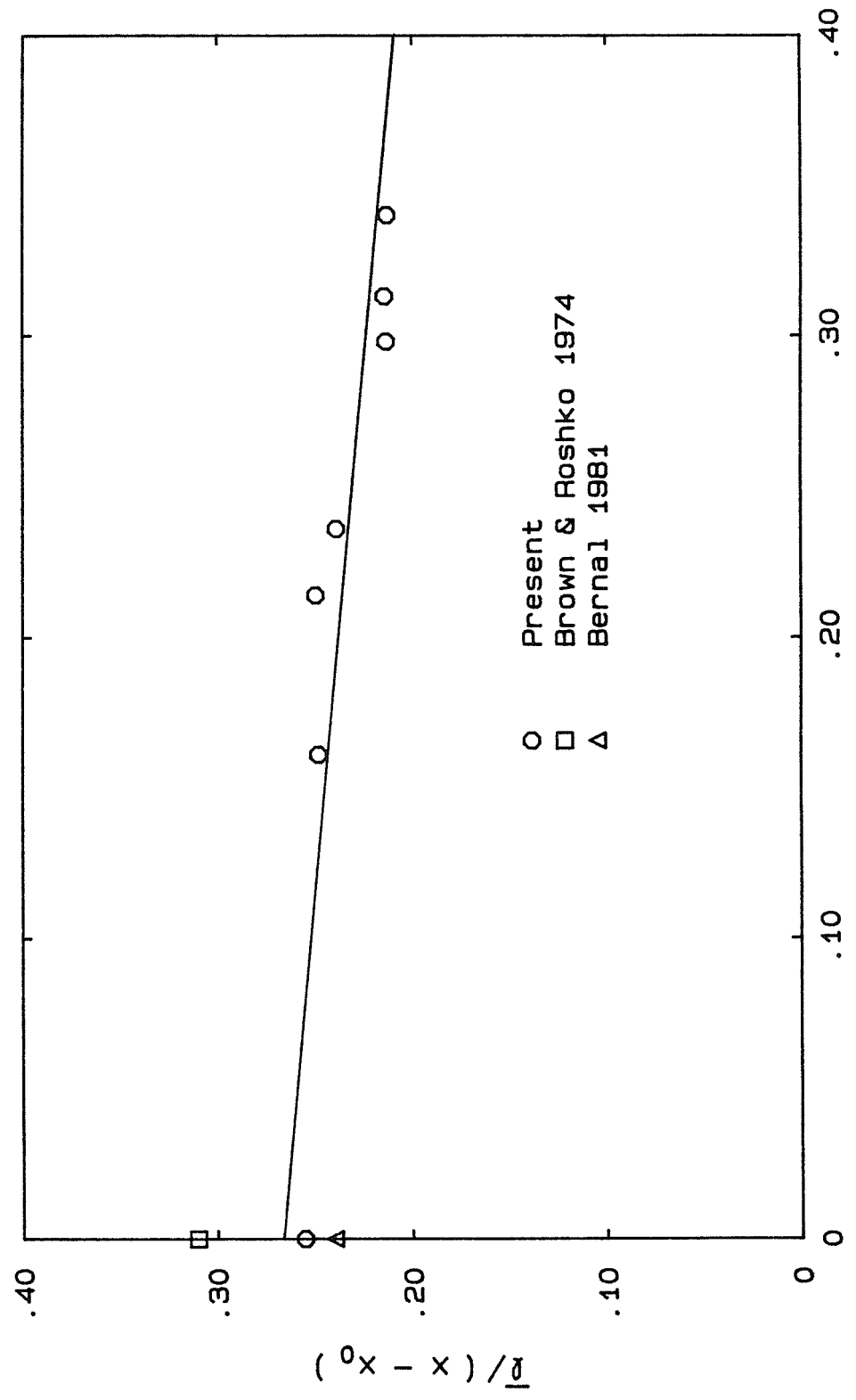

Figure 3.32 Mean Vortex Spacing, $\bar{\ell}/(x - x_0)$, versus Heat Release

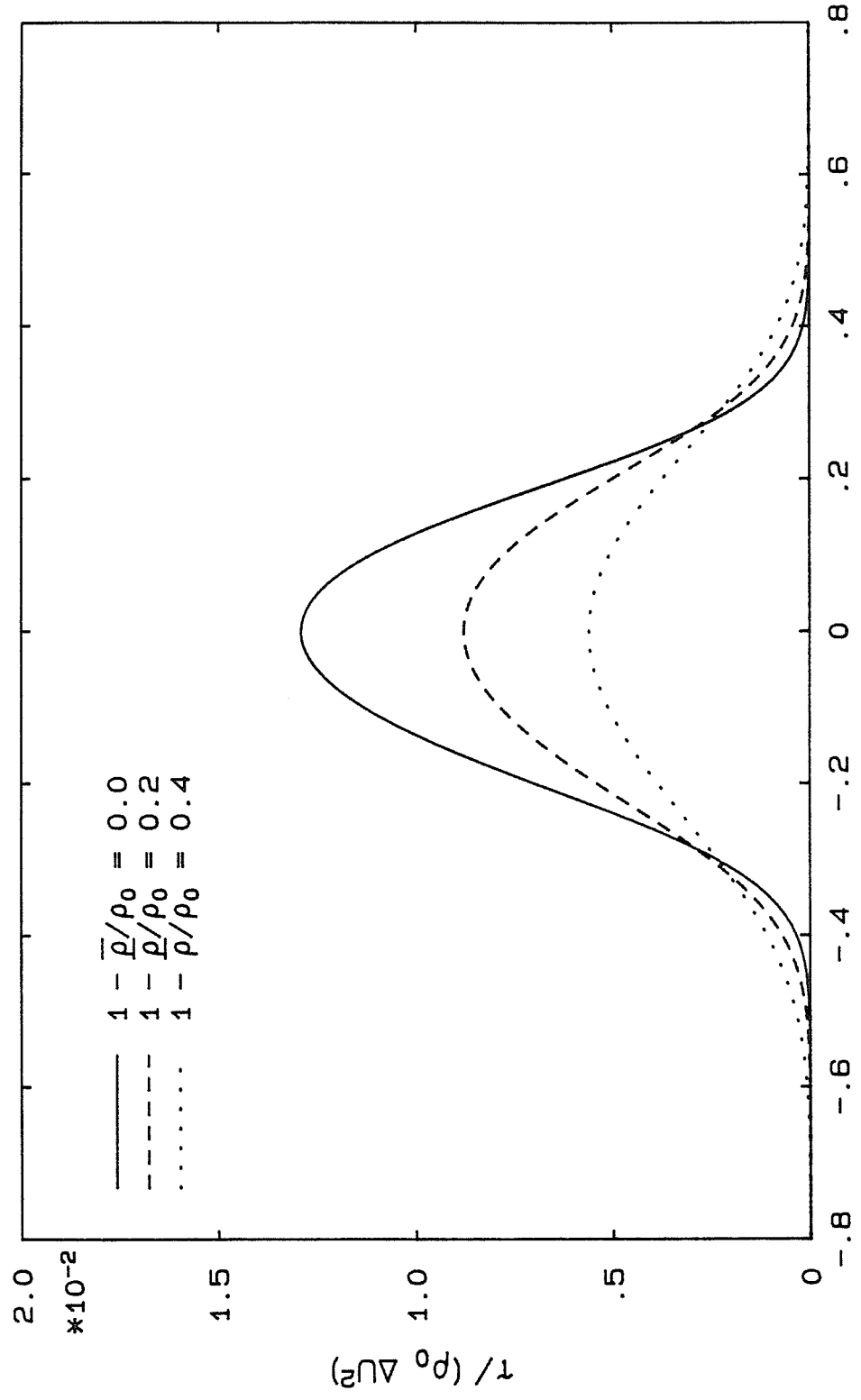

Figure 4.1 Calculated Shear Stress Profiles

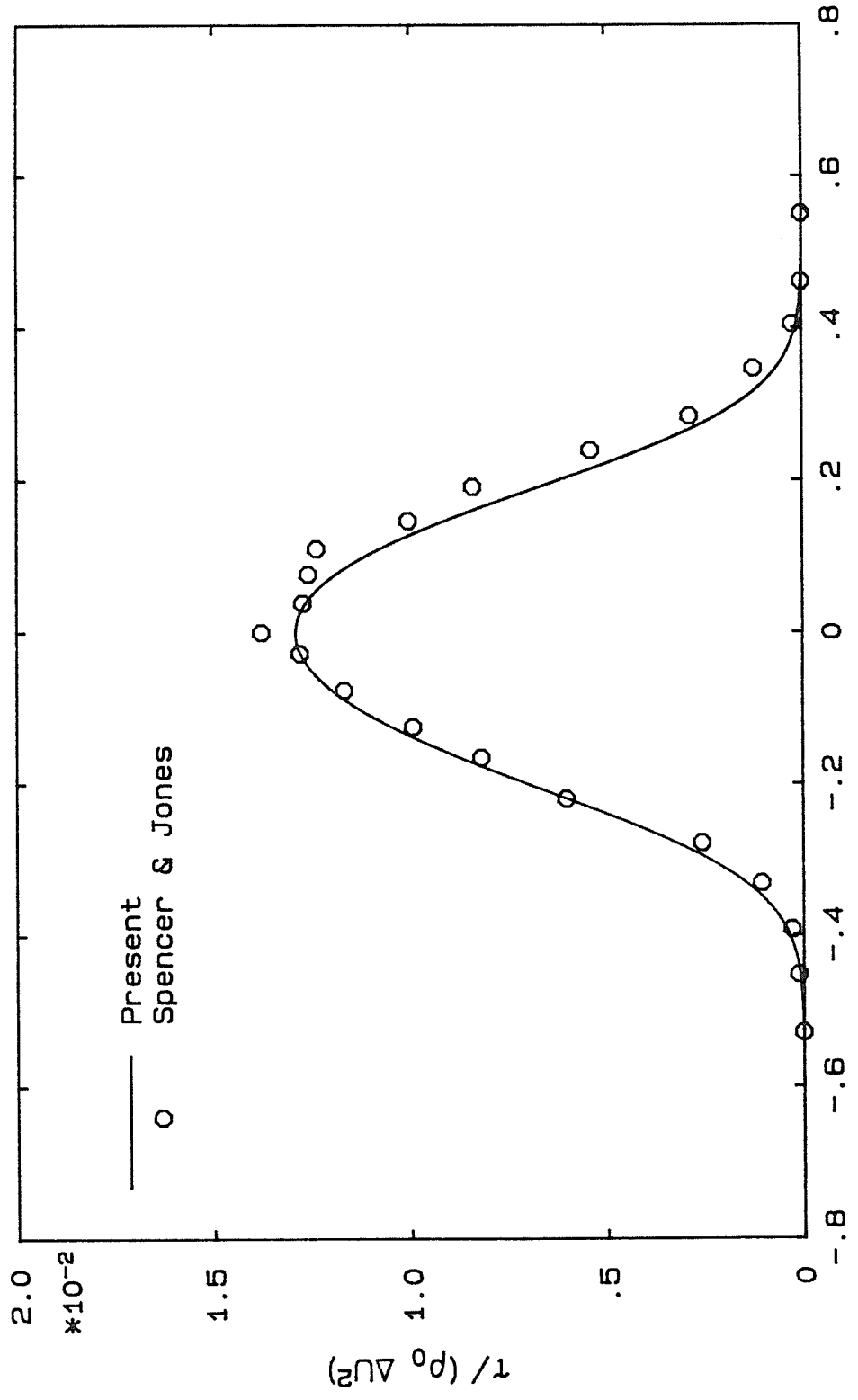

Figure 4.2 Comparison of Calculated Shear Stress Profile with Spencer and Jones

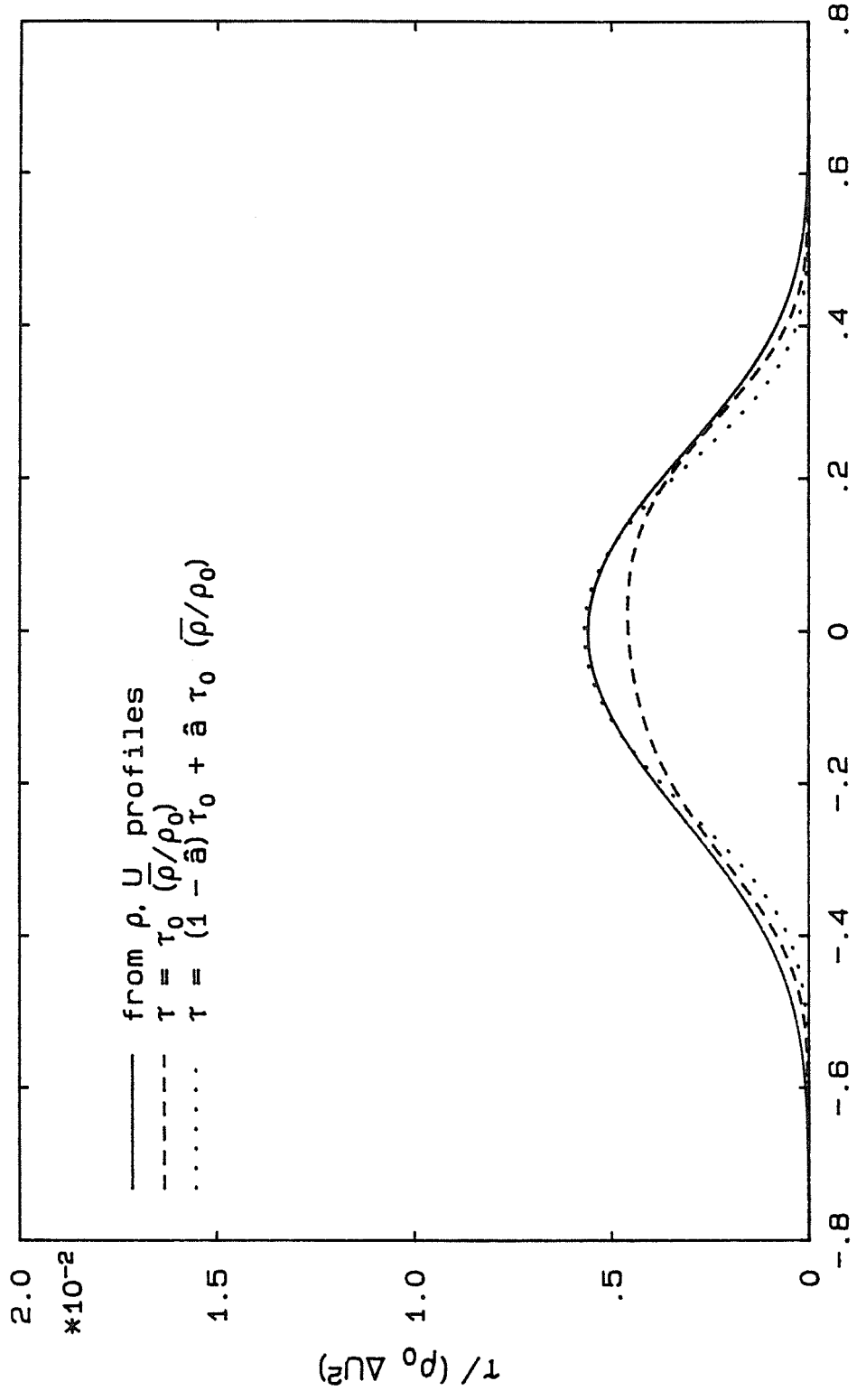

Figure 4.3 Comparison of Different Models for Shear Stress Estimation of High Heat Release

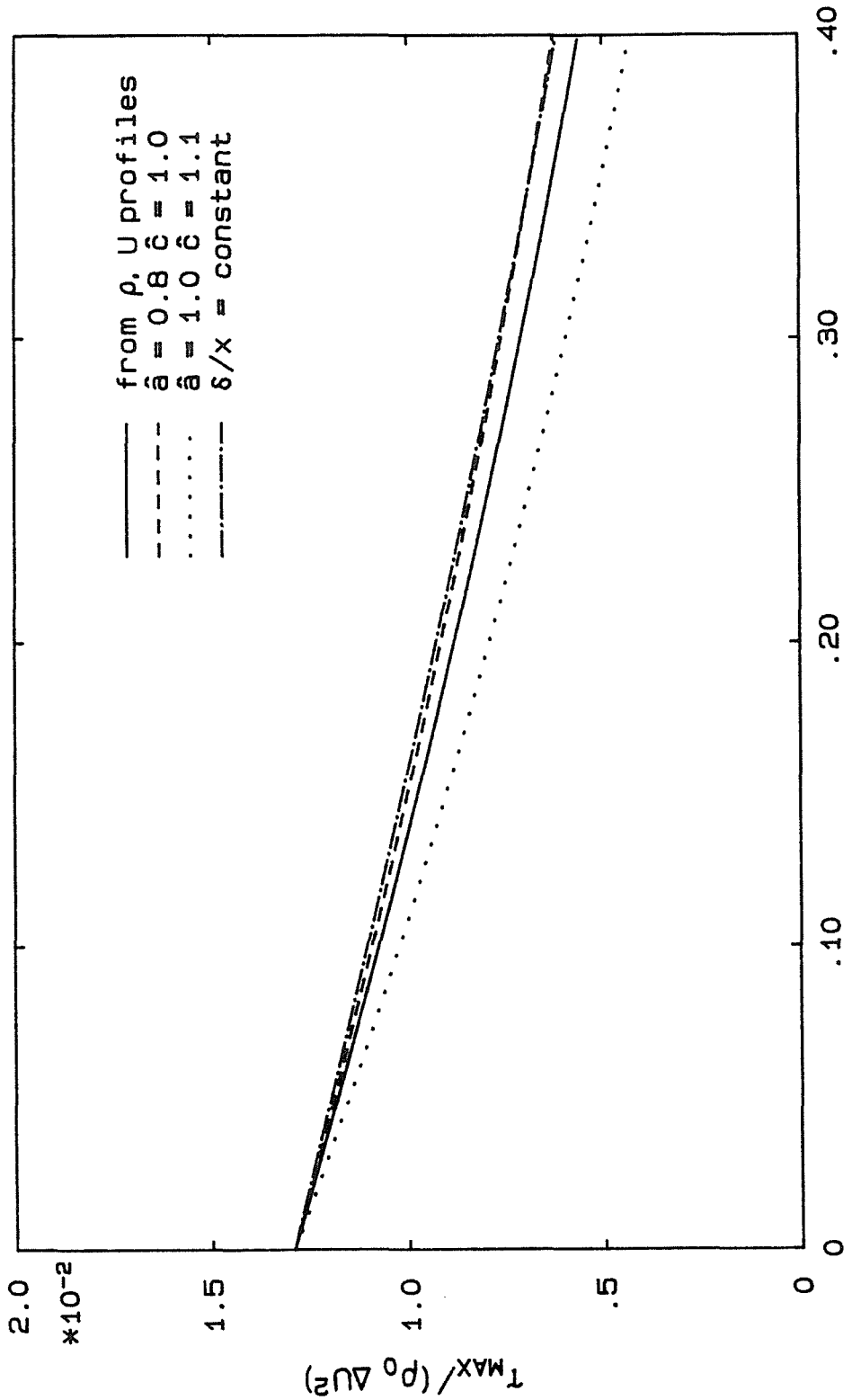

Figure 4.4 Reduction in Maximum Shear Stress with Heat Release

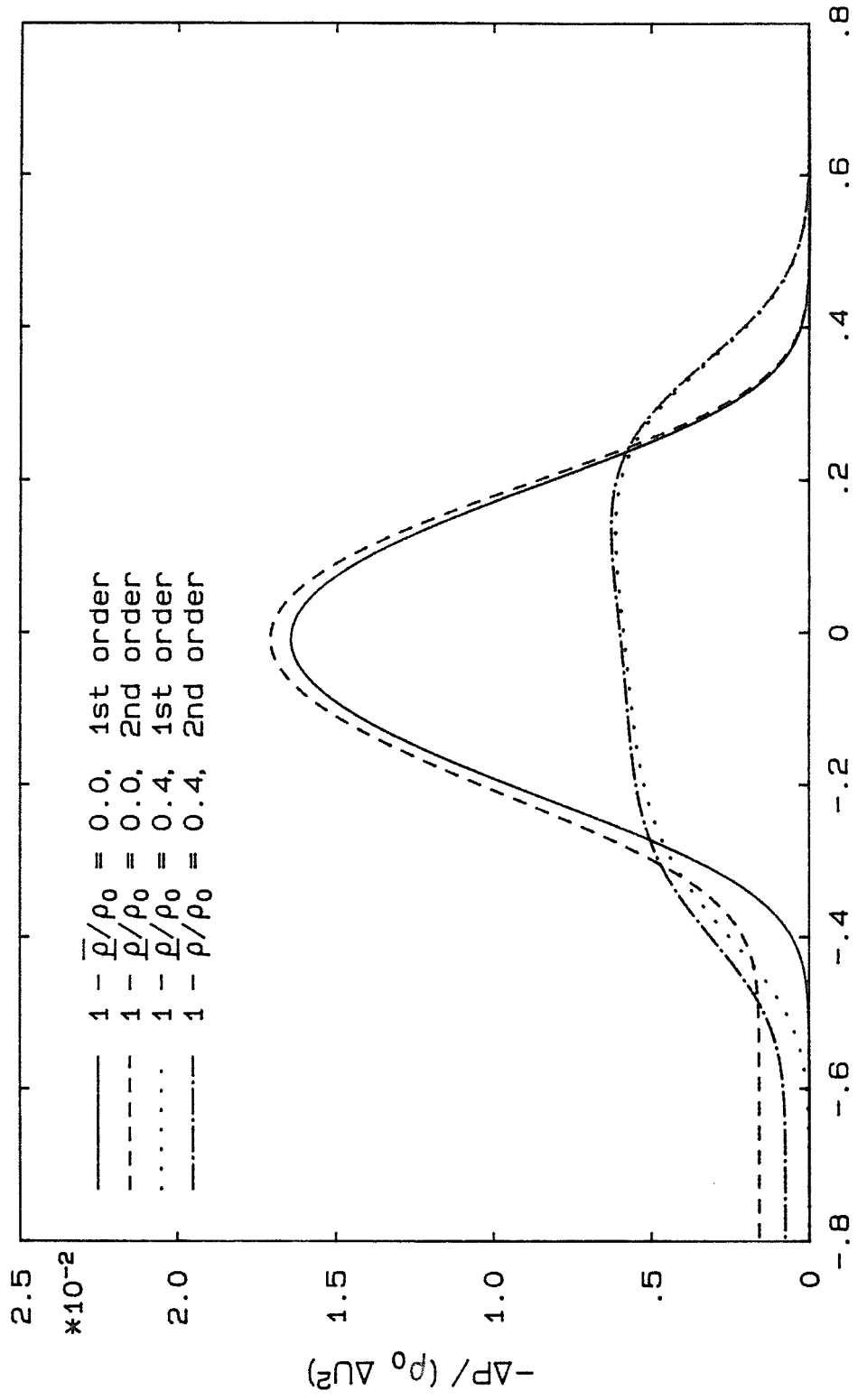

Figure 4.5 Estimated Static Pressure Transverse Profiles

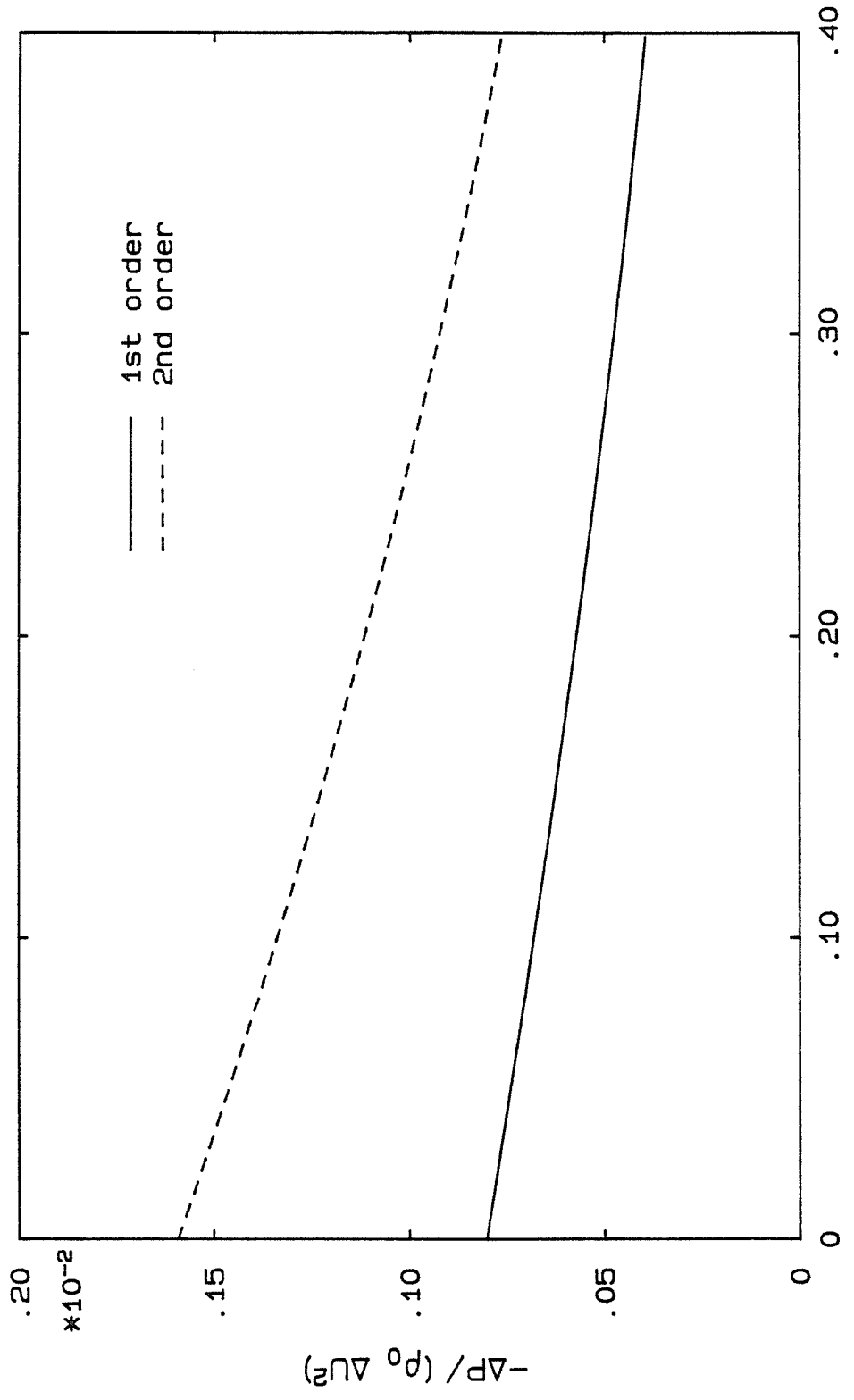

Figure 4.6 Estimated Effect of Heat Release on Static Pressure Decrement Across Layer

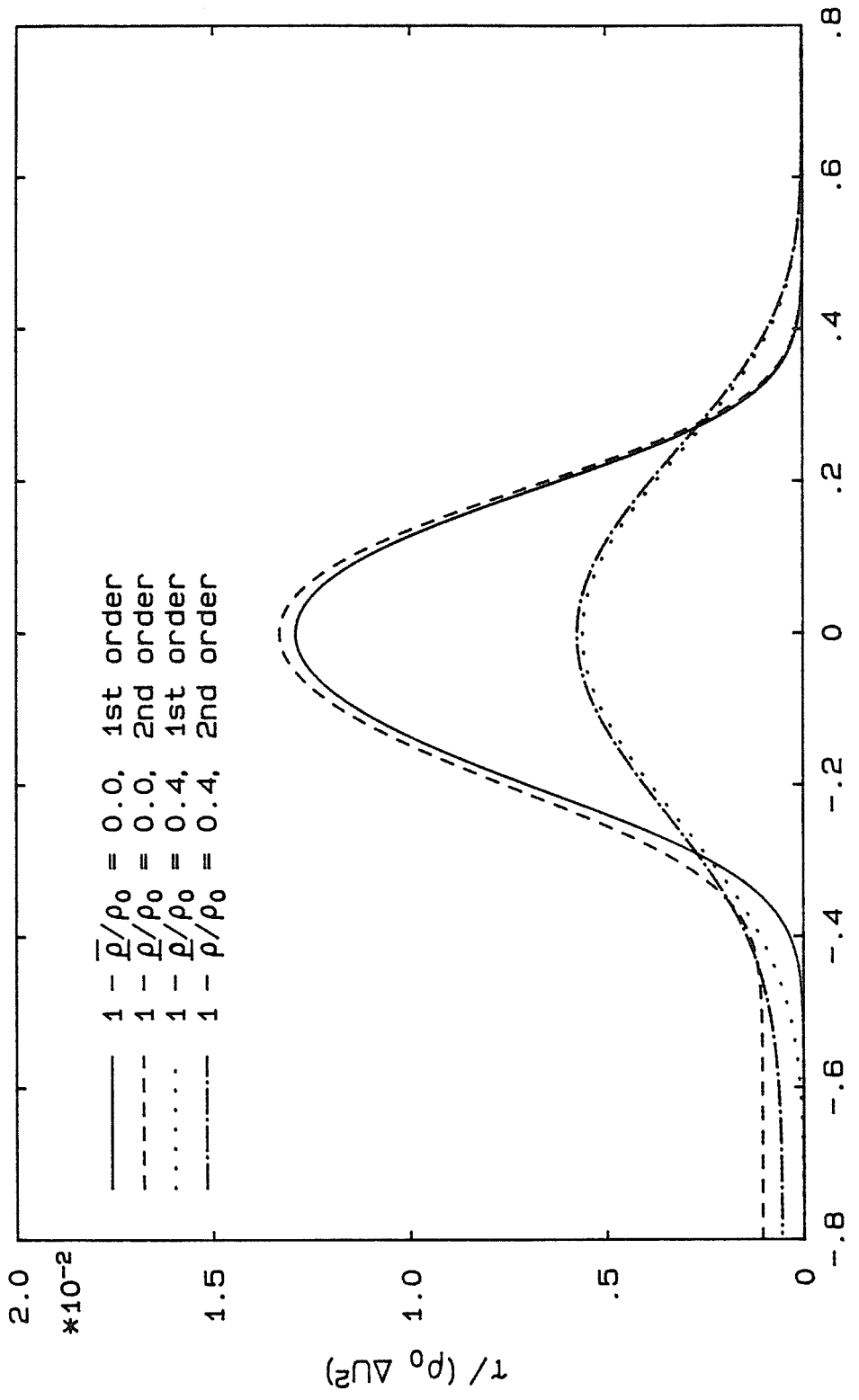

Figure 4.7 Higher Order Shear Stress Calculation

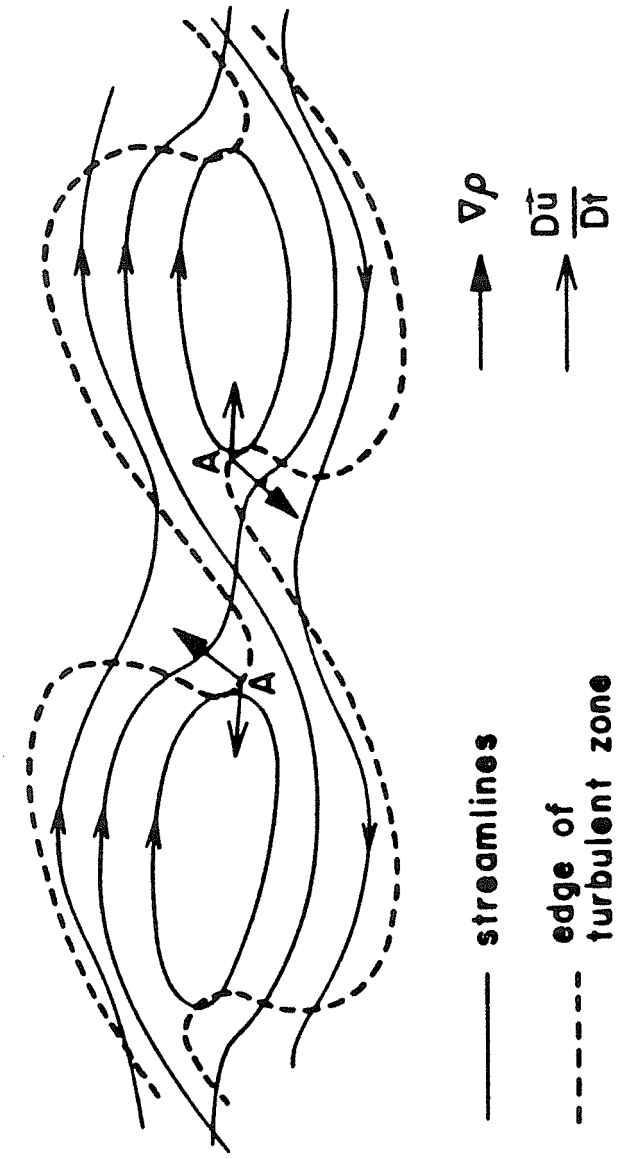

Figure 4.8 Wallace View of Baroclinic Torque Action

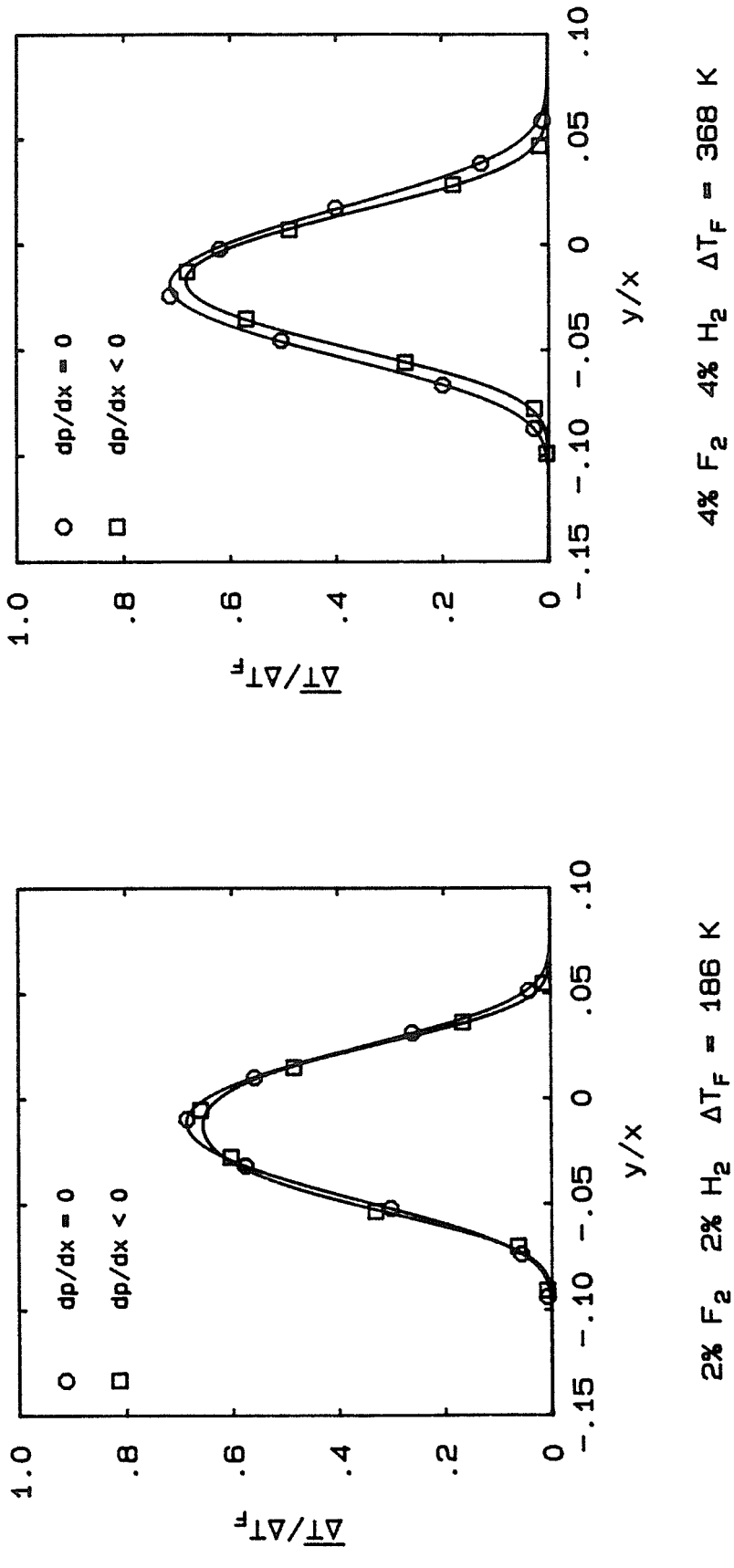

Figure 5.1 Comparison of Mean Temperature Profiles with and without Streamwise Pressure Gradient

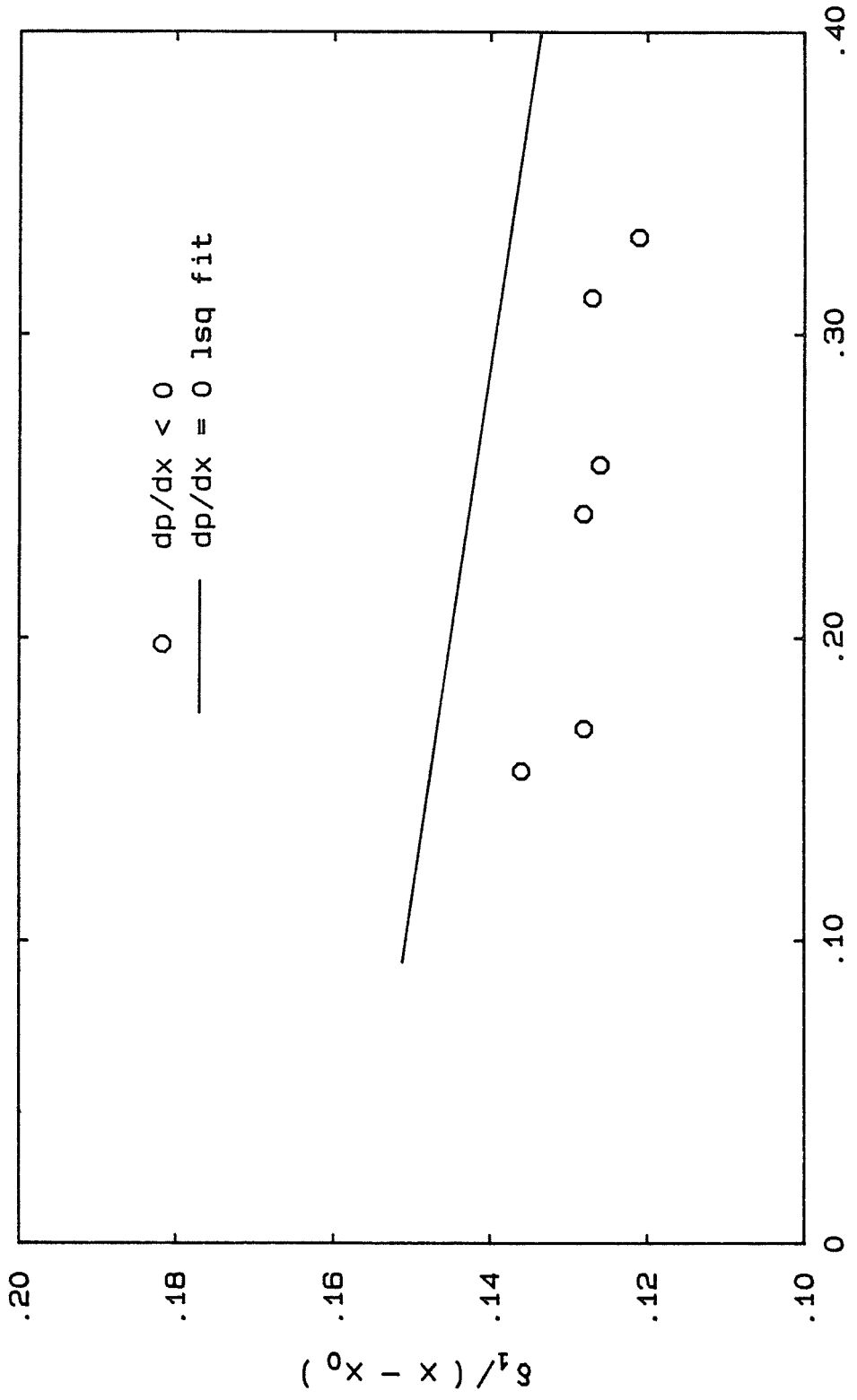

Figure 5.2 Effect of Streamwise Pressure Gradient on Layer Growth Rate

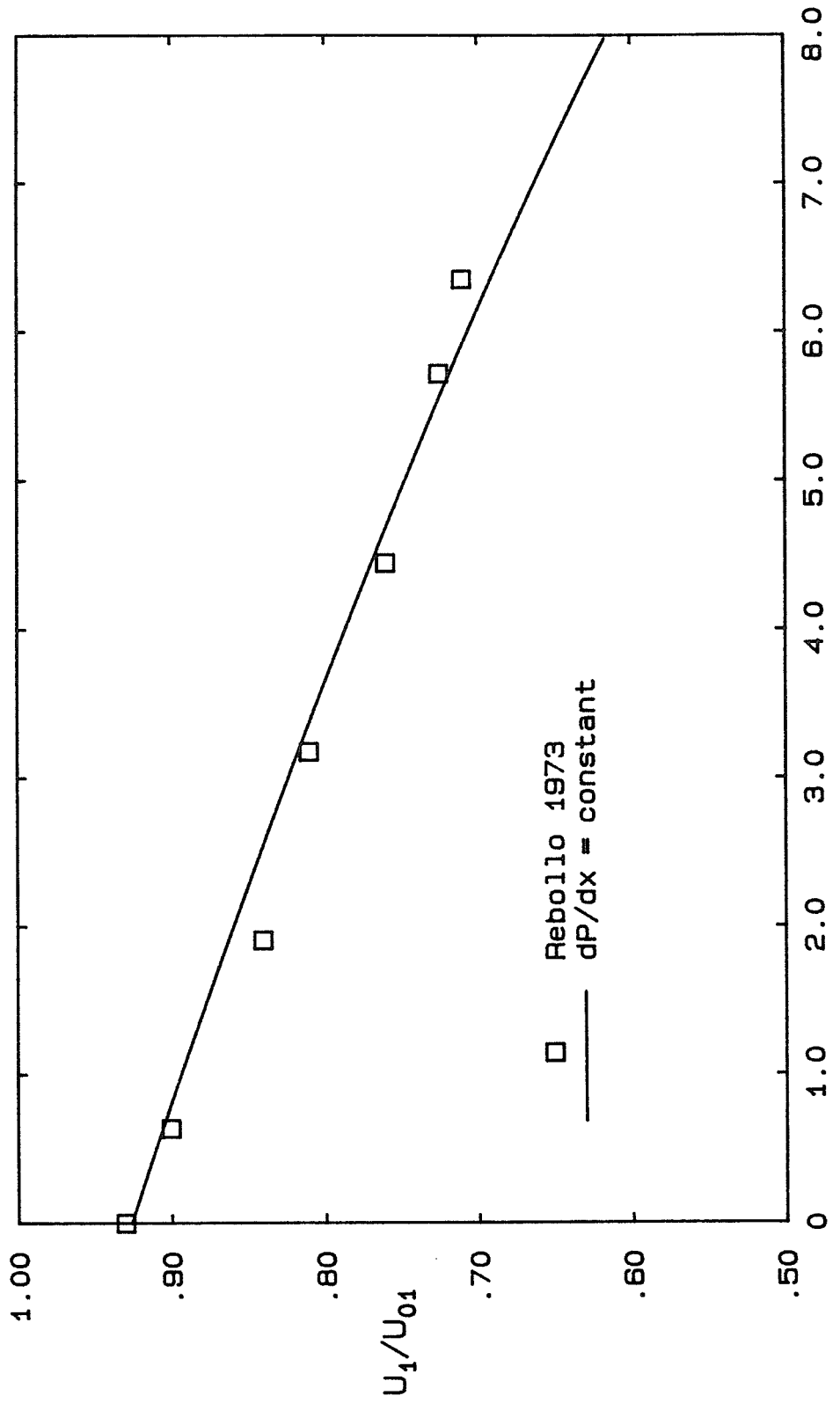

Figure 5.3 Comparison of Calculated Velocity with Rebollo

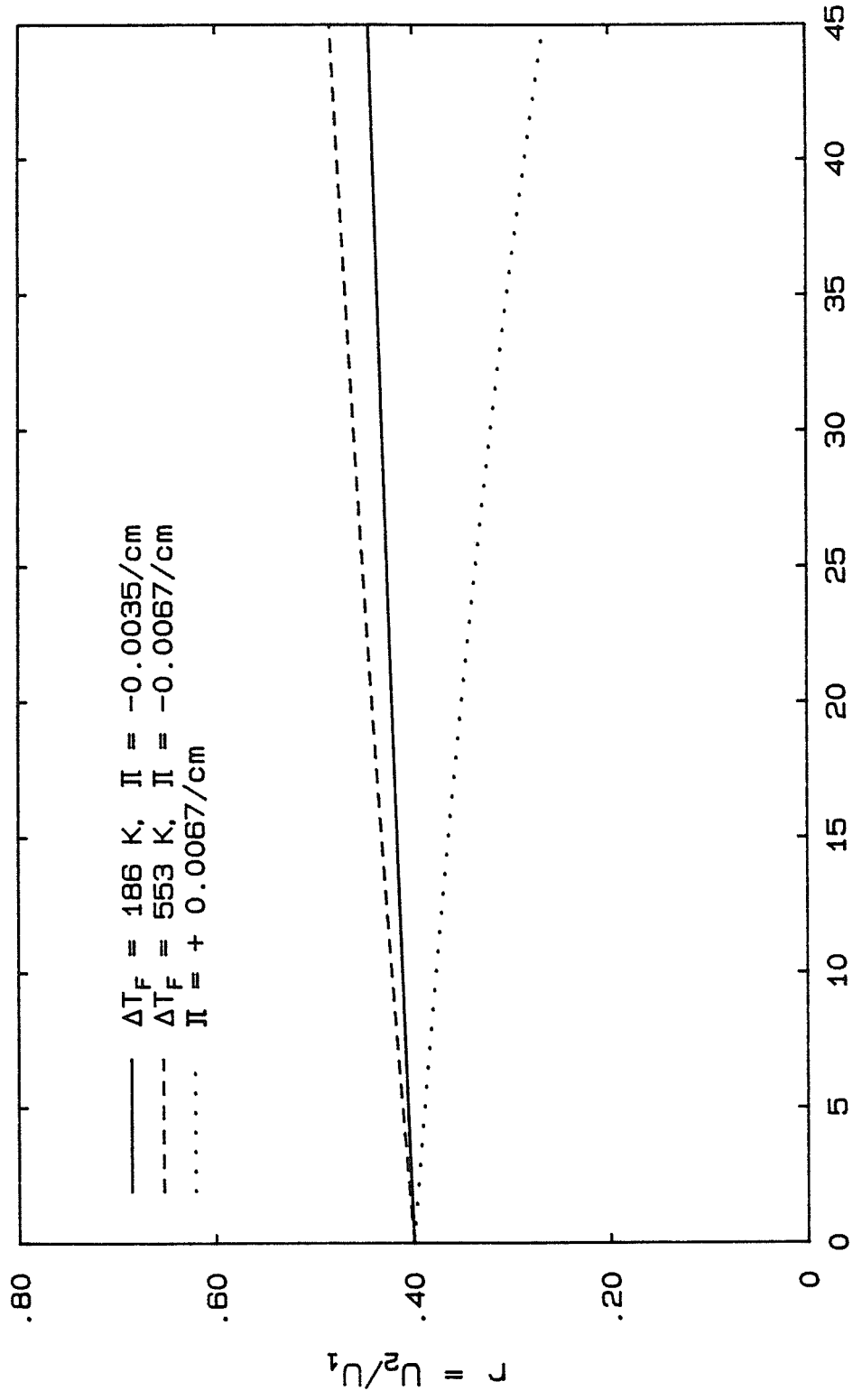

Figure 5.4 Effect of Pressure Gradient on Speed Ratio

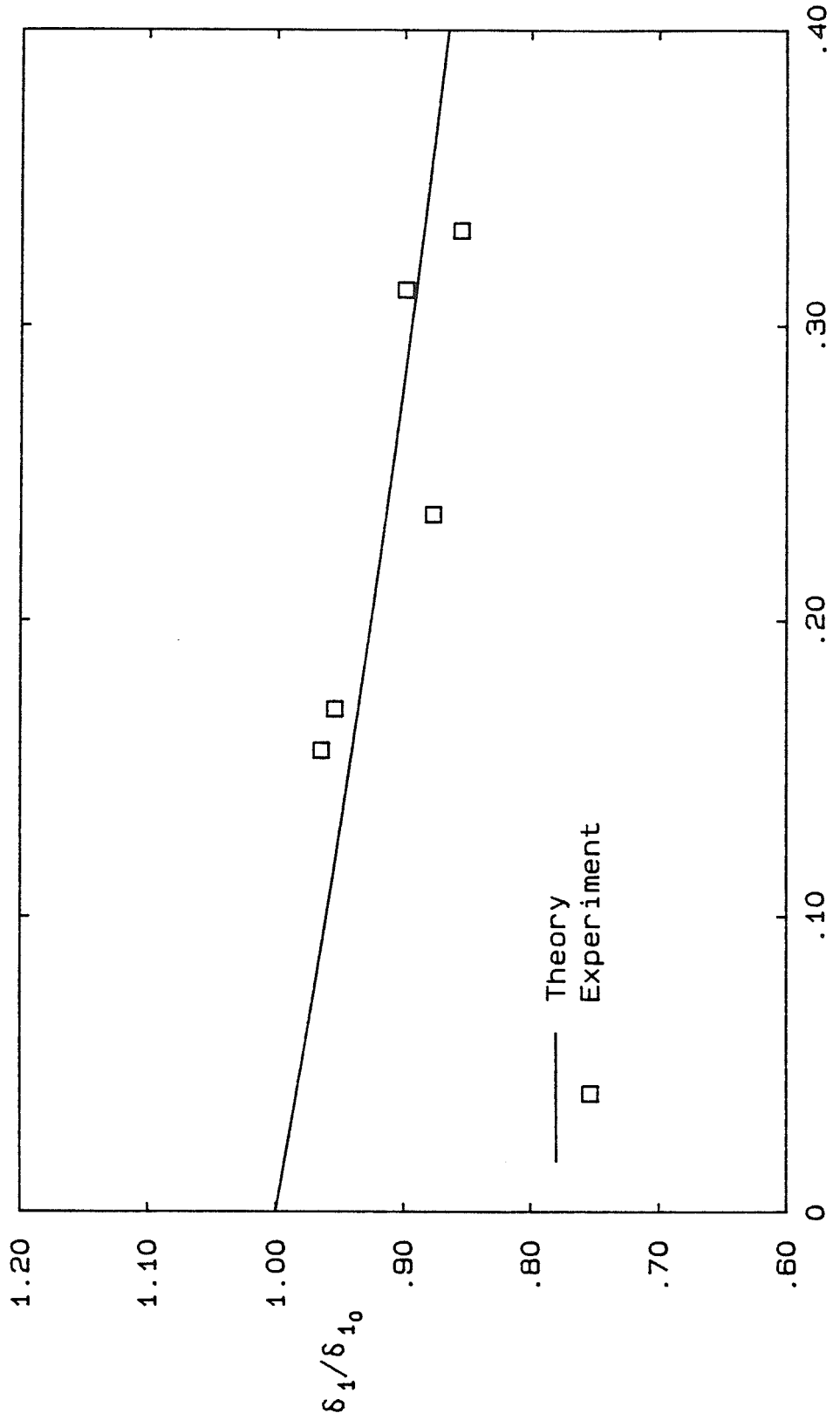

Figure 5.5 Layer Growth with Streamwise Pressure Gradient
Theory versus Experiment

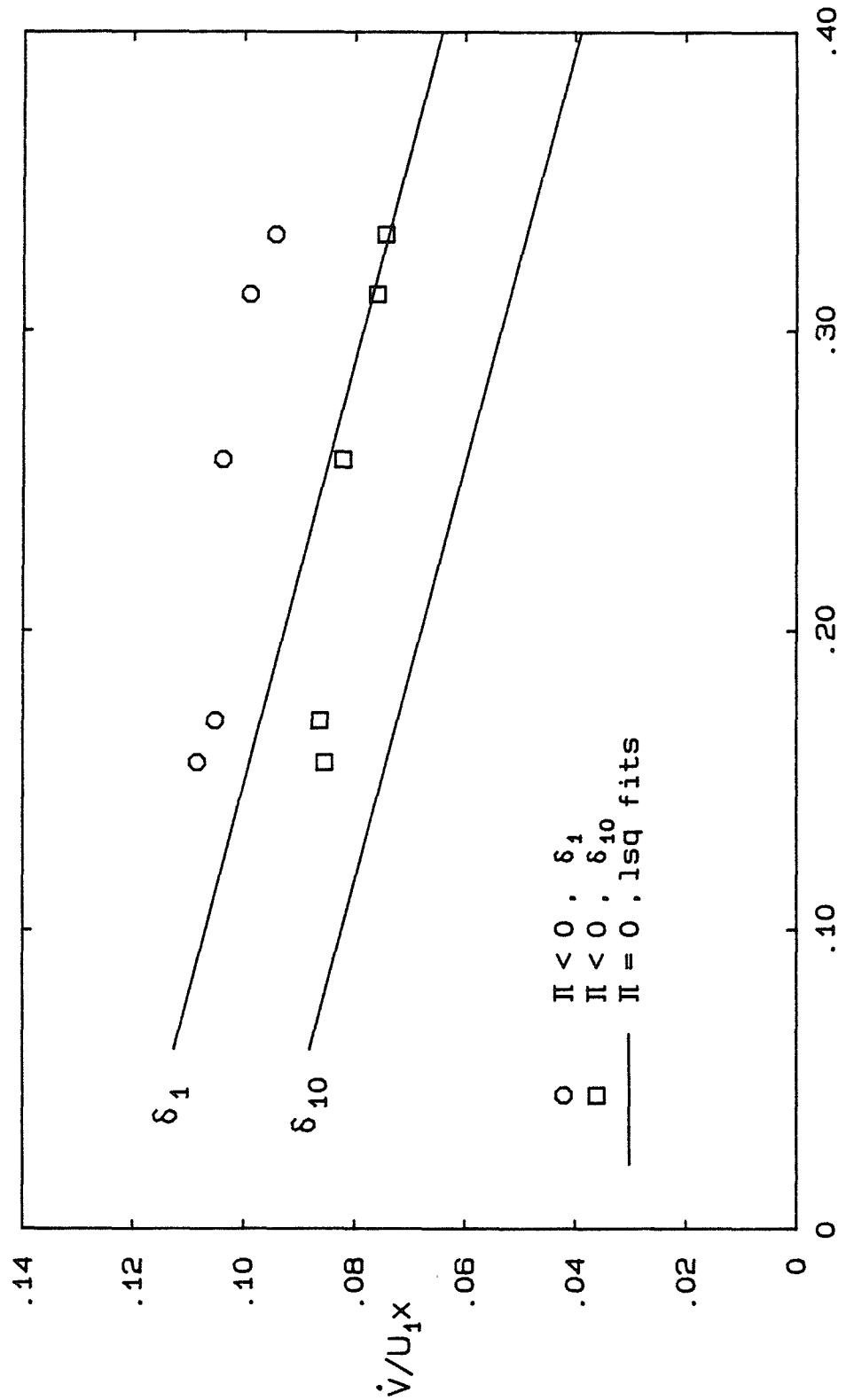

Figure 5.6 Overall Layer Entrainment with Streamwise Pressure Gradient

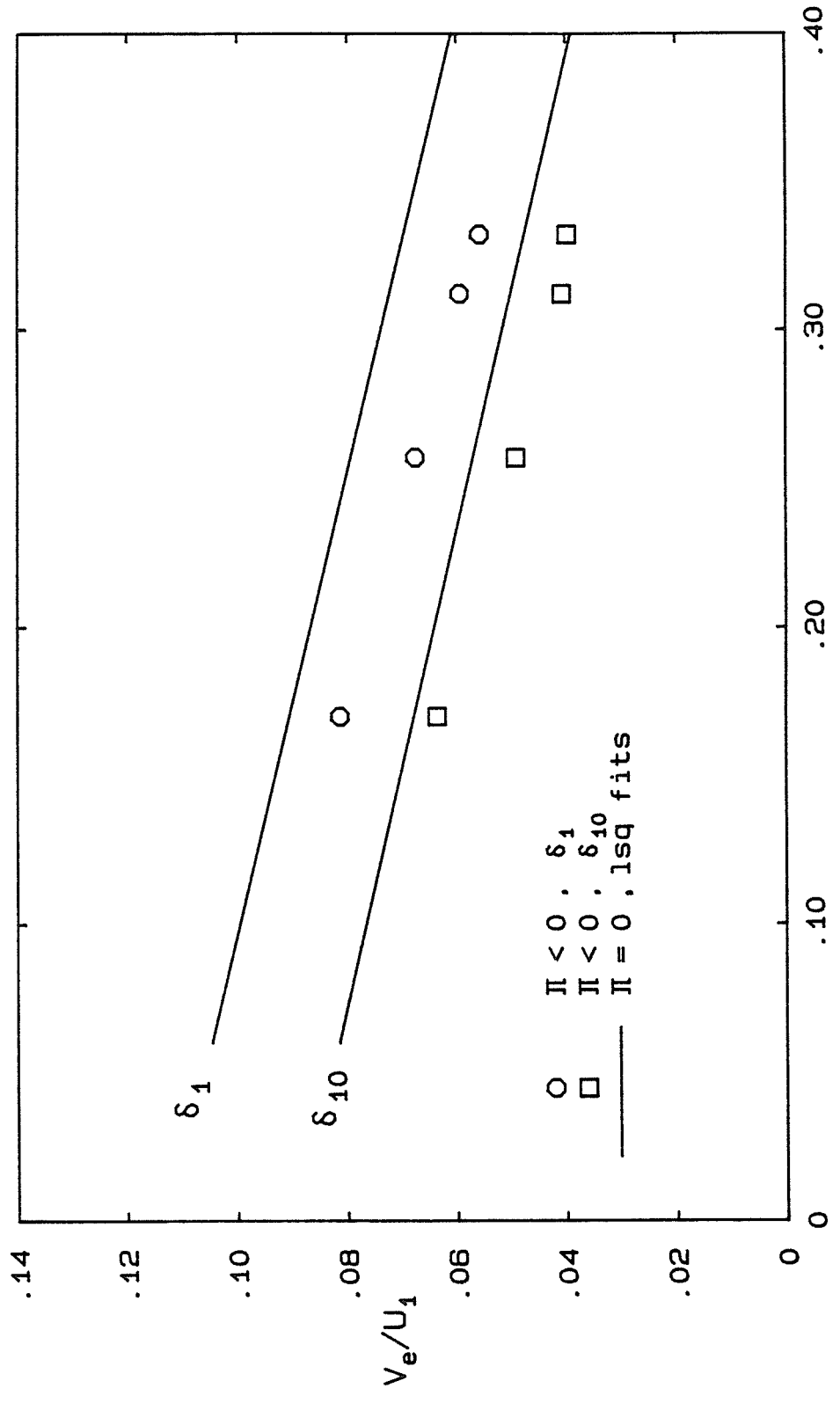

Figure 5.7 Local Entrainment with Streamwise Pressure Gradient

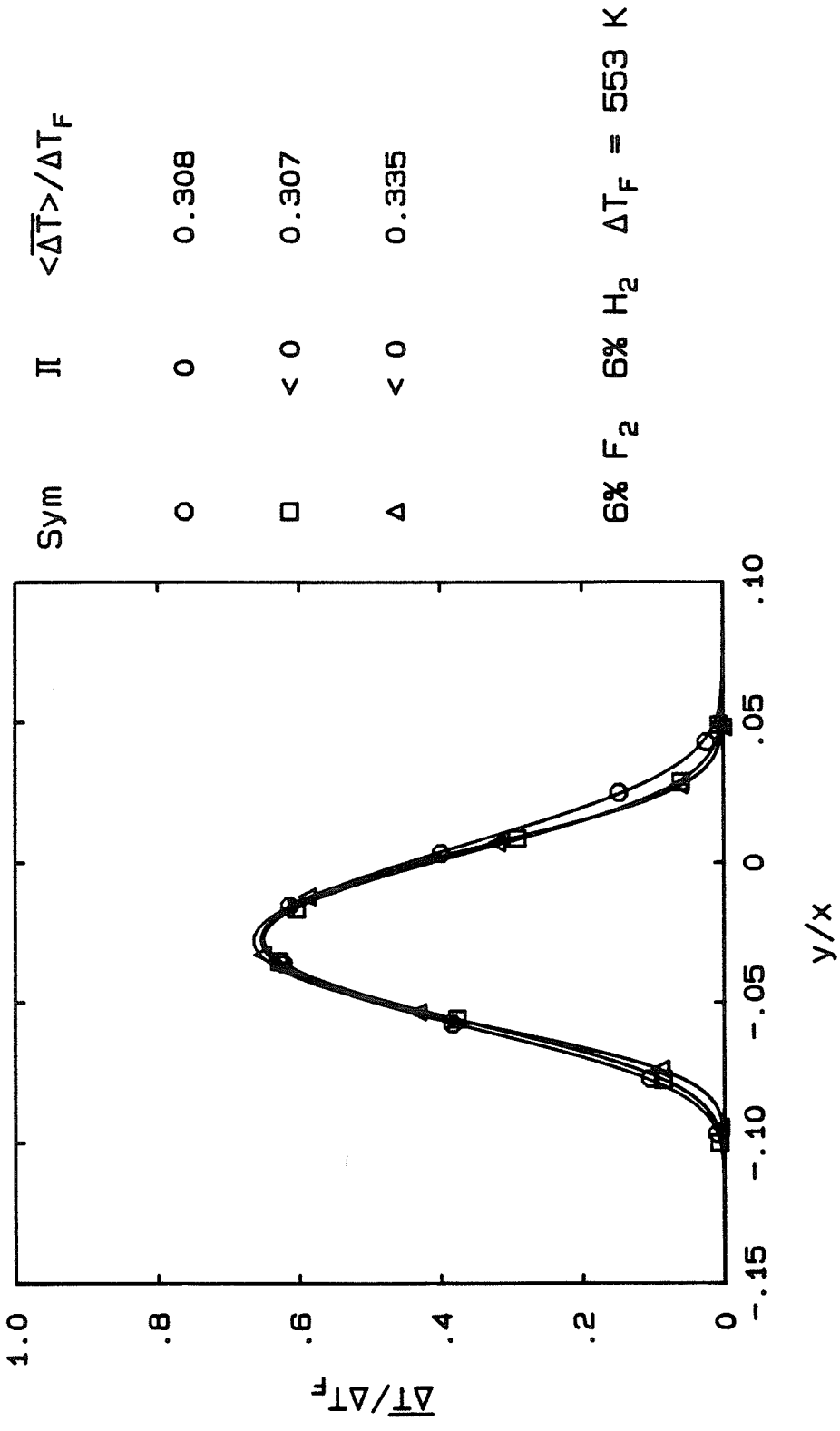

Figure 5.8 Pressure Gradient Effect on Mean Temperature Profile, 6% F_2:6% H_2

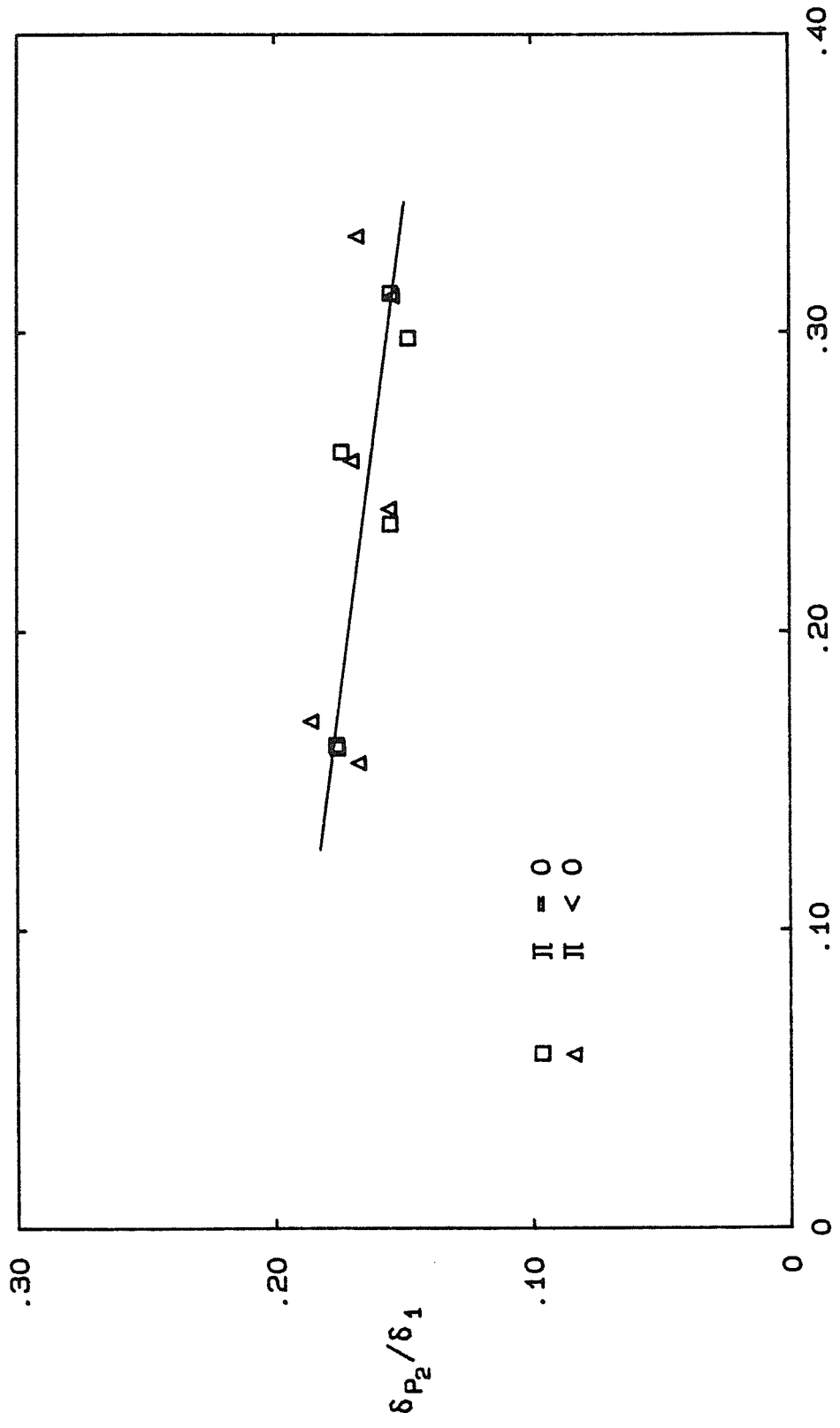

Figure 5.9 Streamwise Pressure Gradient Effect on Product Fraction Thickness

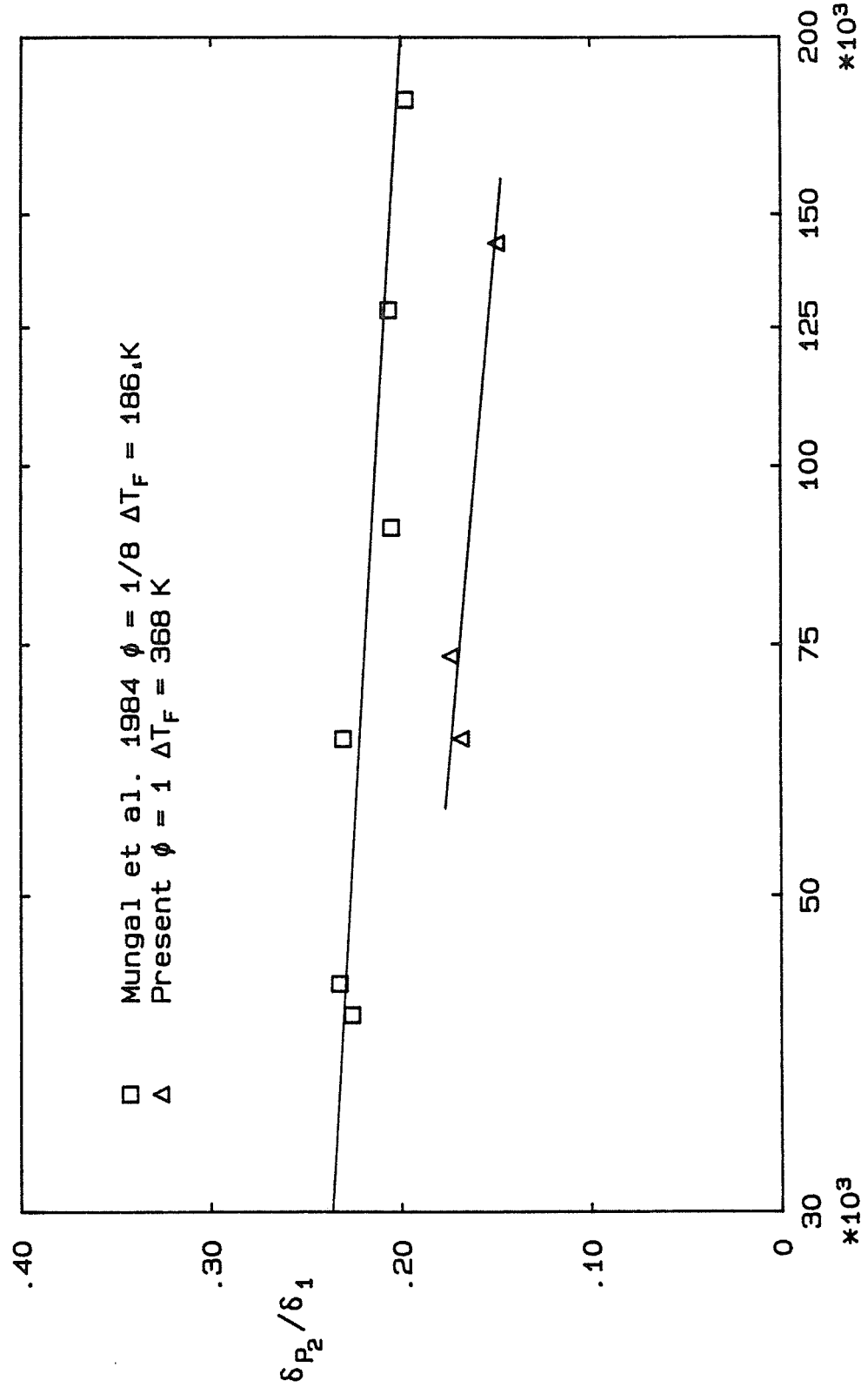

Figure 5.10 Reynolds Number Effect on Product Fraction Thickness

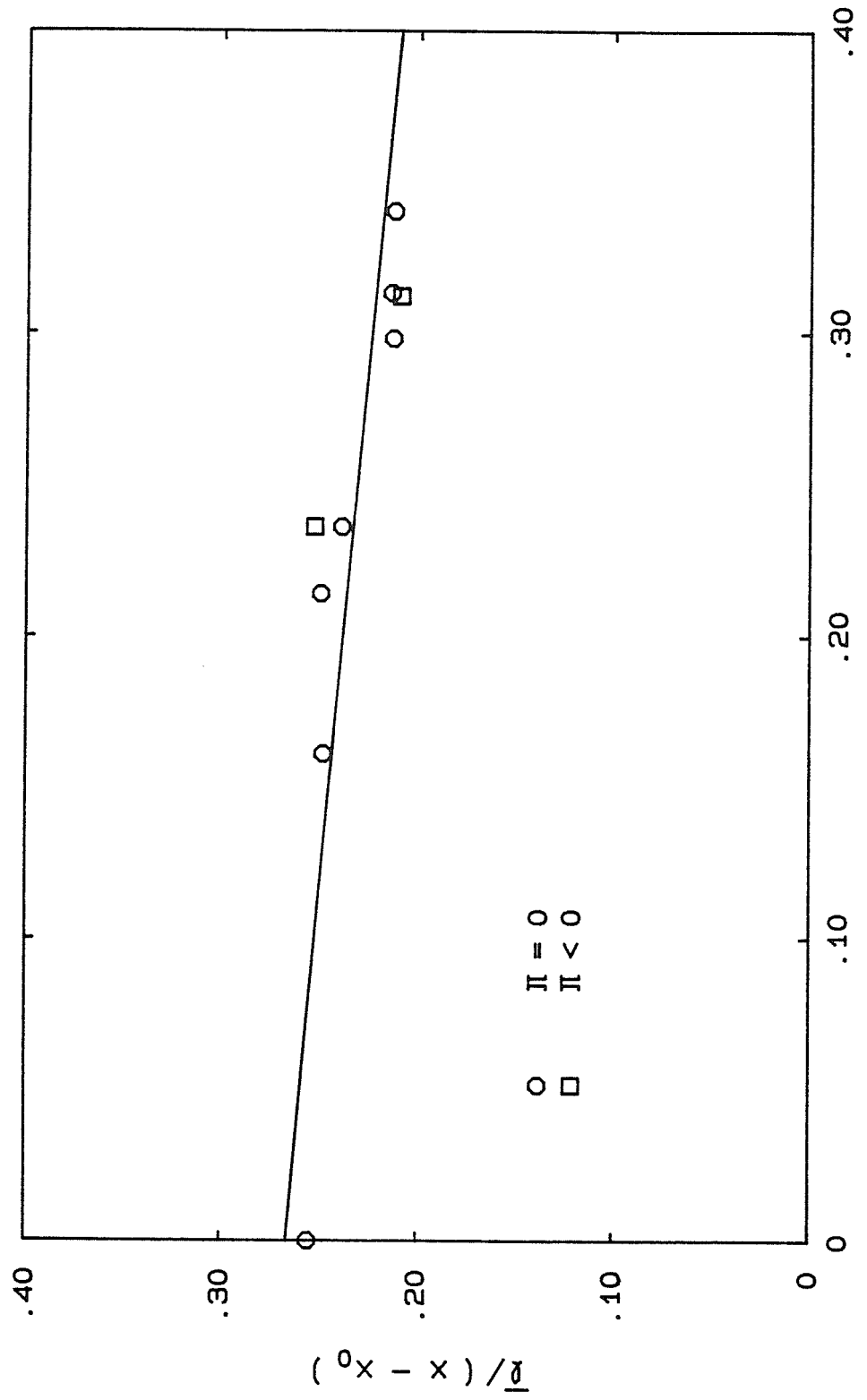

Figure 5.11 Pressure Gradient Effect on Mean Vortex Spacing

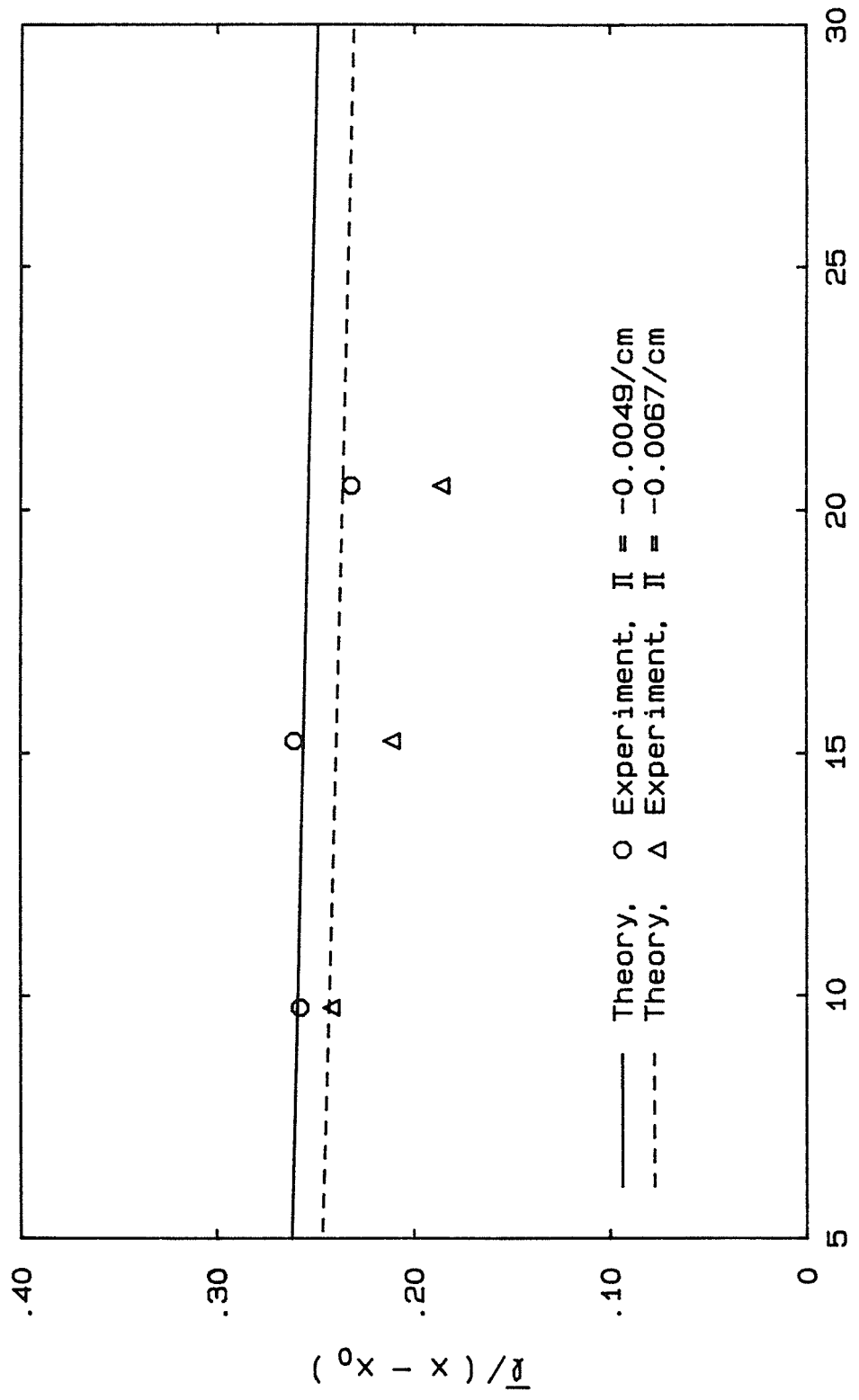

Figure 5.12 Change in Vortex Spacing with Downstream Distance

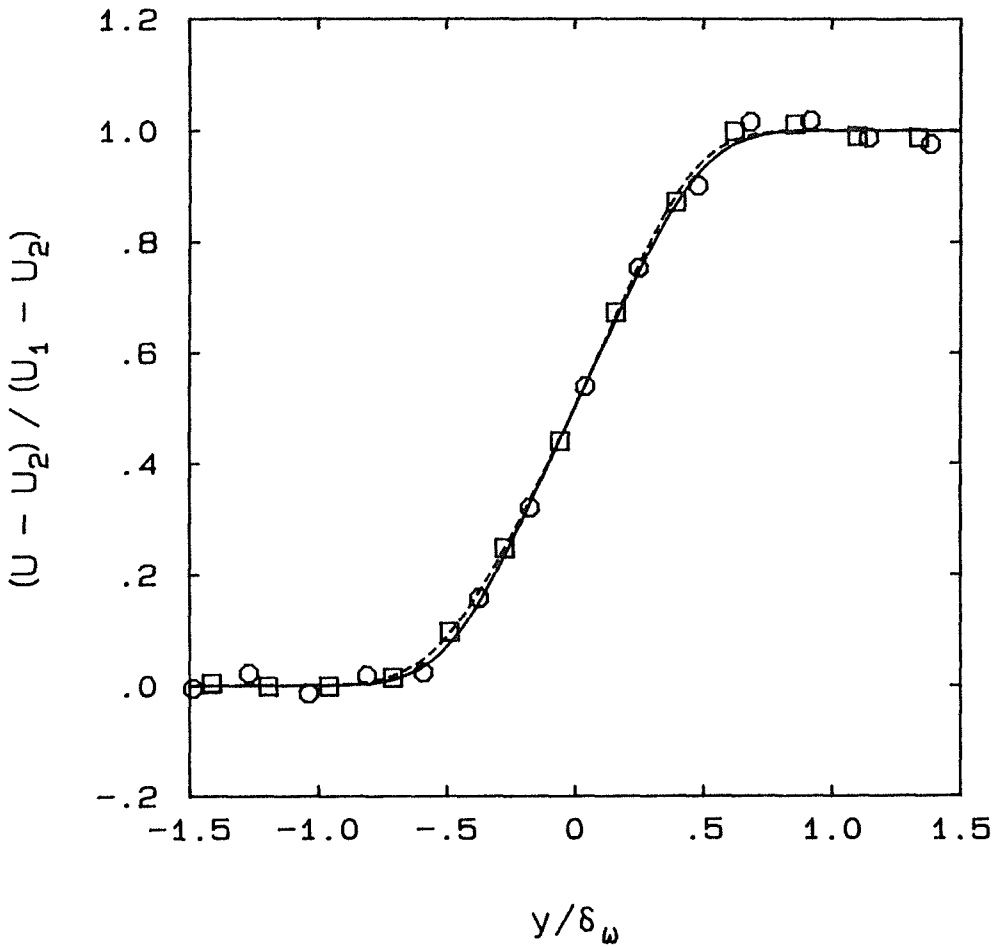

Symbol	○	□
Π / cm^{-1}	0	-0.0064
$\delta_\omega/(x - x_0)$	0.072	0.068

6% F_2 6% H_2 ΔT_F = 553 K

Figure 5.13 Mean Velocity Profiles, with and without Streamwise Pressure Gradient